Davy-Faraday Research Laboratory,

The Royal institution of Great Britain

Department of Chemistry, University College London,

University of London

Magnetic and Electronic Properties of Ternary Chalcogenide Spinels

Thesis submitted for PhD degree

By

Dinah Rosenwyn Parker

Abstract

Compounds with the spinel structure have been extensively studied in the past as they exhibit a wide range of interesting electronic and magnetic properties. The structure, with the general formula AB_2X_4 (where A and B are metal ions and X is O, S, Se or Te), can undergo many different cation and anion substitutions. One example of a magnetically interesting spinel is $CuCr_2Se_4$, which is a high T_C ferromagnet. Substituting copper with zinc on the A-site results in a range of magnetic behaviour that includes collinear ferromagnetism, conical ferromagnetism, canted antiferromagnetism and spin glass. The other end member of the $Cu_{1-x}Zn_xCr_2Se_4$ series, $ZnCr_2Se_4$, is an antiferromagnet with a helical magnetic structure.

The electronic and magnetic properties of these compounds are dependent on the delicate balance of near-neighbour and further-neighbour magnetic interactions taking place between the chromium ions, which leads to the highly diverse behaviour observed across the series.

Compounds from the $Cu_{1-x}Zn_xCr_2Se_4$ series have been synthesized and their properties investigated using a variety of techniques. Structural analysis has been carried out using X-ray powder diffraction methods. The magnetic properties have been studied using DC SQUID magnetometry, AC susceptibility and neutron diffraction. High pressure AC susceptibility has also been used to study the effect of changing the Cr-Cr bond distance on the magnetic properties, while the composition remains unchanged.

Electrical transport measurements have revealed a change from metallic to semiconducting behaviour across the series with increasing x. A magnetoresistance effect is observed in compounds across the series. Where $x \geq 0.1$, a crossover between negative and positive magnetoresistance is seen from low to high temperature.

Compounds in the $Cu_{1-x}Zn_xCr_2Se_{4-y}S_y$ and $CuCr_2Se_{4-y}Br_y$ series have also been prepared to study the effect of substitutions on the X-site on the magnetic properties.

Table of contents

Table of Figures

Acknowledgements

I would first like to thank my supervisors, Dr Mark Green and Professor Steven Bramwell for their help and inspiration and for making my PhD an enjoyable experience. Much thanks also to everyone in the Green and Bramwell groups for their support and friendship throughout; a special thank you to Katie Jewell for the GSAS lessons given with much patience at the beginning of my PhD.

I would also like to thank Professor James Schilling and his group for allowing me to use their high pressure AC susceptibility equipment in Washington University and for making me feel so welcome during my visit. Thanks especially to Takahiro Tomita for giving up a his time to help me with the experiments during my stay.

Much thanks to everyone I have worked with at the Royal Institution and UCL for their help and support. I would particularly like to thank Scott Turner and Simon Carling for their assistance and advice on the SQUID and Maglab, Ian Watts for his help with everything experimental and Andrew Wills for helping me, both in theory and practice, with the neutron diffraction experiments.

Finally, thank you to all my friends and family for their support during my PhD, especially during the last few months of the write up when I have needed it most.

Chapter 1 Introduction

1.1 The Spinel Series

The spinel series of compounds have been widely studied due to the great variety of cation combinations possible within the group and the extensive range of physical properties achievable. The structure is named after the naturally occurring compound spinel, $MgAl_2O_4$.

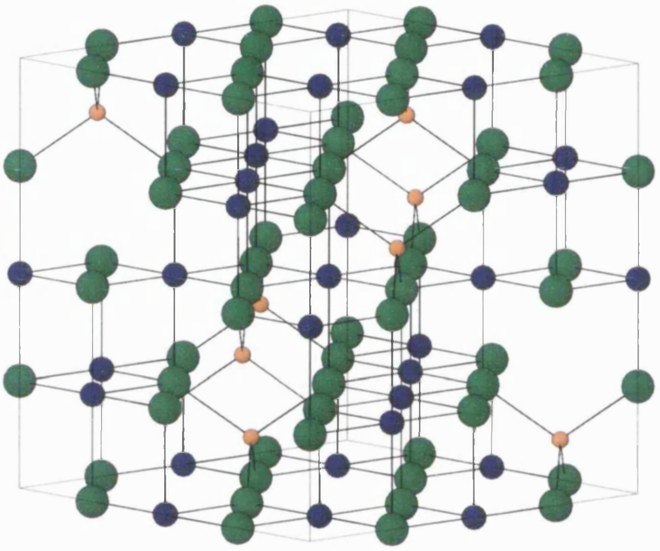

Figure 1.1 *Diagram of the spinel structure, general formula* AB_2X_4, *where the red, blue and green spheres represent the A, B and X ions respectively.*

Spinel compounds show a diverse range of chemical and physical properties. It is possible to prepare many solid solutions, with properties varying continuously with composition, leading to great potential in materials design for a variety of applications. Sections 1.1 and 1.2 discuss the structure and magnetic and electronic properties of spinels, in particular the chalcogenide spinels AB_2X_4 (where X = S, Se or Te).

1.1.1 The Spinel Structure

The spinel structure was first identified in 1915 by Bragg [1] and Nishikawa [2] and has the space group $Fd\bar{3}m$. The general structure takes the form AB_2X_4 where A and B are metal ions and X is O, S, Se or Te. The ions form an almost close packed *fcc* array of anions with holes partially filled by cations. In the normal spinel the cation distribution is $A[B_2]X_4$. A distribution of $B[AB]X_4$ corresponds to the inverse spinel. Intermediate cation distributions have also been observed, i.e. $(A_{1-\partial}B_\partial)[A_\partial B_{2-\partial}]X_4$ where ∂ is the degree of inversion and has a value of zero and one for the normal and inverse distributions respectively

In a normal spinel the A ions (usually divalent) lie in the tetrahedral sites and form a diamond lattice which can also be thought of as two T_d *fcc* Bravais lattices (figure 1.2 a). The B ions (usually trivalent) lie in the octahedral sites and form four Bravais lattices with the point group D_3d (figure1.2 b). Twice as many octahedral as tetrahedral sites are occupied by the cations. Not all of the holes are filled by cations in an elementary cube of thirty-two anions, only eight (i.e.1/8) of the A-type sites and 16 (i.e. 1/2) of the B-type sites are occupied.

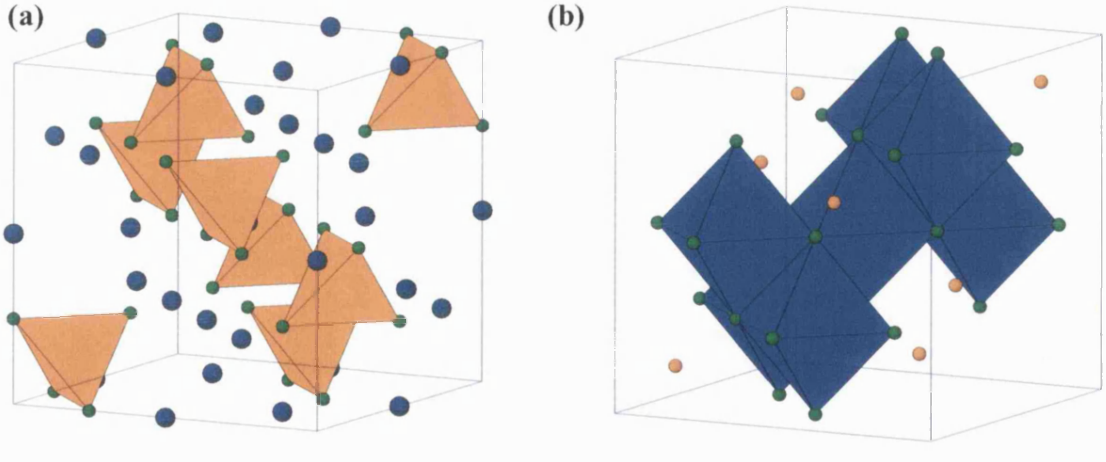

Figure 1.2 *Diagram of the spinel unit cell showing the AX_4 tetrahedra (a) and BX_6 octahedra (b)*

The smallest unit cell is rhombohedral and contains two AB_2X_4 molecules; however the structure is usually described with a cubic cell containing eight molecules. The X atom is not usually located in the exact position in the fcc sub lattice and the extent of deviation is given by a parameter *u*, defined in figure 1.3. This reflects the adjustment of the crystal structure to accommodate different cation radius ratios in the tetrahedral and octahedral sites.

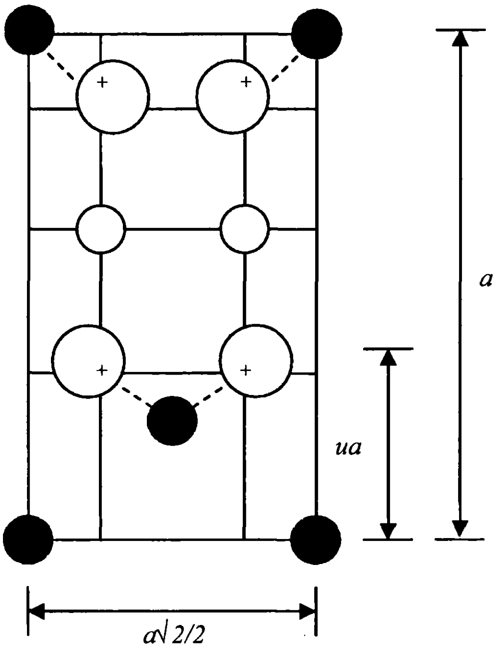

Figure 1.3 *Diagram defining the deformation parameter u, depicting half of a* $(\bar{1}10)$ *plane. The tetrahedral cations (black) cause a displacement of the X atoms (large circles) along the ‹111› direction.*

For the ideal spinel structure with a close-packed array of X atoms *u* is equal to 0.375. The deformation is caused by the extent of the A cations which are almost always too large for the ideal space allowed by the close packed X atoms, resulting in a displacement along the ‹111› without changing the overall $\bar{4}3m$ symmetry.

1.1.2 Cation site preference

The spinel crystal structure is very stable and the bonding is predominantly ionic; however covalent bonding effects can influence which sites are occupied by certain cations [3].

Crystal field theory (which is described in detail in chapter 2, section 2.4.1) has been found to predict cation site occupation with extreme accuracy in spinel compounds. For example, in chromium spinels the Cr^{3+} is always in the octahedral site, corresponding to high octahedral site stabilisation energy, where as in ferrites the site occupancy is dependent on the divalent cation as there is zero crystal field stabilisation. Where there is little occupational preference for the divalent ion the ferrites take the mixed spinel structure.

Crystal field theory is able to predict the cation distribution within the compound with unusual accuracy due to the lack of influence of the Madelung energy (the electrostatic interaction between the atoms in the crystal). This is usually a dominant factor in crystal structures, and the change in u parameter between a normal and inverse spinel would normally result in a change in Madelung energy of several eV. However in spinel compounds the lattice parameter is able to vary to accommodate changes in u which leaves the electrostatic energy practically unchanged and therefore the crystal field splitting of the d orbital takes on increased significance.

Polarisation effects can also influence the site preference of the cations. Where there is very little polarisation, i.e. the electronic charge distribution remains nearly spherical, the bonding will be covalent and the tetrahedral sites will be preferred. It is normally only the cations ions with a d^5 or d^{10} spherical symmetry such as Fe^{3+}, Ga^{3+} or Zn^{2+} that show a tetrahedral site preference. In the case of Fe^{3+} and Ga^{3+} this results in the formation of the inverse spinel structure.

1.1.3 Inverse Spinels

The degree of inversion δ of an inverse spinel can be partially controlled by synthesis conditions. Quenching of the reaction mixture can retain the high temperature distribution, expected to be a statistical distribution where $\delta \sim 2/3$. Under slow cooling synthesis conditions the distribution will be dependent on the rate of cation redistribution within the sample.

It is common to see ordering of the cations in an inverse spinel where more than one atom is occupying the same crystallographic site. For example in inverse ferrites (001) layers of octahedral sites are occupied alternately by divalent (D) and trivalent (T) cations. Ordering of the octahedral site has also been found in compounds with a D:T ratio of 1:3, and ordering of tetrahedral sites can be seen in a 1:1 ratio.

1.2 Chalcogenide spinels

1.2.1 General features of Chalcogenide Spinels

The chalcogenide spinels (i.e. AB_2X_4 where A and B are metals and X is S, Se or Te) exhibit a wide range of physical properties, far more diverse than that of the oxide spinels [4]. Oxide spinels are generally semiconducting or insulating with antiferromagnetic interactions, whereas chalcogenide spinels can also show metallic and superconduction and have ferri- and ferromagnetic as well as antiferromagnetic interactions. For example $CdCr_2S_4$ is a ferromagnetic semiconductor and $ZnCr_2Se_4$ an antiferromagnetic semiconductor. $MnCr_2S_4$ and $FeCr_2S_4$ are both ferrimagnetic semiconductors whereas $CuCr_2Se_4$ is a ferromagnetic metal. Extensive research has been carried out on chalcogenide spinel compounds prompted largely by the existence of interesting and useful magnetic and electronic properties, such as high T_C ferromagnetism and semiconductivity.

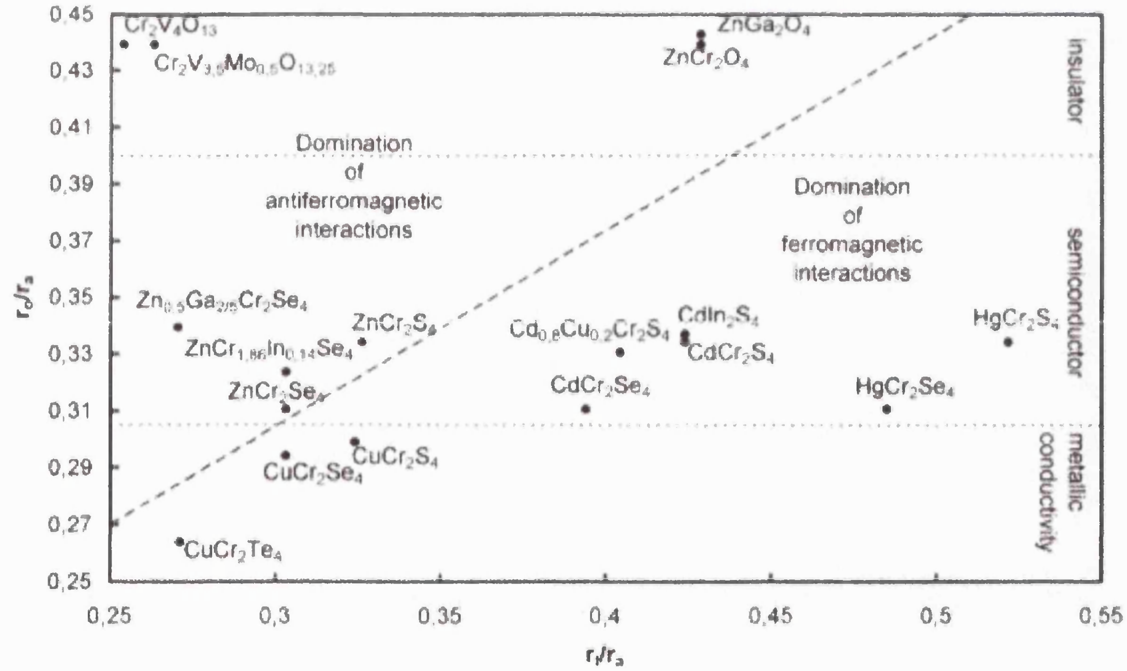

Figure 1.4 *Diagram showing the variation of magnetic and electronic properties achievable in a selection of spinel compounds, in terms of cation/anion ratio. Where r_t is the radius of the tetrahedrally coordinated cation, r_o the radius of the octahedrally coordinated cation and r_a the radius of the anion. Taken from reference [5].*

It has been proposed that the correlations between the ionic radii of the cations and anions within the lattice have a significant role to play in determining the electronic and magnetic properties of spinel compounds [5]. This is shown in figure 1.4, which also illustrates well the wide range of physical properties observed.

The diverse range of behaviour found in these compounds is due to a number of factors. The magnetic exchange interactions (discussed in section 1.2.2) are complex and depend a great deal on the B ion bond distances. The ability of the spinel structure to incorporate a variety of cation substitutions on the A and B sites, involving ions of different size and magnetic character, is also a significant feature.

1.2.2 Exchange interactions in chromium chalcogenide spinels

Chromium containing chalcogenide spinels show a particularly wide range of magnetic and electronic properties. A combination of antiferromagnetic near neighbour interactions and ferromagnetic further neighbour superexchange interactions lead to a diversity in behaviour that is not seen in the corresponding oxide spinels, which are usually antiferromagnetic [4].

The interaction between the spins (S) of two nearest neighbour Cr^{3+} ions (*a* and *b*) can be written $-\mathbf{J}\mathbf{S}_a \cdot \mathbf{S}_b$. It results from nine interactions $-J_{ij}s_i \cdot s_j$ where s_i represents the spins of the three electrons in the *d* states of ion *a* ($d^a_{xy}, d^a_{yz}$and d^a_{zx}) and s_j represents the spins of the three electrons on the *d* states of ion *b* ($d^b_{xy}, d^b_{yz}$and d^b_{zx}). Due to the symmetry of the Cr^{3+} ions there are four independent interactions within the nine. J_d is the direct exchange between the spins of the electrons in the d_{xy} orbitals, J_π is the superexchange between electrons in *d* states overlapping with the same ligand *p* state, J'_c is the superexchange between electrons in *d* states overlapping with two orthogonal *p* orbitals of the same anion and J_c is the interaction between electrons in *d* states overlapping with *p* states on different anions. These interactions are shown schematically in figure 1.5.

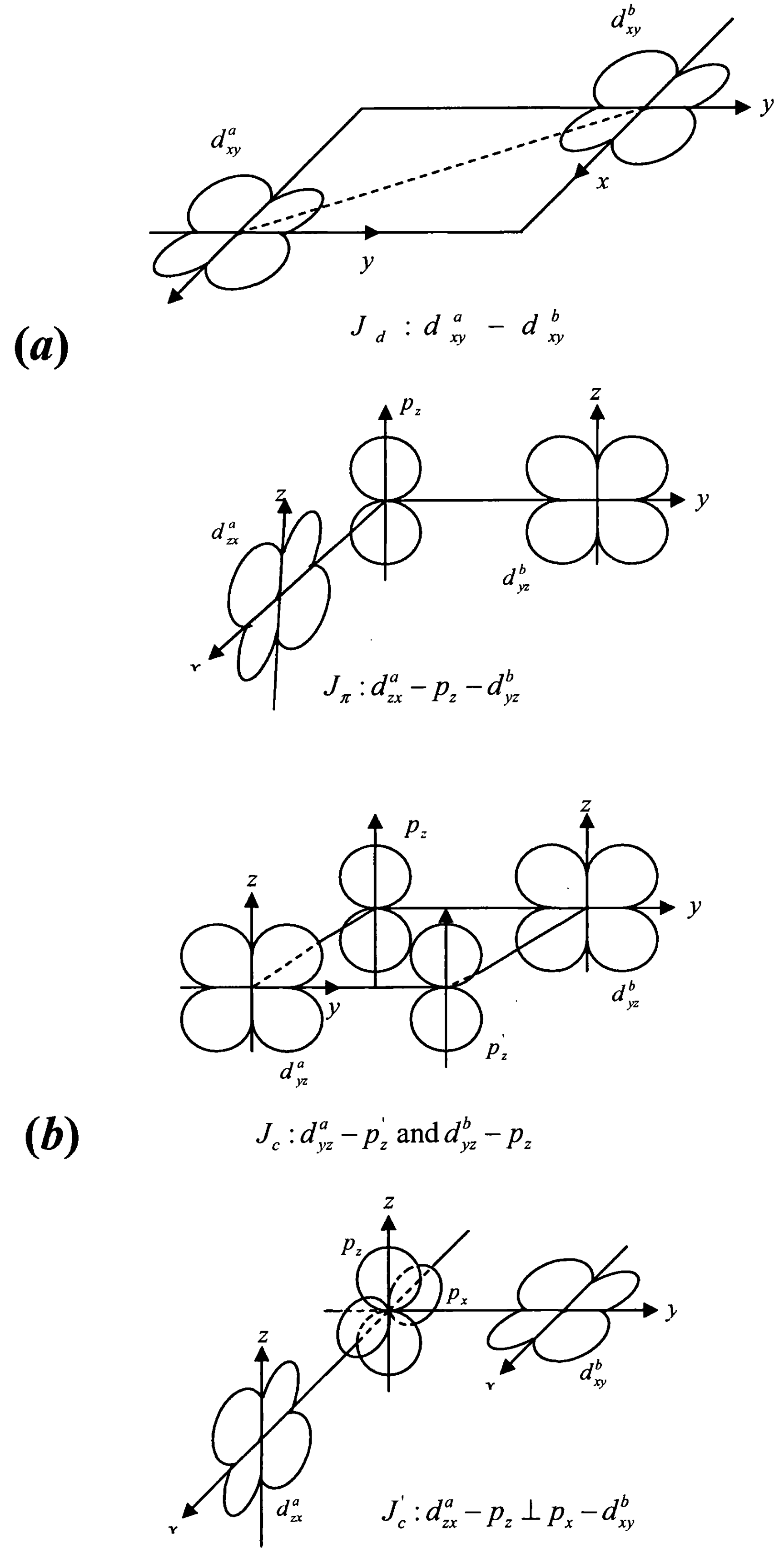

Figure 1.5 *Negative (a) and positive (b) interactions in the 90°* Cr^{3+}*-*Cr^{3+} *superexchange*

Analysis of these exchange interactions can explain the difference in behaviour of the oxide and chalcogenide chromium spinels. The antiferromagnetism in the oxide spinels arise from the relatively short Cr^{3+}-Cr^{3+} bond distance (2.94 Å in $ZnCr_2O_4$) which leads to a strong *d-d* overlap and a negative interaction. In the chalcogenide spinels this Cr^{3+}-Cr^{3+} distance is greater (3.53 Å for $ZnCr_2S_4$ and 3.71 Å for $ZnCr_2Se_4$), which leads to a weakening of the negative interaction and a ferromagnetic Cr^{3+}-X^{2-}-Cr^{3+} superexchange interaction dominates. This positive superexchange interaction is thought to lead to the unusual feature of a positive asymptotic Curie temperature (θ) in antiferromagnetic chalcogenide spinels such as $ZnCr_2Se_4$ and $ZnCr_2S_4$. Values of θ have been found to increase with increasing lattice parameter or Cr^{3+}-Cr^{3+} distance [6]. The nature of the magnetism (ferromagnetic or antiferromagnetic) in chalcogenide spinels is determined by the relative strengths of the negative Cr^{3+}-Cr^{3+} and positive Cr^{3+}-X^{2-}-Cr^{3+} superexchange interactions.

1.3 $CuCr_2Se_4$

1.3.1 General properties of $CuCr_2Se_4$

The work in this thesis is based around $CuCr_2Se_4$ and related compounds. $CuCr_2Se_4$ takes a normal spinel structure where each selenium atom is surrounded by one copper and three chromium atoms, with the copper and chromium atoms situated in the tetrahedral and octahedral sites respectively

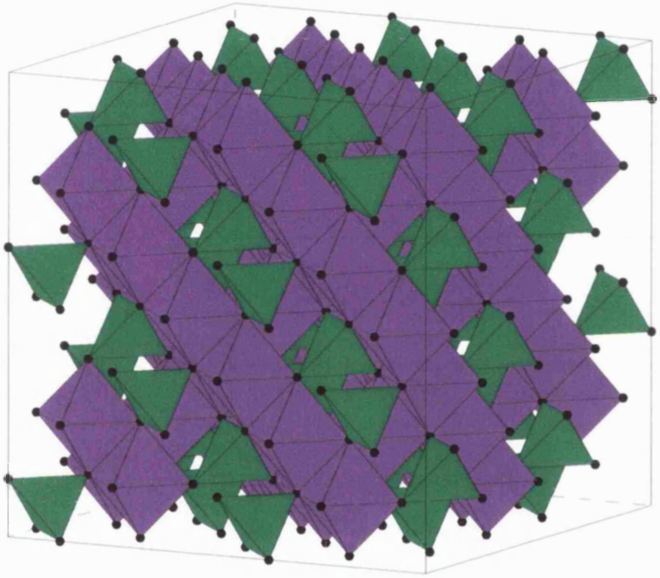

Figure 1.6 *Diagram of the structure of* $CuCr_2Se_4$ *showing the tetrahedral copper positions (green) and the octahedral chromium positions (purple)*

The compound is a ferromagnet with a Curie temperature of around 460 K [4]. The conductivity is p-type metallic down to 1K; at room temperature the resistivity has been reported as 2×10^{-4} Ωcm [7].

1.3.2 The valence of Cr in $CuCr_2Se_4$

There have been two models suggested to describe the valence distribution within the $CuCr_2Se_4$ compound [4, 8, 9]. The first, suggested by Goodenough [10], assumes that the copper ion is divalent, giving a distribution of $Cu^{2+}[Cr^{3+}]_2[Se^{2-}]_4$. In this model the net magnetization of 5 μ_B/mol is accounted for by the sum of the 6 μ_B/mol contribution of the ferromagnetically coupled Cr^{3+} spins and the -1 μ_B/mol fully polarised copper band. The exchange between the Cr^{3+} ions was proposed to be a combination of ferromagnetic 90° Cr-Se-Cr superexchange and antiferromagnetic Cr-Cr superexchange. Conduction is proposed to take place in a narrow band of copper *3d* states, enhancing the ferromagnetic interactions within the lattice.

In the second model, proposed by Lotgering and Van Stapele [11], the copper ion is monovalent and the chromium ions are mixed valence, which can be written $Cu^{+}[Cr^{3+}Cr^{4+}][Se^{2-}]_4$. P-type metallic conduction is accounted for by a small number of δ holes/mol in the valence band introduced by the presence of Cr^{4+} ions (or holes in the Cr^{3+} states) situated below the top of the valence band. This can also be described as $Cu^{1+}[Cr^{3+}{}_{1+\delta}Cr^{4+}{}_{1-\delta}][Se^{2-\delta}]_4$ with $\delta \approx 0.1$.

Both models give a theoretical magnetic moment of 5 μ_B/mol, which creates some difficulty in establishing experimentally the correct valence structure. Several experiments have been carried out to determine which model is correct. Powder neutron diffraction experiments by Robbins [12] and Colominas [9] both found zero moment on the copper ion, which indicates that it is in the +1 state, in agreement with the Lotgering and Van Stapele model. They also concluded that all chromium ions were in the Cr^{3+} state which gives a theoretical moment of 6 μ_B/mol. The experimental value of 4.9 μ_B/mol was explained by the existence of a delocalised moment of 1 μ_B/mol in opposition to the Cr^{3+} moment. However a later study of a $CuCr_2Se_4$ single crystal using polarised neutrons found a small negative moment (-0.07 ± 0.02 μ_B) on the copper ion and 2.64 ± 0.04 μ_B on the chromium ions. The measured value of the saturation magnetisation was found to be 5.01 μ_B/mol and the disagreement between this and the measured Cr moments was attributed to a uniform polarization of -0.20 ± 0.11 μ_B/mol. This supports the Lotgering and Van Stapele model with a value of 0.2 holes per molecule in the valence band.

More recent powder neutron diffraction and magnetic susceptibility studies have revealed a change in the magnetic moment of the chromium ions at the ordering temperature [8]. In the ferromagnetic phase (at 10K) analysis of the interatomic distances found the bonding around the chromium to be ionic with chromium in the +3 and +4 oxidation states, supporting the Lotgering and Van Stapele model. Magnetic susceptibility results gave the moment on the chromium ions to be 2.81 μ_B/mol, in agreement with the mixed valence model. In the paramagnetic phase however the oxidation state of the chromium ions was found to be between +2 and +3.

Self consistent calculations using the discrete variational Xα method have been carried out by Ogata *et. al.* on the electronic band structure of $CuCr_2Se_4$ [13]. They obtained valence values of $Cu^{1.25+}[Cr^{1.41+}]_2[Se^{1/02-}]_4$, which agrees with neither the Goodenough nor the Lotgering and Van Stapele model. It is possible that this may be due to the bonding within the system being more covalent than ionic in character, which is also suggested by X-ray photoelectron spectroscopy of $Cu_xGa_yCr_zSe_4$ single crystals [14].

In general, there appears to be more evidence for the Lotgering and Van Stapele model for the valence distribution within $CuCr_2Se_4$ than for the Goodenough model. This model also supports the double exchange mechanism for ferromagnetism in this material [4, 11, 15, 16]. This mechanism involves the indirect coupling of the chromium *d*-shells via the electrons in the conduction band. The most stable configuration for unpaired electrons in an atom or ion is with all spins aligned parallel. The conduction electrons cannot change their spin as the energy needed would be too great and therefore they are only free to move through the system if the spins of the incomplete *d*-shells are aligned parallel (see chapter 2, section 2.3.5.2.3).

Greater insight into $CuCr_2Se_4$ can be gained by studying the effect of cation and anion substitutions on the structural and physical properties. This is discussed in sections 1.3.3 and 1.3.4.

1.3.3 Cation substitutions in $CuCr_2Se_4$

1.3.3.1 $Cu_xT_{1-x}Cr_2Se_4$

Cation substitutions on the A site where T is a trivalent diamagnetic ion such as Al^{3+}, Ga^{3+} or In^{3+} are possible in $CuCr_2Se_4$. It has been found that this leads to 1:1 ordering on the tetrahedral sites in compounds where $x = ½$. This ordering leads to a change in symmetry of the spinel structure from $Fd3m$ to $F\bar{4}3m$ and consequently the tetrahedra around the Cu^+ and T^{3+} ions are no longer equivalent. These two types of tetrahedra contain no common Se^{2-} ions and do not share the same bond length. In the case of $Cu_{0.5}In_{0.5}Cr_2Se_4$ the bond distances differ by 5% [4].

Studies of the mixed crystals $Cu_xIn_yCr_2Se_4$ and $Cu_xGa_yCr_2Se_4$ have found that in both cases the saturation moment and T_C are dependent on x [17, 18]. T_C decreases with increasing copper content whereas the saturation moment increases with copper content.

1.3.3.2 $Cu_{1-x}Cd_xCr_2Se_4$

The end members of the $Cu_{1-x}Cd_xCr_2Se_4$ series are both ferromagnets with T_C of 140K and 460K for $CdCr_2Se_4$ and $CuCr_2Se_4$ respectively. In $CdCr_2Se_4$ the cadmium ion has a charge of +2, leading to a valence distribution of $Cd^{2+}[Cr^{3+}]_2[Se^{2-}]_4$. Studies of the magnetic properties of the series have found that the magnetic saturation moment increases with increasing cadmium substitution [19]. For $0 \leq x \leq 0.1$ the Curie temperature remains almost constant at approximately 460K. As x increases to 0.8 T_C falls gradually to 140K and then remains constant for $0.8 \leq x \leq 1$. It is concluded that each Cu^+ ion substituted in $CdCr_2Se_4$ produces on average one Cr^{4+} ion. The introduction of Cr^{4+} into the system facilitates the double exchange interaction which enhances the ferromagnetism and raises the Curie temperature. This demonstrates well that double exchange plays an important role in the magnetism of $CuCr_2Se_4$, and leads to a much higher T_C than is seen for chromium chalcogenide spinels where superexchange is the only mechanism for ferromagnetism.

1.3.3.3 $Cu_{1-x}Zn_xCr_2Se_4$

Extensive studies have been carried out on the magnetic and electronic properties of the $Cu_{1-x}Zn_xCr_2Se_4$ series [20-37].

The solubility of the series under normal synthesis conditions is limited to $x \geq 0.98$ [38], however with rapid quenching of the reaction mixture from temperatures above 500 °C, complete solubility can be achieved [37]. The end members of this series, $CuCr_2Se_4$ and $ZnCr_2Se_4$, are a ferromagnet and an antiferromagnet with a magnetic spiral structure respectively. $ZnCr_2Se_4$ is discussed in detail in section 1.4.

Substituting one Cu^+ ion for a Zn^{2+} ion in $ZnCr_2Se_4$ produces on average one Cr^{4+} in the system [33]. The system undergoes a transition from ferromagnetism at $x = 0$, through a conical magnetic structure ($0.8<x< 0.95$) to helimagnetism at $x= 1$. In the conical region of the series, the behaviour is predominantly antiferromagnetic, with T_N of approximately 20 K. This transition has been found to be a second order magnetic phase transition, accompanied by spontaneous positive temperature dependent magnetostriction [34].

The ferromagnetism in the region $0<x<0.8$ is thought to be driven by the double exchange mechanism as described for $CuCr_2Se_4$ in section 1.3. The Curie Temperature increases with copper content from 380 K at $x = 0.8$ to 460 K at $x = 0$.

Studies of the magnetic properties of single crystals with $0.1 \leq x \leq 0.9$ found that ordering of the moments was non-collinear and that the moment decreases with increasing zinc content [25]. The bonding within the crystals is predominantly ionic but covalent bonding exists and is stronger in the tetrahedral than octahedral coordinations.

For samples with $x \neq 0$ there is an anomalous rise in magnetic susceptibility below 100K [24]. This is thought to be connected with the transition to a non-collinear magnetic structure at low temperature. There is also a change in electrical behaviour across the series from p-type metallic for $0 < x < 0.8$ to semiconducting at $0.8 < x < 1$. These changes in conductivity are related to the increasing concentration and mobility of carriers introduced into the system with the increase in number of Cu^{4+} ions [21].

1.3.4 Anion substitutions in $CuCr_2Se_4$

1.3.4.1 $CuCr_2Se_{4-y}X_y$, where X is S or Te

Substitution of the Se ions in $CuCr_2Se_4$ with various cations can result in dramatic and usually systematic changes in the electronic and magnetic properties.

The series $CuCr_2Se_{4-y}X_y$ where X is S or Te, have been investigated. The compounds $CuCr_2S_4$ and $CuCr_2Te_4$ are both metallic and ferromagnetic with T_C of 420K and 365K respectively [39]. In the case of X = S complete solubility has been observed, with a linear variation of lattice parameter with y [40]. However the Curie temperature of the series does not have a linear dependence on y, first decreasing almost linearly for $0 \leq y \leq 3$ from approximately 470 K to 350 K and then increasing gradually for $3 \leq y \leq 4$ to 440 K. It was also found that there were anomalies in the X-ray powder diffraction intensities for the compound where $y = 3$ which may indicate a non statistical distribution of the ions, possibly related to anion ordering which could be responsible for the non-linear variation of T_C with y.

A later investigation by Belov *et al.* also found an anomalously low ferromagnetic moment for compounds with $2 \leq y \leq 3$ [41]. They also observed that the sample with $y = 3$ had a negative temperature coefficient of resistivity whereas the other samples studied in the series had a positive coefficient. Lack of further work on these compounds makes it difficult to draw any definite conclusions on the exact nature of this series. It is possible that the changes across the series are related to the different electronegativities of the selenium and sulphur anions. As selenium has a lower electronegativity than sulphur it may trap the holes in the valence band that are responsible for the conduction and ferromagnetism, leading to a configuration $Cu^+[Cr^{3+}]_2Se^-[S^{2-}]_3$ for $y = 3$, which would provide and explanation for the low T_C and semiconductivity in this compound.

The series $CuCr_2Se_{4-y}X_y$ where X = Te has only limited solubility from $2.8 \geq y \geq 4$. In this region the lattice parameters vary linearly with y indicating a good homogenous mixing of the anions [42].

1.3.4.2 $CuCr_2Se_{4-y}X_y$, where X is Cl or Br

More extensive studies have been carried out on substitutions with halogen anions, in particular Cl^- and Br^- [39, 43-46]. It had been found that it is not possible to substitute more than one X atom (where $X = Br^-$ or Cl^-) for Se in the polycrystalline material. Pink *et al.* [47] found that it was possible to substitute up to two Br^- ions, but that this also resulted in loss of Cu^+, a factor which can have significant influence on the magnetic and electronic properties. Hence the effects of Br^- substitution in pure $CuCr_2Se_4$ have only been investigated for $y \leq 1$.

In the case of Cl^- substitution, compounds with $y \geq 0.6$ are very hygroscopic and therefore it has not been possible to carry out any analysis on the magnetic or electronic properties of these compositions [39, 44]. For both Cl^- and Br^- substitution with $y \leq 1$ the lattice parameter has been found to vary linearly with composition.

Substitution of Br^- and Cl^- results in a linear reduction of T_c with increasing y. For Br^- the T_C decreases from 434 K at $y = 0$ to 274 K at $y = 1$ [39]. It was initially thought that a transition from metallic to semiconducting behaviour occurred at $y \approx 0.5$ but a more recent study as showed that in fact the transition is at $y = 0.98$ and is accompanied by a sudden decrease in T_C [46]. Magnetisation per formula unit has been found to increase linearly with y from 4.76 μ_B at $y = 0$ to 5.67 μ_B at $y = 1$ [44].

As the 3*d* electrons of the chromium ions in $CuCr_2Se_4$ are believed to occupy only the spin up band, the magnitude of the Cr moment in μ_B can provide a direct indication of the number of Cr 3*d* electrons. Yamaguchi *et al.* found that the number of 3*d* electrons increased from 2.64 ± 0.04 for $y = 0$ to 2.77 ± 0.07 for $y = 0.5$ [45]. It can be concluded that the electrons introduced by substitution of Br^- for Se^{2-} occupy the 3*d* orbital of the chromium ions, leading to a configuration of $Cu^+[Cr^{3+}]_2[Se^{2-}]_3[Br^-]$ at $y = 1$ [46]. This theory is supported by the experimental result of a lowering of the T_C and a change in electrical behaviour as both these features depend heavily on the heterovalency of the Cr^{3+} ions in $CuCr_2Se_4$.

1.4 $ZnCr_2Se_4$

$ZnCr_2Se_4$ is a normal cubic spinel with an antiferromagnetic spiral structure [48]. The spiral structure orders below 20.4 K, accompanied by a small tetragonal distortion of the cubic structure. In the paramagnetic region the magnetic susceptibility follows the Curie Weiss law and the asymptotic Curie temperature (θ) is +115K. The unusual value of θ is due to the balance of ferromagnetic and antiferromagnetic interactions taking place within the compound, as discussed in section 1.2.2. It is clear that the ferromagnetic coupling components play an important role in this compound. Various attempts have been made to quantify the exchange interactions which lead to the magnetic spiral structure but as yet no conclusive explanations have been drawn [48-50].

Dwight and Menyuk [50] considered five distant neighbour interactions taking place around a trivalent chromium ion in octahedral coordination (i.e. the chromium on the spinel B-site) and analysed them into their constituent superexchange terms.

The e_g orbitals involved in σ bonding are empty whereas the t_{2g} orbitals involved in π bonding are half filled. The Goodenough-Kanamori rules of superexchange state that superexchange between two empty or half filled orbitals will be negative (antiferromagnetic) and superexchange between one half filled and one empty orbital will be positive (ferromagnetic) It was therefore concluded that all σ-Δ-σ and π-Δ-π interactions would be negative and all σ-Δ-π interactions positive. As π overlap tends to be smaller than σ overlap, superexchange interactions tend to be weaker via π bonds than via σ bonds. The σ-Δ-σ interactions would consequently be expected to be the strongest and the π-Δ-π interactions the weakest.

Figure 1.7 shows the arrangement of Cr moments in the magnetic spiral structure, which is directed along the [001] axis. The propagation vector is along the symmetry axis of the spiral. The angle between the magnetic moments on the adjacent Cr [001] planes varies from 42° at 4.2K to 38° at 21K.

Studies of the magnetic structure in different applied fields have found some interesting behaviour [48, 49]. In zero field domains are present in which the helical axis is aligned along the edge of the cubic cell. In applied fields of 3Oe the domains of preferred orientation expand and in higher fields as conical structure is formed, resulting in increasing net magnetisation.

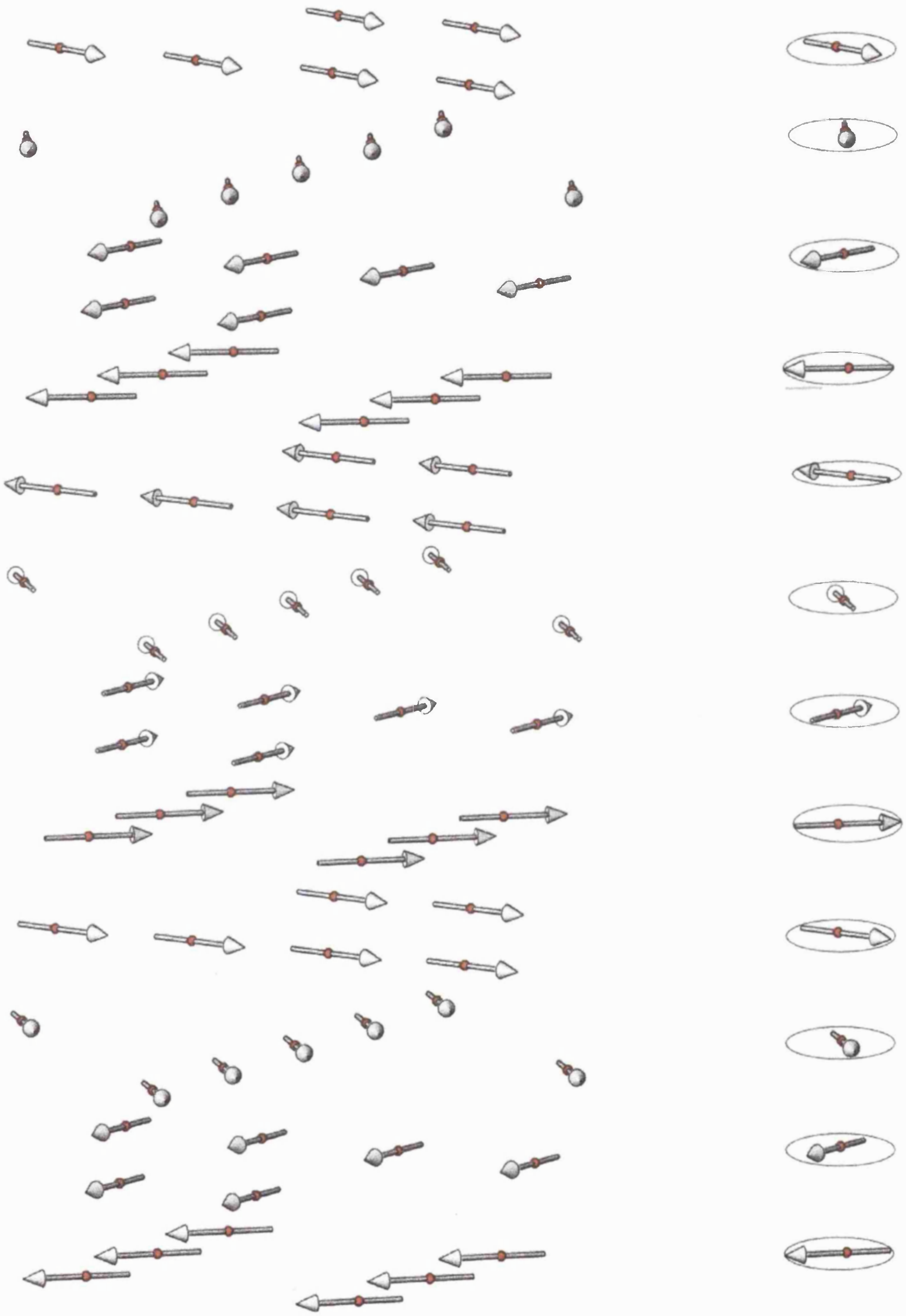

Figure 1.7 *Diagram showing the orientation of the chromium moments in the* $ZnCr_2Se_4$ *magnetic spiral structure. The angle of rotation between the moments is 42° The orientation of the moments in each plane is pictured on the right to show the spiral structure.*

1.5 Magnetoresistance

Magnetoresistance is the change in the electrical resistance of a material produced on applying a magnetic field, H. It is usually expressed as a percentage and defined by the equation

$$MR = \frac{\Delta\rho}{\rho(0)} = \frac{\rho(H) - \rho(0)}{\rho(0)}$$ **Equation 1.1**

where ρ(H) and ρ(0) are the resistances at a given temperature in the applied and zero magnetic fields respectively.

There is a great deal of interest in materials that show a magnetoresistance effect due to their potential applications for magnetic information storage or as magnetic field sensors [51]. Materials with a small magnetoresistance effect (e.g. permalloy, which shows a magnetoresistance of 2-3% at room temperature and low applied fields) are already being used in the reading heads for hard disk drives.

Magnetoresistance is observed in all metals but in general this effect is very small (less than 1 %). Ferromagnetic metals such as iron and cobalt show a greater effect (up to 15%) than non magnetic metals. Materials with enhanced magnetoresistance effects, known as Giant or Colossal Magnetoresistance, are discussed in the following section.

1.5.1 Giant Magnetoresistance

An effect known as Giant Magnetoresistance (GMR) has been observed in transition metal multilayer systems such as Fe/Cr where the magnetoresistance is typically 20-40 % [52]. These materials are comprised of alternating magnetic layers, where at a certain thickness of the Cr layer, the spins of adjacent ferromagnetic Fe layers are aligned antiparallel, driven by an antiferromagnetic interlayer exchange coupling [53]. When a field is applied the moments of the Fe layers align ferromagnetically which lowers the resistance, as scattering of the conduction electrons from non-aligned spins is significantly reduced. This is shown schematically in figure 1.8.

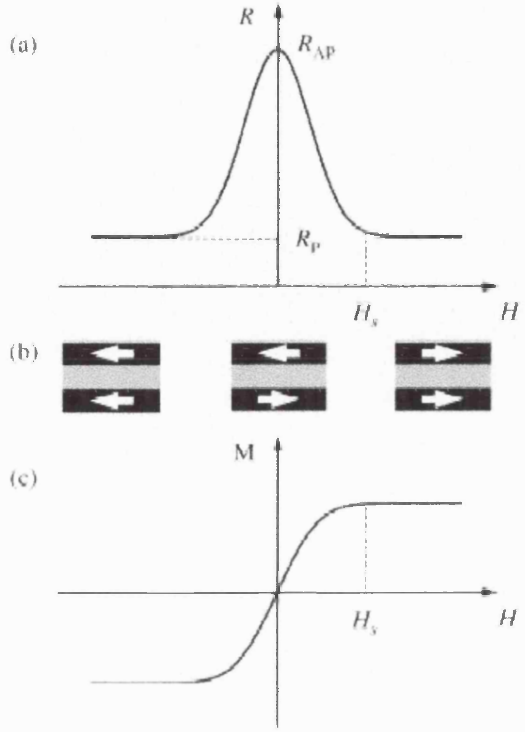

Figure 1.8 *Schematic diagram of the GMR effect, (a) The change in resistance of the magnetic multilayer as a function of applied magnetic field. (b) The magnetic configurations in the multilayer in different applied fields. The moments are aligned antiparallel in zero applied field and parallel when the applied field (H) is greater than the saturation field (H_s). (c) The magnetisation curve of the mulitlayer.*

This GMR effect can be produced in a variety of systems as spin dependent conduction is seen in many ferromagnetic transition metal alloys. GMR can also be observed in granular films of nanometric ferromagnetic metals embedded in a non-ferromagnetic matrix, for example in granular Cu-Co films [54, 55]. These granular films have to advantage of being much simpler to prepare than the multilayer systems.

1.5.2 Colossal Magnetoresistance

Recently materials showing nearly 100% magnetoresistance have been discovered. The mechanism for the MR effect in these compounds is not the same as that for the GMR compounds and hence this new effect has been termed Colossal Magnetoresistance (CMR). There are three main groups of materials that have been found to exhibit CMR, the perovskite manganates, the pyrochlore manganates and the chalcogenide spinels.

1.5.2.1 Perovskite Manganates

The perovskite manganates are the most widely studied of the CMR materials, and show effects of up to 100% [56, 57]. They have the general formula $Ln_{1-x}A_xMnO_3$, where Ln is a trivalent rare earth cation and A a divalent cation (e.g.Ca, Sr, Ba). The perovskite structure consists of corner shared MnO_6 octahedra, often with an orthorhombic symmetry (space group *Pnma*).

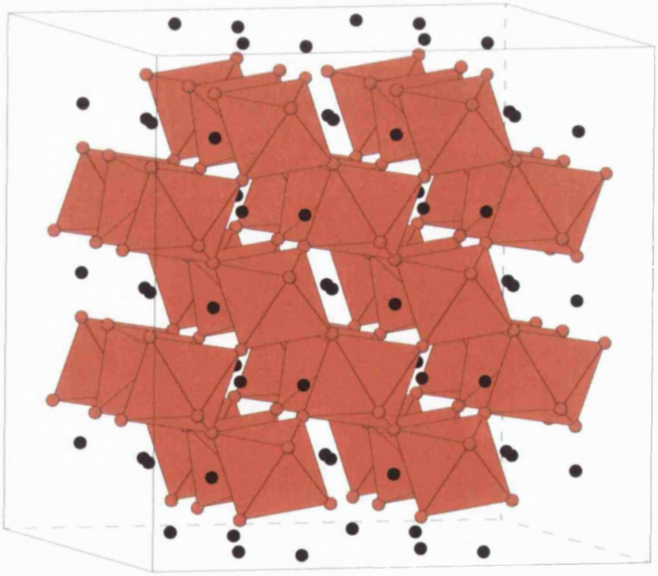

Figure 1.9 *Diagram of the perovskite structure with space group Pmna showing the MnO_6 octahedra.*

The most widely investigated CMR perovskite is $La_{1-x}Ca_xMnO_3$ [56, 58]. The end members, $LaMnO_3$ and $CaMnO_3$, are both anti-ferromagnetic insulators with manganese in the 3+ and 4+ oxidation states respectively. The Mn-O-Mn bond angle is around 180°, leading to an antiferromagnetic superexchange interaction between the manganese ions. In the doping range $x = 0.2 - 0.4$ the material becomes a ferromagnetic metal.

The ferromagnetism is though to be due to the double exchange mechanism which arises from the mixed valency of manganese ions, Mn^{3+} and Mn^{4+}. This involves the hopping of an e_g^1 electron between Mn^{3+} and Mn^{4+} ions in which the t_{2g} electrons are aligned ferromagnetically. The double exchange mechanism is described in more detail in the chapter 2, section 2.3.5.2.3. .

Ferromagnetism is only seen below T_C, when the t_{2g} electrons are ordered. Above this temperature the material is paramagnetic and the e_g electron cannot move between manganese ions due to the spin disorder scattering, *i.e.* the t_{2g} electrons are no longer aligned parallel. Therefore a metal/insulator transition is observed at T_C. Applying a magnetic field increases T_C by aligning the t_{2g} electrons. The magnetoresistance effect is produced by applying a magnetic field at a temperature just above T_C, forcing the metal/insulator transition.

It has been found that double exchange alone cannot account for the sudden change in resistivity at T_C [59]. It is thought that magnetic polaron effects arising from strong Jahn-Teller splitting of the Mn^{3+} ion also play a significant role. The electronic behaviour involves a crossover between a high temperature polaron dominated magnetically disordered regime and a low temperature metallic magnetically ordered regime.

1.5.2.2 $Tl_2Mn_2O_7$

Another compound that has attracted much interest is the pyrochlore $Tl_2Mn_2O_7$. It exhibits CMR at 142 K with an applied field as low as 0.5T [60]. There are many similarities between $Tl_2Mn_2O_7$ and the hole-doped perovskite manganates discussed earlier but there are also some fundamental differences that lead to a new CMR mechanism.

The pyrochlore structure takes the form $A_2Mn_2O_7$. A diagram of the structure is shown in figure 1.10.

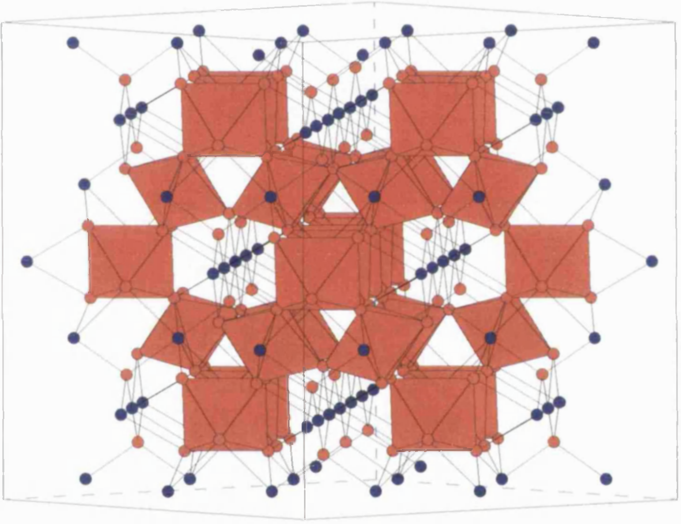

Figure 1.10 *Diagram of the pyrochlore structure with space group Fd3m showing the* MnO_6 *octahedra.*

The structure is face centred cubic with the space group *Fd3m* and consists of corner shared MnO_6 octahedra. This octahedral coordination leads to a strong localised magnetic moment on the manganese ions as seen in the perovskite manganate CMR materials.

Unlike in the perovskite manganates, there is no mixed valency of the manganese ions in $Tl_2Mn_2O_7$ and there is therefore no possibility of a double exchange interaction taking place [61]. It has also been concluded that there is no Jahn-Teller distortion of the MnO_6 octahedra, which is a significant feature in the CMR mechanism of the perovskites [60]. It has been found that the ferromagnetism in $Tl_2Mn_2O_7$ is due to a superexchange interaction taking place between the Mn^{4+} ions via the oxygen atoms [62, 63]. If the angle between these bonds were 180° the interaction would result in an antiferromagnetic spin arrangement whereas a ferromagnetic array is expected for an angle of 90°. The Mn-O-Mn bond angle found in $Tl_2Mn_2O_7$ is 130-133°, which indicates that a ferromagnetic superexchange interaction is taking place.

It was also found that the ferromagnetic interaction was enhanced by hybridisation of the thallium *6s* orbital with the oxygen *2p* and manganese *3d* orbitals. This hybridisation is also thought to be responsible for the metallic behaviour of the compound [63]. The pyrochlore structure can be considered as two intertwined sublattices, MnO_6 octahedra responsible for the ferromagnetism and Tl-O chains responsible for the conductivity.

Correlations between the resistivity and magnetic moment arise from an unusually large incoherent scattering of the conduction electrons from spin fluctuations that accompany the ferromagnetic ordering. Hence the CMR effect results from the magnetic induction of spin-polarised conduction due to the alignment of local spins giving a ferromagnetic and metallic state.

1.5.2.3 Chalcogenide Spinels

Magnetoresistance has been reported in various chalcogenide spinels, with the largest effects being observed in indium doped $HgCr_2Se_4$ [64] and copper doped $FeCr_2S_4$ [65, 66]. It is clear that different mechanisms exist for the MR in these compounds than for the manganates discussed above, as there is neither a double exchange mechanism nor a Jahn-Teller effect taking place within these compounds.

$HgCr_{1.9}In_{0.1}Se_4$ is an *n*-type semiconductor that shows a large and sudden drop in conductivity above T_C ($\approx$ 120K) [64]. Negative MR is seen over a wide temperature range, increasing from around 10% at 6 K to a maximum of 60% at T_C and then falling to around 6% at 200K for applied fields of 9.55×10^5 A/m. The magnetoresistance effect becomes saturated in higher fields. In single crystal measurements the magnitude of the MR was found to be independent of the direction of the magnetic field. The MR effect is thought to be due to a change in carrier mobility near the T_C rather than a change in carrier concentration [67]. The temperature dependent mobility of the electrons has been explained in terms of spin-disorder scattering which arises from interactions between localised moments and charge carriers.

$FeCr_2S_4$ and $Fe_{0.5}Cu_{0.5}Cr_2S_4$ show MR effects of approximately 20 and 7% respectively for applied fields of 6 T [68]. $FeCr_2S_4$ is a *p*-type and $Fe_{0.5}Cu_{0.5}Cr_2S_4$ an *n*-type semiconductor. The exact mechanism for the MR in these compounds does not seem to have been found but a mechanism involving exchange interactions on three cations has been proposed by Palmer and Greaves [69]. In addition to the ferromagnetic superexchange interaction that occurs via 90° Cr-S-Cr σ/π bonding (described in section 1.1.4) there is also an antiferromagnetic exchange occurring between half-filled Cr π orbitals and the Fe σ orbitals.

A Cr-S-Fe angle of 123.2° enables the S 3*p* orbitals to form bonds simultaneously with the Cr e_g orbitals (σ) and the Fe *e* orbitals (π). This combination of interactions leads to the exchange of the minority spin *e* electron on Fe^{2+} to the Cr e_g level (leading to the formation of Cr^{2+}), only if the Fe^{2+} and Cr^{3+} ions are couple antiferromagnetically. Transfer from Cr^{2+} to Fe^{3+} gives overall Fe^{2+}-Fe^{3+} exchange which stabilises both the ferrimagnetic spin arrangement and the mobility of the minority spin electron. The presence of Cr^{2+} in these compounds has been previously reported from analysis of Mössbauer spectra which supports this 'triple exchange' theory [65].

1.6 Aims of the present work

The work reported in this thesis concerns the detailed study of the magnetic and electronic properties of the $Cu_{1-x}Zn_xCr_2Se_4$ spinel series. In addition, the magnetic properties of compounds in the $Cu_{1-x}Zn_xCr_2Se_{4-y}S_y$ and $CuCr_2Se_{4-y}Br_y$ series are also investigated in order to determine the effect of chemical substitutions for selenium on the magnetic properties.

The first aim was to prepare these compounds using solid state synthesis techniques and to subsequently analyse the structures of these compounds using powder X-ray diffraction.

The second aim was to analyse the magnetic properties of these compounds using DC SQUID magnetometry, neutron diffraction and AC susceptibility at high pressure. The high pressure AC susceptibility technique provides an opportunity to study the effect of varying the bond distances within the compounds whilst the chemical composition remains unchanged, allowing a unique insight into the magnetic interactions taking place within the lattice.

The third aim of the work was to investigate the possibility of a magnetoresistance effect in these compounds. As ferromagnetism in the $Cu_{1-x}Zn_xCr_2Se_4$ series is thought to arise partly from the double exchange mechanism, which leads to the CMR effects seen in some perovskite manganates, it is possible that the same mechanism could lead to a magnetoresistance effect in these compounds. In the known double exchange CMR materials, the maximum magnetoresistance effect is seen at temperatures close to T_C. As the Curie temperatures of the ferromagnetic compounds in the $Cu_{1-x}Zn_xCr_2Se_4$ series are above 300 K and tuneable by varying x (see section 1.3.3.3) there is the possibility of a large room temperature magnetoresistance effect in these compounds.

1.7 References

1. Bragg, W.H., *Philosophical Magazine*, 1915. **30**: p. 305.
2. Nishikawa, S., *Proceedings of the Mathematical and Physical Society of Tokyo*, 1915. **8**: p. 199.
3. Valenzuela, R., *Magnetic Ceramics*. 1994, New York: Cambridge University Press.
4. van Stapele, R.P., *Sulphospinels*. Ferromagnetic Materials: a handbook on the properties of magnetically ordered substances, ed. E.P. Wohlfarth. Vol. 3. 1982, Amsterdam: North-Holland. 603-745.
5. Krok-Kowalski, J., Warczewski, J., and Nikiforov, K., *J. Alloy. Compd.*, 2001. **315**: p. 62-67.
6. Baltzer, P.K., Wojtowicz, P.J., Robbons, M., and Lopatin, E., *Phys. Rev.*, 1966. **151**(2): p. 367-377.
7. Lotgering, F.K. in *International conference on magnetism*. 1964. Nottingham, England: The Institute of Physics and the Physical Society, London.
8. Rodic, D., Antic, B., Tellgren, R., Rundlof, H., and Blanusa, J., *J. Magn. Magn. Mater.*, 1998. **187**: p. 88-92.
9. Colominas, C., *Phys. Rev.*, 1967. **153**(2): p. 558-560.
10. Goodenough, J.B., *Solid State Commun.*, 1967. **5**: p. 577-580.
11. Lotgering, F.K. and van Stapele, R.P., *J. Appl. Phys.*, 1968. **39**(2): p. 417-423.
12. Robbins, M., Lehmann, H.W., and White, J.G., *J. Phys. Chem. Solids*, 1967. **28**: p. 897.
13. Ogata, F., Hamajima, T., Kambara, T., and Gondaira, K.I., *J. Phys. C-Solid State*, 1982. **15**: p. 3483-3492.
14. Winiarski, A., Okonska-Kozlowska, I., Heimann, J., and Neumann, M., *J. Alloy. Compd.*, 1996. **232**: p. 63-66.
15. Zener, C., *Phys. Rev*, 1951. **82**: p. 403-405.
16. Zener, C., *Phys. Rev.*, 1951. **81**(4): p. 440-444.
17. Payer, A., Schöllhorn, R., Ritter, C., and Paulus, W., *J. Alloy. Compd.*, 1993. **191**: p. 37-42.
18. Okonska-Kozlowska, I., Maciazek, E., Wokulska, K., and Heimann, J., *J. Alloy. Compd.*, 1995. **219**(1): p. 97-99.

19. Krok-Kowalski, J., Warczewski, J., and Mydlarz, T., *J. Phys-Paris*, 1988. **Colloque C8 49**: p. C8-881-C8-882.
20. Groń, T., *Phil. Mag. B*, 1994. **70**: p. 121-132.
21. Groń, T., Duda, H., and Warczewski, J., *J. Phys-Paris*, 1988. **49**(12): p. 869.
22. Groń, T., Duda, H., and Warczewski, J., *Phys. Rev. B*, 1990. **41**(18): p. 12424.
23. Hidaka, M., Tokiwa, N., Wai, T.T., Fujii, H., Ohoyama, K., Mizusima, S., Sakaurai, J., Ichikawa, F., and Itoh, K., *Phase Transit.*, 2002. **75**(3): p. 273-287.
24. Iikubo, S., Yasui, Y., Oda, K., Ohno, Y., Kobayashi, Y., Sato, M., and Kakurai, K., *J. Phys. Soc. Jpn.*, 2002. **71**(11): p. 2792-2799.
25. Jendrzejewska, I., Mydlarz, T., Okonska-Kozlowska, I., and Heimann, J., *J. Magn. Magn. Mater.*, 1998. **186**: p. 381-385.
26. Juszczuk, S., *J. Magn. Magn. Mater.*, 1988. **72**: p. 67-70.
27. Juszczuk, S., Johansson, C., Hanson, M., and Gogolowicz, M., *Phys. Lett. A*, 1994. **192**(1): p. 429-434.
28. Juszczyk, S., *Physica B*, 1989. **161**: p. 183-185.
29. Juszczyk, S. and Gogolowicz, M., *J. Magn. Magn. Mater.*, 1991. **92**(1): p. 388-396.
30. Juszczyk, S. and Gogolowicz, M., *J. Magn. Magn. Mater.*, 1993. **128**(1): p. 163-170.
31. Juszczyk, S. and Gogolowicz, M., *Physica B*, 1993. **192**(1): p. 338-342.
32. Khan, M.N., Venkatachalam, A., Ahmad, A., and Darshane, V.S., *J. Mater. Sci.*, 1990. **25**: p. 595-598.
33. Krok, J., Spalek, J., Juszczyk, S., and Warczewski, J., *Phys. Rev. B*, 1983. **28**(11): p. 6499-6509.
34. Kusz, J., Juszczyk, S., and Warczewski, J., *J. Appl. Crystallogr.*, 1988. **21**: p. 898-901.
35. Menth, A., Von Neida, A.R., Shick, L.K., and Malm, D.L., *J. Phys. Chem. Solids*, 1971. **33**(6): p. 1338-1341.
36. Okonska-Kozlowska, I., Jedrzejewska, I., and Wokulska, K., *J. Alloy. Compd.*, 1995. **219**(1): p. 100-102.
37. Okonska-Kozlowska, I. and Krok, J., *Z. Anorg. Allg. Chem.*, 1978. **447**: p. 235.
38. Lotgering, F.K., *J. Phys. Chem. Solids*, 1968. **29**: p. 699-709.
39. Robbins, M., Baltzer, P.K., and Lopatin, E., *J. Appl. Phys.*, 1968. **39**(2): p. 662-666.

40. Ohbayashi, K., Tominaga, Y., and Iida, S., *J. Phys. Soc. Jpn.*, 1968. **24**: p. 1173-1174.
41. Belov, K.P., Tret'yakov, Y.D., Gordeev, I.V., Koroleva, L.I., Ped'ko, A.V., Smirnovskaya, E.I., Alfrerov, V.A., and Saksonov, Y.G., *Sov. Phys. Solid State*, 1973. **14**: p. 1862.
42. Reidel, E. and Horvath, E., *Z. Anorg. Allg. Chem.*, 1973. **399**: p. 219.
43. White, J.G. and Robbins, M., *J. Appl. Phys.*, 1968. **39**(2): p. 664-666.
44. Yamashita, O., Yamauchi, H., Yamaguchi, Y., and Watanabe, H., *J. Phys. Soc. Jpn.*, 1979. **47**(2): p. 450-457.
45. Yamaguchi, Y., Ohishi, Y., M., O., Yamashita, O., and Watanabe, H., *Jpn. J. Appl. Phys.*, 1980. **19**(19-3): p. 291-293.
46. Miyatani, K., Minematsu, K., Wada, K., and al., e., *J. Phys. Chem. Solids*, 1971. **32**(7): p. 1429-1434.
47. Pink, H., Unger, W.K., Schafer, H., and Goebel, H., *Appl. Phys.*, 1974. **4**: p. 147.
48. Plumier, R., *J. Phys-Paris*, 1966. **27**: p. 213-219.
49. Plumier, R., *J. Appl. Phys.*, 1966. **37**(3): p. 964-965.
50. Dwight, K. and Menyuk, N., *Phys. Rev.*, 1967. **163**(2): p. 435.
51. Mapps, D.J., *Sensors and Actuators A*, 1997. **59**: p. 9-19.
52. Baibich, M.N., Broto, J.M., Fert, A., Vandau, F.N., Petroff, F., Eitenne, P., Creuzet, G., Friederich, A., and Chazelas, J., *Phys. Rev. Lett.*, 1988. **61**(21): p. 2472-2475.
53. Grunberg, P., Schreiber, R., Pang, Y., Walz, U., Brodsky, M.B., and Sowers, H., *J. Appl. Phys.*, 1987. **61**(8): p. 3750-3752.
54. Pattanaik, G.R., Kashyap, S.C., and Pandya, D.K., *J. Magn. Magn. Mater.*, 2000. **219**(3): p. 309-316.
55. Berkowitz, A.E., Mitchell, J.R., Carey, M.J., Young, A.P., Zhang, S., Spada, F.E., Parker, F.T., and Thomas, G., *Phys. Rev. Lett.*, 1992. **68**(25): p. 3745-3748.
56. Rao, C.N.R. and Cheetham, A.K., *Chem. Mater.*, 1996. **8**: p. 2421-2432.
57. Ramirez, A.P., *J. Phys.-Condes. Matter*, 1997. **9**(39): p. 8171-8199.
58. Radaelli, P.G., Cox, D.E., Marezio, M., Cheong, S.-W., Schiffer, P.E., and Ramirez, A.P., *Phys. Rev. Lett.*, 1995. **75**(24): p. 4488-4491.
59. Millis, A.J., Littlewod, P.B., and Shraiman, B.I., *Phys. Rev. Lett.*, 1995. **75**(25): p. 5144-5147.

60. Shimakawa, Y., Kubo, Y., Manako, T., Sushko, Y.V., Argyriou, D.N., and Jorgensen, J.D., *Phys. Rev. B*, 1997. **55**(10): p. 6399-6404.

61. Subramanian, M.A., Toby, B.H., Ramirez, A.P., Marshall, W.J., Sleight, A.W., and Kwei, G.H., *Science*, 1996. **273**: p. 81-84.

62. Roder, H., Zhang, J., and Bishop, A.R., *Phys. Rev. Lett.*, 1996. **76**: p. 1356.

63. Hwang, H.Y., Cheong, S.-W., Radaelli, P.G., Marezio, M., and Batlogg, B., *Phys. Rev. Lett.*, 1995. **75**: p. 941-917.

64. Koguchi, N. and Masumoto, K., *J. Phys. Chem. Solids*, 1980. **41**(2): p. 1279-1284.

65. Ando, K. and Nishihara, Y., *J. Phys. Chem. Solids*, 1980. **41**(2): p. 1273-1278.

66. Lang, O., Felser, C., Seshadri, R., Renz, F., Kiat, J.M., Ensling, J., Gutlich, P., and Tremel, W., *Adv. Mater.*, 2000. **12**(1): p. 65-+.

67. Lehmann, H.W., *Phys. Rev.*, 1967. **163**(2): p. 488-496.

68. Ramirez, A.P., Cava, R.J., and Krajewski, J., *Nature*, 1997. **386**: p. 156-159.

69. Palmer, H.M. and Greaves, C., *J. Mater. Chem.*, 1999. **9**: p. 637-640.

Chapter 2 Theory

2.1 Solid Solutions

A solid solution is formed when atoms or molecules of two substances take up positions on a common crystal lattice, forming a single phase. Solid solutions can be divided into two categories, substitutional (random or ordered) and interstitial. An ordered substitutional solid solution is also known as a superlattice; this situation can only occur at a fixed temperature or over a very small range of composition.

The formation of a solid solution is limited by the strain put on the lattice. Certain rules, worked out by W. Hume-Rothery, dictate the conditions under which a solid solution can be formed in metal systems [1]. Although the systems described in this thesis are substantially ionic, it should nevertheless be useful to describe these rules.

a) If the relative size difference of two atoms is 14% or less then substitutional solid solution formation is favourable. If the difference is more than 14% then a solid solution will either not be formed or the substitution will be limited to small amounts. In the case of interstitial solid solutions, formation is only favourable if the atoms of the solute are very small compared to those in the solvent lattice.

b) If there is a high chemical affinity between two metals (for example if one is highly electronegative and one highly electropositive) then the formation of a solid solution is very restricted.

c) If the relative valence of the atoms is different then the electron ration of the system will be changed. Crystal systems are very sensitive to a decrease in electron count and therefore a metal of a high valency cannot dissolve much of a metal of a low valency, whereas a metal of a low valency can dissolve an appreciable amount of a metal of high valency.

d) If two metals are of the same crystal lattice type then, provided all other conditions are favourable, a solid solution can be formed over a very wide compositional range. If the atom size does not differ by more than 7 percent then complete solid solubility is possible.

2.2 Theory of Diffraction

This discussion is based on information gathered from references [2-4] and [5]

2.2.1 Scattering from a crystal lattice

Diffraction is the modification of the behaviour of a wave resulting from its interaction with a solid object. When a beam of light passes though a diffraction grating, where the spacing in the grating is similar to the wavelength of light, regions of dark and light are produced as a result of positive and negative interference. A similar effect is seen when a beam of radiation passes through a crystal, with the crystal lattice acting as the diffraction grating. The resulting pattern can be interpreted to gain valuable information on the crystal structure.

A crystal structure is composed of an infinite array of lattice points related to each other by the primitive vectors ***a***, ***b*** and ***c*** and defined by the lattice translational vector ***t***.

$$\boldsymbol{t} = n_1\boldsymbol{a} + n_2\boldsymbol{b} + n_3\boldsymbol{c} \qquad \{n_i = \text{any integer}\}$$ **Equation 2.1**

The crystal structure also has a 'basis' which is the smallest repeating unit of atoms showing the full symmetry of the crystal structure. The unit cell of a crystal structure is the volume used to generate the structure purely by translational symmetry.

Unit cells must have a shape such that they can be stacked to fill three-dimensional space and as a result of this restriction, there are in fact only seven plausible unit cells. Bravais lattices are the fourteen distinct crystal lattices which are derived from the seven crystal systems available to lattice arrays.

In order to study crystal structures with diffraction, it is important to understand the concept of a reciprocal lattice. Each Bravais lattice is associated with a reciprocal lattice, a lattice in k-space. The reciprocal lattice, which takes the vectors ***a****, ***b**** and ***c****, is related to the direct lattice by the equations

$$a^* = \frac{b \times c}{a.(b \times c)}, \; b^* = \frac{c \times b}{a.(b \times c)}, \; c^* = \frac{a \times b}{a.(b \times c)}$$ **Equation 2.2**

so that the reciprocal lattice vector

$$t^* = ha^* + kb^* + lc^*$$

is perpendicular to the direct lattice planes with Miller indices (hkl). The magnitude of t^* is $2\pi/d_{hkl}$ where d is the d-spacing.

In a diffraction experiment, coherent elastic scattering results from constructive interference from the set of lattice planes (h, k, l) at a direction where there is zero phase change between beams reflected from adjacent planes. The condition for constructive interference is described by Bragg's law, $n\lambda = 2d \sin\theta$, which is demonstrated in figure 2.1.

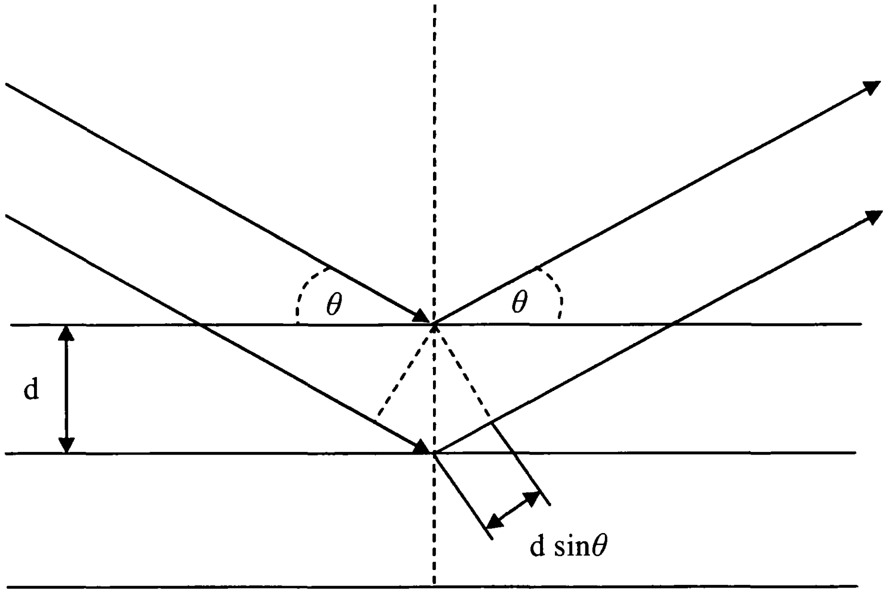

$n\lambda = 2d \sin\theta$

Figure 2.1 *Diagrammatic representation of Bragg's Law*

The condition for the existence of a diffracted beam can also be illustrated by means of a Ewald construction, as shown in figure 2.2. This consists of a sphere, drawn in k-space, the origin, O, which is the point where the incident beam, k_0, terminates. The radius of the sphere is $1/\lambda$ and the centre is marked as the point C. The Bragg condition is met where a reciprocal lattice point (such as P) lies on the surface of the sphere, the scattering angle being 2θ.

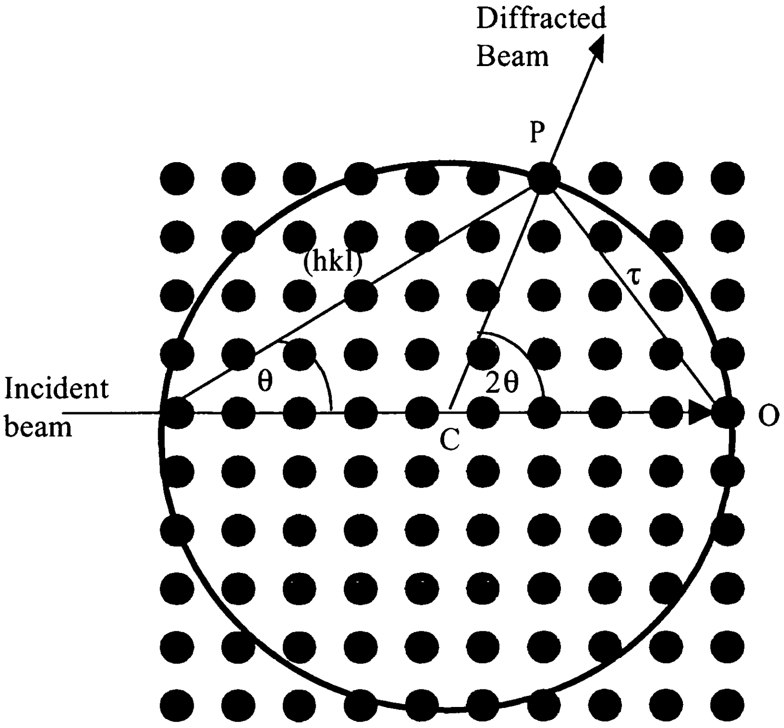

Figure 2.2 *The Ewald Construction*

The occurrence and positioning of Bragg reflections is determined by the nature of the lattice of a compound. In a diffraction experiment the intensity, I_{hkl}, of the Bragg peaks as well as the position is measured.

The intensity, I_{hkl}, of a Bragg reflection is determined by the type of atoms within the crystal and their positions relative to each other. The intensity is proportional to the square of the modulus of the structure factor, F_{hkl}, which is given by equations 2.3 and 2.4 for X-ray and neutron diffraction respectively.

$$F_{hkl} = \sum_i f_i \exp[-2\pi i(hx_i + ky_i + lz_i)]\exp(-W_i) \qquad \textbf{Equation 2.3}$$

$$F_{hkl} = \sum_i b_i \exp[-2\pi i(hx_i + ky_i + lz_i)]\exp(-W_i) \qquad \textbf{Equation 2.4}$$

where x_i, y_i and z_i are the fractional coordinates of the ith atom, f_i is the X-ray scattering amplitude, b_i is the neutron scattering length and W_i is the Debye-Waller isotropic temperature factor defined by

$$W_i = \frac{8\pi^2 \sin^2 \theta \langle u_i^2 \rangle}{\lambda^2}$$ **Equation 2.5**

where $\langle u_i^2 \rangle$ is the mean square thermal displacement of the ith atom.

In X-ray scattering the structure factor is dependent on the number of atomic electrons whereas in neutron scattering it depends on the neutron scattering length.

In some cases systematic absences occur ($F_{hkl} = 0$) where the lattice planes of a crystal are arranged so that reflection from them results in a total destructive interference of the diffracted beam.

2.2.2 The Powder Diffraction Technique

In a single crystal diffraction experiment a set of planes, *hkl*, satisfying the Bragg condition will scatter radiation in a well defined direction. The intensity of this reflection can be measured by placing a detector in the path of the scattered beam and by moving either the crystal or the detector, intensities of reflections from other planes can be measured.

In a powder diffraction experiment, the sample being studied consists of many small, randomly orientated single crystals, such that that for any reflection there will be a finite number of planes inclined at the correct Bragg angle. Because the orientation of the crystallites around the beam is not fixed the scattered radiation emerges not in a single beam of fixed direction, but as a cone of intensity with its axis orientated along the incident beam direction.

These cones of intensity will be produced simultaneously for all reflections and a powder pattern containing a large amount of structural information can be recorded simply by measuring intensity over a range in 2θ.

2.2.3 X-ray Powder Diffraction

In an X-ray diffraction experiment, scattering occurs by an interaction of the X-ray photons, of wavelength λ, with the charge field of the extranuclear electrons of the atoms. Constructive and destructive interference of the scattered X-rays is governed by the geometry of the crystal lattice, as described in section 2.2.1.

The atomic scattering factor, f_x, is proportional to the atomic number and hence the number of electrons. This can create difficulties in analysing X-ray diffraction data collected from crystal structures in which there are both light and heavy atoms as the scattering due to the light atoms will be comparatively very small. Problems are also encountered when attempting to refine crystal structures in which two atoms have a very similar number of electrons as they are effectively indistinguishable by X-ray diffraction. Where these situations arise, neutron scattering is a useful tool as the scattering is from the nucleus and hence the scattering factor is not dependent on atomic number.

In a laboratory based X-ray diffractometer, X-rays are produced by bombarding a metal target (typically copper, cobalt or molybdenum) with a beam of electrons emitted from a heating filament. This beam of electrons ionises electrons from the 1*s* shell of the metal; X-rays are emitted when electrons from filled higher energy shells (2*p* or 3*p*) lose energy to fill the now vacant 1*s* shell in the case of a copper source. This gives two intense lines in the emission spectrum, $\mathrm{Cu}k\alpha$ and $\mathrm{Cu}k\beta$. The beam can be monochromated either by using a filter or by reflecting an X-ray beam from a crystal monochromater.

X-ray diffraction using laboratory based equipment is normally sufficient for indexing and obtaining the lattice parameter of a crystal structure. Where solving of a crystal structure is required, a more intense source of X-rays, such as a synchrotron can be used which gives a better signal to noise ratio and well defined peak shapes.

2.2.4 Neutron Powder Diffraction

In a neutron diffraction experiment, elastic scattering occurs as a result of the interaction of the neutrons with the atomic nuclei of the atoms in a lattice. Unlike in X-ray diffraction, there is additional scattering arising from the interaction of the magnetic moments of the neutrons with permanent moments of the atoms or ions.

As the atomic scattering is from the nucleus, the scattering factor is not proportional to the atomic number: the neutron scattering cross section is unique to each atom. The magnetic scattering is dependent on the magnetic structure of the crystal. If there is no applied field and the material is paramagnetic, the moments will be aligned randomly and the magnetic scattering will not result in peak but in a diffuse background around the Bragg peaks which decreases in magnitude with increasing scattering angle, θ. This can be evaluated by subtracting all other contributions from the spectrum, provided that the magnetic contribution is sufficiently large and the data of high quality.

Where the structure is ferromagnetic and the spins of the adjacent atoms are aligned parallel, magnetic structure reflections result. These lie in the same position as the nuclear reflections and are therefore superimposed. By measuring patterns at temperatures above and below the Curie temperature, the magnetic contribution can be distinguished from the nuclear.

In a simple antiferromagnet, where the magnetic moments on adjacent atoms are aligned antiparallel, the magnetic unit cell will effectively be twice the size of the crystallographic unit cell, as the repeat distance is twice the length. This leads to a halving of the repeat distance in the reciprocal lattice. Consequently the magnetic peaks appear at values of $\sin\theta$ which are half those expected for the nuclear peaks, usually leading to the appearance of the magnetic peaks between the nuclear peaks.

In a complex antiferromagnetic structure, such as a helical antiferromagnet, the magnetic peaks appear in pairs either side of the nuclear peaks; these are known as satellite peaks. These arise from the additional periodicity of the system due to the helix which can be described by the vector $\mathbf{q}$. The axis of the helix is along the vector $\mathbf{q}$ and the pitch of the helix is equal to $2\pi/|\mathbf{q}|$. Therefore, additional Bragg reflections are seen at the nuclear position $\boldsymbol{\tau}^* \pm \mathbf{q}$. The distance of these satellite peaks from the nuclear peaks can provide information on the direction of the helical axis and the magnitude of the turning angle between successive helical planes.

Neutrons are produced for diffraction either by thermal methods in a nuclear reactor or in a spallation process. The neutron diffraction study reported in chapter 7 of this thesis was performed using neutrons produced by a spallation process so this method only will be discussed here.

In the spallation process, a particle accelerator emits a beam of high energy (~ 800 MeV) protons which are fired at a heavy metal target (*e.g.* tantalum). A violent interaction (known as spallation) occurs between these protons and the target nuclei and high energy neutrons of varying wavelength are emitted, along with a variety of lighter nuclear fragments. Each proton produces around 15 neutrons for a non-fissile target or about 25 for a fissile target.

The neutrons are then reduced in energy by a moderator so that they have wavelengths suitable for neutron scattering experiments, i.e. with a wavelength of order of magnitude comparable to the interatomic spacing in crystalline materials.

Most accelerator based neutron sources are pulsed (~ 50 Hz) which enables the use of the 'time-of-flight' neutron diffraction technique. In this technique the time of flight, *t*, taken for a neutron to travel the total flight path, L, from the moderator to the detector, via the sample, is measured. Assuming that the scattering is elastic and the initial energy of the neutron is the same as the final energy then the equation

$$t = \frac{m_n}{h} L\lambda \qquad \textbf{Equation 2.6}$$

can be used to calculate the wavelength, λ of the neutron, where m_n is the mass of the neutron and h is Planck's constant. Therefore, there is no need to monochromate the neutron beam in the time of flight technique and a considerable proportion of the neutrons produced can be used for diffraction, giving a high flux.

As the wavelength of the neutrons arriving at the detector can be calculated, the d spacing can also be found using Bragg's law (see section 2.2.1, figure 2.1). As neutrons of many different wavelengths are detected, a wide range of d-spacing can be measured at a single scattering angle, using a single detector. Usually, however, a large number of detectors are used to reduce the counting time of the experiment. The detectors are arranged in banks, each with its own *d*-spacing range, count rate and resolution. The resolution of the diffractometer is defined by the timing uncertainty, angular uncertainty and flight path uncertainties. The experiment is stopped when it is considered that sufficient statistical accuracy has been achieved.

The ability to use a single detector to collect a whole diffraction pattern is often exploited when performing experiments that require a particular sample environment (such as low temperature or high pressure). Using suitable shielding, the detector can be placed in such a way that there are no extra Bragg peaks in the pattern as a result of scattering from the sample containment apparatus. In order to do this the detector must be placed in a position where there is a free path between it and the sample and shielding must be placed between the sample containment apparatus and the detector.

2.2.5 Rietveld Refinement

Rietveld refinement is an optimisation technique in which least squares refinements are carried out until the best fit is obtained between an entire observed powder diffraction pattern taken as a whole and the entire calculated pattern. The calculated model can take into account various parameters including crystal structure, diffraction optic effects, instrumental factors and other specimen characteristics such as lattice parameters.

Other powder data refinement methods involve the separation of the data into a set of integrated intensities for individual diffraction peaks and subsequent structure refinement with the so-derived Bragg intensities is carried out as separate, non-interacting procedures. This is known as pattern decomposition and involves the breaking down of the observed pattern into its component Bragg reflections without reference to a crystal structure model [6]. Rietveld refinement extracts the maximum amount of information from powder diffraction data in which the Bragg reflections unavoidably overlap and for this reason it is particularly successful in analysing complex diffraction patterns with severely overlapping Bragg peaks.

In the Rietveld method, least-squares refinement searches for a minimum in the function:

$$M = \sum_i w_i \left[y_i(obs) - \frac{1}{c} y_i(calc) \right]^2 \qquad \textbf{Equation 2.7}$$

where the summation is over all points, i, in the pattern, c is an overall scale factor and w_i is the least-square weighting factor and is equal to $1/y_i$. The observed intensity is given by the difference between the total intensity at each point, $2\theta_i$, and the background intensity, B_i, i.e. $y_i(obs) = Y_i - B_i$.

The powder diffraction pattern can be considered as a series of individual reflection profiles, each defined by a set of parameters such as peak height, position, and width. The integrated area of the peaks is proportional to the Bragg intensity I_K where K refers to the Miller indices h,k and l. I_K is proportional to the square of the absolute value of the structure factor, $|F_K|^2$

The intensity, calculated from the structural model, y_i(calc), is given by

$$y_i(calc) = s\sum_K L_K \left|F_K\right|^2 \phi\left(2\theta_i - 2\phi_K\right) P_K A + y_{bi}$$ **Equation 2.8**

where s is the scale factor, L_K the Lorenz, polarisation and multiplicity factors, ϕ is the reflection profile function, P_K is the preferred orientation function, A is an absorption factor, F_K is the structure factor for the Kth Bragg reflection and y_{bi} is the background intensity at the ith step.

It is important to remember that Rietveld is a structural refinement rather than a structural solution method and therefore a fairly accurate initial structural model is required. Once a particular structural model has been refined the agreement between the observed and calculated profiles is assessed by examination of the R-factors (R_{wp}, R_p, R_I and R_{exp}) quoted in the analysis. The definition of these factors is given below.

(i) The 'Weighted Profile' R-factor indicates how well the refinement of the structural model accounts for the relatively small and large Bragg peaks across the diffraction profile. It is given by:

$$R_{wp} = \left[\frac{\sum_i w_i \left|y_i(obs)\text{-}y_i(calc)\right|^2}{\sum_i w_i y_i^2(obs)}\right]^{1/2}$$ **Equation 2.9**

As the numerator of equation 2.9 is the residual being minimised in the refinement process, R_{wp} is mathematically the most meaningful of the R-factors and therefore a good measure of the progress of the refinement.

(ii) 'Profile' R-factor

$$R_p = \frac{\sum_i \left|y_i(obs)\text{-}\ y_i(calc)\right|}{\sum_i y_i(obs)}$$ **Equation 2.10**

(iii) The 'Bragg'/'Integrated Intensities' reliability factor, R_I, measures the quality of the fit on the structural parameters.

$$R_I = \frac{\sum_k \left| I_k(obs) - \frac{1}{c} I_k(calc) \right|}{\sum_k I_k(obs)} \qquad \textbf{Equation 2.11}$$

(iv) The 'Expected' reliability factor accounts for the statistical quality of the data and the number of variables used in the refinements.

$$R_{\mathrm{exp}} = \left[\frac{(N - P + C)}{\sum_i w_i y_i^2(obs)} \right]^{1/2} \qquad \textbf{Equation 2.12}$$

where N = number of observations, P = number of refinable parameters and C = number of constraints used.

The satisfactory fit quality is monitored during the course of the refinement by the χ^2 factor:

$$\chi^2 = \left(\frac{R_{wp}}{R_{\mathrm{exp}}} \right)^2 = \frac{\sum_i w_i \left| y_i(obs) - y_i(calc) \right|^2}{N - P + C} \qquad \textbf{Equation 2.13}$$

The closer the value of χ^2 is to 1, the more accurate the fit to the observed profile.

It is important to consult the graphical fit during the course of the refinement, as certain factors can lead to misleading values of R_{wp} and χ^2. For example, R_{wp} can become large if there are extra peaks in the observed pattern, arising from impurities in the sample or scattering from the experimental apparatus. Conversely, a low value of R_{wp} can arise if the fitted background is high, even if the fit of the model to the data is poor. χ^2 can also be misleading as it is influenced directly by R_{wp} and R_{exp}. If there is insufficient counting time, the statistical errors will become large, leading to a high value of R_{exp} which will in turn give low values of χ^2. Artificially low values of R_{wp} will have the same effect. Normally values of χ^2 between 1 and 1.5 indicate that the fit of the model to the data is good. Values of χ^2 less than 1 are not reliable and suggest that the model contains more parameters than can be justified by the data. For these reasons it is vital that values of R_{wp} and χ^2 are used in conjunction with careful examination of the graphical fit to judge the quality of the refinement.

2.3 Magnetism

The discussion in this section is based on information gathered from references [3, 7-10] and [2]

2.3.1 Behaviour of materials in a magnetic field

A magnetic material contains a large number of atoms with magnetic moments. When placed in a magnetic field, *H*, magnetic materials have a magnetisation, *M*, which is defined as the magnetic moment per unit volume. In this thesis, all magnetisation data will be presented in cgs units which are most commonly used for interpreting magnetic properties.

Using this system, *H* and *M* are related to the flux density, *B*, by

$$B = H + 4\pi M$$ **Equation 2.14**

where *H* is in Oersted and *B* is in Gauss. In SI units the relationship is given by

$$B = \mu_0 \left(H + M \right)$$ **Equation 2.15**

where *H* and *B* are in Am^{-1} and Tesla respectively and μ_0 is the permittivity of free space. In small magnetic fields, the susceptibility of a magnetic material, χ, is given by

$$\chi = \frac{M}{H}$$ **Equation 2.16**

A more general relationship is given by

$$\chi = \left(\frac{\partial M}{\partial H} \right)_T$$ **Equation 2.17**

2.3.2 Classification of Magnetic Behaviour

The magnetic behaviour of a material depends largely on the interactions taking place between the moments of individual atoms and can fall into one of several well defined categories. The main types of magnetism are discussed below.

2.3.2.1 Diamagnetism

Diamagnetism arises in elements in which the atoms have filled electron shells and hence no permanent magnetic moment. When exposed to a magnetic field the induced magnetisation opposes the direction of the applied field, resulting in a negative susceptibility. This is independent of temperature and proportional to the applied field. This is a unique property of diamagnets and results from the interaction of the applied magnetic field with the small magnetic field produced by the orbital motion of the electrons, in an atomic version of Lenz's law.

The susceptibility of a diamagnet is given by

$$\chi = -\frac{\mu_0 Z e^2 n \langle r^2 \rangle}{6 m_e}$$ **Equation 2.18**

where n is the number of atoms per unit volume, Z is the number of electrons per atom, e is the electronic charge, m_e is the electronic mass and $\langle r^2 \rangle$ is the root mean square atomic radius. Diamagnetic susceptibility is much smaller than paramagnetic or ferromagnetic susceptibility and as it is related to the motion of the orbital electrons it is largely temperature independent. The typical susceptibility of a diamagnetic is around -10^{-5} $\mathrm{ergOe^{-2}mol^{-1}}$. A special case of 'giant' diamagnetism is a superconductor, where the susceptibility is caused by the macroscopic currents circulating in the material which oppose the applied field, rather than the changes in orbital motion of the closely bound electrons.

2.3.2.2 Paramagnetism

Paramagnetism is usually seen in materials where the atoms or molecules have odd numbers of electrons, leading to a net magnetic moment from the unpaired electron spin. The susceptibility of a paramagnet is positive and small (compared to a ferromagnet), in the order of 10^{-3}-10^{-5} ergOe^{-2}mol^{-1}, and dependent on both field and temperature.

The temperature dependence of the susceptibility of a paramagnet is often described by the Curie Law

$$\chi = \frac{C}{T} \qquad \textbf{Equation 2.19}$$

where T is the temperature in Kelvin and C is the Curie constant. The Curie law is discussed in more detail in section 2.3.3. This relationship is followed by 'dilute' paramagnets where there is little interaction between magnetic moments localised on atomic or ionic sites and surrounded by non-magnetic atoms, for example in hydrated transition metal salts. The Curie Law states that paramagnetic susceptibility is inversely proportional to temperature and therefore a plot of $1/\chi_{\text{para}}$ versus temperature should give a straight line which intercepts at the origin.

The magnetisation of a paramagnet varies linearly with field (provided the field is not very high) and the susceptibility remains relatively unchanged. As there is no significant coupling between the moments in zero field they are aligned randomly by thermal motion. On the application of a magnetic field the moments begin to align in the direction of the field but the fraction of moments deflected is small unless the applied field is very large.

Figure 2.3 shows the variation of magnetisation of a paramagnet with temperature and applied field as described by the classical Langevin function

$$M / nm = \coth\left(\frac{\mu_0 mH}{k_B T}\right) - \left(\frac{k_B T}{\mu_0 mH}\right) \qquad \textbf{Equation 2.20}$$

where n is the number of atoms per unit volume, m is the magnetic moment per atom, k_B is the Boltzmann constant and T is the temperature in Kelvin.

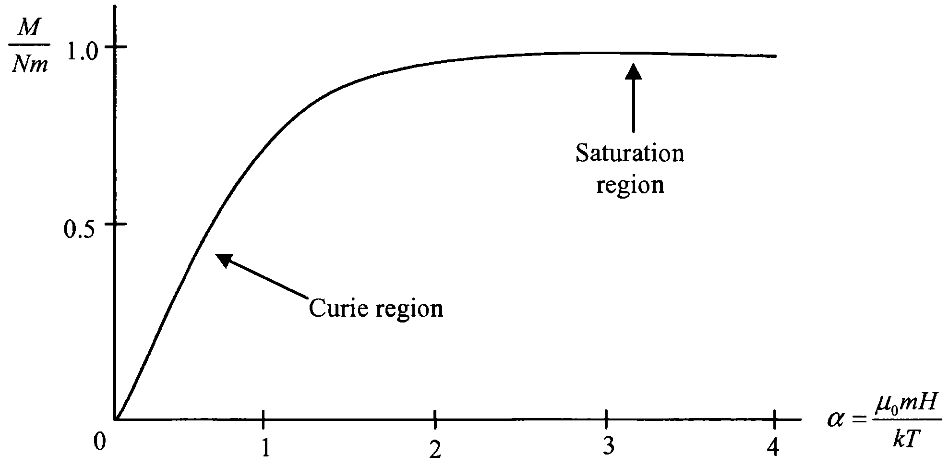

Figure 2.3 *Variation of magnetisation with temperature and applied field for a typical paramagnet, interpreted using the classical Langevin equation.*

2.3.2.3 Ferromagnetism

Ferromagnetic materials have large and positive magnetic susceptibility, typically in the range χ = 50- 10,000 ergOe^{-2}mol^{-1}. The magnetic moments are aligned parallel and exhibit a long range order, leading to much greater values of susceptibility and magnetisation than seen in paramagnetic materials.

In crystalline ferromagnetic materials there is a preferred direction of orientation of the spins known as the 'easy axis'. This exists even for cubic systems, although strictly speaking the cubic symmetry is not sustained after the onset of long range magnetic order and below T_C the symmetry is uniaxial. For this reason a magnetostriction effect can occur where the length of the crystal unit cell axes change on magnetisation.

Ferromagnets display magnetic hysteresis in an applied field as shown in figure 2.4. It can be seen from the hysteresis loop that, initially, the magnetisation of the ferromagnet is zero. On applying a field the magnetisation increases in the field direction until a saturation value is reached, at which time all the magnetic dipole moments within the material are aligned in the direction of the applied field.

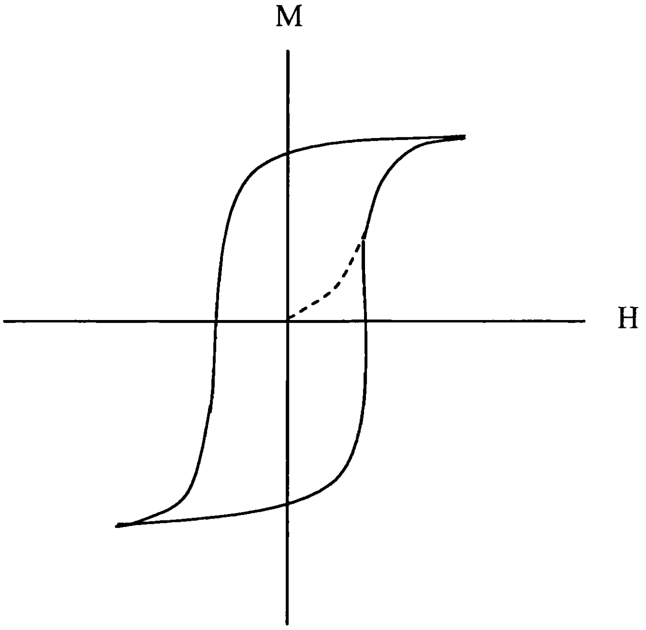

Figure 2.4 *Hysteresis loop of a typical ferromagnetic material.*

As the moments in a ferromagnet are aligned parallel, it appears inconsistent that there should be no net magnetisation in zero field, which suggests a net random alignment of spins. This anomaly can be explained by the existence of magnetic domains consisting of 10^{12}-10^{18} atomic moments aligned ferromagnetically whereas the alignment from domain to domain is random giving an overall net magnetisation of zero. Applying a field results in the reorientation of the domains so that either more domains are aligned with the field or the volume of domains in line with the field is greater than that of those aligned against the field.

As the temperature of a ferromagnet is increased the thermal energy also increases, whilst the energy of the interaction between the magnetic moments remains unchanged. Eventually the randomising effect of the thermal energy on the orientation of the moments will overcome the aligning effect of the magnetic interaction and the system will become disordered. This occurs at a critical temperature known as the Curie temperature, T_C, above which the behaviour of the material is paramagnetic in behaviour.

2.3.2.4 Antiferromagnetism

In an antiferromagnet nearest neighbour moments are aligned anti-parallel, giving a net magnetization of zero. Often antiferromagnetic systems can be considered to consist of two intertwined ferromagnetic sublattices of equal magnitude, one with moments pointing up and the other with moments pointing down. The nearest neighbour of each moment will belong to the other sublattice.

The behaviour of the magnetisation in a field is heavily dependent on temperature. At very low temperatures there is no response to a magnetic field as there is no deviation from the antiparallel arrangement of moments. At higher temperatures the increased thermal energy allows some of the moments to break free of the antiparallel arrangement and align with the external field and a small magnetisation is achieved. This effect reaches a maximum before thermal activity of the atoms leads to disorder of the spins and the magnetisation decreases gradually with increasing temperature. This maximum is known as the Néel temperature, T_N.

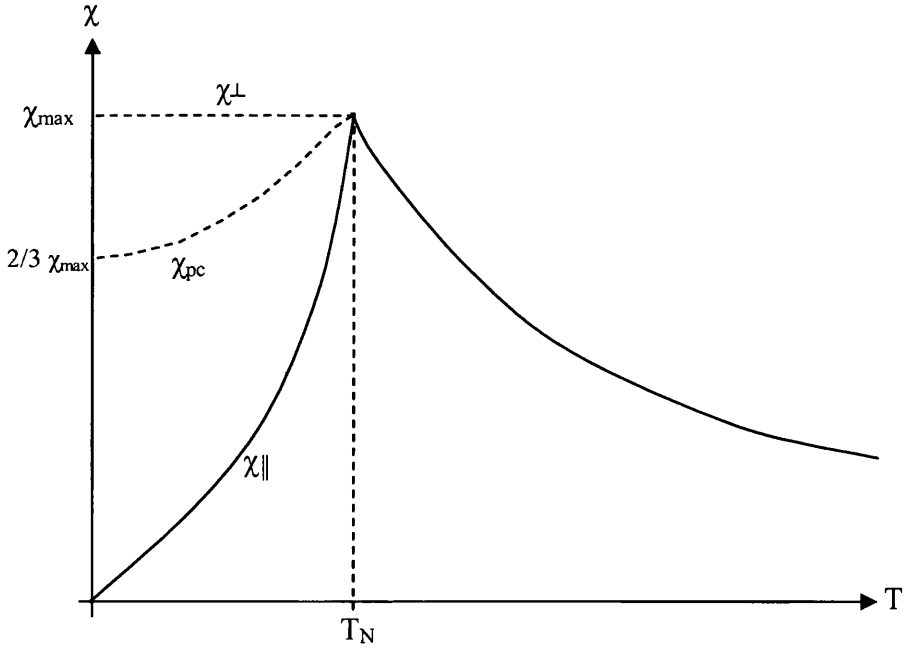

Figure 2.5 *The susceptibility vs. temperature plot of a simple antiferromagnet*

Figure 2.5 shows the behaviour of the susceptibility of a simple (ideal) antiferromagnet in three conditions; for a single crystal, with the applied field perpendicular ($\chi_\perp$) and parallel ($\chi_{||}$) to the easy axis of the sublattices, and for a polycrystalline material (χ_{pc}).

A field applied perpendicular to the easy axis will result in a small canting of the spins resulting in a net moment. This is proportional only to the magnitude of the field and the susceptibility will be independent of temperature below T_N.

A field applied parallel to the easy axis of one of the sublattices (and therefore antiparallel to the direction of the other sublattice) will have no effect at T = 0 as the magnetisation of the two sublattices has reached saturation and there is zero net moment, giving $\chi_{\|} = 0$. As the temperature is increased, the applied field enhances the magnetisation in one of the sublattices and reduces it in another, resulting in an increase in $\chi_{\|}$ below T_N.

For a polycrystalline sample, the susceptibility, χ_{pc}, is equal to $\frac{2}{3}\chi_{\perp} + \frac{1}{3}\chi_{\|}$ below T_N. Above T_N, in the paramagnetic regime, the behaviour of the susceptibility follows the Curie Weiss Law. The susceptibility of an antiferromagnetic material is much less than that of a paramagnetic material.

2.3.2.5 Ferrimagnetism

Ferrimagnets are a group of materials similar to antiferromagnets in that they consist of at least two ferromagnetic sublattices which are coupled antiferromagnetically. However in the case of ferrimagnets, either these sublattices have very different magnitudes or contain different numbers of spins, which leads to an overall net magnetisation.

The magnetic behaviour is very similar to that of the ferromagnets on a macroscopic scale; they exhibit spontaneous magnetisation below the Curie temperature, hysteresis and a saturation magnetisation. Another similarity with the ferromagnets is the existence of magnetic domains within the solid. Magnetisation and susceptibility curves for ferrimagnets are highly dependent on the nature of the constituent sublattices and can therefore be very complex.

2.3.2.6 Helimagnetism

Helimagnetism often arises in crystal structures where the magnetic atoms lie in layers, as is the case for many rare-earth metals. Between successive layers, or basal planes, there is a rotation of the moment of angle θ. If the ordering is ferromagnetic within the layers, the interaction between the layers can be considered in terms of a nearest neighbour exchange interaction (J_1) and a next-nearest neighbour exchange interaction (J_2). The energy of the system is given by

$$E = -2NS^2\left(J_1 \cos\theta + J_2 \cos 2\theta\right)$$ **Equation 2.21**

where N is the number of atoms in each layer. The energy will be at a minimum when $\partial E/\partial \theta = 0$, which gives

$$\left(J_1 + 4J_2 \cos\theta\right)\sin\theta = 0$$ **Equation 2.22**

There are two solutions to this; $\sin\theta = 0$ where θ must be 0 or π (*i.e.* ferromagnetism or antiferromagnetism) or

$$\cos\theta = -\frac{J_1}{4J_2}$$ **Equation 2.23**

which represents the helimagnetic structure. The helical configuration is favoured when $J_2 < 0$ and $|J_1| < 4|J_2|$. The pitch of the spiral is not constrained to be commensurate with the lattice parameter of the crystal structure, so generally, no two planes will have the same spin orientation.

Structures can also exist where the direction of the moment is not constrained to the basal plane and a component in another direction is added. The direction of the spin is then defined by the surface of a cone with opening angle φ and the tuning angle θ. These structures are known as spiral or conical structures and can be ferromagnetic or antiferromagnetic in nature.

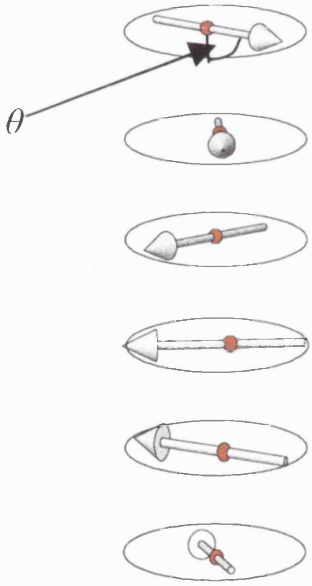

Figure 2.6 *Configuration of spins in a helimagnetic structure.*

2.3.2.7 Spin glasses

A spin glass is a material in which magnetic atoms are distributed randomly and sparsely in a non-magnetic lattice. The magnetic atoms must be sufficiently far apart so that there is no crystallographic order between them but close enough together for some magnetic interaction to occur. The magnetic atoms are commonly metals, as long range RKKY interactions (see section 2.3.5.2.2) can exist between them.

At high temperatures the spin glass behaves similarly to a paramagnet, with high frequency spin fluctuations taking place. As the temperature is decreased, these spin fluctuations become less rapid and eventually at a characteristic temperature, T_g, become almost static. This is known as 'spin freezing' and results from the increasing effectiveness of the long range interactions as the temperature falls. T_g is sometimes also referred to as T_f, the freezing temperature.

Despite this, however, there is still no long-range order in the system and the 'frozen' spins are randomly orientated. The two key reasons for this absence of long-range order are frustration and percolation, both of which are related to the large separation of the spins within the system. Frustration occurs when a spin is being influenced by two opposing long-range interactions (i.e. ferromagnetic and antiferromagnetic) and can therefore satisfy neither and long-range order cannot be established. Percolation occurs where the distance between spins is too great for the long-range interaction to be effective and this leads to small regions of exchange coupled atoms but no long-range order.

The susceptibility versus temperature curve of a spin glass can look similar to that of an antiferromagnet, with T_f being easily mistaken for T_N, however frequency dependent AC susceptibility measurements and hysteresis studies can tell them apart. In an AC measurement, a change in T_f accompanied by a decrease in susceptibility will occur with changes in frequency, as near the spin frozen state the spins are unable to fluctuate fast enough to follow the field even relatively low frequencies. Spin glasses also differ from antiferromagnets in that they show some magnetic hysteresis.

Another feature of spin glasses is that they show a time dependent response to changes in external magnetic field below T_f. This is known as the aging effect. In a ferromagnet or antiferromagnet, equilibrium is very rapidly attained following a change in applied field and therefore the subsequent magnetisation is constant with time. In a spin glass, however, the spins are frozen into a particular orientation and relaxation to an equilibrium state (following a change in applied field) occurs over a extended time period via a combination of short-range (equilibrium) and long-range (non equilibrium) dynamic processes. An analogy can be made here between the magnetic aging seen in a spin glass and the physical aging observed in glassy polymers.

The equilibrium processes follow a logarithmic decay as given by the equation

$$M(t) - M(0) = SH \log_{10} t \qquad \textbf{Equation 2.24}$$

where M is the magnetisation, t is the time elapsed following the change in field (H) and S is the relaxation rate of the magnetisation.

2.3.2.8 Superparamagnetism

If a ferromagnetic particle is sufficiently small (1-10 nm) it will be single domain, as the energetic advantage of demagnetisation will be outweighed by the energy cost of forming a domain wall. These small ferromagnetic particles are able to change the direction of their magnetisation, to lie either parallel or antiparallel to a particular direction and the energy required to bring about this change is known as the crystalline anisotropy energy. It is given by the equation

$$\Delta E = KV \qquad \textbf{Equation 2.25}$$

where V is the volume of the particle and K is a constant which quantifies the energy density associated with the anisotropy. If the particles are small enough, so that $KV < k_BT$, the direction of magnetisation of the particles can be changed simply by thermal fluctuations.

When these small ferromagnetic particles are distributed sparsely in a non-magnetic matrix, the system will behave in a similar fashion to a paramagnet. Systems such as this are termed 'superparamagnets' where the independent moments are small, single domain ferromagnetic particles rather than individual atomic moments.

At high temperatures the moments fluctuate rapidly, as in a paramagnet and the relaxation time, τ, of the moment is given by

$$\tau = \tau_0 \exp\left(\frac{KV}{k_B T}\right)$$ **Equation 2.26**

As the material is cooled, the relaxation time becomes longer and therefore the fluctuations are slower. Eventually the fluctuations will slow down sufficiently, so that the timescale of the relaxation is longer than the timescale, *t*, of the experimental technique being used to observe it. The fluctuations will then appear to have ceased and this occurs at certain temperature, known as the blocking temperature, T_B. This temperature will vary depending on *t*, for example for inelastic neutron scattering *t* is 10^{-12}-10^{-10}s whereas for Mössbauer spectroscopy *t* is 10^{-10}-10^{-7}s.

T_B will also be dependent on the size of the ferromagnetic particles, so if the system contains different sized particles the blocking will occur gradually over a range of temperatures.

2.3.3 The Curie and Curie-Weiss Laws

The effective magnetic moment of a single atom in a magnetic solid is given by:

$$\mu_{eff} = g\mu_B M_J$$ **Equation 2.27**

where μ_B is the Bohr magneton, $M_J = [J(J+1)]^{1/2}$ where J is the total orbital angular momentum of an electron and *g* is the Landé factor. The Landé factor is a measure of the relative contributions of the spin and orbital angular momentum to the moment.

When no magnetic field is applied all m_J states are degenerate. In the presence of a magnetic field, the energy, E, is dependent on which of the possible orientations, represented by the $2J+1$ values of M_J, is adopted. This is given by

$$E_M = g\mu_B M_J H$$ **Equation 2.28**

The relative population of the various sublevels for N non-interacting atoms is determined according to the Boltzmann distribution. Assuming that the spacing of the multiplet levels is very large compared with the splitting of the magnetic sublevels, then the mean magnetisation in the field direction may be expressed as:

$$M = NJg\mu_B B_J\left(\frac{gJ\mu_B\mu_0 H}{k_B T}\right)$$ **Equation 2.29**

where B_J is the Brillouin function, defined as

$$\mathrm{B_J}(x)=\left(\frac{(2J+1)}{2J}\right)\coth\left(\frac{(2J+1)x}{2J}\right)-\left(\frac{1}{2J}\right)\coth\left(\frac{x}{2J}\right)$$ **Equation2.30**

It can be estimated that for a paramagnet in normal experimental conditions, x will be much less than 1, which gives

$$B_J(x)=\frac{x(J+1)}{3J}$$ **Equation 2.31**

Substituting this into equation 2.30 with equation 2.15 and equation 2.27 then gives

$$\chi=\frac{N\mu_{eff}^2\mu_B^2}{3k_BT}=\frac{C}{T}$$ **Equation 2.32**

which is the Curie Law.

In real solids, the atomic moments are usually interacting and hence the paramagnetic susceptibility is more often described by the Curie-Weiss Law:

$$\chi=\frac{C}{T\text{-}\theta}$$ **Equation 2.33**

C is the Curie constant (as in the Curie law) and θ is a constant in units of temperature. For paramagnetic materials where there is little interaction between the atomic moments, θ is zero and equation 2.33 becomes equation 2.32, the Curie law. When θ is positive it represents the temperature at which a paramagnetic to ferromagnetic transition is observed, the Curie temperature, T_C. For antiferromagnetic materials, θ is negative and is known as the Weiss constant.

The effective moment, μ_{eff}, can also be defined as

$$\mu_{eff} = g\sqrt{J(J+1)}$$ **Equation 2.34**

where J is the total angular momentum (the sum of the orbital and spin momenta, L and S) and g is the gyromagnetic ratio, usually approximated to 2. By using the spin only approximation ($L = 0$ and $S = J$), which is usually applicable for first row transition metals, and substituting equation 2.34 into equation 2.32 we get

$$C = \frac{N\mu_B^2\left(g\sqrt{S(S+1)}\right)^2}{3k}$$ **Equation 2.35**

which can be rearranged to give

$$S(S+1) = \left(\frac{3k}{N\mu_B^2 g^2}\right)C$$ **Equation 2.36**

The constant $\left(\frac{3k}{N\mu_B^2 g^2}\right)$ can be evaluated to 2.0 $G^2molK^{-1}erg^{-1}$ which gives

$$C = \frac{S(S+1)}{2}$$ **Equation 2.37**

The number of unpaired electrons, n, can therefore be calculated from the constant C as $n = 2S$.

2.3.4 Models of Exchange

2.3.4.1 The Heisenberg Model

The exchange interaction between two spins can be described by the Heisenberg Hamiltonian

$$H = -J\boldsymbol{S}_1 \cdot \boldsymbol{S}_2 \qquad \textbf{Equation 2.38}$$

where J is the exchange constant. If J is positive the interaction favours the parallel alignment of the spins and if J is negative and antiparallel alignment is more stable. In a solid where each ion is surrounded by several others the Heisenberg interaction can be written as a sum over all neighbours;

$$\mathrm{H} = -\sum_{i,j} J_{ij}\boldsymbol{S}_i \cdot \boldsymbol{S}_j \qquad \textbf{Equation 2.39}$$

In this model the spins, $\boldsymbol{S}_i$, are allowed to point in any direction in three dimensional space and the exchange is assumed to be fully isotropic. The latter assumption introduces a serious restriction to the model and strictly speaking it can only apply to cubic systems.

2.3.4.2 The Ising Model

The Ising model makes the assumption that all the spins are located on the lattice points of the crystal. In this model the spins are only allowed to orientate themselves along one axis (conventionally the z-axis) and the exchange interaction is taken to be a simple pair interaction between two spins. The exchange integral, J, is the same for any pair of spins and if we assume S= ½ , reducing $(S_z)_i$ to two possible values, the Hamiltonian is

$$\mathrm{H} = \sum_{i,j} J_{ij}\boldsymbol{S}_i^z \boldsymbol{S}_j^z \qquad \textbf{Equation 2.40}$$

The Ising model applies to highly anisotropic magnets and is particularly useful for looking at one dimensional systems.

2.3.4.3 The XY Model

The XY model is similar to the Ising model, with the difference that the spins are now allowed to orientate in two directions, x and y. This gives the Hamiltonian

$$\mathrm{H} = -\sum_{i,j} J_{ij}\left[S_i^x S_j^x + S_i^y S_j^y\right] \qquad \textbf{Equation 2.41}$$

The XY model can be used for modelling planar magnets.

2.3.5 Exchange Interactions

Many different types of exchange contribute to the total exchange constant, |J|. These are described in the following sections.

2.3.5.1 Direct exchange

Direct exchange describes interactions between electrons in neighbouring magnetic atoms. The role of direct exchange is usually less significant than may be expected in describing the behaviour of a magnetic system, as it requires a high level of orbital overlap. In systems such as those involving rare earth metals, where the electrons are held close to the nucleus, there is insufficient overlap between the neighbouring magnetic orbitals for direct exchange to take place. In other systems, such as the transition metal compounds, where the orbital overlap is increased, direct exchange does not seem to fully account for the magnetic properties. Therefore, another type of exchange must be occurring, and this is known as indirect exchange.

2.3.5.2 Indirect Exchange

Indirect exchange describes the exchange taking place between two magnetic atoms via an intermediary. The main types of indirect exchange are discussed below.

2.3.5.2.1 Superexchange

Superexchange describes an exchange interaction occurring in an ionic solid between to magnetic ions, via a non-magnetic intermediate ion. This type of interaction is commonly seen in transition metal oxides and usually results in antiferromagnetic exchange, although ferromagnetic exchange is also possible [11] [12].

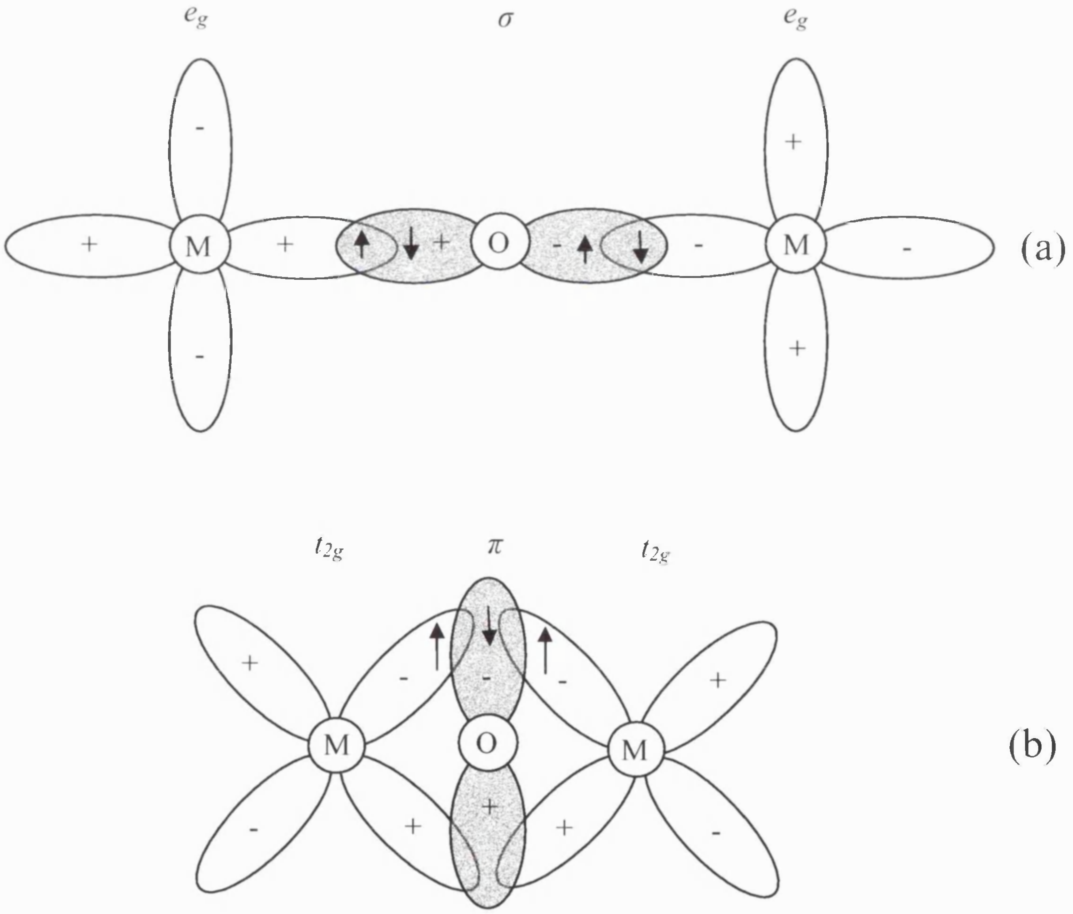

Figure 2.7 *(a) σ-transfer and (b) π- transfer superexchange interactions taking place between two metal ions in a metallic oxide.*

Figure 2.7 shows the antiferromagnetic superexchange interaction between two metal *d* (e_g) orbitals via an oxygen *p* (σ) orbital in a 180° M-O-M bond. In the ground state configuration, the oxygen contains one electron in each lobe of the *p* orbital. These electrons must have opposite spins (to satisfy the Pauli exclusion principle) and this in turn leads to opposing spins in the metal ions and hence, an antiferromagnetic configuration. This can take place in the form of σ-transfer (a) or π-transfer (b).

It is also possible for a ferromagnetic superexchange interaction to take place. This interaction is much weaker than the antiferromagnetic interaction and is rarely a dominating influence on the magnetic properties. The superexchange interaction is sensitive to bond angle, as deviations from the 180° configuration will directly affect the degree of overlap between the metal and oxygen orbitals. In compounds with a bond angle near 180°, the superexchange is usually antiferromagnetic, whereas in compounds where the bond angle is nearer 90°, ferromagnetic exchange occurs.

2.3.5.2.2 The RKKY interaction

The RKKY interaction (named after the authors who first proposed the mechanism, Ruderman, Kittel, Kasuya and Yoshida) describes magnetic exchange interactions that can occur in metallic compounds, via the conduction electrons. The localised moment on a magnetic ion can spin-polarize a conduction electron, which in turn can then couple with a magnetic ion some distance, r, away, thereby resulting in a coupling between two magnetic ions not connected by direct exchange. The exchange integral, J_{RKKY}, is given by

$$J_{RKKY} \propto \frac{\cos(2k_F r)}{r^3}$$ **Equation 2.42**

where k_F is the Fermi momentum. This equation gives a periodic function, so the interaction can be positive or negative (*i.e.* ferromagnetic or antiferromagnetic) depending on the separation between the magnetic ions. This mechanism is also sometimes known as 'itinerant exchange'.

2.3.5.2.3 Double Exchange

Double exchange is a mechanism for ferromagnetism in compounds in which the magnetic ion has mixed valency [13] [14]. A common example of a double exchange material is the perovskite manganate compound $La_{1-x}Sr_xMnO_3$, which is ferromagnetic for values of x up to 0.175. In this region of the series, there is mixture of Mn^{3+} and Mn^{4+} ions in the system. Figure 2.8 below illustrates the double exchange mechanism for a mixed valence manganese compound.

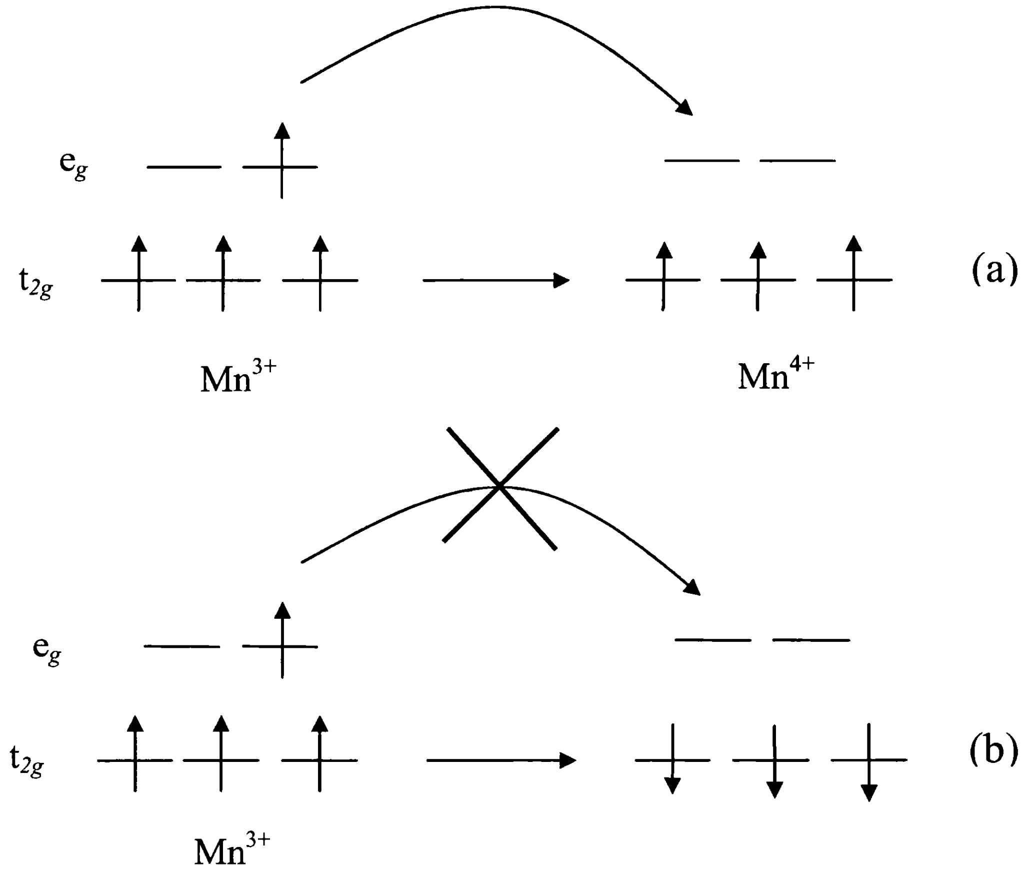

Figure 2.8 *The double exchange mechanism for ferromagnetism in a mixed valence manganese compound.*

As shown in figure 2.8, the Mn^{3+} ion is in the high spin configuration with three unpaired electrons in the t_{2g} orbital and one unpaired electron in the e_g orbital. The Mn^{4+} ion has three unpaired electrons in the t_{2g} orbital and the e_g orbital is empty. The e_g electron from the Mn^{3+} ion can hop to the empty e_g orbital on the Mn^{4+} ion, provided that it is not required to change its spin. Hund's first rule dictates that there is a strong single-centre exchange interaction favouring the alignment of the t_{2g} and e_g orbitals and consequently the Mn^{3+} e_g electron is only able to hop if the t_{2g} electrons of the Mn^{3+} and Mn^{4+} ion are aligned ferromagnetically.

This hopping, and consequently the ferromagnetic alignment, are favourable as the energy of the system as a whole is reduced. In addition, the hopping of the e_g electrons through the crystal gives the system metallic character which is dependent on the ferromagnetism.

2.3.6 Magnetic measurements

The magnetic measurements reported in this thesis were performed by means of DC SQUID magnetometry and AC susceptibility. These methods are described below.

2.3.6.1 Squid Magnetometry

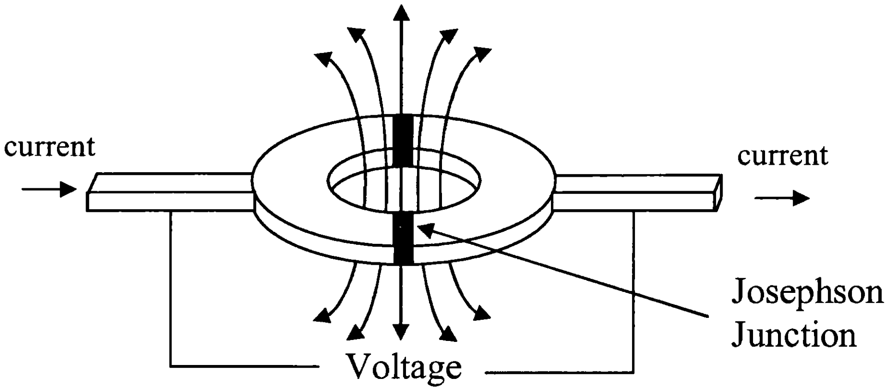

Figure 2.9 *Schematic diagram of a DC SQUID magnetometer.*

A DC SQUID comprises of a superconducting ring with two thin regions of insulating material, known as Josephson junctions, through which a superconducting current can tunnel. When a current is applied across the SQUID, as shown schematically in figure 2.9, it divides between the two Josephson junctions. If this current is greater than the maximum supercurrent which can tunnel through the Josephson junctions, known as the critical current, then the ring will have a non-zero resistance and a voltage is produced across it.

The magnetic flux, the product of the area of the ring and the magnetic field enclosed by it, is quantised whilst the ring is superconducting. The presence of the Josephson junction enables the trapped flux in the ring to vary by discrete amounts and this results in changes in the voltage which are very sensitive to flux change.

The relationship between the flux density in the ring and the flux density due to the applied field is

$$\Phi = \Phi_a + LI_s$$ **Equation 2.43**

where Φ is the flux density in the ring, Φ_a is the flux due to the applied field, L is the inductance of the ring and I_s is the supercurrent which produces a flux of $\Phi_s = LI_s$.

In the Josephson junction the superconducting current, I_s, is related to the critical current, I_c, determined by the properties of the weak link.

$$I_s = I_c \sin\theta \qquad \textbf{Equation 2.44}$$

where θ is the phase difference of the electron wave functions across the weak link. It follows that

$$\Phi = \Phi_a + LI_c \sin\theta \qquad \textbf{Equation 2.45}$$

As stated previously, if the ring is completely superconducting, the flux will be quantised and the total flux will be $N\ \Phi_0$ where N is an integer and Φ_0 is the flux quantum. Where there is a Josephson junction, the phase angle, θ, will vary with flux by the relationship

$$\theta = 2\pi N - 2\pi(\Phi / \Phi_0) \qquad \textbf{Equation 2.46}$$

As N is an integer,

$$\begin{aligned}\sin\theta &= \sin(-2\pi\Phi / \Phi_0)\\ &= -\sin(2\pi\Phi / \Phi_0)\end{aligned} \qquad \textbf{Equation 2.47}$$

and the flux density in the ring can be related to the applied flux by

$$\Phi = \Phi_a - LI_c \sin(2\pi\Phi / \Phi_0) \qquad \textbf{Equation 2.48}$$

When $\sin(2\pi\Phi/\Phi_0) = 0$ then Φ/Φ_0 and Φ_a/Φ are equal, however at values when the flux is not at an integer multiple of Φ_0 (when it is not quantised) they are not equal. Therefore the SQUID is capable of measuring changes in the flux which are smaller than the flux quantum and the device is extremely sensitive.

In a SQUID magnetometer, the magnetic field produced by the sample is used to induce a supercurrent in a pick-up loop. The loop forms part of a circuit with a coil, which generates a magnetic field in the SQUID. In order to increase the sensitivity of the SQUID, the coil is wound several times to increase the field experienced by the SQUID relative to that induced in the pick-up loop. The voltage across the SQUID is measured whilst moving the sample through the pick-up coil, the field inducing current in the pick-up loop being proportional to the magnetic moment of the sample divided by the cube of the distance between the sample and the loop. Measurement of how the voltage across the

SQUID varies with this distance allows the magnetic dipole of the sample to be determined and this in turn can be converted to a magnetisation or susceptibility.

2.3.6.2 AC Susceptibility

In an AC susceptibility measurement, an AC driven magnetic field is superimposed on the DC field which gives a time dependent moment on the sample. This fluctuating moment is then measured by a SQUID as described in section 2.3.6.1. Although the experimental technique is similar to that of the DC measurement, the AC measurement can provide different information on the magnetic properties of the sample being studied.

Where the AC frequency is very low, the results will be similar to that of a DC experiment as the magnetic moments move with the changing field. The moment induced by the AC field, m_{AC}, is given by

$$m_{AC} = \left(\frac{dM}{dH}\right) H_{AC} \sin(\omega t)$$ **Equation 2.49**

where H_{AC} is the amplitude of the driving AC field, ω is the driving frequency and $\chi = \left(\frac{dM}{dH}\right)$ is the susceptibility, or the gradient of the magnetisation against field curve.

Where the frequency of the AC field is high, the results of the AC and DC experiments differ. The driving field is changing too quickly for the sample to respond, and consequently a phase shift develops between the driving field and the induced moment. This can be detected by the magnetometer and therefore two quantities are measured in an AC experiment, the susceptibility, χ, and the phase shift relative to the drive field, φ. This is normally represented by giving two values of the susceptibility. These are the in-phase, or 'real', component, χ' and the out of phase, or 'imaginary' component, χ''.

These two parts of the susceptibility are defined by the equations

$$\chi' = \chi \cos\varphi$$ **Equation 2.50**

$$\chi'' = \chi \sin\varphi$$ **Equation 2.51**

$$\chi = \sqrt{(\chi')^2 (\chi'')^2}$$ **Equation 2.52**

$$\varphi = \arctan\left(\frac{\chi''}{\chi'}\right)$$ **Equation 2.53**

When the driving frequency of the AC field is low, the real component, χ', resembles the DC susceptibility and the imaginary component, χ'', provides information on energy losses in the sample. Studying both parts of the susceptibility can help identify specific behaviour in materials. For example, when a material becomes superconducting, (*i.e.* perfectly diamagnetic) a large χ'' component will be seen in the susceptibility and the real component will become negative. In spin glasses, both the imaginary and real components of the susceptibility are dependent on the frequency of the AC field. A non-zero value of the imaginary, component, χ'', is found in ferromagnets where there is irreversible domain wall movement.

2.4 Electronic Properties of Solids

There are two principle theories used to describe the electronic properties of solids, crystal field theory and band theory. Crystal field theory is a localised approach which examines the electronic structure at a particular crystallographic site. Band theory considers the electronic properties of an atom in relation to the whole crystal structure and is particularly useful in the study of semiconducting solids.

2.4.1 Crystal Field Theory

Crystal field theory describes how the *d*-orbitals of a transition metal ion are influenced by the coordination of the crystal environment in which they are placed. The *d*-orbitals of transition metal ions in a crystal can lose degeneracy, due to the interaction of their charge density with that of the crystal environment. In the case of an octahedral coordination the *d*-orbitals split into a lower energy triplet known as the t_{2g} set and a higher energy doublet known as the e_g set. The t_{2g} set consists of the d_{xy}, d_{yz} *and* d_{zx} orbitals and the e_g set the d_{x^2} and $d_{x^2-y^2}$ orbitals.

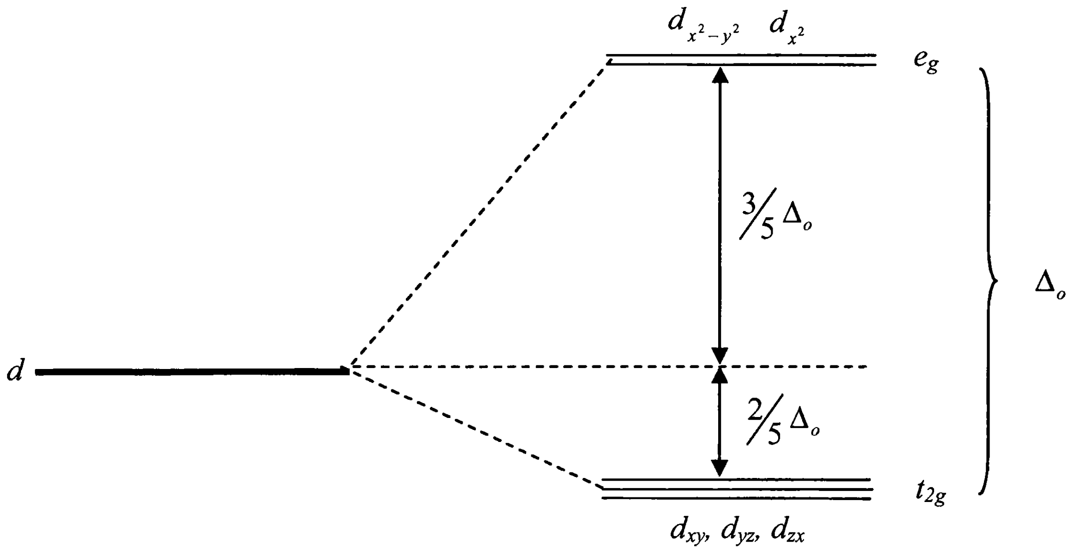

Figure 2.10 *The crystal field splitting of a transition metal cation in an octahedral coordination, where* Δ_o *is the energy difference between the doublet and the triplet.*

The energy of the triplet is decreased as these orbitals are orientated towards an area of low charge density, whereas the orbitals of the doublet are orientated directly towards the anions, increasing their energy. This is represented schematically in figure 2.10

The most stable state for the octahedral coordination is the high spin state, *i.e.* with the greatest number of unpaired electrons. For d^1, d^2 and d^3 cations in an octahedral coordination the *d* electrons are in the lower energy triplet. Cations with a d^3 electron distribution (e.g. Cr^{3+}) are particularly stable in the octahedral coordination. Another highly stable configuration arises from d^8 cations (e.g. Ni^{2+}) where the lower energy triplet is filled with paired electrons and the higher energy doublet is filled with unpaired electrons. When the crystal field splitting energy becomes very large it is preferable to fill only the lower energy triplet. For example, Rh^{3+} (d^6) is found in the octahedral coordination where the lowest energy configuration is with all 6 electrons paired in the lower energy triplet.

In a tetrahedral coordination the crystal field splitting is reversed, i.e. the doublet is of lower energy than the triplet. The energy difference between the doublet and the triplet (*i.e.* the splitting) is much less (about 4/9) than in the octahedral coordination. Cations such as Fe^{3+} with a d^5 electron distribution in the high spin state adopt spherical distribution and therefore have no preference for either the octahedral or tetrahedral coordination.

2.4.2 Band Theory

Band theory is used to describe how electrons move when they are in a periodic lattice, such as a crystal structure. When atoms are brought together in a crystal structure, their energy can no longer be considered to be the same as that when they are in a free state. The discrete energy levels are spread out into a range of sublevels which are so close together that they can be described as a band. The width of these bands is denoted E_b. The band into which the ground state valence level splits is termed the valence band; the bands with energy lower than the valence band correspond to the inner lying electronic levels in the free atom state. The lower energy bands are usually not considered in the construction of an energy band scheme as they do not contribute to the bulk electronic properties of the solid. As the bands each consists of many discrete energy levels they will fill from low to high energy with one electron per energy state to comply with the Pauli exclusion principle.

The energy level above the valence band is known as the conduction band; this is the first excited state. The energy gap between the valence band and the conduction band is denoted by E_g. Another energy, known as the Fermi level, E_F, must also be considered in band theory. This is the energy below which all energy states are occupied and is usually defined at absolute zero where there is no thermal excitation of the electrons. The electronic properties of a solid can be explained in terms of the energies defined above.

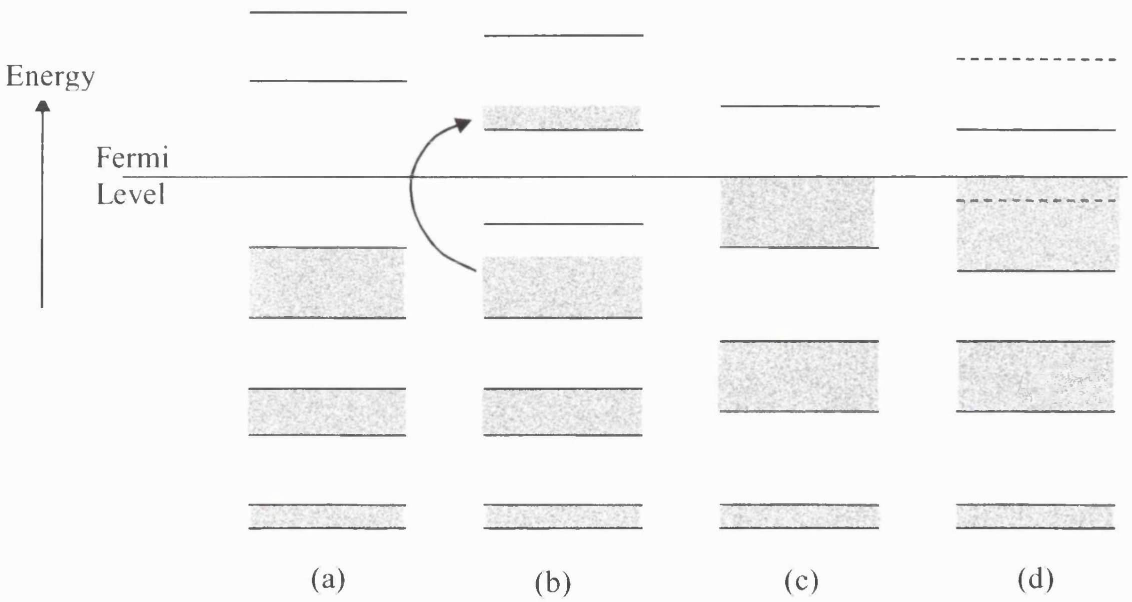

Figure 2.11 *Schematic representation of the energy band scheme for(a) an insulator, (b) a semiconductor, (c) a metal with a partially filled valence band and (d) a metal with two overlapping partially filled bands. Adapted from [2]*

Figure 2.11 shows the band model describing four situations which represent different electronic behaviour in solids. Model (a) represents the band structure of an insulator; here the valence band is full and there is a large energy gap, E_g, which prevents electrons being promoted into the conduction band. Model (b) represents the band structure of a semiconductor; here the situation is similar to that of an insulator, but E_g is smaller allowing the possibility of excitation of the electrons from the valence to the conduction band. A typical value of E_g for a semi conductor is 1.0 eV (compared to 4 eV for an insulator) which allows the promotion of electrons to the conduction band at room temperature.

Model (c) represents the band structure of a metal; here the valence band is only partially full, allowing the excitation of electrons, even at low temperatures, to positions above the Fermi level within the same band. This gives rise to a high conductivity in metals. In some situations, such as that of divalent metals (*e.g.* calcium) where the valence band would be expected to be full, conduction can still occur due to the band overlap.

2.4.3 Experimental measurement of electrical properties

Electrical transport measurements reported in this thesis have been performed using the 4-probe technique. This method enables the actual resistance of the sample to be measured whilst eliminating the resistance contributions of the experimental setup, such as the residual contact resistance and the impedance of the leads. The resistance due to the leads is often high when low temperature conductivity measurements are performed and the leads have to be poor thermal conductors and usually very long. The contact resistance is particularly large when measuring the resistance of a semiconductor for the following reason.

The Fermi level in a semiconductor or a metal is a measure of its chemical potential and therefore when two conductors are in electrical contact the Fermi levels will equalise by means of a flow of charge. This gives rise to a potential difference known as the contact potential. In a metal this contact potential is concentrated around a narrow region at the point of contact and therefore there is little barrier to electron tunnelling. In a semiconductor-metal junction, the relatively small number of carriers in the semiconductor prevents a large potential gradient from developing; there is a limit to the rate at which the potential can change with distance into the semiconductor. Therefore when a metal and a semiconductor come into contact, the electrons from the surface of the semiconductor flow into the metal giving a spatially extended depletion region which forms a barrier through which the conduction electrons cannot tunnel. This results in a large contact resistance.

Using the 4-probe method, shown in schematically in figure 2.12, the contact resistance can be eliminated from the measured resistance. A current is passed between wires (1) and (4) and the voltage is measured between wires (2) and (3) using a high impedance voltmeter. This means that effectively there is no current flowing through the voltmeter and therefore there can be no contribution to the resistance from the contacts or the wires and the voltage measured is the true voltage across the sample. The resistance in the sample can then be calculated using the relationship $V = IR$.

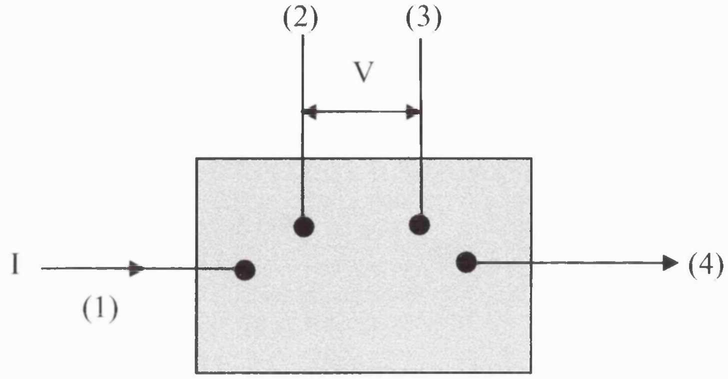

Figure 2.12 *Schematic diagram of the 4-probe technique for measuring resistivity.*

2.5 References

1. John, V.B., *Introduction to engineering materials*. 1992: Macmillan.
2. Rudden, M.N. and Wilson, J., *Elements of Solid State Physics*. 1993, Chichester: John Wiley and Sons.
3. Blakemore, J.S., *Solid State Physics*. Second Edition ed. 1969, Cambridge: Cambridge University Press.
4. Suryanayana, C. and Grant Norton, M., *X-ray Diffraction*. 1998: Plenum Press.
5. Young, R.A., *The Rietveld Method*. 1 ed. IUCr Monographs on Crystallography. Vol. 5. 1993, Oxford: Oxford Science Publications. 298.
6. Toraya, H., *Position-constrained and unconstrained powder-pattern-decomposition methods*, in *The Rietveld Method*, R.A. Young, Editor. 1993, Oxford University Press: New York. p. 254-275.
7. Blundell, S.J., *Magnetism in condensed matter*. Oxford master series in condensed matter physics. 2001, Oxford: Oxford University Press.
8. Cox, P.A., *The Electronic Structure and Chemistry of Solids*. 1 ed. Oxford Science Publications. 1993, Oxford: Oxford University Press. 259.
9. Harrison, W.A., *Electronic structure and the properties of solids*. 1 ed. 1989, New York: Dover Publications, INC. 586.
10. Mydosh, J.A., *Spin glasses: an experimental introduction*. 1993, London: Taylor and Francis.
11. Anderson, P.W., *Phys. Rev.*, 1950. **79**(2): p. 350-356.
12. Anderson, P.W., *Phys. Rev.*, 1959. **115**(1): p. 2-13.
13. De Gennes, P.-G., *Phys. Rev.*, 1960. **118**(1): p. 141-154.
14. Zener, C., *Phys. Rev*, 1951. **82**: p. 403-405.

Chapter 3 Synthesis and Characterisation

3.1 Experimental

3.1.1 Synthesis of $CuCr_2Se_4$ and $ZnCr_2Se_4$

Synthesis of $CuCr_2Se_4$ and $ZnCr_2Se_4$ was carried out using standard solid state synthesis methods from direct combination of the elemental metals copper, zinc, chromium and selenium. All starting materials were purchased from Aldrich and in the form of a fine powder of 99.99% purity. The required stoichiometric quantities of the starting materials were weighed out accurately (to within 0.1 mg) and ground together using an agate pestle and mortar until a homogeneous power was obtained. Approximately 2 g of total starting material was used in each case unless the sample was being prepared for powder neutron diffraction measurements where 10 g starting material was needed. The powder was placed in a quartz tube (diameter 5mm) which was connected to a vacuum line using Teflon Swagelok seals and evacuated using a turbo-molecular pump to a pressure of 10^{-6} torr and sealed. The tube was then placed in a furnace; a firing temperature of 600 °C was used for both compounds as reported in the literature [1, 2]. After firing for two days the reaction mixture was cooled slowly in the furnace at a rate of approximately 2 Kmin^{-1}. The progress of the synthesis was monitored at each stage using X-ray diffraction; the firing process was continued until the compounds appeared phase pure.

3.1.2 Synthesis of $Cu_{1-x}Zn_xCr_2Se_4$

Samples in the series $Cu_{1-x}Zn_xCr_2Se_4$ were prepared with $1 \geq x \geq 0$; standard solid state synthesis methods were used as for the pure $CuCr_2Se_4$ and $ZnCr_2Se_4$ compounds. It was found that a higher firing temperature (850 °C) was needed for the mixed Cu/Zn compounds in order to increase the mobility of the Zn^{2+} ions in the reaction mixture. It was also found that there was a tendency for phase disproportionation of the product into a $CuCr_2Se_4/ZnCr_2Se_4$ mixture; this was overcome by quenching the sample to room temperature immediately after firing by immersing the quartz tubing in cold water.

The progress of the synthesis was monitored after each firing by powder X-ray diffraction. In general, each sample required three firings before synthesis was complete. Samples in the high Zn doping range (above $x = 0.9$) were formed more readily than those in the lower doping range as noted in previous work by Krok *et. al.*[3]. Compounds with $x \leq 0.9$ were susceptible to phase disproportionation which could not be completely overcome by quenching the reaction mixture. Partly for this reason, work presented in this thesis has mainly concentrated on the investigation of compounds in the $Cu_{1-x}Zn_xCr_2Se_4$ series with $x \geq 0.9$. This region of the series has also been found to contain compounds exhibiting a diverse range of magnetic and electronic properties which can be investigated at temperatures below 400 K. Compounds containing higher concentrations of copper have magnetic transitions above 400 K which are difficult to study as specialist equipment is required. This is discussed in more detail in chapter 4 of this thesis.

Details of compositions prepared in the $Cu_{1-x}Zn_xCr_2Se_4$ are given in section 3.2.2.

3.1.3 Synthesis of $CuCr_2Se_{4-y}S_y$, $ZnCr_2Se_{4-y}S_y$ and $Cu_{1-x}Zn_xCr_2Se_{4-y}S_y$

Synthesis of $CuCr_2Se_{4-y}S_y$, $ZnCr_2Se_{4-y}S_y$ and $Cu_{1-x}Zn_xCr_2Se_{4-y}S_y$ was carried out using standard solid state synthesis methods. Compounds containing copper only on the A-site were fired at 600 °C and cooled in the furnace after firing at a rate of approximately 2 $Kmin^{-1}$. Compounds containing zinc on the A-site were fired at 850 °C and quenched rapidly to room temperature after firing.

It was found that it was possible to substitute up to two sulphur ions onto the X-site of $CuCr_2Se_4$; above this amount a multi-phase product was obtained in which no single spinel phase could be identified. Table 3.1 below details the compositions in the $Cu_{1-x}Zn_xCr_2Se_{4-y}S_y$ series which have been successfully prepared and studied in this thesis.

x	y				
	0.0	**0.5**	**1.0**	**1.5**	**2.0**
0.00	•	•	•	•	•
0.70			•		•
0.90	•		•		•
0.95	•		•		•
1.00	•	•	•	•	•

Table 3.1 *Compositions prepared in the* $Cu_{1-x}Zn_xCr_2Se_{4-y}S_y$ *series.*

3.1.4 Synthesis of $CuCr_2Se_{4-y}Br_y$

Synthesis of $CuCr_2Se_{4-y}Br_y$ was carried out for $y = 0.25$, 0.5 and 0.75 using standard solid state synthesis methods via the following reaction scheme:

$$(1-y)\mathrm{Cu} + y\mathrm{CuBr} + 2\mathrm{Cr} + (4-y)\mathrm{Se} \longrightarrow \mathrm{CuCr_2Se_{4-y}Br_y}$$

As CuBr is hydroscopic it was added to the reaction mixture in a N_2 glove box to prevent water contaminating the reaction process. Firing was carried out at 800 °C and subsequently the reaction mixture was cooled slowly in the furnace at a rate of approximately 2 $\mathrm{Kmin^{-1}}$. It was found that a maximum of 0.75 Br could be substituted onto the X-site; above this amount a multi-phase product was formed in which no spinel phase could be identified.

3.1.5 Powder X-ray diffraction and Rietveld Refinement

All samples were characterised using room temperature powder X-ray diffraction carried out on a Bruker D8 diffractometer fitted with a primary monochromater. The instrument operates in Bragg-Brentano reflection geometry using CuKα_1 (λ = 1.54056 Å) and tube current and voltage settings of 30mA and 40 kV respectively. The datasets were collected over the range $12 \leq 2\theta$ (°) ≤ 70 with a step size of 0.04° and 2 s scan time per step. Powder X-ray diffraction data for structural refinement were collected using the same instrument but over the range of $10 \leq 2\theta$ (°) ≤ 100 with a step size of 0.02° and 15 s scan time per step. The X-ray beam slits were kept constant at 1°, 1°, 0.3°, 0.015° for all experiments. During diffraction the sample was rotated in the horizontal plane at a speed of 30 rpm to increase the powder averaging. Details of the loading of these samples are given in section 3.2.1.

All refinements of the X-ray powder diffraction data were carried out by means of the Rietveld method using the refinement program GSAS [4]. All structures were refined in the $Fd\bar{3}m$ space group using the atom positions given in table 3.2 below. The parameter u is discussed in the introduction, section 1.1.1 and is a measure of the adjustment of the spinel structure to accommodate different cation radius ratios.

	x	y	z
A-site (Cu/Zn)	0.125	0.125	0.125
B-site (Cr)	0.5	0.5	0.5
X-site (Se/S/Br)	u	u	u

Table 3.2 *Atom positions for a cubic spinel in the* $Fd\bar{3}m$ *space group*

All thermal parameters quoted are the isotropic U values given by the GSAS program and all standard deviations in the refined values are also taken from the GSAS output. Profile coefficients used were from the type 2 pseudoVoigt function and the background was refined using a 6 term shifted Chebyshev function.

3.2 Results

3.2.1 $CuCr_2Se_4$ and $ZnCr_2Se_4$

Figures 3.1 and 3.2 show the Rietveld refinements of the powder X-ray diffraction patterns taken from $CuCr_2Se_4$ and $ZnCr_2Se_4$ respectively. The structural data obtained from these refinements and goodness of fit parameters are given in table 3.3.

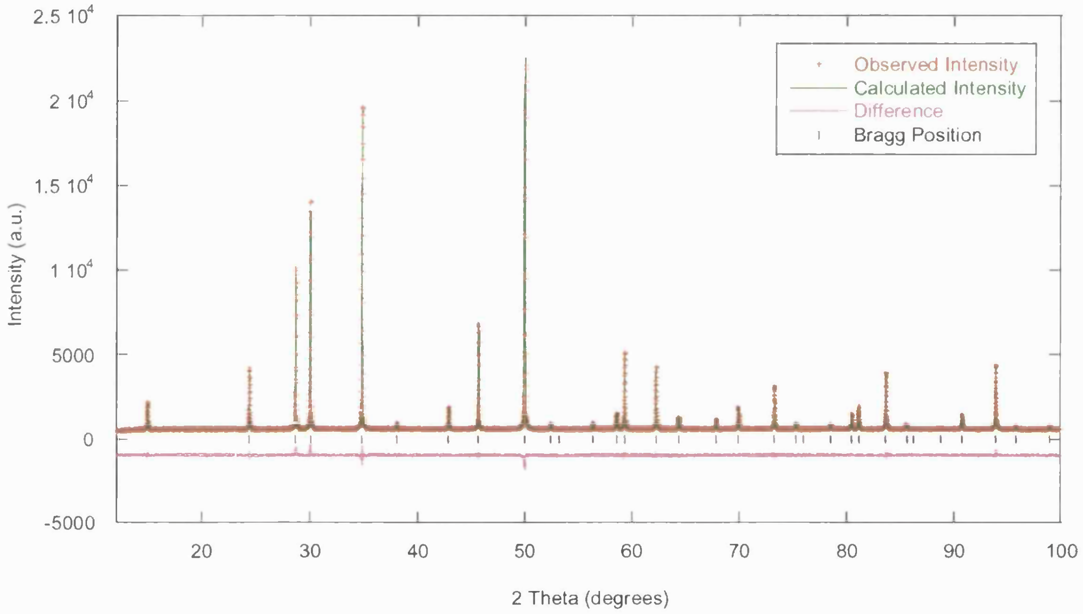

Figure 3.1 *Rietveld refinement of the powder X-ray diffraction pattern of* $CuCr_2Se_4$ *showing the observed, calculated and difference intensity plots.*

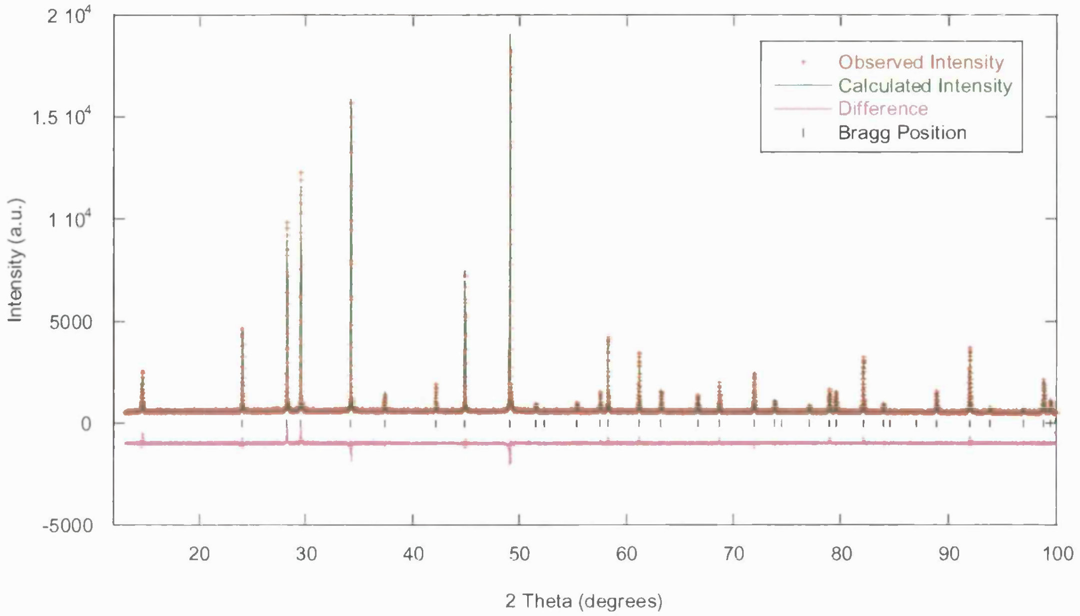

Figure 3.2 *Rietveld refinement of the powder X-ray diffraction pattern of* $ZnCr_2Se_4$ *showing the observed, calculated and difference intensity plots.*

Compound	Lattice parameter, a, (Å)	Selenium 'u' parameter	Thermal U parameters × 100 (Å^2)			χ^2	R_{wp} (%)
			Cu/Zn	Cr	Se		
$CuCr_2Se_4$	10.33423(9)	0.2575(2)	2.4(5)	1.8(3)	1.9(1)	1.235	4.16
$ZnCr_2Se_4$	10.4978(7)	0.2602(3)	1.6(6)	1.4(4)	0.7(2)	1.535	4.75

Table 3.3 *Structural Parameters and goodness of fit values obtained from the Rietveld refinement of* $CuCr_2Se_4$ *and* $ZnCr_2Se_4$.

It can be seen from figures 3.1 and 3.2 that both compounds are free from impurities and appear to be single phase. There are some small inconsistencies between the observed and calculated intensities of certain reflections in both compounds. The extent of this discrepancy was found to depend significantly on the experimental setup of the powder X-ray diffraction measurement. Initially the samples were measured using a Siemens D500 diffractometer where the powder sample was pressed into the sample holder with a glass slide to achieve a flat surface. Rietveld refinements of the patterns recorded from this experimental setup show a very significant difference between the observed and calculated intensities of the (111), (222), (400) and (444) reflections. Figure 3.3 shows an example of this in $ZnCr_2Se_4$.

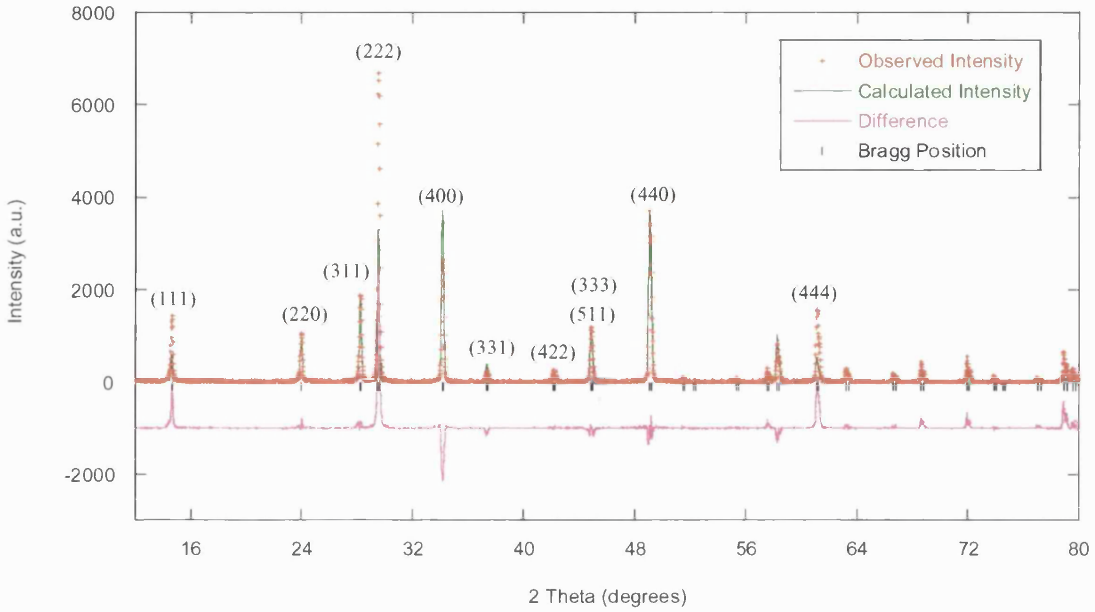

Figure 3.3 *Rietveld refinement of the powder X-ray diffraction pattern of* $ZnCr_2Se_4$ *recorded on a Siemens D500 diffractometer showing the observed, calculated and difference intensity plots.*

It was found that repeating the measurements several times, reloading the sample on each occasion, gave different intensities on the (111), (222) and (444) reflections. It was therefore concluded that the problems with the observed intensities were related to the packing of the sample in the sample holder. Anomalous intensities of these peaks will affect the calculated intensities on other peaks during the Rietveld refinement process as the program tries to compensate for the irregularity.

In order to try and reduce this effect, the diffraction experiments were repeated on the Brucker D8 diffractometer which has the facility to rotate the flat-plate sample holder in the horizontal plane during the measurement, hence increasing the powder averaging effect. In addition to this a Bruker zero background silicon (510) sample holder was used onto which the sample was sprinkled and held in place by a thin layer of grease; the sample surface was not pressed down. This method was found to significantly reduce the intensity problems as can be seen in figures 3.1 and 3.2.

This effect of sample loading on the observed intensities of the (111), (222) and (444) reflections suggests that there is a tendency for preferred orientation of the crystallites in the powder sample. This effect has been reported previously for a variety of cubic compounds such as NaCl [5]. It occurs when there is a tendency for crystallites in a powder sample to align in the sample holder in a certain orientation, often exacerbated by pressing the surface of the sample flat with a glass slide. When this occurs there will be a disproportionate exposure of one or more particular crystal faces to the X-ray beam and this will give an increased intensity to certain reflections.

Spinel compounds are known to form octahedral crystals, the largest surfaces of which are the (111) faces [6]. Examination of the powder samples using an electron microscope has revealed that there are large amounts of small (approx 20 µm across), well formed, octahedral crystallites present amongst the powder. The presence of these crystallites is likely to give rise to a preferred orientation effect in the diffraction patterns.

Powder neutron diffraction experiments (discussed in chapter 7 of this thesis) do not show any anomalies in reflection intensity. This is to be expected as preferred orientation is unlikely to be a factor in a neutron experiment where the bulk of the powder, rather than the surface, is being probed. In addition a much larger quantity of sample is used which will increase the powder averaging effect.

It could also be considered that the anomalies in intensity may arise from stacking faults, however this idea is inconsistent with the experimental observations described above.

3.2.2 The $Cu_{1-x}Zn_xCr_2Se_4$ Series

All compounds in the $Cu_{1-x}Zn_xCr_2Se_4$ series were characterized using powder X-ray diffraction and subsequent Rietveld refinement. The structural parameter and goodness of fit values obtained are given in table 3.2 which includes the structural parameters of $CuCr_2Se_4$ and $ZnCr_2Se_4$ for comparison. Plots of all other Rietveld refinements from compounds in this series, not shown in this section, are included in the appendix, section 8.2.1. As Cu^+ and Zn^{2+} have the same number of electrons it is not possible to distinguish them using the simple powder X-ray diffraction techniques employed in this study. It was therefore not possible to refine the fractional occupancy of copper and zinc on the A-site, which for the purposes of the Rietveld refinements was considered to contain only zinc ions.

x	**Lattice parameter, a, (Å)**	**Selenium u parameter**	**Thermal U parameters × 100 (Å²)**			χ^2	R_{wp}
			Cu/Zn	**Cr**	**Se**		
0.00	10.33423(9)	0.2575(2)	2.4(5)	1.8(3)	1.9(1)	1.235	4.16
0.25	10.3792(8)	0.256(1)	3(2)	3(1)	3.4(7)	6.752	10.01
0.50	10.4190(6)	0.2579(7)	6.32(5)	5.57(5)	5.15(6)	9.186	11.25
0.75	10.4596(6)	0.2588(4)	3.1(8)	2.0(5)	3.0(3)	1.894	4.94
0.80	10.4659(9)	0.2593(2)	2.2(5)	1.2(3)	1.5(1)	1.392	4.31
0.85	10.4759(8)	0.2595(2)	2.5(5)	1.7(4)	1.9(2)	1.555	4.38
0.90	10.4832(7)	0.2600(3)	2.1(6)	1.3(4)	1.0(2)	1.905	4.01
0.905	10.4838(6)	0.2593(2)	1.4(5)	1.0(1)	1.1(1)	1.270	4.55
0.91	10.4847(7)	0.2597(2)	2.7(5)	1.9(4)	2.3(2)	1.527	4.33
0.92	10.487(1)	0.2594(2)	0.7(5)	0.1(3)	0.1(1)	1.142	4.56
0.93	10.4864(7)	0.2593(2)	2.2(4)	1.6(3)	1.9(1)	1.168	3.81
0.95	10.490(1)	0.2593(3)	2.0(6)	1.7 (4)	2.1(2)	1.309	4.13
0.96	10.4920(7)	0.2600(2)	1.4(5)	0.9(4)	0.6(2)	1.788	4.87
0.97	10.4940(1)	0.2602(3)	1.1(5)	1.7(7)	0.7(2)	2.667	5.84
0.99	10.4968(1)	0.2604(2)	2.2(5)	1.4(4)	0.8(1)	1.936	4.97
1.00	10.4978(7)	0.2602(3)	1.6(6)	1.4(4)	0.7(2)	1.535	4.75

Table 3.4 *Structural Parameters and goodness of fit values obtained from the Rietveld refinement of compounds from the* $Cu_{1-x}Zn_xCr_2Se_4$ *series.*

The results of the refinements showed compounds with $0.9 \leq x \leq 1.0$ to be highly crystalline and free from impurities. Figure 3.4 shows an example of a refinement of a compound in this region of the series, $Cu_{0.07}Zn_{0.93}Cr_2Se_4$. In a few cases (e.g. $Cu_{0.01}Zn_{0.99}Cr_2Se_4$ and $Cu_{0.04}Zn_{0.96}Cr_2Se_4$) there was some difficulty in correctly refining the intensities of certain reflections ((111), (222), (400) and (444)) and this is reflected in the larger values of χ^2 for these refinements. This is attributed to possible preferred orientation effects as discussed in section 3.2.1. Repeating the diffraction experiments for these samples gave slightly different intensities on each occasion for these reflections and it can therefore be concluded that the problem is related to the packing of the powder sample. It is not clear, however, why the effect should be enhanced for these particular compounds. One possible explanation is that the crystallites are larger in some samples than others which may reduce the powder averaging and give increased preferred orientation effects.

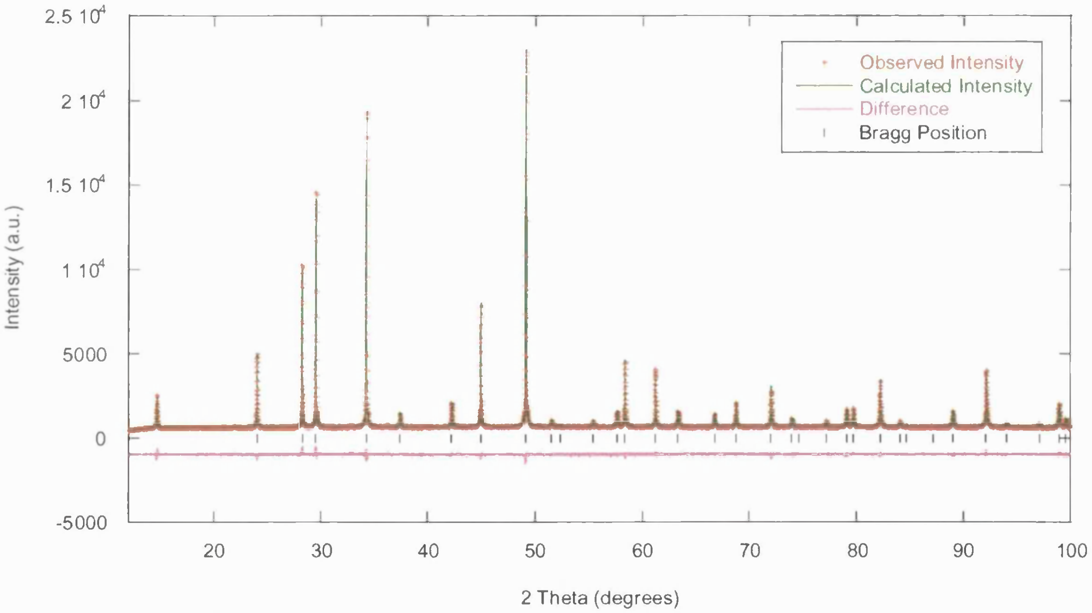

Figure 3.4 *Rietveld refinement of the powder X-ray diffraction pattern of* $Cu_{0.07}Zn_{0.93}Cr_2Se_4$ *showing the observed, calculated and difference intensity plots.*

For compounds with $x \leq 0.9$ it was found that, despite quenching the reaction mixture (see section 3.1.2), there was still a tendency for phase separation which increased with increasing copper content. The X-ray diffraction patterns show a broadening at the base of the peaks which can be attributed to the presence of a number of other phases of composition close to that of the main phase (see figure 3.5). This effect was found to be greatly reduced by quenching the sample after firing, but not totally eradicated. It has been reported in the literature that complete solid solubility (without quenching) is only possible in this series for $x \geq 0.98$ [7], but that quenching from temperatures above 600 °C gave solubility throughout the series [8].

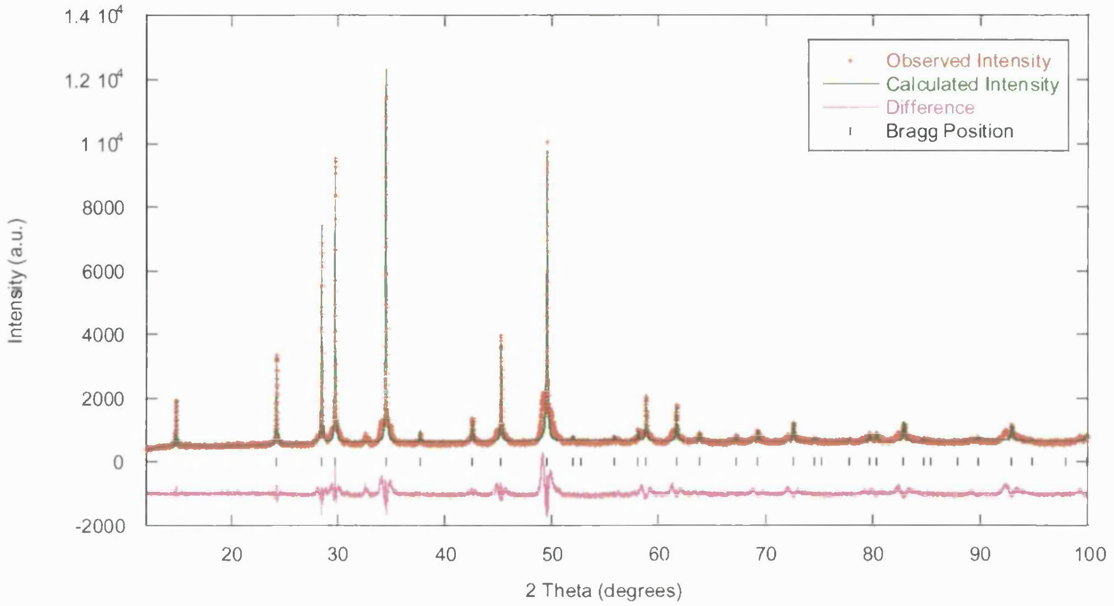

Figure 3.5 *Rietveld refinement of the powder X-ray diffraction pattern of* $Cu_{0.50}Zn_{0.50}Cr_2Se_4$ *showing the observed, calculated and difference intensity plots.*

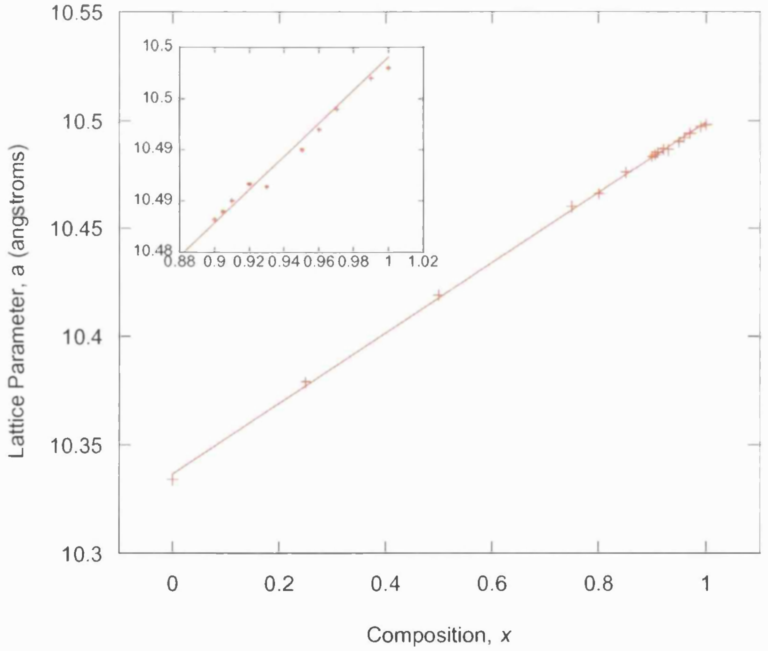

Figure 3.6 *Plot of lattice parameter 'a' vs. composition 'x' for compounds in the series* $Cu_{1-x}Zn_xCr_2Se_4$*. with inset detail in the composition region* $0.9 \leq x \leq 1.0$*.*

Figure 3.6 shows a plot of lattice parameter versus composition for compounds in the $Cu_{1-x}Zn_xCr_2Se_4$ series. The lattice parameters obtained are comparable with those reported in the literature [8-10]. It can be seen that there is a linear relationship between the lattice parameter and the composition in accordance with Vegard's Law. This is indicative that a solid solution can be formed throughout the series when the reaction mixture is quenched, although impurities are present in the region below $x = 0.9$ As it was not possible to refine the fractional occupancy of zinc and copper ions on the A-site it must be assumed for the purposes of analysing this data that the compositions are reasonably accurate, although there may in fact be some small deviations from the intended compositions. There is further evidence from the analysis of the magnetic behaviour of these compounds (see chapter 4 of this thesis) that these compositions are reasonably accurate.

3.2.3 The $Cu_{1-x}Zn_xCr_2Se_{4-y}S_y$ series

Compounds in the $Cu_{1-x}Zn_xCr_2Se_{4-y}S_y$ series have been characterised by powder X-ray diffraction and subsequent Rietveld refinement. Table 3.5 contains key structural information and goodness of fit parameters from these refinements. Where relevant, the fractional occupancy of the Se^{2-} and S^- ions on the X-site has been refined, constrained to total unity. The thermal U parameters and atom positions of the sulphur and selenium ions were constrained to be the same. There is good agreement in all cases between the fractional occupancy of the X-site and the intended composition of the compounds. Figure 3.7 shows the variation of composition with lattice parameter for compounds in the $Cu_{1-x}Zn_xCr_2Se_{4-y}S_y$ series. As no data was available for the lattice parameter of $Cu_{0.30}Zn_{0.70}Cr_2Se_4$, a value was estimated from figure 3.6 for comparison.

Composition		**Lattice parameter, a, (Å)**	**X-site occupancy***		**Se/S'u' parameter**	**Thermal U parameters × 100 (Å^2)**			χ^2	R_{wp}
x	y		**Se**	**S**		**Cu/Zn**	**Cr**	**Se/S**		
0.00	**0.0**	10.33423(9)	n/a	n/a	0.2575(2)	2.4(5)	1.8(3)	1.9(1)	1.235	4.16
0.00	**0.5**	10.2749(2)	0.87(3)	0.12(3)	0.273(8)	2.1(7)	1.4(5)	1.5(2)	1.993	5.41
0.00	**1.0**	10.208(1)	0.74(3)	0.25(3)	0.259(3)	3.2(7)	2.1(5)	2.3(2)	1.609	4.58
0.00	**1.5**	10.154(3)	0.62(4)	0.37(4)	0.259(2)	2.9(8)	1.3(6)	2.0(3)	1.314	4.60
0.00	**2.0**	10.091(2)	0.49(4)	0.50(4)	0.262(2)	4.1(7)	2.6(5)	2.7(4)	1.625	4.42
0.70	**1.0**	10.3244(4)	0.748(2)	0.252(2)	0.260(2)	3.5(4)	2.2(2)	2.6(2)	1.241	3.83
0.70	**2.0**	10.1955(2)	0.50(3)	0.50(3)	0.262(1)	3.6(5)	1.6(4)	2.3(3)	1.145	4.37
0.90	**0.0**	10.4832(7)	n/a	n/a	0.26000(3)	2.1(6)	1.3(4)	1.0(2)	1.905	4.01
0.90	**1.0**	10.3480(1)	0.774(3)	0.226(3)	0.2642(2)	3.0(4)	1.8(3)	2.2(2)	1.166	3.99
0.90	**2.0**	10.2235(6)	0.534(2)	0.466(2)	0.2614(6)	3.5(5)	2.0(4)	2.5(3)	1.172	3.85
0.95	**0.0**	10.490(1)	n/a	n/a	0.2593(3)	2.0(6)	1.7(2)	2.1(4)	1.309	4.13
0.95	**1.0**	10.3583(7)	0.74(3)	0.25(3)	0.258(2)	2.7(4)	1.5(3)	1.8(2)	1.199	4.13
0.95	**2.0**	10.223(1)	0.51(3)	0.48(3)	0.256(1)	3.2(4)	1.8(3)	2.2(3)	1.155	3.81
1.00	**0.0**	10.4978(7)	n/a	n/a	0.2602(3)	1.6(6)	1.4(4)	0.7(2)	1.535	4.75
1.00	**0.5**	10.4327(7)	0.87(2)	0.12(2)	0.2580(4)	2.2(5)	1.2(3)	1.5(2)	1.287	4.18
1.00	**1.0**	10.367(1)	0.74(3)	0.25(3)	0.259(2)	3.7(2)	2.4(4)	2.9(2)	1.268	4.05
1.00	**1.5**	10.2998(2)	0.63(3)	0.36(3)	0.263(1)	2.4(5)	1.0(4)	1.3(3)	1.359	4.12
1.00	**2.0**	10.233(3)	0.49(3)	0.50(3)	0.263(7)	4.4(6)	2.9(4)	3.2(4)	1.275	4.28

Table 3.5 *Structural Parameters and goodness of fit values obtained from the Rietveld refinement of compounds from the* $Cu_{1-x}Zn_xCr_2Se_{4-y}S_y$ *series*

---

* Constrained to total unity

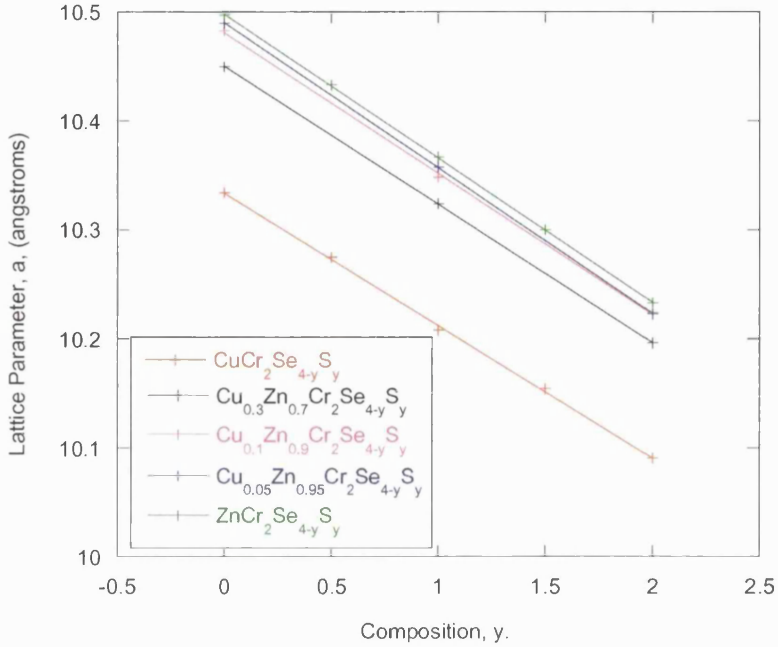

Figure 3.7 *Plot of lattice parameter vs. composition for compounds in the* $Cu_{1-x}Zn_xCr_2Se_{4-y}S_y$ *series.*

Figure 3.7 shows a linear variation of lattice parameter with composition for the $Cu_{1-x}Zn_xCr_2Se_{4-y}S_y$ series, in accordance with Vergard's Law.

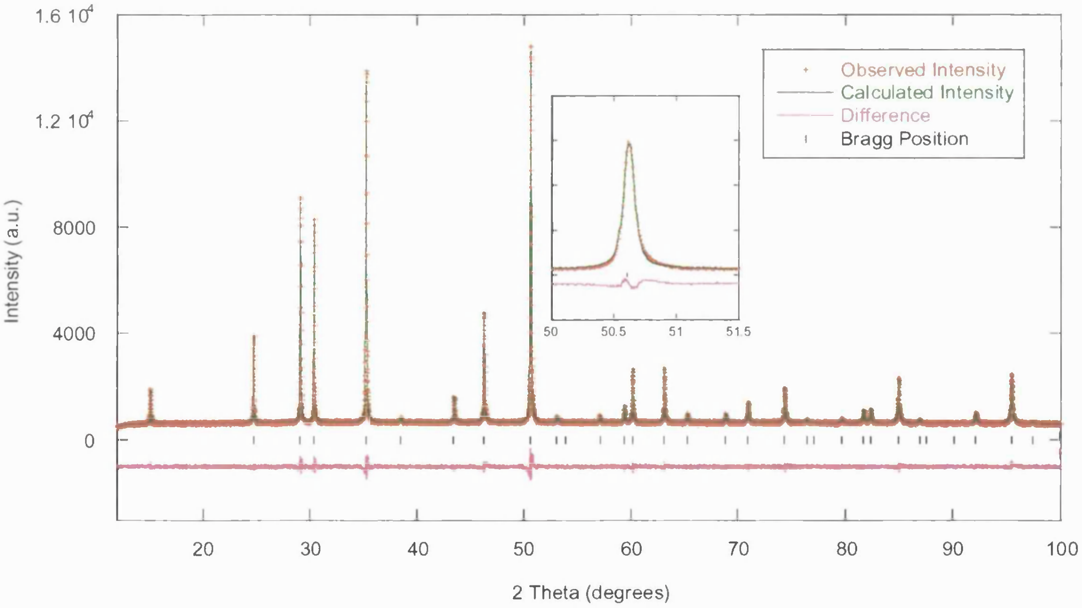

Figure 3.8 *Rietveld refinement of the powder X-ray diffraction pattern of* $CuCr_2Se_3S$ *showing the observed, calculated and difference intensity plots and inset detail of the (440) reflection.*

Analysis of the X-ray diffraction patterns of compounds in the series $CuCr_2Se_{4-y}S_y$ found them to be crystalline and free from impurity phases. Figure 3.8 shows the Rietveld refinement of $CuCr_2Se_3S$. It can be seen that there is an asymmetric broadening of the peaks which cannot be satisfactorily fitted with the pseudovoigt peak shape function. This feature is not seen in the refinements of the zinc containing compounds in this series. It is possible that this broadening is due to strain in the spinel lattice created by the substitution of the smaller sulphur ions onto the X-site [5]. The presence of larger zinc ions on the A-site may relieve this strain which would explain the lack of broadening of the peaks in the zinc containing compounds. The difference in synthesis conditions (see section 3.1.3) may also be influential. Attempts were made to prepare the $CuCr_2Se_{4-y}S_y$ compounds at the higher temperature of 850 °C but this was unsuccessful and resulted in mixed phase products.

Figure 3.9 shows the Rietveld refinement of $ZnCr_2Se_3S$, in which there is no broadening of the peaks. All zinc containing compounds refined satisfactorily with the exception of some small intensity problems on the (111), (222) and (444) reflections as discussed in section 3.2.1. All refinements of compounds in the $Cu_{1-x}Zn_xCr_2Se_{4-y}S_y$ not shown in this section are included in section A.2.2 of the appendix.

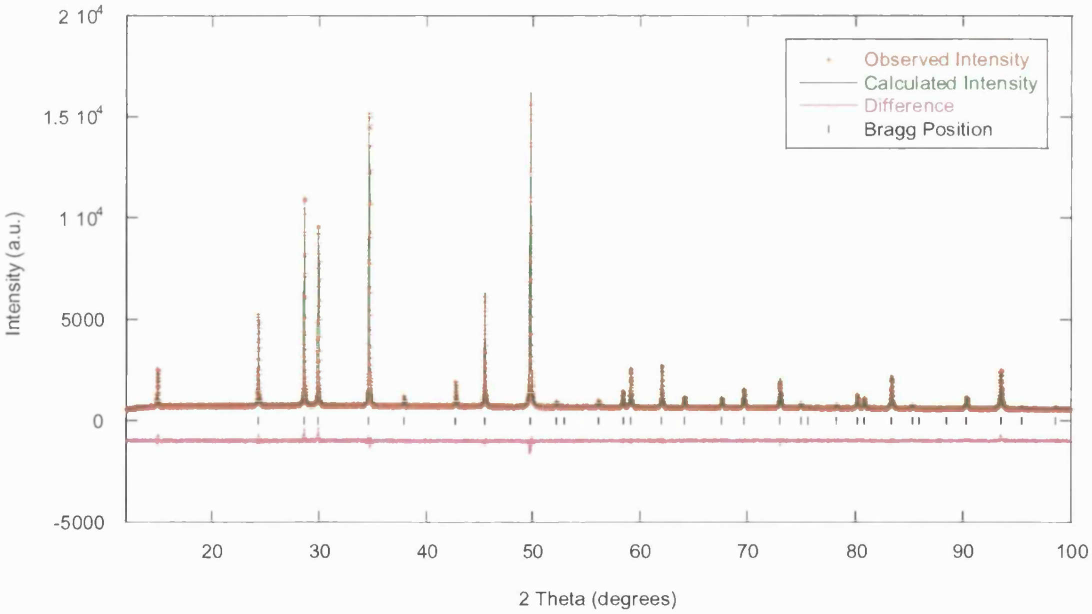

Figure 3.9 *Rietveld refinement of the powder X-ray diffraction pattern of* $ZnCr_2Se_3S$ *showing the observed, calculated and difference intensity plots.*

3.2.4 $CuCr_2Se_{4-y}Br_y$

Compounds in the $CuCr_2Se_{4-y}Br_y$ series were characterised by powder X-ray diffraction and subsequent Rietveld refinement. Key structural parameters and goodness of fit values are given in table 3.6. It was not possible to refine the relative occupancy of Se^{2-} and Br^- on the X-site as these ions are isoelectronic and are therefore indistinguishable by X-ray diffraction. For the purposes of these refinements therefore, all atoms on the X-site were treated as Se^{2-}.

Composition y	**Lattice parameter,** a, (Å)	**Se/Br'u' parameter**	**Thermal U parameters × 100 (Å²)**			χ^2	R_{wp}
			Cu	**Cr**	**Se/Br**		
0.00	10.33423(9)	0.2575(2)	2.4(5)	1.8(3)	1.9(1)	1.235	4.16
0.25	10.349(1)	0.256(6)	2.2(4)	1.2(3)	1.6(2)	1.390	4.54
0.50	10.365(1)	0.255(2)	1.2(5)	1.2(2)	0.4(2)	1.476	5.54
0.75	10.393(1)	0.256(4)	2.5(6)	0.9(3)	1.2(1)	1.157	4.21

Table 3.6 *Structural Parameters and goodness of fit values obtained from the Rietveld refinement of compounds from the* $CuCr_2Se_{4-y}Br_y$ *series*

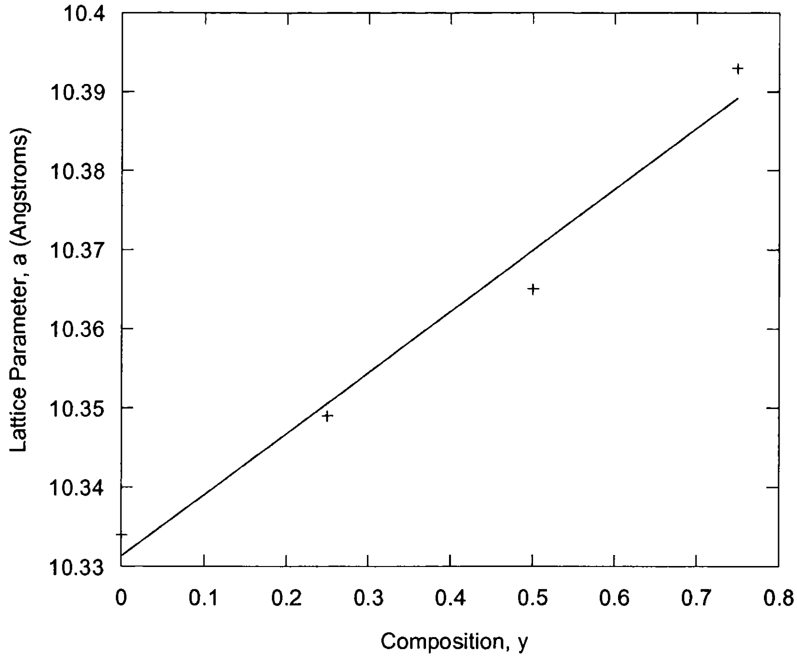

Figure 3.10 *Plot of Lattice parameter vs. composition for compounds in the series* $CuCr_2Se_{4-y}Br_y$.

Figure 3.10 shows the variation of lattice parameter with composition for compounds in the series $CuCr_2Se_{4-y}Br_y$. It can be seen that there is a deviation from a linear relationship between the lattice parameter and composition which could be related to the substitution of a 1- ion for a 2- ion on the X-site which is likely to cause increased structural deformation. This could also be an explanation for why it is not possible to prepare compounds in this series with $y > 0.75$. It has been reported in the literature that up to two Br^- can be substituted in to $CuCr_2Se_{4-y}Br_y$ but that for $y \geq 1$ there was a significant loss of copper on the A-site [11].

Figure 3.11 shows an example of a refinement of a compound in the $CuCr_2Se_{4-y}Br_y$ series; refinements of other compounds in the series are given in the appendix, section A.1.3. All compounds were found to be highly crystalline and free from impurities; there was some difficulty in refining the intensities of certain reflections as discussed in section 3.2.1.

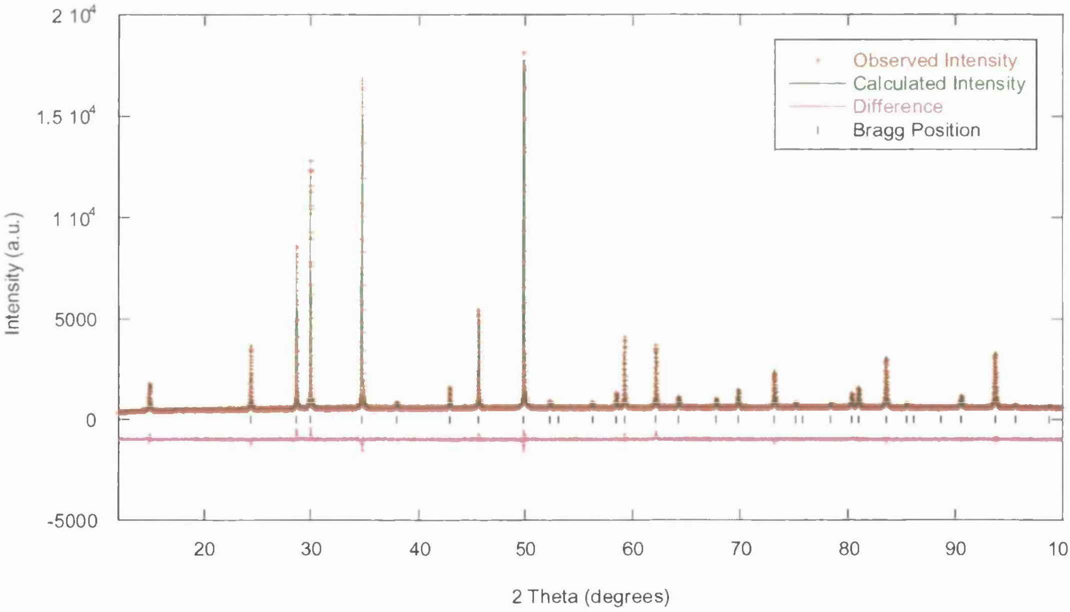

Figure 3.11 *Rietveld refinement of the powder X-ray diffraction pattern of* $CuCr_2Se_{3.75}Br_{0.25}$ *showing the observed, calculated and difference intensity plots.*

3.3 Discussion

In general, the compounds prepared for study in this thesis appear to be highly crystalline and free from impurities. The problems encountered in refining the intensity of some of the peaks appear to be related to a preferred orientation effect and there is further evidence from the neutron diffraction data, reported in chapter 7, to support this theory. Other factors which may lead to anomalies in the observed intensity of a diffraction pattern include stacking faults and deficiency in the occupation of crystallographic sites but there is no evidence to suggest that either of these is occurring in this case.

Phase separation was found to occur in compounds in the $Cu_{1-x}Zn_xCr_2Se_4$ series; this could be prevented by quenching of the reaction mixture after firing in compounds with $x \geq 0.9$. For compounds with $x \leq 0.9$ quenching did not give a phase pure sample and small amounts ($\approx\leq 3$ %) of impurity phases were present. It is possible that with more rapid methods of quenching, such as using a liquid nitrogen bath, single phase products may have been obtained.

Total solubility could not be achieved for either the $CuCr_2Se_{4-y}Br_y$ or the $CuCr_2Se_{4-y}S_y$ series. The ionic radii of the Se^{2-}, S^{2-} and Br^- ions in a 6 coordinate octahedral configuration are 198, 184 and 196 pm respectively. Hume-Rothery's rules for solid solubility state that if the difference between the sizes of two atoms is less than 14 % then the formation of a solid solution is favourable, however, total solubility is only seen when the size difference is less than 7 % [12]. The size difference between the selenium and sulphur ions here is approximately 8 %, which may explain why total solubility of the $CuCr_2Se_{4-y}S_y$ has not been observed. The ionic radii of Se^{2-} and Br^- are very similar (198 and 196 pm respectively) so this cannot be the reason for lack of total solid solubility in the $CuCr_2Se_{4-y}Br_y$ series. The reason for lack of solubility in this case is more likely to be due to the difference in electronegativity between the two ions. As Br^- is much more electronegative than Se^{2-} it is likely that this results in instability in the lattice and prevents total solubility.

Total solubility has been reported previously for the $CuCr_2Se_{4-y}S_y$ series with a linear variation in lattice parameter [13], however, at $y = 3$ anomalies were observed in the magnetic behaviour and in the intensity of peaks of the diffraction patterns. This is discussed in more detail in the introduction, section 1.3.4.1. In the $CuCr_2Se_{4-y}Br_y$ series a maximum of $y = 1$ has been achieved [14, 15], which is in fairly good agreement with the results reported here.

The relative site occupancies of the A and X sites could not be refined in the case of the $Cu_{1-x}Zn_xCr_2Se_4$ and $CuCr_2Se_{4-y}Br_y$ series as Cu^+ and Br^- are isoelectronic with Zn^{2+} and Se^{2-} respectively. In the case of the $Cu_{1-x}Zn_xCr_2Se_4$ series, the composition was found to vary linearly with lattice parameter in agreement with Vegard's Law which confirms that the intended composition was obtained during synthesis. However for compounds in the $CuCr_2Se_{4-y}Br_y$ series there was some deviation from Vegard's Law suggesting that there may be some deviation from the intended composition. This could have been confirmed by chemical analysis but this was considered to be an unnecessary expense as the deviation did not appear to be very large. The synthesis of both series should, in theory, have given the intended composition in all cases as the solid state reactions did not give any by-products and the reactions occurred in sealed tubing. However it is possible that a small percentage of the starting material could have been lost during the grinding process which could have led to a deviation from the intended composition.

3.4 References

1. Nakatani, I., Nose, H., and Masumoto, K., *J. Phys. Chem. Solids*, 1978. **39**: p. 743-749.
2. Lotgering, F.K. and van Stapele, R.P., *J. Appl. Phys.*, 1968. **39**(2): p. 417-423.
3. Krok, J., Spalek, J., Juszczyk, S., and Warczewski, J., *Phys. Rev. B*, 1983. **28**(11): p. 6499-6509.
4. Larson, A.C. and Von Dreele, R.B., *General Structural Analysis System*. 1998, University of California.
5. Young, R.A., *The Rietveld Method*. 1 ed. IUCr Monographs on Crystallography. Vol. 5. 1993, Oxford: Oxford Science Publications. 298.
6. Okonska-Kozlowska, I., Kopyczok, J., Wokulska, K., and Kammel, J., *J. Alloy. Compd.*, 1992. **189**: p. 1-7.
7. Lotgering, F.K., *J. Phys. Chem. Solids*, 1968. **29**: p. 699-709.
8. Okonska-Kozlowska, I. and Krok, J., *Z. Anorg. Allg. Chem.*, 1978. **447**: p. 235.
9. Khan, M.N., Venkatachalam, A., Ahmad, A., and Darshane, V.S., *J. Mater. Sci.*, 1990. **25**: p. 595-598.
10. Groń, T., *Phil. Mag. B*, 1994. **70**: p. 121-132.
11. Pink, H., Unger, W.K., Schafer, H., and Goebel, H., *Appl. Phys.*, 1974. **4**: p. 147.
12. John, V.B., *Introduction to engineering materials*. 1992: Macmillan.
13. Ohbayashi, K., Tominaga, Y., and Iida, S., *J. Phys. Soc. Jpn.*, 1968. **24**: p. 1173-1174.
14. Yamashita, O., Yamauchi, H., Yamaguchi, Y., and Watanabe, H., *J. Phys. Soc. Jpn.*, 1979. **47**(2): p. 450-457.
15. Robbins, M., Baltzer, P.K., and Lopatin, E., *J. Appl. Phys.*, 1968. **39**(2): p. 662-666.

Chapter 4 Magnetisation Measurements

4.1 Introduction

Several studies have been carried out on the magnetic properties of the $Cu_{1-x}Zn_xCr_2Se_4$ series [1-7]. The end members, $ZnCr_2Se_4$ and $CuCr_2Se_4$, are an antiferromagnet (T_N = 22K) with a spiral magnetic structure and a double exchange ferromagnet (T_C = 460 K) respectively [8, 9]. The magnetic properties of these compounds are discussed in more detail in chapter 1, sections 1.3.1 and 1.4.

The $Cu_{1-x}Zn_xCr_2Se_4$ system has been found to be ferromagnetic for $0 \leq x \leq 0.8$ due to the influence of the double exchange mechanism; the Curie temperature of these compounds decreases with increasing zinc content [7]. In this region of the series, an anomalous peak is seen in the magnetic susceptibility at low temperature (≈ 20 K) which has been attributed to a transition to a non-collinear structure at low temperature [6].

For $0.8 < x < 0.95$, a conical magnetic structure exists where the behaviour is predominantly antiferromagnetic with values of T_N close to 20 K [5]. It has also been suggested that a spin glass state can be found in some compounds in this region of the series [10].

The magnetism of the $CuCr_2Se_{4-y}S_y$ series has also been investigated; it was found that the T_C decreases with increasing sulphur content for $0 \leq y \leq 3$ [11]. The effects of substituting selenide by bromide have also been found to result in a lowering of T_C [12]. These studies are discussed in more detail in sections 1.3.4.1 and 1.3.4.2 in the introduction.

The magnetic properties of the $Cu_{1-x}Zn_xCr_2Se_4$, $Cu_{1-x}Zn_xCr_2Se_{4-y}S_y$ and $CuCr_2Se_{4-y}Br_y$ series are investigated in this thesis using DC SQUID magnetometry. The variation of the magnetisation with temperature has been studied for all compounds and hysteresis loops have been measured at low temperature (5 K) in high and low fields. In some cases, additional measurements have been carried out to study aging phenomena in the DC magnetisation. AC susceptibility techniques have also been used to further investigate the magnetic behaviour of $Cu_{0.05}Zn_{0.95}Cr_2Se_4$.

4.2 Experimental

4.2.1 Squid Magnetometry

For the magnetic measurements discussed in this research, samples of accurately known mass were placed in gelatin capsules (Agar Scientific size 4, 5mm diameter, 0.21 mL volume). Data were collected using a Quantum Design MPMS7 SQUID magnetometer; sample capsules were mounted in a clear and colourless plastic drinking straw, with 3 empty capsules on either side to prevent movement during measurement and to automatically correct for the gelatin capsule susceptibility. The straws were then attached to the end of the sample rod using non-magnetic Kapton tape.

All magnetisation data was recorded in a field of 100 Gauss unless otherwise stated. The temperature range of the SQUID magnetometer is 1.8 to 400 K; zero field cooled and field cooled magnetisation was measured for each sample. In the studies of antiferromagnetic samples, magnetisation was measured every 2 K between 1.8 and 50 K and then every 5 K to 300 K. In the studies of ferromagnetic samples, magnetisation was measured every 2 K from 2 to 30 K and then every 5 K to 400 K.

Magnetic hysteresis measurements were performed at 5 K; samples were cooled in zero field and then the magnetisation was measured every 50 Gauss as a field was applied from 0 → 1000 → -1000 → 0 Gauss. High field hysteresis measurements were performed measuring every 2000 Gauss as a field was applied from 0 → 70,000 → -70,000 → 0 Gauss.

4.2.2 AC Susceptibility

The AC susceptibility of $Cu_{0.05}Zn_{0.95}Cr_2Se_4$ was measured using the MagLab^{2000} instrument. Experiments were performed in AC fields ranging between 10 Gauss and 1 Tesla; AC susceptibility was measured in the temperature range 2 to 150 K using a sweep rate of 2 Kmin^{-1}. A driving field of 1 Oe was used and range of frequencies between 500 and 10,000 kHz.; the sample was loaded as for the DC magnetisation measurements.

4.3 Results

4.3.1 Magnetisation of the $Cu_{1-x}Zn_xCr_2Se_4$ series

4.3.1.1 Magnetisation versus temperature

The AC susceptibility versus temperature of $CuCr_2Se_4$ is shown in figure 4.1. As this compound was known to have a Curie temperature of more than 400 K (which is above the temperature range of the SQUID magnetometer) it was studied using a high sensitivity (KLY-2) susceptibility bridge with a high temperature attachment, capable of measuring a temperature range of room temperature to 500 K.* It is not possible to compare quantitively any of this data with data from other compounds in the series which were taken using the SQUID magnetometer. The Curie temperature (taken as the point of maximum gradient in the AC susceptibility versus temperature curve) is approximately 436 K; values of T_C reported in the literature vary from 414 K to 465 K [5, 9, 13-17].

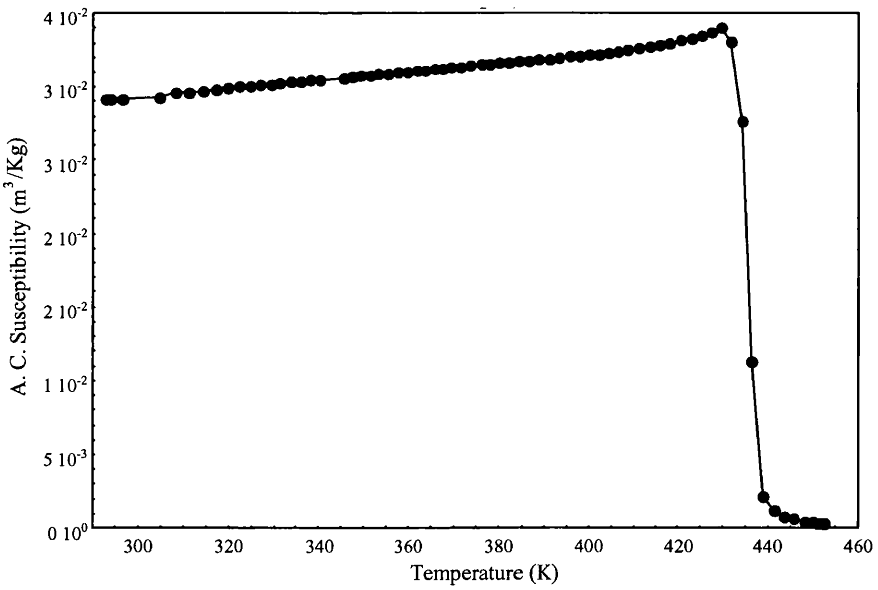

Figure 4.1 *AC susceptibility vs. temperature of* $CuCr_2Se_4$

As the temperature range of the SQUID magnetometer is limited to 1.8-400 K, it was decided to concentrate on studying compounds in the series with T_C less than 400 K. These compounds, with high zinc content, were also found from X-ray diffraction studies (see chapter 3) to have a higher degree of phase purity than those in the high copper concentration region of the series.

---

* This equipment was kindly loaned by Dr Ellen Platzman of the Rock/Paleo Magnetics laboratory in the Department of Geology, University College London.

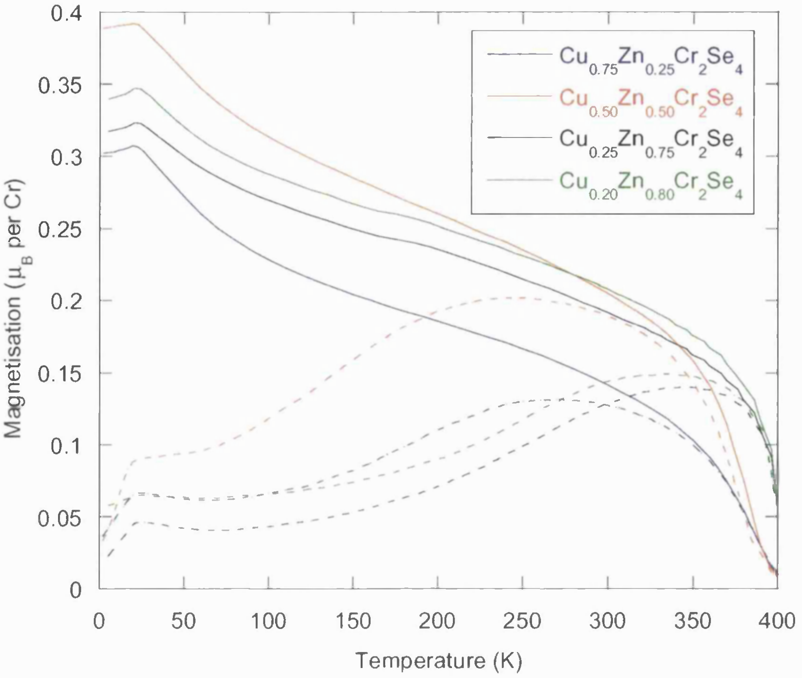

Figure 4.2 *Magnetisation vs. Temperature plot of compounds in the* $Cu_{1-x}Zn_xCr_2Se_4$ *series where* $x \leq 0.80$. *Dashed and full lines represent the zero field cooled and field cooled data respectively.*

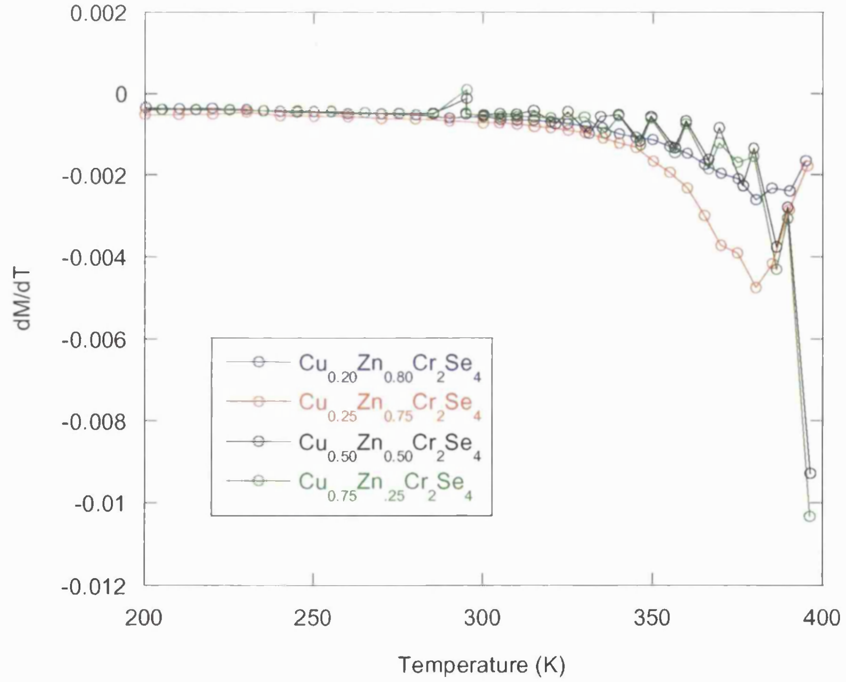

Figure 4.3 *Plot of dM/dT vs. temperature for compounds in the* $Cu_{1-x}Zn_xCr_2Se_4$ *series.(M = Magnetisation)*

Figure 4.2 shows the magnetisation versus temperature plot for compounds in the series $Cu_{1-x}Zn_xCr_2Se_4$ with $0.25 \leq x \leq 0.80$. These compounds are ferromagnetic with T_C decreasing with increasing zinc content. The Curie temperature for each compound has been obtained by taking the minimum point of dM/dT, as shown in figure 4.3; the results are summarised in table 4.1, page 126. As the transition from a ferromagnetic to a paramagnetic state in these compounds occurs over a relatively broad temperature range it is hard to determine whether this is an accurate assessment of the Curie temperature, but it was considered the to be most appropriate method available. It was not possible to determine the T_C of $Cu_{0.75}Zn_{0.25}Cr_2Se_4$ and $Cu_{0.50}Zn_{0.50}Cr_2Se_4$ as they occur above 400 K. The values of T_C reported here agree well with those given by Krok *et. al.* [7] and Juszcyzk [18], but not with those reported by Kahn *et. al.* who report a sudden drop in T_C for $x = 0.8$ to 281 K [16].

It can also be seen in figure 4.2 that there is a peak in the magnetisation curve in all compounds at around 20 K. This has been reported in the literature [19] and attributed to a gradual transition to a non-collinear spin structure at low temperature. Hidaka *et. al.* interpreted the low temperature peak as a magnetic transition from a spiral antiferromagnetic to a ferromagnetic state.[6] It is also possible that this second peak could be due to impurity phases, which were identified in these compounds in chapter 3 of this thesis. As compounds with high zinc content show a peak at around 20 K (see figure 4.4) their presence as a second phase in ferromagnetic compounds in this series could give rise to this feature. This seems unlikely however as the impurity phases detected were only present in small concentrations (a few percent) and would be unlikely to have such a pronounced effect on the magnetisation curves, especially as the magnetisation of these compounds is so low in comparison with the copper rich phases.

Figure 4.4 shows the magnetisation versus temperature plots for compounds in the series with $0.15 \leq x \leq 1.00$. For clarity, only the field cooled magnetisation curves are shown; accurate values of the low temperature transition have been obtained by taking the temperature at which $dM/dT = 0$, and are given in table 4.1, page 126.

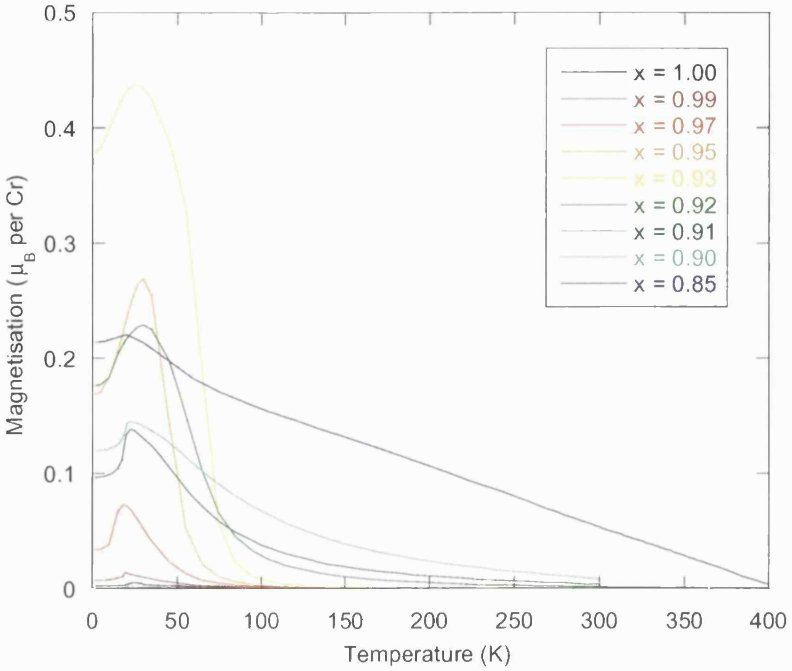

Figure 4.4 *Magnetisation vs. temperature plot in 100 Gauss of compounds in the $Cu_{1-x}Zn_xCr_2Se_4$ series where $1.00 \geq x \geq 0.15$.*

Compounds with $0.15 \leq x \leq 0.91$ show a maximum in magnetisation at approximately 20 K followed by a gradual decrease in magnetisation at higher temperatures. In this temperature range the magnetisation assumes values typical of a ferromagnet (~ 0.1 μ_B per atom) but the steep decrease with temperature is more suggestive of a blocked or glassy state than a true ferromagnetic state. Plots of $1/\chi$ versus temperature for these compounds (figure 4.5) show no linear region at high temperature which confirms that a paramagnetic state is not reached for these compounds below 400 K. The magnitude of the magnetisation decreases with increasing zinc constant.

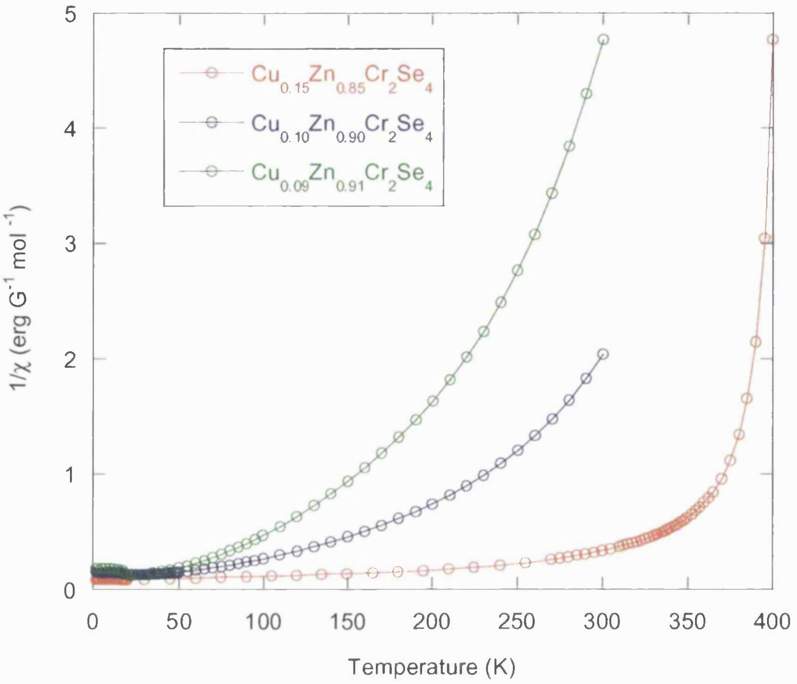

Figure 4.5 *Plot of 1/ χ vs. temperature for compounds in the* $Cu_{1-x}Zn_xCr_2Se_4$ *series where* $x = 0.85$, *0.9 and 0.91.*

$Cu_{0.08}Zn_{0.92}Cr_2Se_4$ shows a greater magnetisation than compounds with $0.15 \leq x \leq 0.91$ and the maximum occurs at approximately 28 K. A paramagnetic state appears to have been reached at high temperature in $Cu_{0.08}Zn_{0.92}Cr_2Se_4$ and a plot of 1/ χ versus T shows a linear region above 385 K (see appendix, section A.2.1, figure 9.27), however, fitting this region with the Curie Law gives a θ_{cw} value of 358.4(3) K which is anomalously high. The value of θ_{cw} obtained by the fitting of the inverse AC susceptibility versus temperature curve of $Cu_{0.08}Zn_{0.92}Cr_2Se_4$, reported in chapter 6 of this thesis, is 167.8(1) K which is in better agreement with the values of θ_{cw} for compounds with higher x reported here. Compounds with $0.93 \leq x \leq 1.00$ show a maximum at temperatures varying from 17 to 19 K and a clear transition to a paramagnetic state is seen in the 1/ χ versus T plots.

The transition temperatures reported here for $0.90 \leq x \leq 1.00$ agree well with the values given by Krok *et. al.* [7] with the exception of those for $Cu_{0.05}Zn_{0.95}Cr_2Se_4$ and $Cu_{0.07}Zn_{0.93}Cr_2Se_4$ which are approximately 10 K larger.

Values of θ_{cw} and the Curie constant, C (given in table 4.1, page 126) have been extracted for compounds with $0.92 \leq x \leq 1.00$ by fitting the linear region of 1/ χ versus T to the Curie law as shown in figure 4.6 for $Cu_{0.05}Zn_{0.95}Cr_2Se_4$ and in figures 9.27-9.32 in the appendix, section A.2.

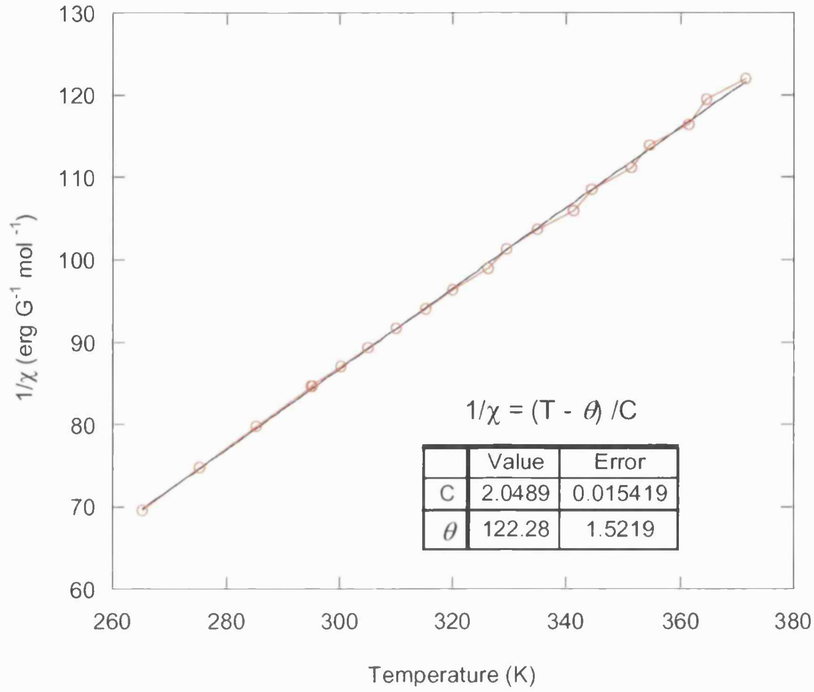

Figure 4.6 *Fit to the Curie law of data in the paramagnetic region of the 1/χ vs. temperature plot of* $Cu_{0.05}Zn_{0.95}Cr_2Se_4$

Values of θ_{cw} are positive for all compounds in this region of the series and decrease with increasing zinc concentration. The values of θ_{cw} measured here differ considerably from those given by Krok *et. al.* although the general trend is the same; they report values increasing from 118 K to 296 K for $x = 1$ to $x = 0.93$ which are much larger than those reported here [7].

This unusual feature of positive values of θ_{cw} for antiferromagnetic compounds has been reported previously for $ZnCr_2Se_4$ [20] and for compounds in the $Cu_{1-x}Zn_xCr_2Se_4$ series [7]. In $ZnCr_2Se_4$ this phenomenon has been attributed to the presence of competing antiferromagnetic and ferromagnetic interactions, which result in the spiral spin arrangement as discussed in the introduction, section 1.4. The increasing values of θ_{cw} and magnetisation with increasing amounts of copper in the series indicate that the ferromagnetic interactions are being strengthened by the addition of copper. This would be consistent with the presence of copper introducing Cr^{4+} into the system, thus enabling the double exchange mechanism and enhancing the ferromagnetism.

The number of unpaired electrons per formula unit, n, has been calculated from the Curie constant, C using the formula

$$C = \frac{S(S+1)}{2}$$ **Equation 4.1**

as derived in chapter 2, section 2.3.3, where the number of unpaired electrons, n, is equal to $2S$. The theoretical values of n were also calculated, assuming that the substitution of one Cu^{+} ion into the system produced, on average, one Cr^{4+} ion and that the number of unpaired electrons present in Cr^{3+} and Cr^{4+} are 3 and 2 respectively. Calculated and experimental values of n are given in table 4.1. page 126. Values of n_{exp} are consistently slightly larger than the values of n_{calc} and increase with decreasing x, hence deviating from n_{calc}. This could be a result of the increasing influence of the double exchange mechanism as copper is introduced into the lattice which results in delocalisation of the unpaired chromium electrons.

Figure 4.7 shows the zero field cooled and field cooled magnetisation curves of a representative selection of compounds from the $Cu_{1-x}Zn_xCr_2Se_4$ series. In $ZnCr_2Se_4$ there is no splitting of the zero field cooled and field cooled magnetisation. For compounds with $0.97 \leq x \leq 0.99$ there is a splitting of the zero field cooled and field cooled magnetisation curves below T_N which is indicative of a spin glass or weakly ferromagnetic state below this temperature; this effect increases with decreasing x. Compounds with $x \leq 0.95$ show splitting of the zero field cooled and field cooled curves to temperatures well above T_N.

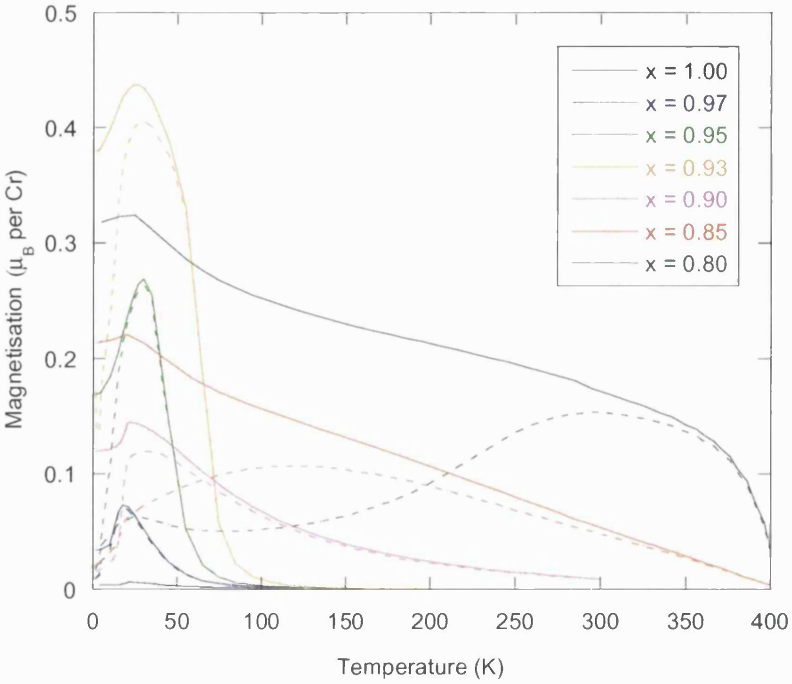

Figure 4.7 *Magnetisation vs. temperature plots in 100 Gauss for compounds in the series* $Cu_{1-x}Zn_xCr_2Se_4$ *where* $0.80 \leq x \leq 1.00$. *Dashed and full lines represent the zero field cooled and field cooled data respectively.*

Figures 4.8 and 4.9 show plots of μ_{eff} per chromium versus temperature for compounds in the $Cu_{1-x}Zn_xCr_2Se_4$ series. Values of μ_{eff} per chromium were calculated using the equation

$$\chi = \frac{N\mu_{eff}^2\mu_B^2}{3k_BT}$$ **Equation 4.2**

which is derived in chapter 2, section 2.3.3.

$$\frac{N\mu_B^2}{3k_B} \approx \frac{1}{8}$$ **Equation 4.3**

which gives

$$\mu_{eff} = \sqrt{8\chi T}$$ **Equation 4.4**

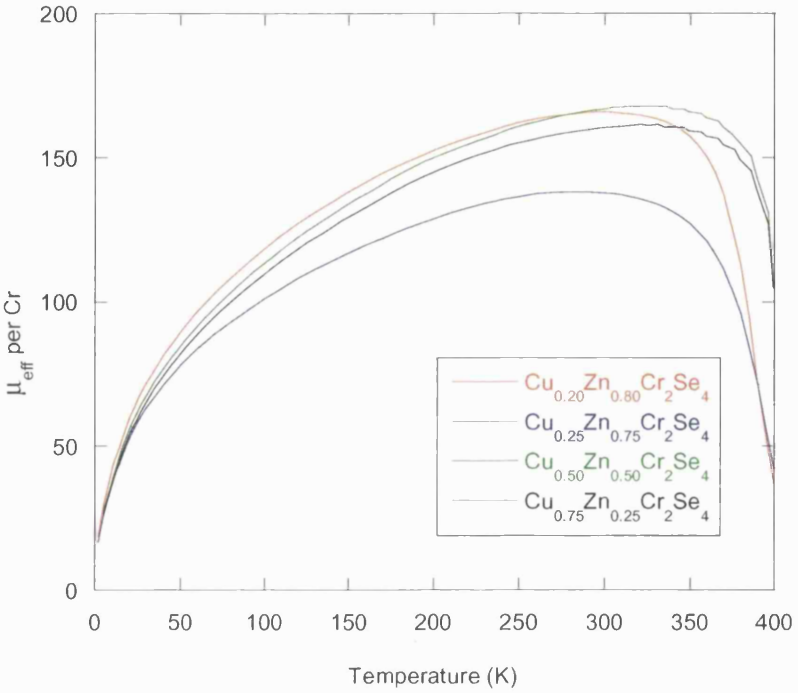

Figure 4.8 *Plot of* μ_{eff} *per chromium vs. temperature for compounds in the* $Cu_{1-x}Zn_xCr_2Se_4$ *series, where* $0.25 \leq x \leq 0.80$.

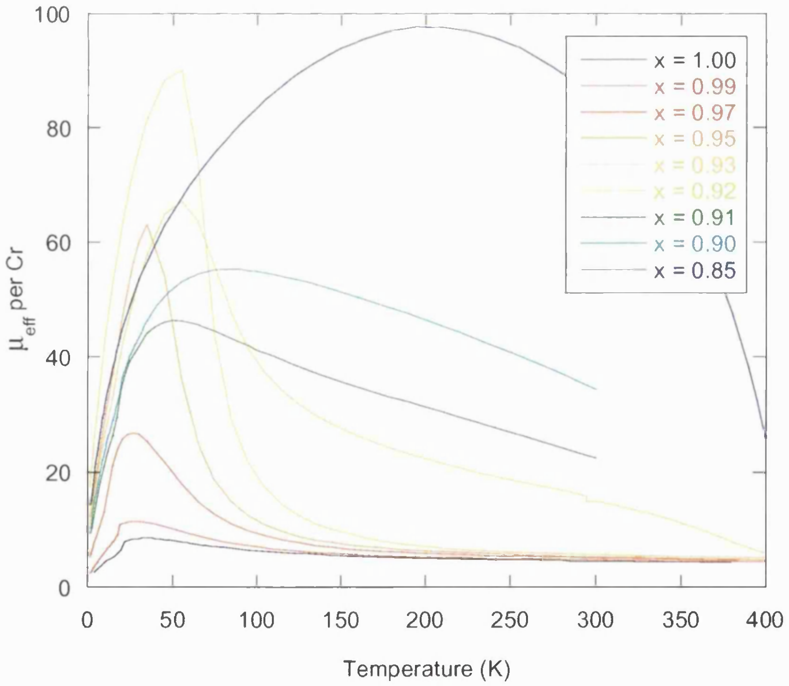

Figure 4.9 *Plot of* μ_{eff} *per chromium vs. temperature for compounds in the* $Cu_{1-x}Zn_xCr_2Se_4$ *series, where* $0.85 \leq x \leq 1.00$.

The magnitude of μ_{eff} gives an indication of the magnitude of the fluctuating magnetic domains. The results shown in figures 4.8 and 4.9 show that there is a gradual change in the behaviour of μ_{eff} across the series which corresponds to the changes seen in the magnetisation data.

Table 4.1, below, summarises the information obtained from the magnetic measurements on compounds in the $Cu_{1-x}Zn_xCr_2Se_4$ series.

Composition, x	Transition Temperature (K)	Curie Constant, C $(ergKmol^{-1}Oe^{-})$	n_{exp}	n_{calc}	Weiss Constant, θ_{cw}, (K)	Saturation Magnetisation, M_s, per Cr (μ_B)	
						$M_{s(exp)}$	$M_{s(calc)}$
0.00	436(4)	[*]	[*]	2.500	[*]	2.20(2)	2.500
0.25	[†]	[*]	[*]	2.625	[*]	2.14(2)[‡]	2.625
0.50	[†]	[*]	[*]	2.750	[*]	2.14(2)[‡]	2.750
0.75	380(10)	[*]	[*]	2.875	[*]	3.00(2)[‡]	2.875
0.80	380(10)	[*]	[*]	2.900	[*]	2.53(2)[‡§]	2.900
0.85	19.4(7)	[*]	[*]	2.925	[*]	2.47(2)[‡]	2.925
0.90	21.7(3)	[*]	[*]	2.950	[*]	2.90(2)[‡]	2.950
0.91	21.1(7)	[*]	[*]	2.955	[*]	2.91(2)[‡]	2.955
0.92	28.4(1)	0.449(3)	1.140(7)	2.960	358.4(3)	2.53(2)	2.960
0.93	24.4(3)	2.25(1)	3.36(1)	2.965	132.1(9)	2.58(2)	2.965
0.95	29.9(7)	2.04(2)	3.18(3)	2.975	122(2)	2.55(2)	2.975
0.97	17.3(3)	1.99(2)	3.12(3)	2.985	119(2)	2.47(2)	2.985
0.99	19.0(8)	1.89(1)	3.02(2)	2.995	96(1)	2.54(2)	2.995
1.00	24.5(7)	1.945(7)	3.06(1)	3.000	88.3(7)	2.52(2)	3.000

Table 4.1 *Summary of information obtained from magnetic measurements on compounds in the series* $Cu_{1-x}Zn_xCr_2Se_4$.

---

[*] Data not available in the paramagnetic region

[†] Transition temperature above 400 K

[‡] Saturation not reached at maximum field

[§] Maximum field 50,000 Gauss

4.3.1.2 Magnetic hysteresis

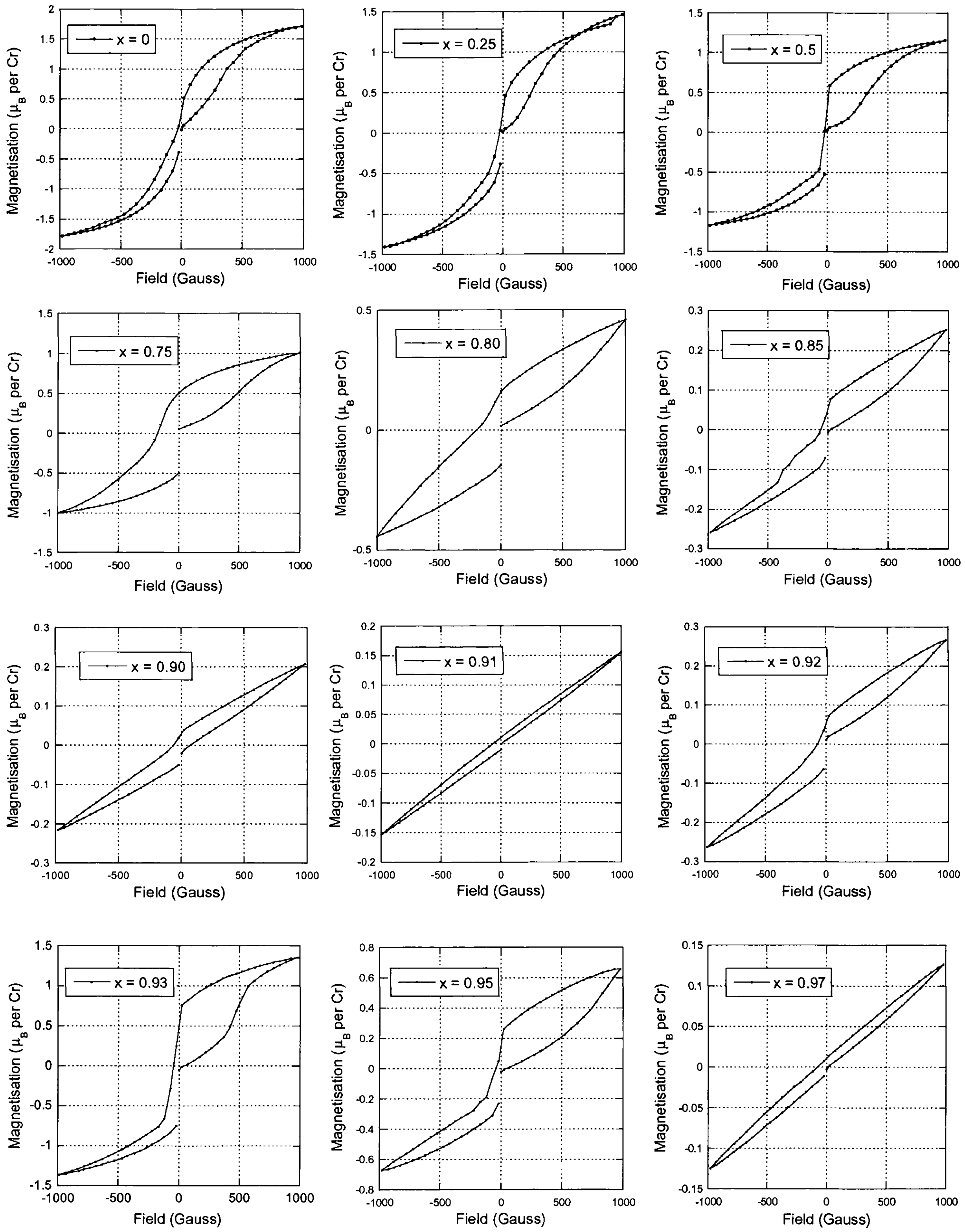

Figure 4.10 *Magnetisation vs. field plots for compounds in the series* $Cu_{1-x}Zn_xCr_2Se_4$ *for field sweeps 0 → 1000 → -1000 → 0 Gauss.*

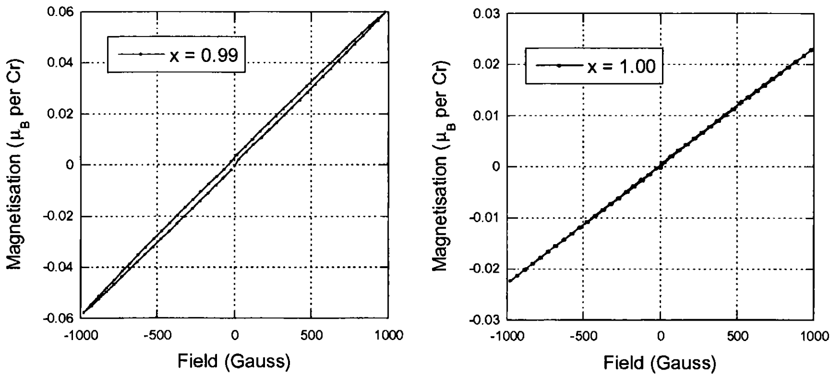

Figure 4.11 *Magnetisation vs. field plots for compounds in the series* $Cu_{1-x}Zn_xCr_2Se_4$ *for field sweeps 0 → 1000 → -1000 → 0 Gauss.*

Figures 4.10 and 4.11 show magnetisation versus field measurements for the low field hysteresis measurements on compounds in the $Cu_{1-x}Zn_xCr_2Se_4$ series. The samples were cooled to 5 K in zero field and then the magnetisation was measured every 50 Gauss as a field was applied from 0 → 1000 → -1000 → 0 Gauss. For compounds with $0.00 \leq x \leq 0.91$, the magnitude of the magnetisation at 1000 Gauss is seen to decrease with increasing x from approximately 1.75 μ_B per Cr ($x = 0$) to 0.16 μ_B per Cr ($x = 0.91$). This trend is in keeping with the variation in the magnitude of magnetisation seen in these compounds in the 100 Gauss magnetisation versus temperature curves shown in figures 4.2 and 4.4. An increase in hysteresis effect is seen from $x = 0$ to $x = 0.75$ followed by a subsequent decrease from $x = 0.75$ to $x = 0.91$. The hysteresis effect seen in these compounds is not typical of that of a simple ferromagnetic, as shown in the theory chapter, figure 2.4, page 67. The shape of the hysteresis curves shown here has a characteristic 'bulge' which is more typical of that of a metamagnetic material. This indicates a situation where spins are aligned antiferromagnetically at low field and as the field is increased a certain point is reached at which the spins are forced to align ferromagnetically, leading to a hysteresis effect in the higher field section of the magnetisation versus field curve.

Compounds $Cu_{0.08}Zn_{0.92}Cr_2Se_4$ and $Cu_{0.07}Zn_{0.93}Cr_2Se_4$ show increasing values of magnetisation at 1000 Gauss followed by steadily decreasing values for compounds with $0.95 \leq x \leq 1.00$, in line with the behaviour seen in the magnetisation versus temperature curves for these compounds. There is a varying hysteresis effect observed which is at a maximum in $Cu_{0.07}Zn_{0.93}Cr_2Se_4$ and then decreases to virtually nothing for $ZnCr_2Se_4$.

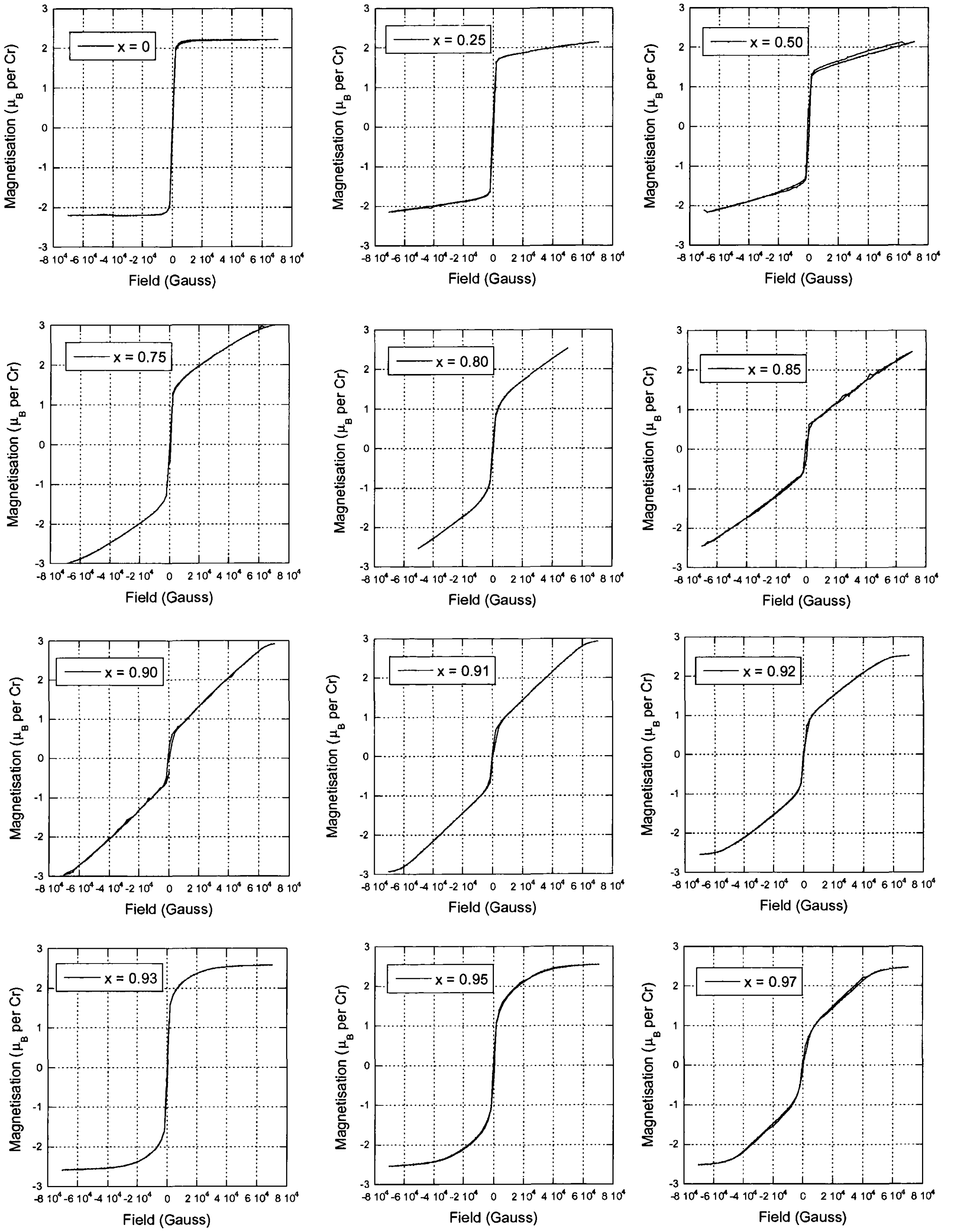

Figure 4.12 *Magnetisation vs. field plots for compounds in the series* $Cu_{1-x}Zn_xCr_2Se_4$ *for field sweeps 0 → 70,000 → -70,000 → 0 Gauss.*

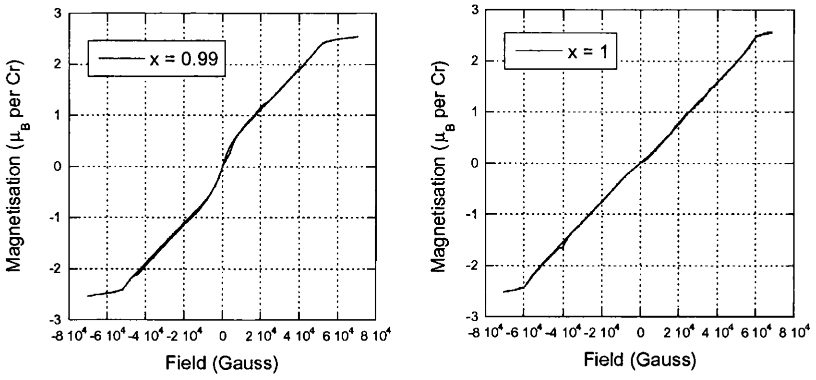

Figure 4.13 *Magnetisation vs. field plots for compounds in the series* $Cu_{1-x}Zn_xCr_2Se_4$ *for field sweeps 0 → 70,000 → -70,000 → 0 Gauss.*

Figures 4.12 and 4.13 show the magnetisation versus field curves for the high field hysteresis measurements on compounds in the $Cu_{1-x}Zn_xCr_2Se_4$ series. Compounds were cooled to 5 K in zero field and the magnetisation measured every 2000 Gauss whilst the field was applied from 0 → 70,000 → -70,000 → 0 Gauss; 70,000 Gauss (7 Tesla) is the maximum field which can be applied using the SQUID magnetometer.

Values of the saturation magnetisation, M_s, are given in table 4.1, page 126. In some cases (where $0.25 \leq x \leq 0.91$) the magnetisation does not seem to fully saturate in 7 Tesla and therefore these values may not represent full saturation. None of the compounds show a hysteresis effect in these high fields.

$CuCr_2Se_4$ shows saturation at about 2 Tesla, at a value of 2.20 μ_B per chromium. This is slightly less than the calculated value of 2.50 μ_B per chromium, which assumes an electronic configuration of $Cu^{1+}Cr^{3+}Cr^{4+}[Se^{2-}]_4$. This configuration is generally accepted to be correct at high temperatures; evidence to support this claim is discussed in the introduction, section 1.3.2. Values reported in the literature of approximately 2.4 μ_B per chromium at 14 Tesla [7] and 2.47 μ_B per chromium at 9 Tesla [21] are also slightly lower than the theoretical value.

Compounds with x = 0.25, 0.50 and 0.75 have a magnetisation of 2.14, 2.14 and 3.00 μ_B per chromium at 7 Tesla respectively. In all cases saturation does not appear to have been reached at maximum field which would suggest that these values are smaller than the true value of M_s. The value of 3.00 μ_B per chromium for x = 0.25 does seem unusually high however and exceeds the calculated value. It is possible that values of M_s for all compounds in region $0.10 \leq x \leq 0.80$ could be affected by a lack of phase purity as identified in chapter 3, section 3.2.2. The presence of small amounts of other phases from the $Cu_{1-x}Zn_xCr_2Se_4$ series could have a significant effect on the values of M_s, either increasing or decreasing the value depending on which impurity phases are present.

$Cu_{0.10}Zn_{0.90}Cr_2Se_4$ and $Cu_{0.09}Zn_{0.91}Cr_2Se_4$ have significantly higher magnetisation values at 7 Tesla than other compounds in the series, although the theoretical values of M_s are not exceeded. These compounds appear to be single phase from the structural investigation so it is unlikely that feature is due to impurities. For compounds with $x \leq 0.92$ the magnetisation appears saturated at 7 Tesla and the values are all close to 2.50 μ_B per chromium, lower than the calculated values. Studies of the series by Krok *et. al.* found similar results for this region of the series; the measurements were taken at 4.2 K and slightly higher values of M_s than reported here were given consistently across the series [7].

4.3.2 Magnetisation of the $Cu_{1-x}Zn_xCr_2Se_{4-y}S_y$ series

4.3.2.1 Magnetisation versus temperature of the $CuCr_2Se_{4-y}S_y$ series

Figure 4.14 shows the magnetisation versus temperature curves for compounds in the series $CuCr_2Se_{4-y}S_y$. It can be seen that the Curie temperature decreases with increasing sulphur content; T_C values have been extracted by taking the minimum in plots of dM/dT, as shown in figure 4.15. The transition from a ferromagnetic to a paramagnetic state is much sharper than in compounds in the $Cu_{1-x}Zn_xCr_2Se_4$ series, (discussed in section 4.3.1.1), which enables a more accurate determination of T_C in these compounds. Values of T_C are summarised in table 4.2, page 142; it was not possible to obtain a value for $CuCr_2Se_{3.5}S_{0.5}$ as the transition occurs above 400 K.

The reduction of Curie temperature with increasing sulphur content from $0 \leq x \leq 2$ is consistent with previous literature reports on this series [11], and the values of T_C are in fairly good agreement. The magnitude of the magnetisation at 100 Gauss does not seem to relate in any way to the sulphur content.

Figure 4.16 shows a plot of μ_{eff} per chromium versus temperature from compounds in the $CuCr_2Se_{4-y}S_y$ series.

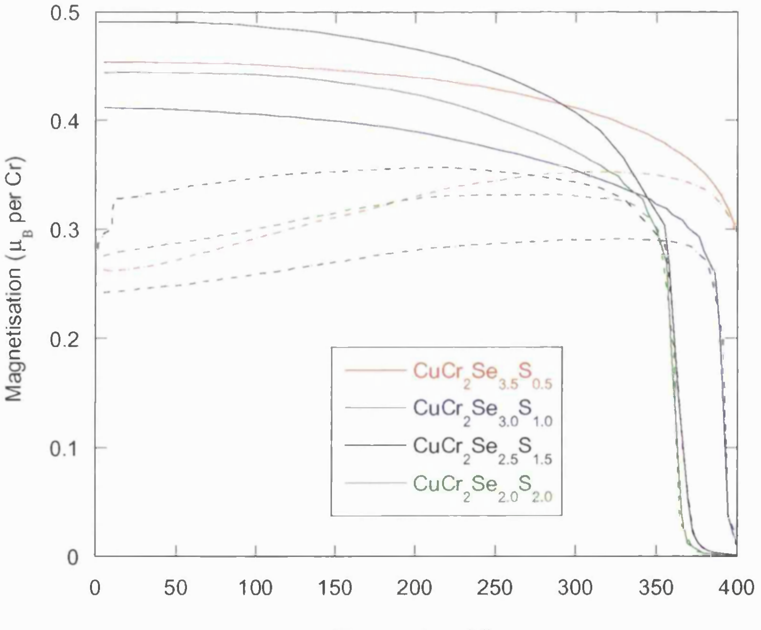

Figure 4.14 *Magnetisation vs. temperature plots in 100 Gauss for compounds in the series* $CuCr_2Se_{4-y}S_y$. *Dashed and full lines represent the zero field cooled and field cooled data respectively.*

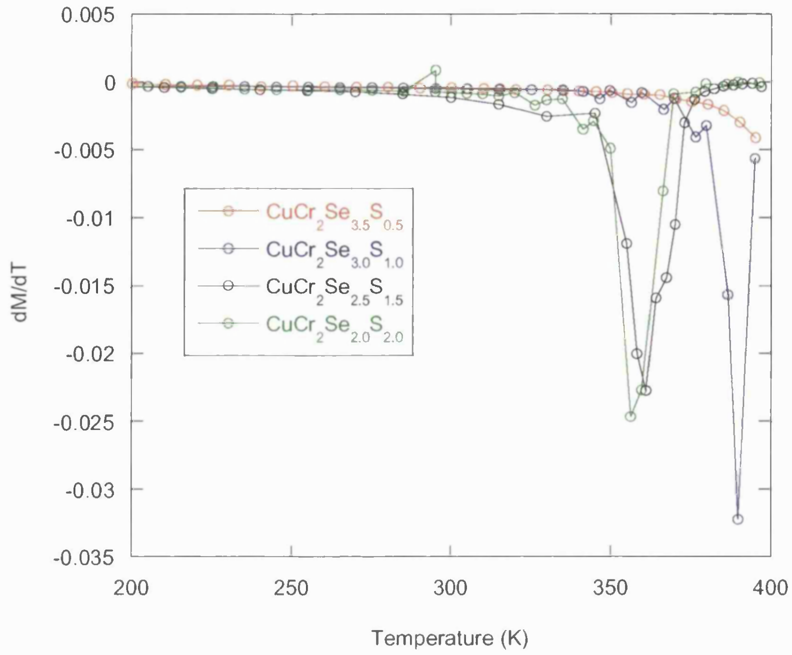

Figure 4.15 *Plot of dM/dT vs. temperature in 100 Gauss for compounds in the $CuCr_2Se_{4-y}S_y$ series. (M = Magnetisation)*

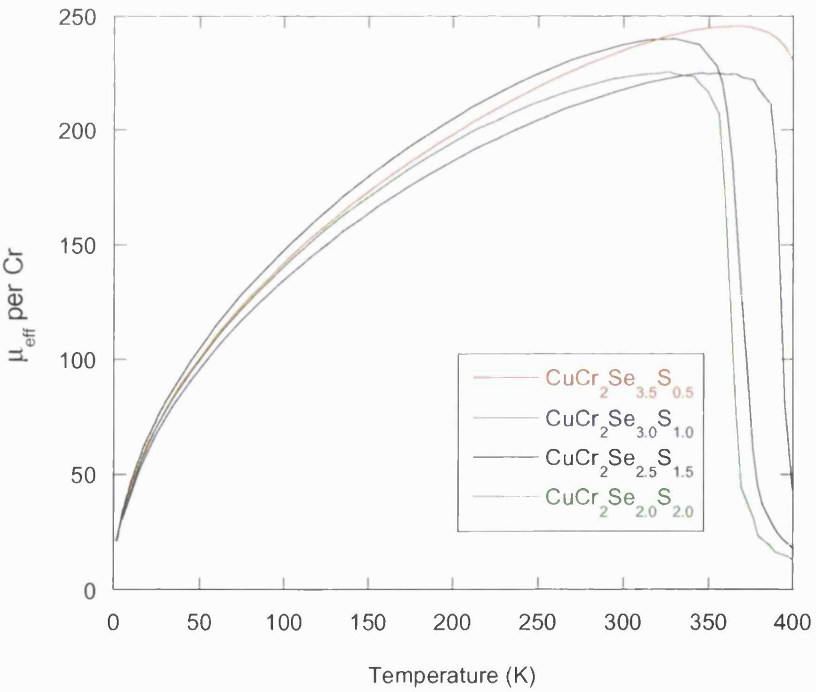

Figure 4.16 *Plot of μ_{eff} per chromium vs. temperature for compounds in the $CuCr_2Se_{4-y}S_y$ series.*

4.3.2.2 Magnetisation versus temperature of the $Cu_{0.3}Zn_{0.7}Cr_2Se_{4-y}S_y$ series.

Figure 4.17 shows the magnetisation versus temperature curves for $Cu_{0.3}Zn_{0.7}Cr_2Se_3S$ and $Cu_{0.3}Zn_{0.7}Cr_2Se_2S_2$; both compounds are ferromagnetic. The transition from a ferromagnetic to a paramagnetic state is much broader than that for compounds in the $CuCr_2Se_{4-y}S_y$ series and resembles more closely the ferromagnetic transitions seen in the $Cu_{1-x}Zn_xCr_2Se_4$ series. It should be noted that there is no low temperature peak in the magnetisation curve for $Cu_{0.3}Zn_{0.7}Cr_2Se_3S$ and $Cu_{0.3}Zn_{0.7}Cr_2Se_2S_2$ as seen in the $Cu_{1-x}Zn_xCr_2Se_4$ series.

The Curie temperature decreases with increasing sulphur content as seen in the $CuCr_2Se_{4-y}S_y$ series; values of the T_C were obtained by taking the minimum in dM/dT as shown in figure 4.18 and are given in table 4.2, page 142. There is also a decrease in the magnitude of the magnetisation with increasing sulphur content.

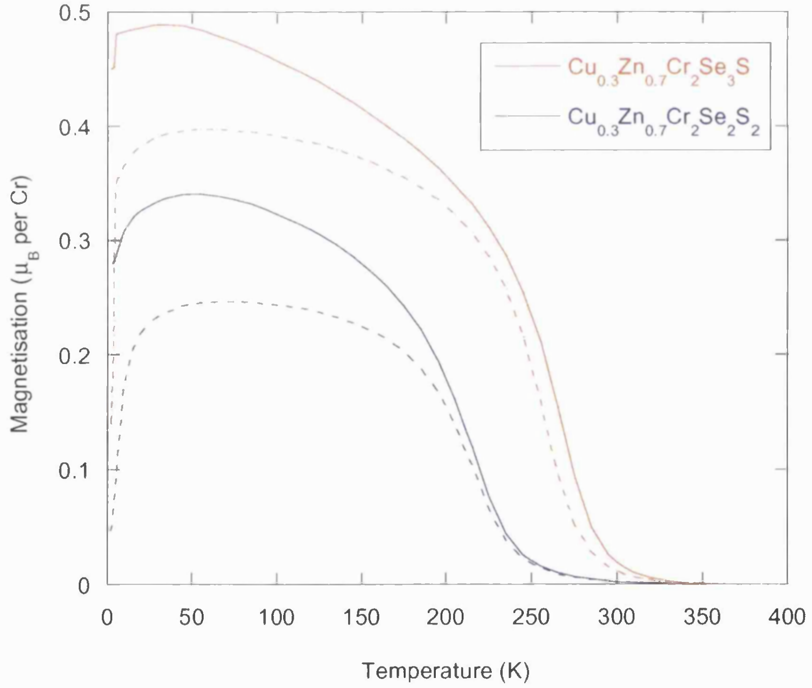

Figure 4.17 *Magnetisation vs. temperature plot in 100 Gauss of $Cu_{0.3}Zn_{0.7}Cr_2Se_3S$ and $Cu_{0.3}Zn_{0.7}Cr_2Se_2S_2$; dashed and full lines represent the zero field cooled and field cooled data respectively.*

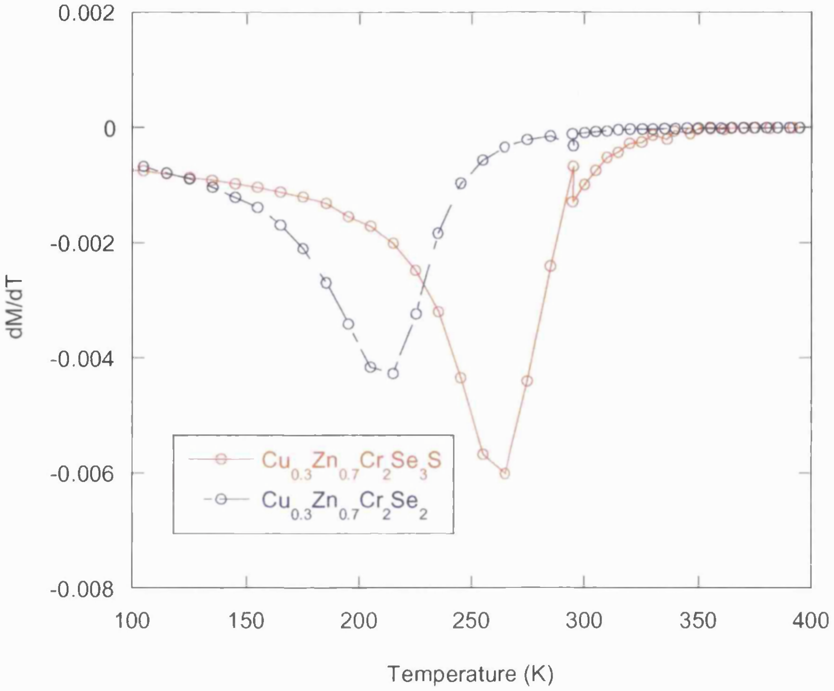

Figure 4.18 *Plot of dM/dT vs. temperature in 100 Gauss for* $Cu_{0.3}Zn_{0.7}Cr_2Se_3S$ *and* $Cu_{0.3}Zn_{0.7}Cr_2Se_2S_2$. *(M = Magnetisation)*

Figure 4.19 shows a plot of μ_{eff} per chromium versus temperature for $Cu_{0.3}Zn_{0.7}Cr_2Se_3S$ and $Cu_{0.3}Zn_{0.7}Cr_2Se_2S_2$; the magnitude of μ_{eff} decreases with increasing sulphur content, suggesting that the addition of sulphur is decreasing the strength of the ferromagnetic interactions.

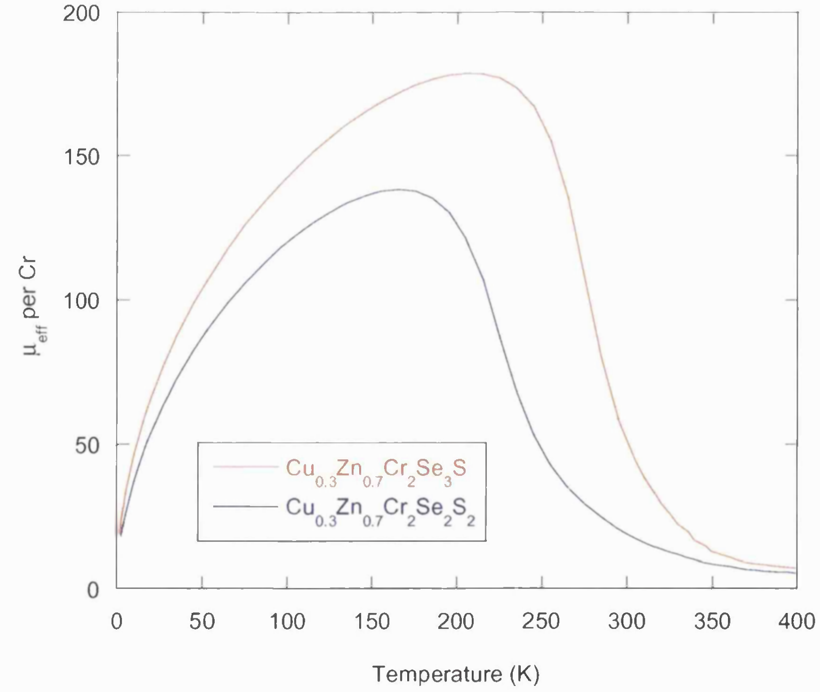

Figure 4.19 *Plot of effective moment per chromium vs. temperature for compounds in the* $Cu_{0.3}Zn_{0.7}Cr_2Se_{4-y}S_y$ *series.*

4.3.2.3 Magnetisation versus temperature of the $Cu_{0.1}Zn_{0.9}Cr_2Se_{4-y}S_y$ series

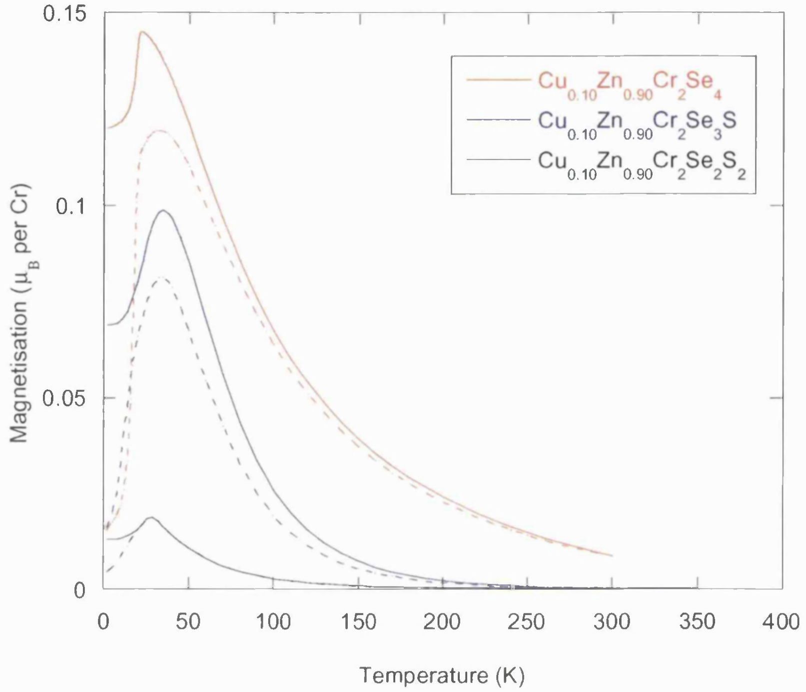

Figure 4.20 *Magnetisation vs. temperature plots in 100 Gauss for compounds in the series* $Cu_{0.1}Zn_{0.9}Cr_2Se_{4-y}S_y$. *Dashed and full lines represent the zero field cooled and field cooled data respectively.*

Figure 4.20 shows the magnetisation versus temperature curves for compounds in the $Cu_{0.1}Zn_{0.9}Cr_2Se_{4-y}S_y$ series. The transition temperature has been evaluated as the point at which $dM/dT = 0$; values are given in table 4.2, page 142. It can be seen that there is a decrease in magnetisation with increasing sulphur content. $Cu_{0.1}Zn_{0.9}Cr_2Se_4$ and $Cu_{0.1}Zn_{0.9}Cr_2Se_3S$ show a splitting between the zero field cooled and field cooled magnetisation curves up to high temperature, whereas $Cu_{0.1}Zn_{0.9}Cr_2Se_2S_2$ only shows a splitting below the transition temperature, which is indicative of spin glass or weakly ferromagnetic behaviour.

Figure 4.21 shows plots of inverse susceptibility versus temperature for compounds in the $Cu_{0.1}Zn_{0.9}Cr_2Se_{4-y}S_y$ series. $Cu_{0.1}Zn_{0.9}Cr_2Se_4$ shows no linear relationship at high temperature (as discussed in section 4.3.1.1) indicating that there is no transition to a paramagnetic state below 300 K. $Cu_{0.1}Zn_{0.9}Cr_2Se_3S$ and $Cu_{0.1}Zn_{0.9}Cr_2Se_2S_2$ do show a linear region at high temperatures and the data has been fitted using the Curie law to give values of θ_{cw} of 231.0(8) and 164(1) respectively. The fits of this data to the Curie law are shown in the appendix, section A.2, figures 9.33 and 9.34.

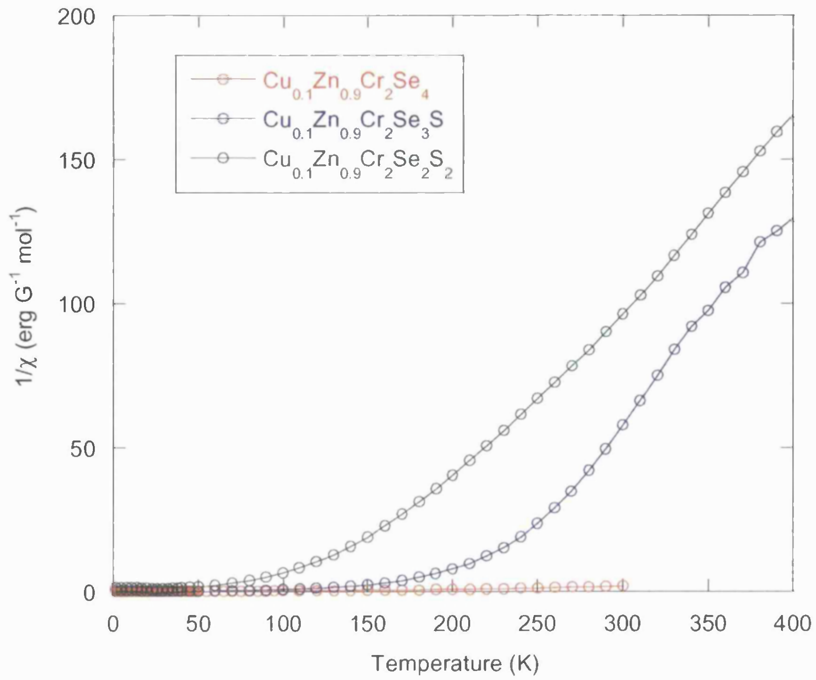

Figure 4.21 *Plots of inverse susceptibility vs. temperature for compounds in the series* $Cu_{0.1}Zn_{0.9}Cr_2Se_{4-y}S_y$.

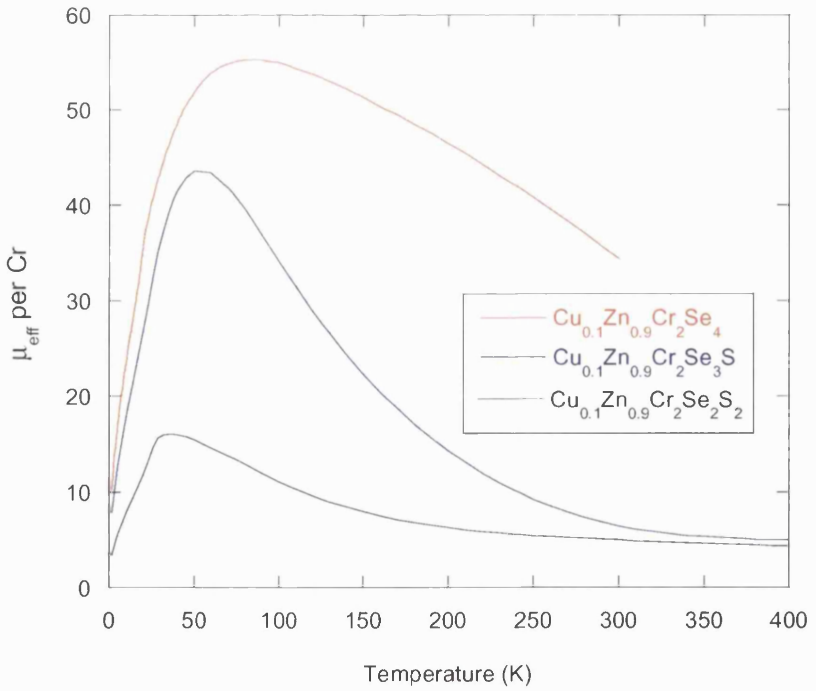

Figure 4.22 *Plot of* μ_{eff} *per chromium vs. temperature for compounds in the* $Cu_{0.1}Zn_{0.9}Cr_2Se_{4-y}S_y$ *series.*

Figure 4.22 shows a plot of μ_{eff} versus temperature for compounds in the $Cu_{0.1}Zn_{0.9}Cr_2Se_4$ series. The magnitude of μ_{eff} is decreases significantly with increasing sulphur content, suggesting a weakening of the ferromagnetic interactions with increasing sulphur content.

4.3.2.4 Magnetisation versus temperature of the $Cu_{0.05}Zn_{0.95}Cr_2Se_{4-y}S_y$ series

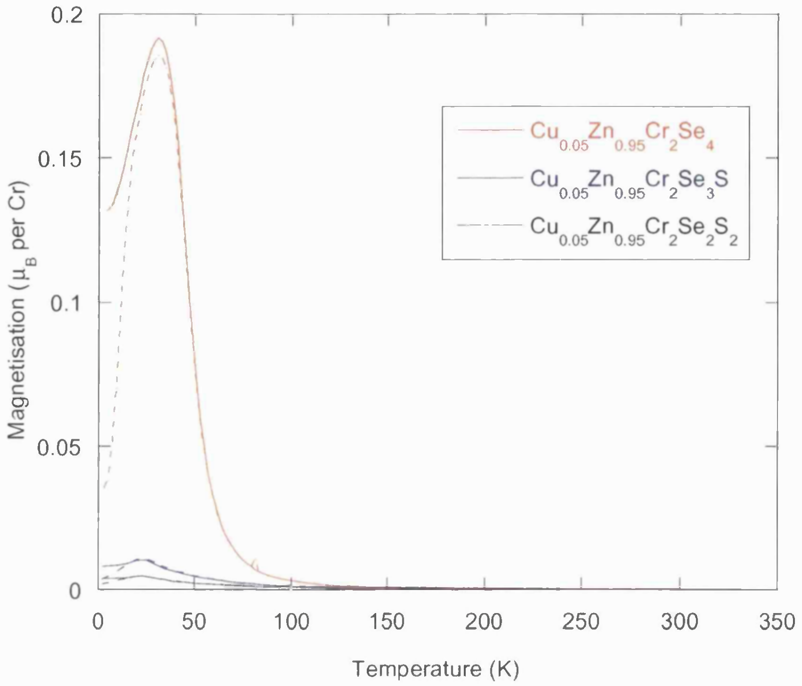

Figure 4.23 *Magnetisation vs. temperature plots in 100 Gauss for compounds in the series* $Cu_{0.05}Zn_{0.95}Cr_2Se_{4-y}S_y$*; dashed and full lines represent the zero field cooled and field cooled data respectively.*

Figure 4.23 shows the magnetisation versus temperature plot for compounds in the series $Cu_{0.05}Zn_{0.95}Cr_2Se_{4-y}S_y$; all compounds appear to be antiferromagnetic. The transition temperature has been evaluated as the point at which $dM/dT = 0$; values are given in table 4.2, page 142. The magnetisation decreases with increasing sulphur content as seen for all other compounds in the $Cu_{1-x}Zn_xCr_2Se_{4-y}S_y$ series. $Cu_{0.05}Zn_{0.95}Cr_2Se_4$ shows splitting between the zero field cooled and field cooled magnetisation curves at temperatures above T_N whereas $Cu_{0.05}Zn_{0.95}Cr_2Se_3S$ and $Cu_{0.05}Zn_{0.95}Cr_2Se_2S_2$ show splitting below the T_N only.

All compounds show a linear relationship between $1/\chi$ and temperature at high temperatures, indicating that there has been a transition to a paramagnetic state. Values of θ_{cw} have been extracted using the Curie law; there is a decrease in θ_{cw} with increasing sulphur content. Fits of the Curie law to the data are shown in plots 9.29, 9.35 and 9.36 in section A.2 of the appendix.

Figure 4.24 shows a plot of μ_{eff} versus temperature for compounds in the $Cu_{0.05}Zn_{0.95}Cr_2Se_4$ series; a significant decrease in the magnitude of μ_{eff} is seen with the addition of sulphur to the system.

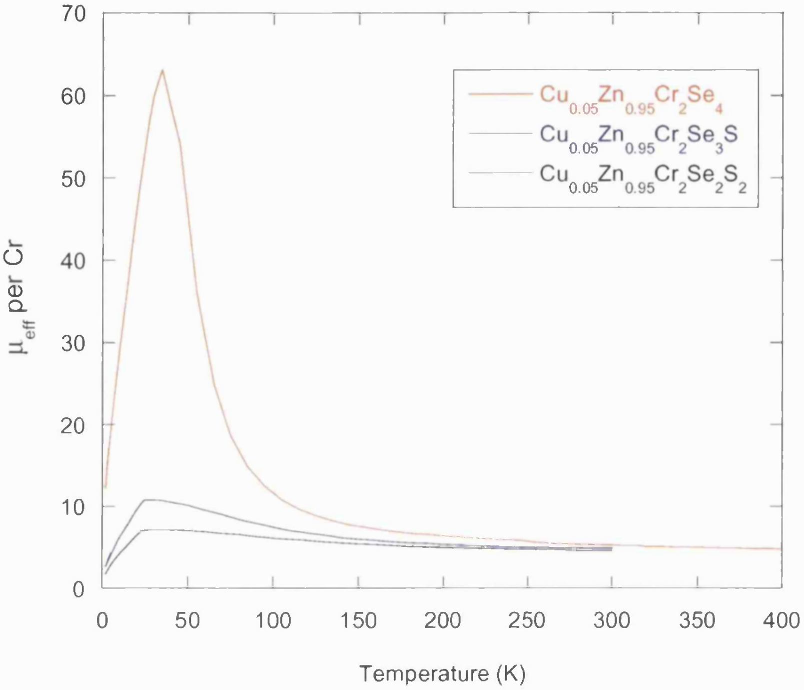

Figure 4.24 *Plot of* μ_{eff} *per chromium vs. temperature for compounds in the* $Cu_{0.05}Zn_{0.95}Cr_2Se_{4-y}S_y$ *series.*

4.3.2.5 Magnetisation versus temperature of the $ZnCr_2Se_{4-y}S_y$ series

Figure 4.25 shows the magnetisation versus temperature curves for compounds in the series $ZnCr_2Se_{4-y}S_y$; all compounds are antiferromagnetic. $ZnCr_2Se_4$ shows no splitting between the zero field cooled and field cooled magnetisation curves in the temperature range studied, whereas there is splitting below T_N for all sulphur doped samples. There is also a significant decrease in T_N when sulphur is introduced, from 24 K to 12 K accompanied by a decrease in magnetisation.

All compounds show a transition to a paramagnetic state above T_N; values of θ_{cw} and the Curie constant, C, were calculated from fitting plots of $1/\chi$ to the Curie law. The fits are shown in plots 9.32 and 9.37-9.40 in the appendix, section A.2 Values of θ_{cw} decrease with increasing sulphur content and are given in table 4.2, page 142.

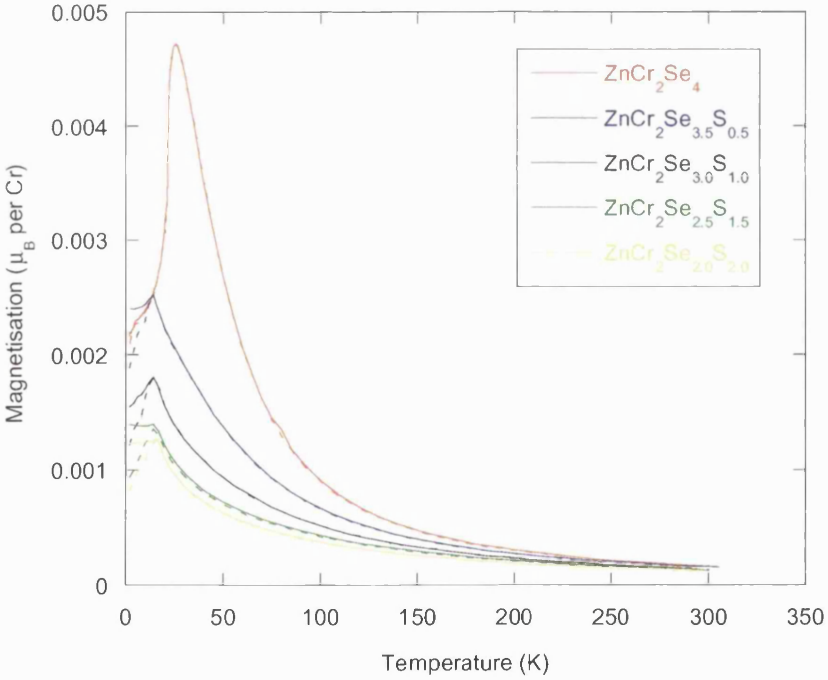

Figure 4.25 *Magnetisation vs. temperature curves for compounds in the series $ZnCr_2Se_{4-y}S_y$; dashed and full lines represent the zero field cooled and field cooled data respectively.*

Figure 4.26 shows a plot of μ_{eff} versus temperature for compounds in the $ZnCr_2Se_{4-y}S_y$ series. There is a consistent decrease in magnitude of μ_{eff} with increasing sulphur content. In $ZnCr_2Se_4$ a clear peak can be seen at low temperature, with a maximum at around 45 K. This peak becomes smaller with increasing sulphur content and the maximum shifts to higher temperature. This suggests that the addition of sulphur is significantly decreasing the strength of the ferromagnetic interactions and the magnitude of the fluctuating ferromagnetic domains within the compound.

Table 4.2 contains a summary of the information obtained from the magnetic measurements of the $Cu_{1-x}Zn_xCr_2Se_4$ series.

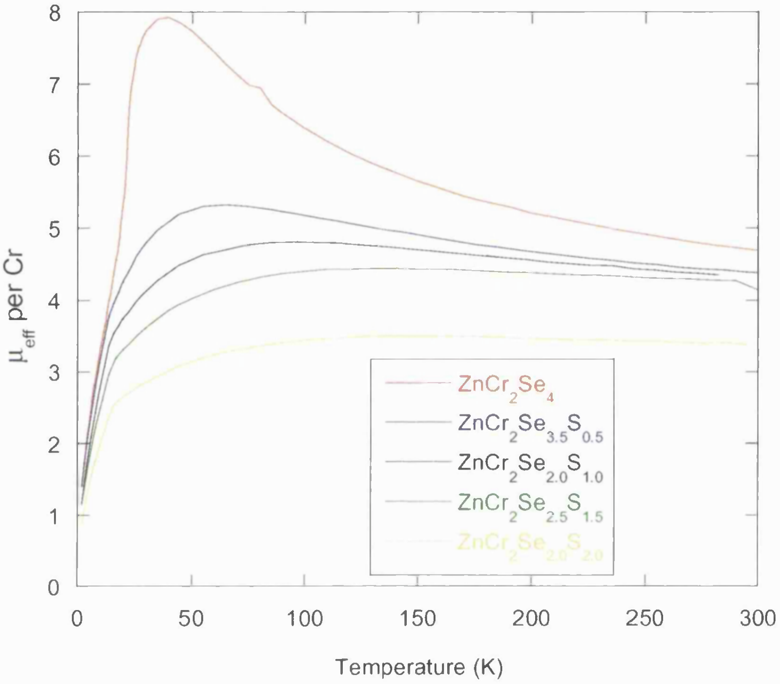

Figure 4.26 *Plot of μ_{eff} per chromium vs. temperature for compounds in the $ZnCr_2Se_{4-y}S_y$ series.*

Composition,		**Transition Temperature (K)**	**Curie Constant, *C*** (*ergKmol*$^{-1}$*Oe*$^{-}$)	n_{exp}	n_{calc}	**Weiss Constant,** θ_{cw}, **(K)**	**Saturation Magnetisation,** M_s, **per Cr** (μ_B)	
y	*x*						$M_{s(exp)}$	$M_{s(calc)}$
0.0	0.00	*	†	†	2.500	†	2.21(2)	2.500
0.5	0.00	*	†	†	2.500	†	2.31(2)	2.500
1.0	0.00	389.5(5)	†	†	2.500	†	2.20(2)‡	2.500
1.5	0.00	361(5)	†	†	2.500	†	1.91(2)‡	2.500
2.0	0.00	356.2(5)	†	†	2.500	†	1.94(2)‡	2.500
1.0	0.70	215(5)	†	†	2.850	†	1.05(2)‡	2.850
2.0	0.70	265(5)	†	†	2.850	†	1.30(2)‡	2.850
0.0	0.90	21.7(2)	†	†	2.950	†	2.92(2)	2.950
1.0	0.90	33.3(2)	1.18(1)	2.24(2)	2.950	231.0(8)	1.27(2)‡	2.950
2.0	0.90	27.3(2)	1.415(9)	2.51(2)	2.950	164(1)	0.97(2)‡	2.950
0.0	0.95	29.9(2)	2.04(2)	3.17(3)	2.975	122(1)	2.55(2)	2.975
1.0	0.95	21.0(2)	2.135(4)	3.250(6)	2.975	81.1(3)	1.17(2)‡	2.975
2.0	0.95	21.4(2)	2.069(6)	3.191(9)	2.975	66.9(5)	0.76(2)‡	2.975
0.0	1.00	24.5(2)	1.945(8)	3.07(1)	3.000	88.3(7)	2.52(2)	3.000
0.5	1.00	12.9(2)	1.926(7)	3.05(1)	3.000	59.4(8)	1.19(2)‡	3.000
1.0	1.00	12.9(2)	1.75(1)	2.88(2)	3.000	49(1)	0.85(2)‡	3.000
1.5	1.00	12.3(2)	2.09(1)	3.21(2)	3.000	24(1)	0.65(2)‡	3.000
2.0	1.00	14.9(2)	1.353(7)	2.44(1)	3.000	19(1)	0.54(2)‡	3.000

Table 4.2 *Summary of information obtained from magnetic measurements on compounds in the series* $Cu_{1-x}Zn_xCr_2Se_{4-y}S_y$.

---

* Transition above 400 K.

† No data available in the paramagnetic region.

‡ Saturation not reached at 7 Tesla.

4.3.2.6 Magnetic hysteresis of the $CuCr_2Se_{4-y}S_y$ series

Figures 4.27 and 4.28 show magnetisation versus field plots for the low field (up to 1000 Gauss) and high field (up to 7 Tesla) hysteresis measurements on compounds in the $CuCr_2Se_{4-y}S_y$ series. The low field measurement shows some hysteresis for all compounds, but there is no effect in the high field measurement. In both measurements there seems to be no linear relationship between the composition and the magnitude of the magnetisation, as was seen in the magnetisation versus temperature measurements.

In the high field measurements, compounds $CuCr_2Se_4$ and $CuCr_2Se_{3.5}S_{0.5}$ appear to reach saturation by about 2 Tesla, whereas the other compounds in the series do not. This effect is not as pronounced as for compounds in the $Cu_{1-x}Zn_xCr_2Se_4$ series as discussed in section 4.3.1.2. Values of the magnetisation of these compounds at 70,000 Gauss are given in table 4.2, page 142.

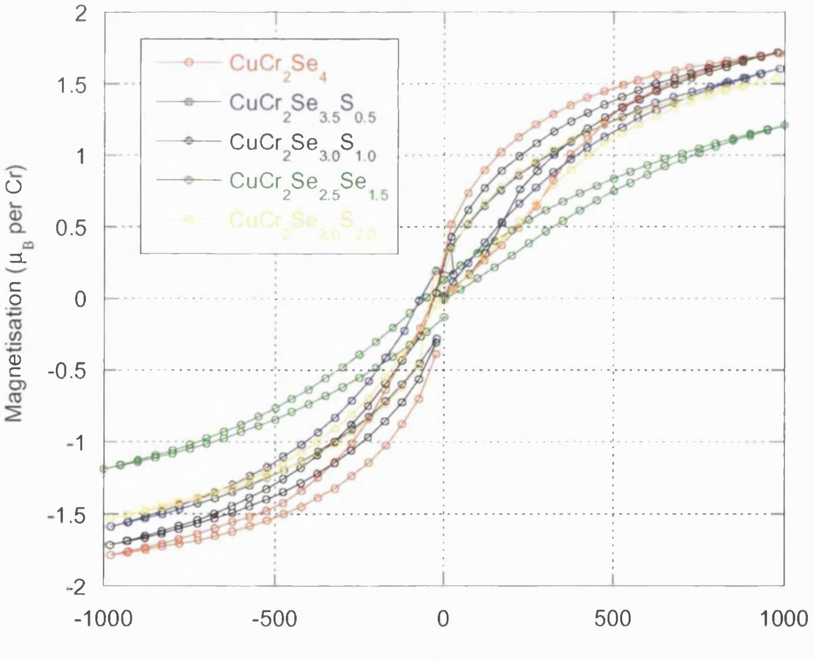

Figure 4.27 *Magnetisation vs. field plots for compounds in the series* $CuCr_2Se_{4-y}S_y$ *for field sweeps 0 → 1000 → -1000 → 0 Gauss.*

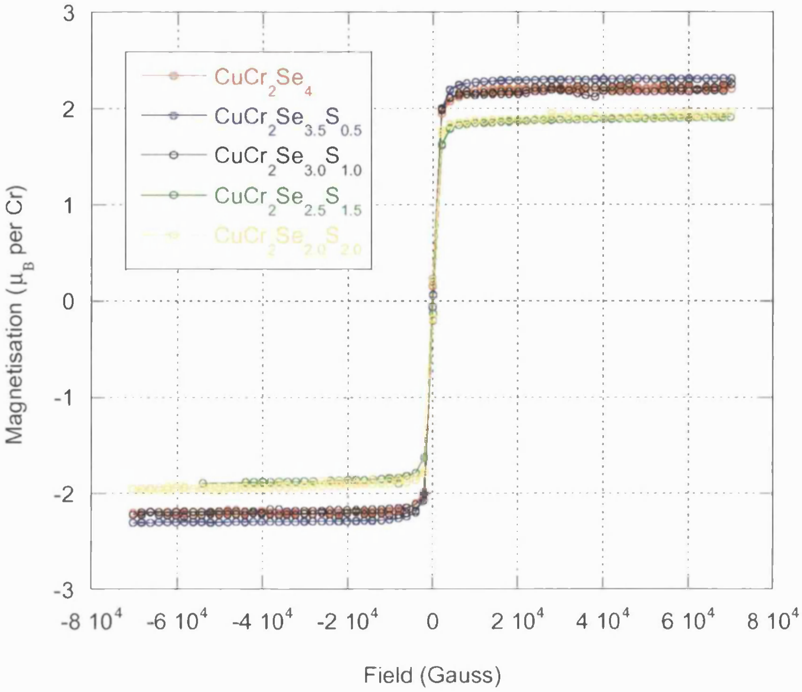

Figure 4.28 *Magnetisation vs. field plots for compounds in the series* $CuCr_2Se_{4-y}S_y$ *for field sweeps 0 → 70,000*

4.3.2.7 Magnetic hysteresis of the $Cu_{0.3}Zn_{0.7}Cr_2Se_{4-y}S_y$ series

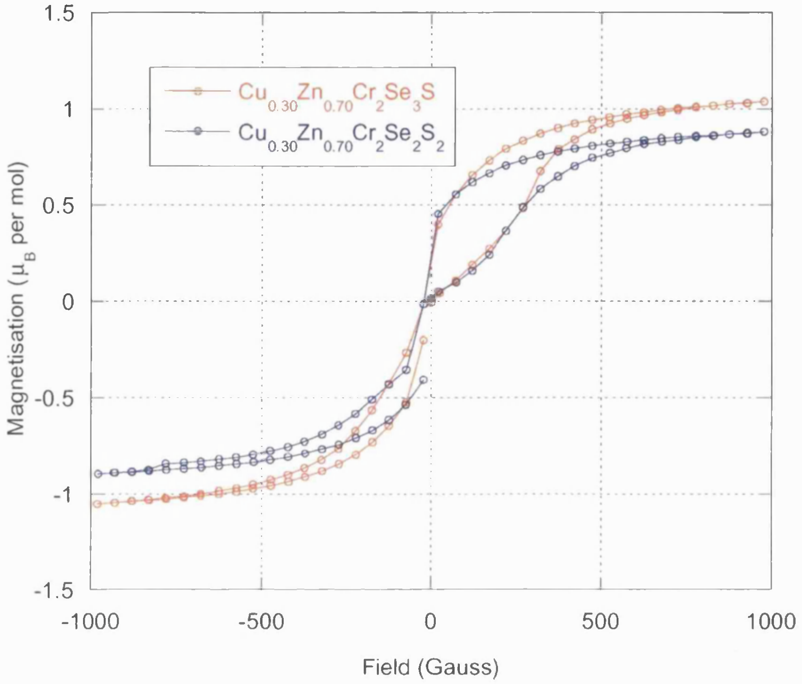

Figure 4.29 *Magnetisation vs. field plots for compounds in the series* $Cu_{0.3}Zn_{0.7}Cr_2Se_{4-y}S_y$ *for field sweeps 0 → 1000 → -1000 → 0 Gauss.*

Figures 4.29 and 4.30 show the magnetisation versus field curves of the low field and high field hysteresis measurements for $Cu_{0.3}Zn_{0.7}Cr_2Se_3S$ and $Cu_{0.3}Zn_{0.7}Cr_2Se_2S_2$. Both measurements show a decrease in magnetisation with increasing sulphur content, as is observed in the magnetisation versus temperature curves. There is a hysteresis effect observed in both low field curves, but noting the high field curves. The hysteresis seen in low field is characteristic of a that of a metamagnet, as was observed for compounds in the $Cu_{1-x}Zn_xCr_2Se_4$ series.

The high field curves show that saturation does not appear to have been reached at 7 Tesla as seen for compounds in the $Cu_{1-x}Zn_xCr_2Se_4$ series with similar zinc content. Values of the magnetisation at 1000 and 70,000 Gauss are given in table 4.2, page 142.

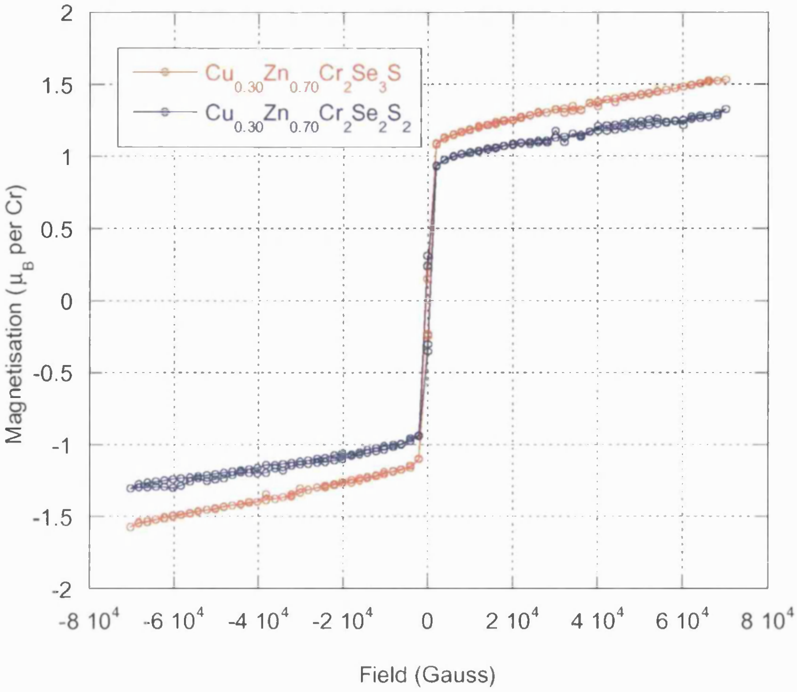

Figure 4.30 *Magnetisation vs. field plots for compounds in the series* $Cu_{0.3}Zn_{0.7}Cr_2Se_{4-y}S_y$ *for field sweeps 0 → 70,000 → 70,000 → 0 Gauss.*

4.3.2.8 Magnetic hysteresis of the $Cu_{0.1}Zn_{0.9}Cr_2Se_{4-y}S_y$ series

Figures 4.31 and 4.32 show magnetisation versus field plots for the low and high field hysteresis measurements respectively of compounds in the $Cu_{0.1}Zn_{0.9}Cr_2Se_{4-y}S_y$ series. In the low field measurement $Cu_{0.1}Zn_{0.9}Cr_2Se_3S$ has a higher magnetisation at 1000 Gauss than $Cu_{0.1}Zn_{0.9}Cr_2Se_4$ which is consistent with the zero field cooled magnetisation versus temperature data at 5 K, as shown in figure 4.16. $Cu_{0.1}Zn_{0.9}Cr_2Se_2S_2$ shows a significantly lower magnetisation which is also consistent with the magnetisation versus temperature data. There is also a decrease in hysteresis effect corresponding to the decrease in magnetisation.

The high field measurement shows a decrease in magnetisation with increasing sulphur content which is consistent with the field cooled magnetisation versus temperature curves shown in figure 4.16. None of the compounds appear to have reached saturation magnetisation at 7 Tesla. Values of the magnetisation at 70,000 gauss are given in table 4.2, page 142.

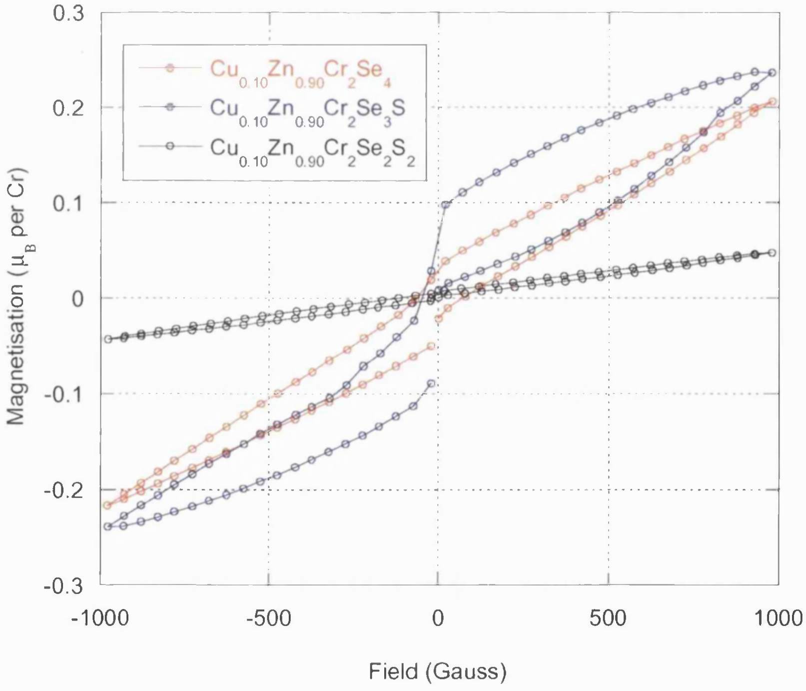

Figure 4.31 *Magnetisation vs. field plots for compounds in the series* $Cu_{0.1}Zn_{0.9}Cr_2Se_{4-y}S_y$ *for field sweeps 0 → 1000 → -1000 → 0 Gauss.*

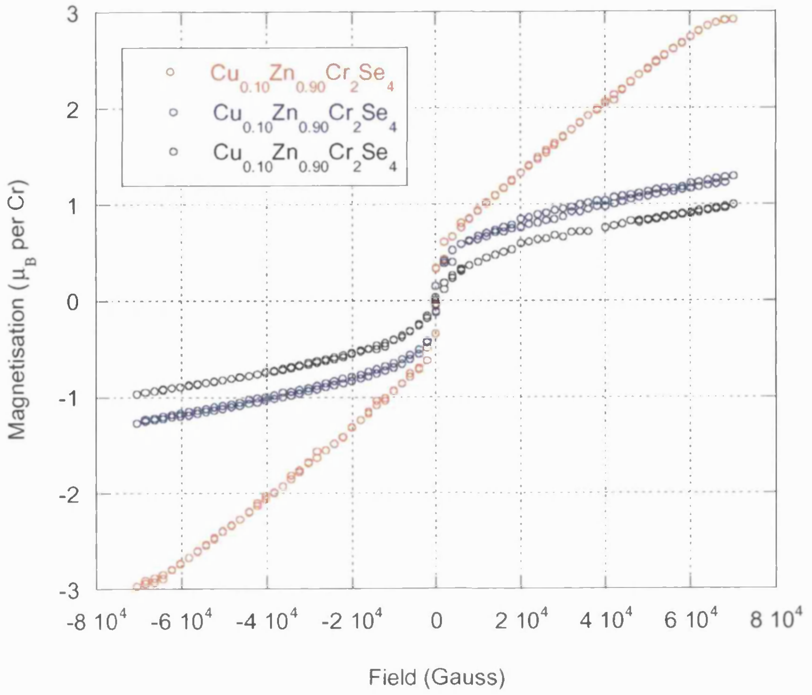

Figure 4.32 *Magnetisation vs. field plots for compounds in the series* $Cu_{0.1}Zn_{0.9}Cr_2Se_{4-y}S_y$ *for field sweeps 0 → 70,000 → 70,000 → 0 Gauss.*

4.3.2.9 Magnetic hysteresis of the $Cu_{0.05}Zn_{0.95}Cr_2Se_{4-y}S_y$ series

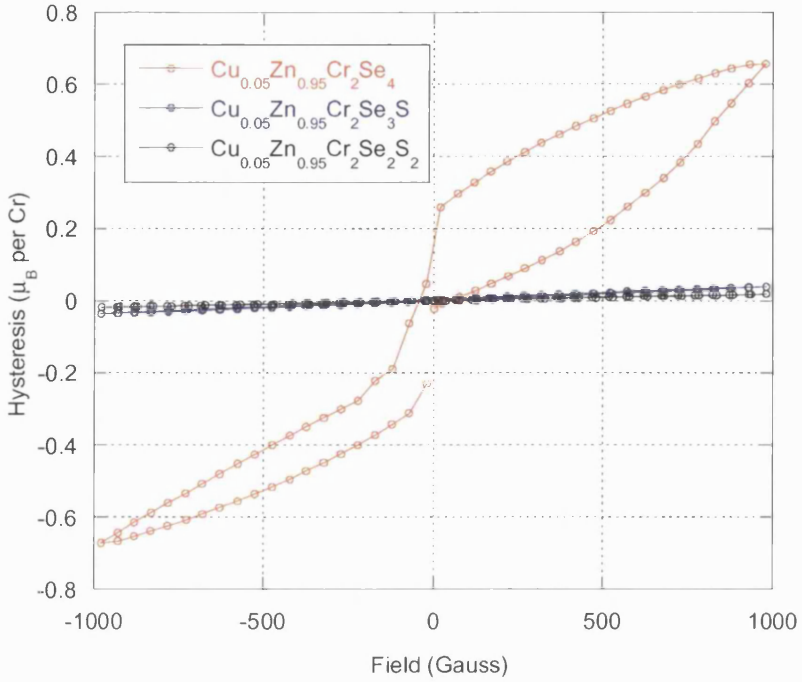

Figure 4.33 *Magnetisation vs. field plots for compounds in the series* $Cu_{0.05}Zn_{0.95}Cr_2Se_{4-y}S_y$ *for field sweeps* $0 \rightarrow 1000 \rightarrow -1000 \rightarrow 0$ *Gauss.*

Figures 4.33 and 4.34 show the magnetisation versus field curves for the low field and high field hysteresis measurements respectively for compounds in the $Cu_{0.05}Zn_{0.95}Cr_2Se_{4-y}S_y$ series. The low field curves show a decrease in magnetisation with increasing sulphur content which corresponds to the effects seen in the magnetisation versus temperature curves for compounds in this series. There is also a very significant decrease in hysteresis effect on the addition of sulphur to the system, which could be related to the change in the splitting between the zero field cooled and field cooled magnetisation versus temperature curves as discussed in section 4.3.2.1.

The high field measurement also shows a decrease in magnetisation with increasing sulphur content; $Cu_{0.05}Zn_{0.95}Cr_2Se_4$ appears to have reached saturation magnetisation at 7 Tesla whereas the sulphur substituted compounds have not. Values of the magnetisation at 70,000 Gauss are given in table 4.2, page 142.

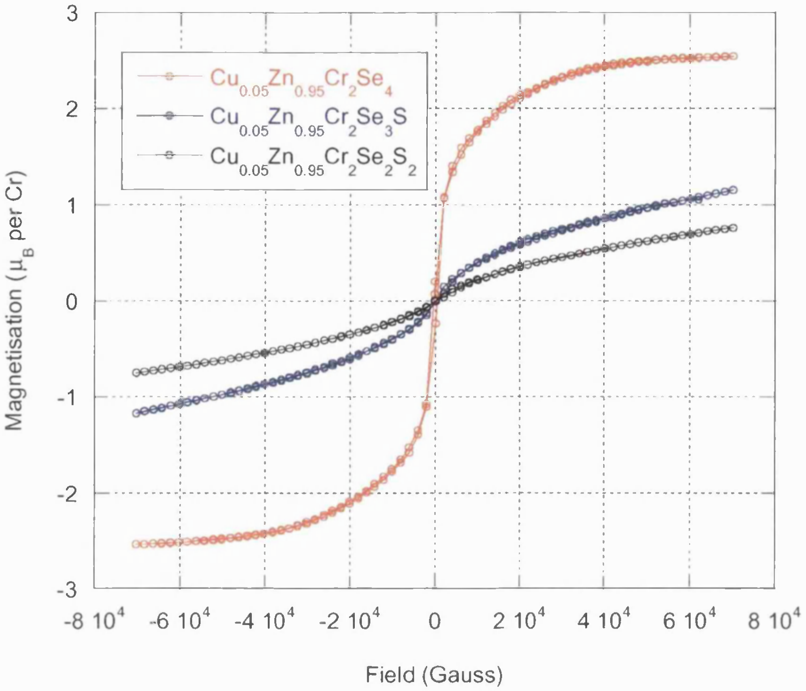

Figure 4.34 *Magnetisation vs. field plots for compounds in the series* $Cu_{0.05}Zn_{0.95}Cr_2Se_{4-y}S_y$ *for field sweeps* 0 → 70,000 → 70,000 → 0 *Gauss.*

4.3.2.10 Magnetic hysteresis of the ZnCr$_2$Se$_{4-y}$S$_y$ series

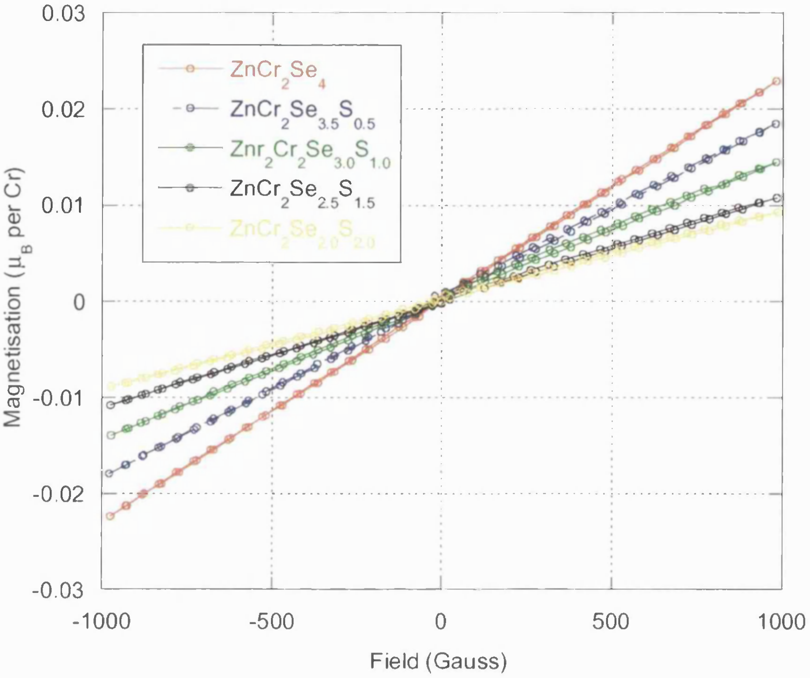

Figure 4.35 *Magnetisation vs. field plots for compounds in the series* ZnCr$_2$Se$_{4-y}$S$_y$ *for field sweeps 0 → 1000 → -1000 → 0 Gauss.*

Figures 4.35 and 4.36 show the magnetisation versus field curves for the low and high field hysteresis measurements of compounds in the series ZnCr$_2$Se$_{4-y}$S$_y$ series. There is a decrease in magnetisation with increasing sulphur content seen in both the low and high field measurements, consistent with the magnetisation versus temperature measurements. There is no hysteresis effect seen in the low or high field measurements; ZnCr$_2$Se$_4$ is the only compounds in this series to reach saturation magnetisation at 7 Tesla. Values of the magnetisation at 70,000 Gauss are given in table 4.2, page 142.

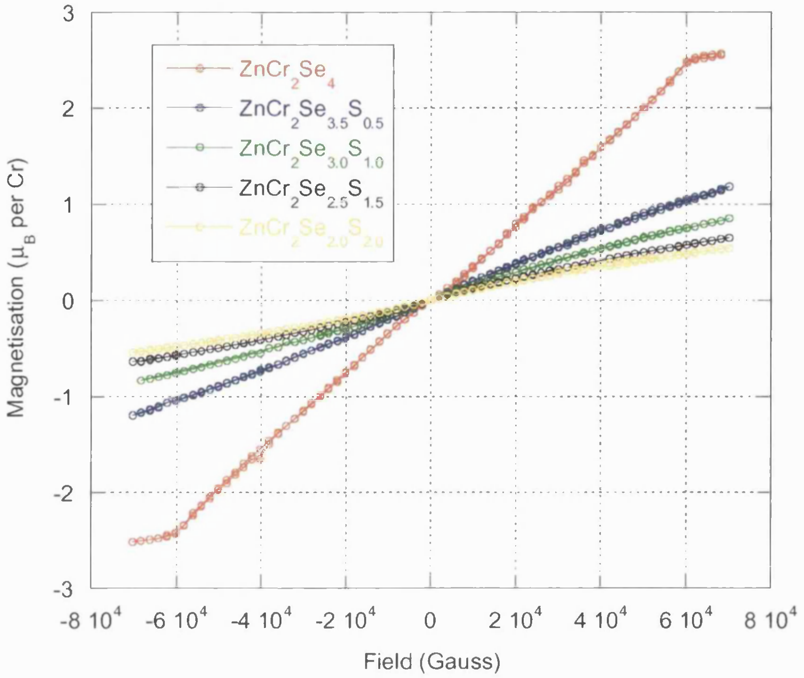

Figure 4.36 *Magnetisation vs. field plots for compounds in the series* $ZnCr_2Se_{4-y}S_y$ *for field sweeps 0 → 70,000 → -70,000 → 0 Gauss.*

4.3.3 Magnetisation of the $CuCr_2Se_{4-y}Br_y$ series

4.3.3.1 Magnetisation versus temperature

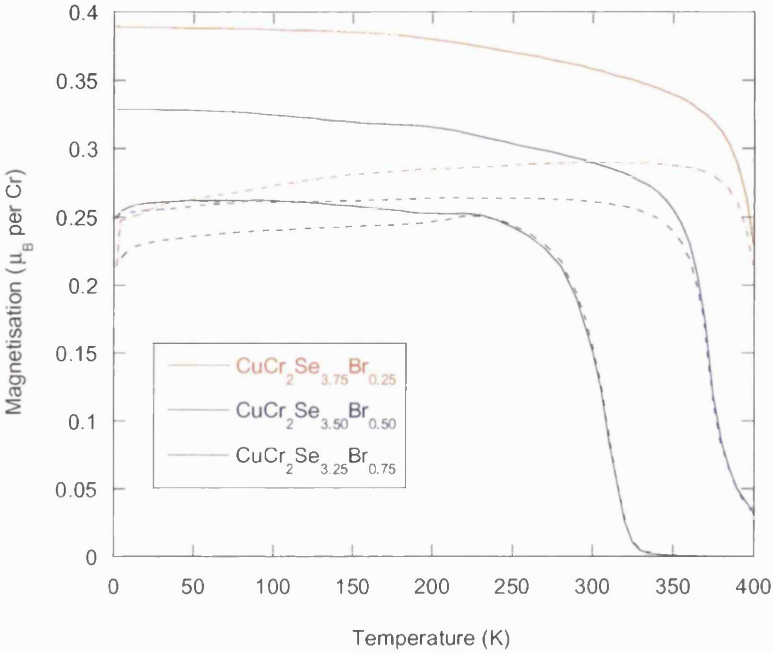

Figure 4.37 *Magnetisation vs. temperature curves in 100 Gauss for compounds in the series* $CuCr_2Se_{4-y}Br_y$*; dashed and full lines represent the zero field cooled and field cooled data respectively.*

Figure 4.37 shows the magnetisation versus temperature plots for compounds in the $CuCr_2Se_{4-y}Br_y$ series. Values of T_C have been extracted by taking the minimum point in a plot of dM/dT versus T (see figure 4.38) and are given in table 4.3, page 156. It was not possible to obtain a value of T_C for $CuCr_2Se_{3.75}Br_{0.25}$ as the transition is above 400 K. The Curie temperature decreases with increasing bromine content, accompanied by a decrease in magnetisation. This reduction in Curie temperature is in agreement with previous literature reports [22, 23] and the values of T_C agree well with the reported values.

Figure 4.39 shows a plot of μ_{eff} versus temperature for compounds in the $CuCr_2Se_{4-y}Br_y$ series. The magnitude of μ_{eff} decreases with increasing bromine content suggesting that the addition of bromine is weakening the ferromagnetic interactions.

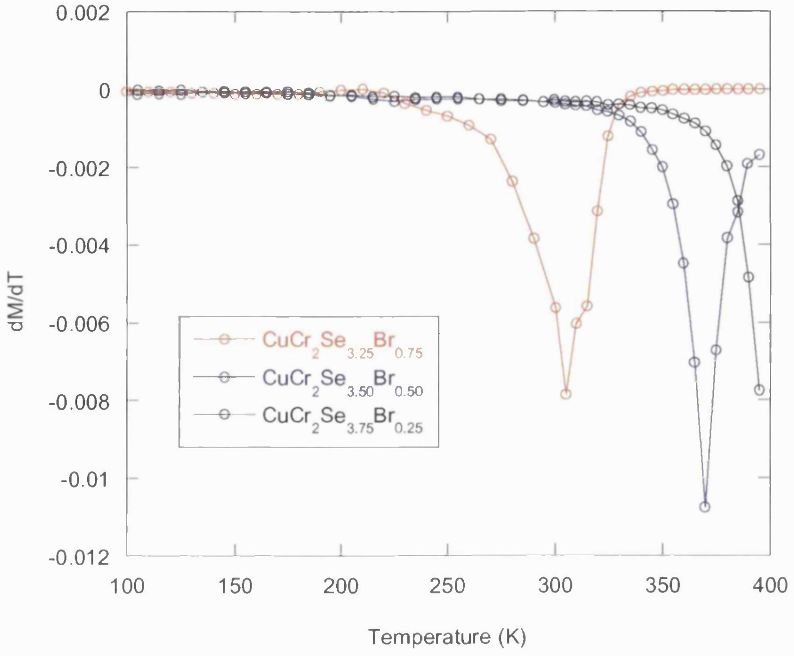

Figure 4.38 *Plot of dM/dT vs. temperature in 100 Gauss for compounds in the* $CuCr_2Se_{4-y}Br_y$ *series. (M = Magnetisation)*

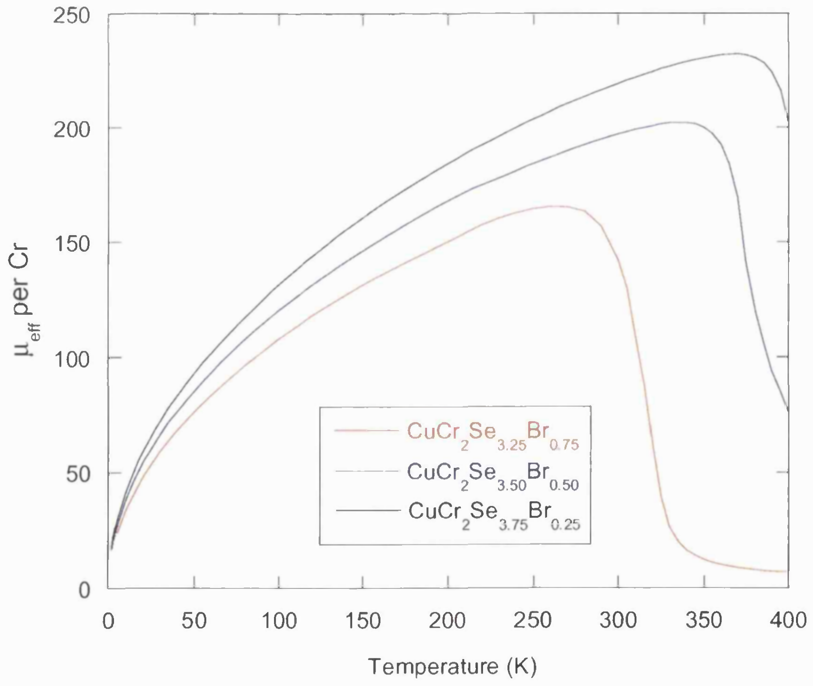

Figure 4.39 *Plot of* μ_{eff} *per chromium vs. temperature for compounds in the* $CuCr_2Se_{4-y}Br_y$ *series.*

4.3.3.2 Magnetic hysteresis

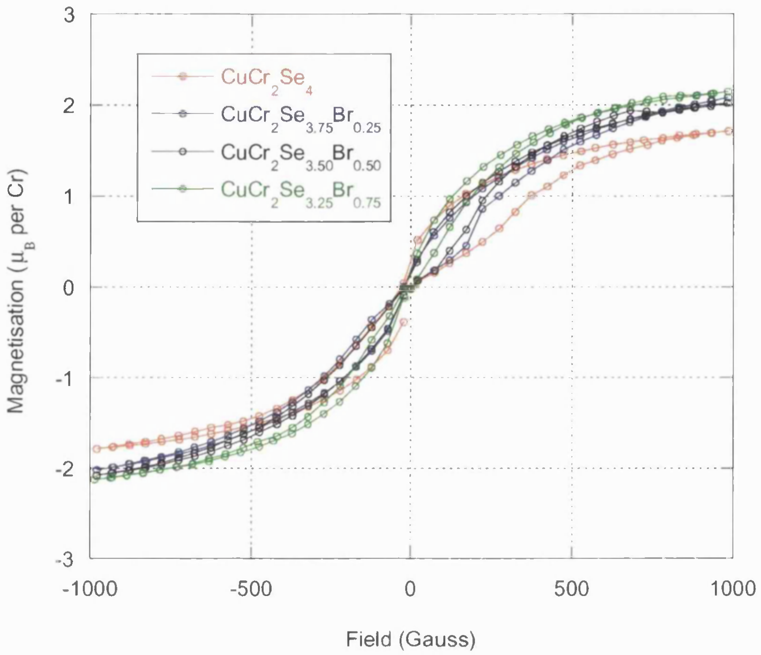

Figure 4.40 *Magnetisation vs. field plots for compounds in the series* $CuCr_2Se_{4-y}Br_y$ *for field sweeps 0 → 1000 → -1000 → 0 Gauss.*

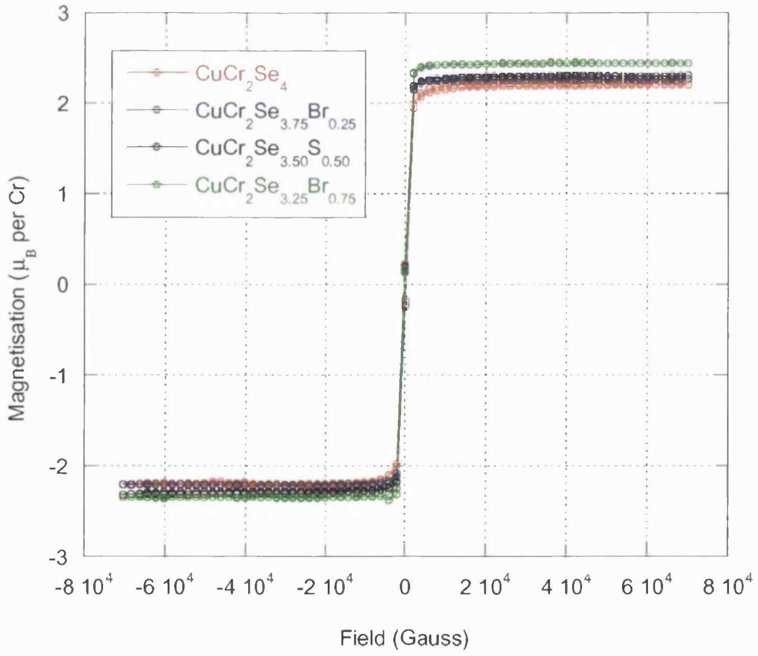

Figure 4.41 *Magnetisation vs. field plots for compounds in the series* $CuCr_2Se_{4-y}Br_y$ *for field sweeps 0 → 70,000 → 70,000 → 0 Gauss.*

Figures 4.40 and 4.41 show the low field and high field hysteresis measurements for compounds in the $CuCr_2Se_{4-y}Br_y$ series. In both cases the magnetisation is seen to increase with increasing bromine content, which is not in agreement with the magnetisation versus temperature data shown in figure 4.37. This increase has been reported previously in the literature [23]; Yamashita *et. al.* studied the series for $1 \geq y \geq 0$ and found an increase in saturation moment per mol from about 5 for $CuCr_2Se_4$ to about 6 for $CuCr_2Se_3Br$, which is in fairly good agreement with the values reported here. The synthesis conditions used were the same as those used in this thesis; it is not clear at what temperature the saturation magnetisation was measured. The authors note that in compounds with $x \geq 0.6$ there is the possibility of copper deficiency on the A-site. Another study by Robbins *et. al.* [12] found lower values of saturation magnetisation of 4.8 μ_B/mol for $y = 0$ to 5.24 μ_B/mol for $y = 1$, recorded at 4 K.

The substitution of bromine into $CuCr_2Se_4$ will result in a reduction of the chromium to give $Cu^{1+}[Cr^{3+}]_2[Se^{2-}]_3Br^{1-}$ at $y = 1$. This reduction will result in a greater saturation moment, rising from a theoretical value of 2.5 μ_B per chromium to 3.0 μ_B per chromium, and this is consistent with the results presented here.

In the low field measurement, all compounds show a hysteresis effect which is smaller for the bromine doped compounds than $CuCr_2Se_4$. The high field measurement shows no hysteresis and all compounds appear to have reached saturation magnetisation at approximately 2 Tesla. Values of the saturation magnetisation are given in table 4.3.

Composition, y	**Transition Temperature (K)**	**Saturation Magnetisation, M_s, per Cr (μ_B)**	
		$M_{s(exp)}$	$M_{s(calc)}$
0.00	*	2.21(2)	2.500
0.25	*	2.27(2)	2.625
0.50	370(5)	2.30(2)	2.750
0.75	305(5)	2.44(2)	2.875

Table 4.3 *Summary of information obtained from magnetic measurements on compounds in the series* $CuCr_2Se_{4-y}Br_y$.

---

* Transition above 400 K

4.3.4 AC susceptibility of $Cu_{0.05}Zn_{0.95}Cr_2Se_4$

From the results of the DC magnetisation experiments it has been found that compounds in the region of the $Cu_{1-x}Zn_xCr_2Se_4$ series with $0.02 \leq x \leq 0.10$ show some characteristics of spin glass materials such as hysteresis and a splitting of the field cooled and zero field cooled magnetisation curves below T_N. To investigate this possibility further, AC susceptibility measurements have been carried out on $Cu_{0.05}Zn_{0.95}Cr_2Se_4$ in a range of frequencies and fields; this compound was chosen for the study as it has also been studied by means of powder neutron diffraction (see chapter 7, section 7.3.2) and electrical transport measurements (see chapter 6, section 6.3.2).

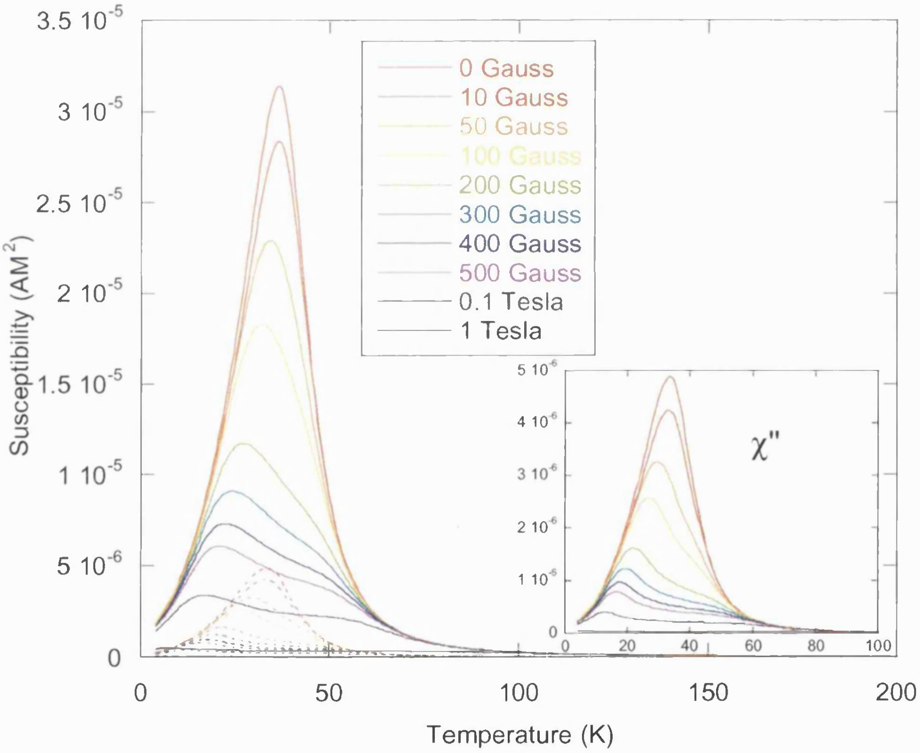

Figure 4.42 *Plot of AC susceptibility vs. temperature of* $Cu_{0.05}Zn_{0.95}Cr_2Se_4$ *in applied fields of 0 to 1 Tesla at frequency of 10 kHz; full and dashed lines represent the* χ' *and* χ'' *curves respectively. Inset: Enlargement of the* χ'' *data.*

Figure 4.42 shows the AC susceptibility versus temperature plot of $Cu_{0.05}Zn_{0.95}Cr_2Se_4$ at a frequency of 10 kHz in applied fields of between 0 and 1 Tesla. It can be seen that in fields above 100 Gauss, a splitting in both the χ' and χ'' peaks begins to emerge and becomes more pronounced with increasing field. This splitting is accompanied by a decrease in the magnitude of the susceptibility.

This splitting of the susceptibility peak at high fields suggests that the applied field may be changing the magnetic structure of the compound. This can also be concluded from the neutron diffraction experiments, reported in chapter 7 of this thesis, where there is evidence to suggest that the application of a field of 1 Tesla and above invokes a change from short range order to long range ferromagnetic order. The large magnetoresistance effect reported at low temperature (see chapter 5 of this thesis) is also indicative of field induced changes in the magnetic structure.

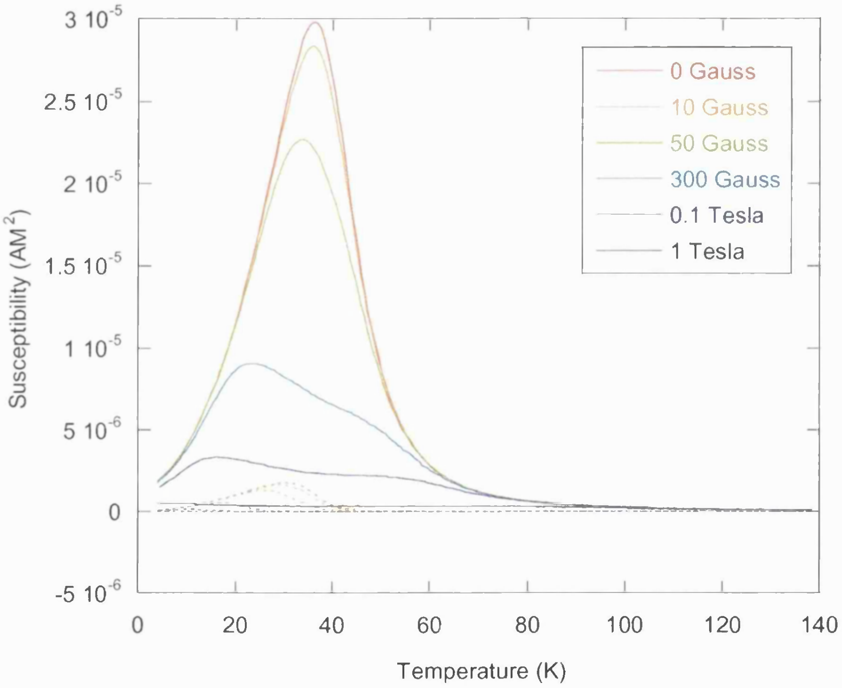

Figure 4.43 *Plot of AC susceptibility vs. temperature of* $Cu_{0.05}Zn_{0.95}Cr_2Se_4$ *in applied fields of 0 to 1 Tesla at frequency of 2.5 kHz; full and dashed lines represent the* χ' *and* χ'' *curves respectively.*

Figures 4.43 and 4.44 show the AC susceptibility versus temperature measurements in fields of 0 to 1 Tesla in 2.5 and 5 kHz respectively. It can be seen from a comparison between these plots and figure 4.42 that the frequency does not seem to influence the field at which the splitting of the peaks occurs. It was not possible to investigate this meaningfully at lower frequencies as the data was very noisy for measurements in an applied field in frequencies below 2.5 kHz.

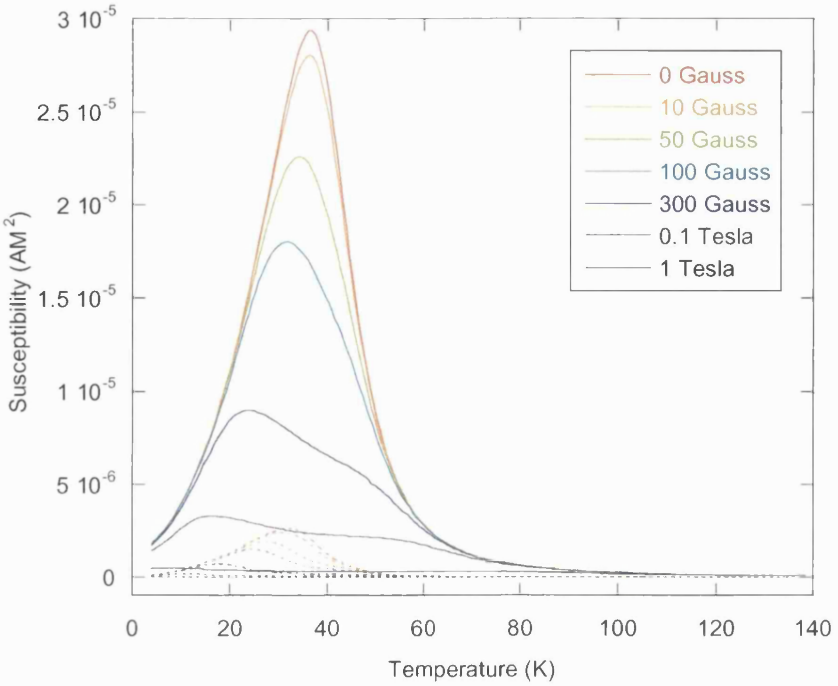

Figure 4.44 *Plot of AC susceptibility vs. temperature of* $Cu_{0.05}Zn_{0.95}Cr_2Se_4$ *in applied fields of 0 to 1 Tesla at frequency of 5 kHz; full and dashed lines represent the* χ' *and* χ'' *curves respectively.*

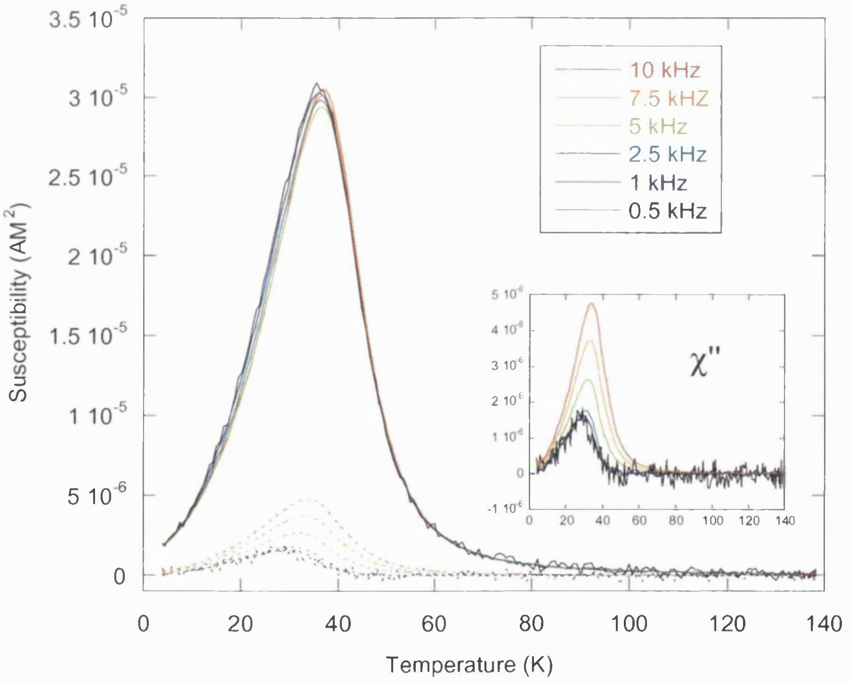

Figure 4.45 *Plot of AC susceptibility vs. temperature of* $Cu_{0.05}Zn_{0.95}Cr_2Se_4$ *in zero field at frequencies between 0.5 and 10 kHz; full and dashed lines represent the* χ' *and* χ'' *curves respectively. Inset: Enlargement of the* χ'' *data.*

The frequency dependence of the magnetic susceptibility was measured at zero field; the results are shown in figure 4.45. There does not appear to be a frequency dependence of the χ' peak within the frequency range measured. The χ'' peak does show a frequency dependence with the maximum shifting to higher temperatures with increasing frequency which suggests that there is a glassy nature to the magnetic structure of this compound. Unfortunately it was not possible to measure frequencies below 500 Hz due to the high noise levels. Conventionally, a much wider range of frequencies (1-10^3 Hz) is used to investigate frequency dependence in spin glass materials where a shift is seen in both the χ' and χ" peaks [24].

4.3.5 Aging experiments on compounds in the $Cu_{1-x}Zn_xCr_2Se_4$ series

A characteristic of a spin glass material is that its magnetisation will react in time to changes in external magnetic field whilst it is in a frozen state [24]. This is referred to as an aging effect and is explained in more detail in the theory chapter, section 2.3.2.7.

This aging effect can be investigated experimentally using DC magnetisation techniques. The method used here was adapted from that used by Wills *et. al.* [25]. The samples were cooled in a field of 100 Gauss from room temperature to below the low temperature magnetic transition, T_N. After a waiting time, t_w, the field was set to zero and the thermal-remnant magnetisation, M_{TRM}, was measured as a function of time. The magnetisation was measured approximately every two minutes and t_w was 500 seconds.

The samples used in the study were from the $Cu_{1-x}Zn_xCr_2Se_4$ series with $x = 1.00$, 0.99, 0.95, 0.93 and 0.75. For these compounds the magnetic transition temperatures are all between 20 and 30 K and a temperature of 15 K was used for these experiments. In $Cu_{0.25}Zn_{0.75}Cr_2Se_4$ the ferromagnetic transition is at high temperature (380 K) but there is also a low temperature transition at approximately 20 K.

The results of the aging experiments are shown in figure 4.46.

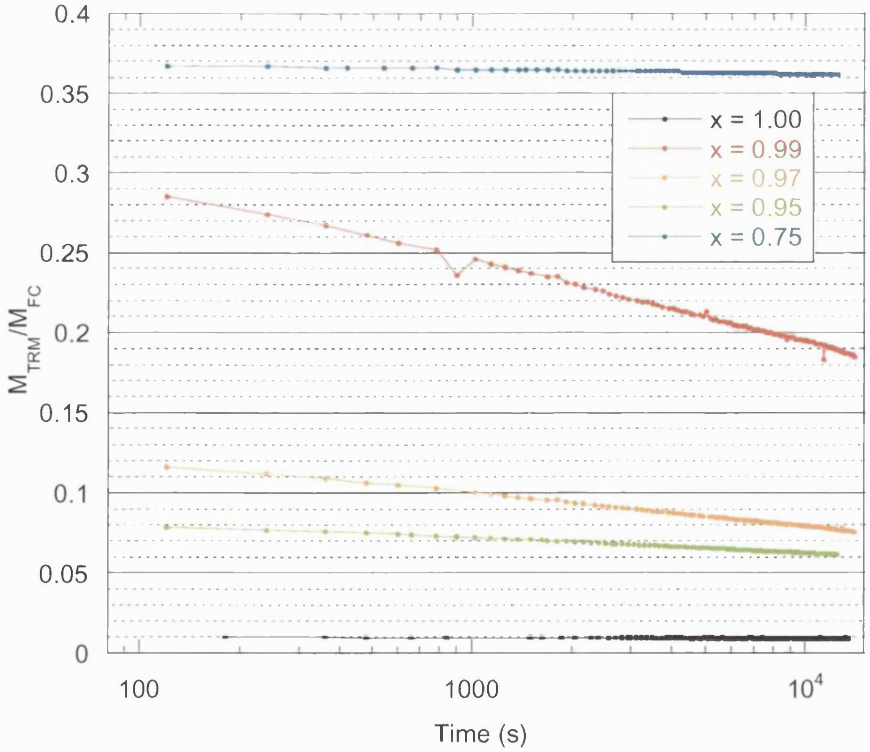

Figure 4.46 *M_{TRM}/M_{FC} vs. time at 15 K where t_w is 500 s, for compounds in the $Cu_{1-x}Zn_xCr_2Se_4$ series.*

In figure 4.46 M_{TRM}/M_{FC} is plotted against time. M_{FC} is the field cooled magnetisation at 100 Gauss and 15 K and therefore when time is equal to 0 seconds, M_{TRM}/M_{FC} should equal 1. In spin glasses there is a logarithmic decay of M_{TRM} with time (see chapter 2, section 2.3.2.7); in order to show this, time has been plotted on a logarithmic scale.

The results shown in figure 4.46 show a variation in aging effect across the $Cu_{1-x}Zn_xCr_2Se_4$ series. $ZnCr_2Se_4$ shows a negligible aging effect, this would be expected as there is no evidence to suggest glassy behaviour in this compound. $Cu_{0.01}Zn_{0.99}Cr_2Se_4$ shows the largest aging effect of all the compounds studied. A significant effect is also seen in $Cu_{0.05}Zn_{0.95}Cr_2Se_4$; here there is further evidence from the neutron diffraction experiments (reported in chapter 7) to suggest that a glassy magnetic state exists in this compound at low temperature. $Cu_{0.07}Zn_{0.93}Cr_2Se_4$ and $Cu_{0.25}Zn_{0.75}Cr_2Se_4$ also show an aging effect although this is smaller than seen for $Cu_{0.05}Zn_{0.95}Cr_2Se_4$.

4.4 Discussion

Studies of the DC magnetisation of the $Cu_{1-x}Zn_xCr_2Se_4$, $Cu_{1-x}Zn_xCr_2Se_{4-y}S_y$ and $CuCr_2Se_{4-y}Br_y$ series have revealed a wide range of magnetic behaviour. The studies of the end members of the $Cu_{1-x}Zn_xCr_2Se_4$ series, $CuCr_2Se_4$ and $ZnCr_2Se_4$ have shown them to be a ferromagnet with a T_C of 436 K and an antiferromagnet with T_N of 24 K respectively. Values of the T_C of $CuCr_2Se_4$ reported in the literature vary a great deal, from 414 to 465 K [26]; this could be due to different authors using different methods to define the T_C. In this thesis, the T_C is defined as the temperature at which the gradient of the magnetisation versus temperature curve is at a maximum during the transition. The value obtained here for the T_N of $ZnCr_2Se_4$ is slightly higher than has been previously reported in the literature, where values vary from 20 to 22 K [26]. The θ_{cw} value of 88 K obtained for this compound is considerably lower than values previously reported in the literature of 115 [8] and 118 K [7].

Compounds in the $Cu_{1-x}Zn_xCr_2Se_4$ series with mixed copper and zinc show a continuous variation of magnetic behaviour with composition. This indicates that the correct compositions of the compounds were achieved during synthesis, as was suggested by the linear variation of lattice parameter with composition, following Vergard's Law, which is discussed in chapter 3.

Compounds with high copper content (where $x \leq 0.8$) exhibit predominantly ferromagnetic behaviour with Curie temperatures above 380 K. The T_C decreases with increasing zinc content, in agreement with literature reports [26]. It was difficult to define the T_C of these compounds accurately as the ferromagnetic transition occurs over a broad temperature range, unlike in $CuCr_2Se_4$ where the ferromagnetic transition is sharp. The broadness of this transition could result from a combination of factors. It is know that there are competing ferromagnetic and antiferromagnetic interactions occurring in the series, the relative strengths of which depend largely on the relative concentrations of copper and zinc. These competing interactions may be leading to a complex domain structure in the material where different domains exhibit slightly different magnetic properties depending on the local concentration of copper and zinc ions. In this case each domain would undergo a transition from a ferromagnetic to a paramagnetic state at a slightly different temperature, which would lead to the broad ferromagnetic transition of the compound as a whole.

Compounds in this region of the series have also been found, from the X-ray diffraction studies discussed in chapter 3, to contain impurity phases comprising of small amounts of other compounds in the $Cu_{1-x}Zn_xCr_2Se_4$ series with varying values of x close to the intended composition. This could also be contributing to the broad ferromagnetic transitions seen, by the same reasoning as for the domain hypothesis, but on a much larger scale. However, this broad transition has been consistently observed by various authors studying the magnetic behaviour of this series where they also report phase purity of the compounds [7] [27] [19]; it is also unlikely that impurities could explain the size of the effect.

These ferromagnetic compounds also show a transition at low temperature, approximately 20 K, which has been observed previously in several studies [6, 19]. This is thought to be a transition to a low temperature non-collinear magnetic structure resembling the spiral antiferromagnetic structure of $ZnCr_2Se_4$. This has been confirmed by neutron diffraction studies at low temperature [19] [6]. The neutron diffraction studies presented in this thesis, in chapter 7, are unfortunately inconclusive on this matter.

When the concentration of zinc in the $Cu_{1-x}Zn_xCr_2Se_4$ series is increased further there is a change in magnetic behaviour. For $0.15 \leq x \leq 0.91$, the high temperature ferromagnetic transition is no longer visible in the magnetisation versus temperature plots and the only clear transition in the temperature range studied (2-400 K) is that at around 20 K. This peak at 20 K is followed by a gradual decrease in magnetisation with temperature which occurs over a wide temperature range (~ 200-300 K). The magnitude of the magnetisation seen in these compounds is typical of ferromagnetic rather than antiferromagnetic behaviour. Plots of $1/\chi$ versus temperature have shown that there is no transition to a simple paramagnetic state below 400 K. At low temperature, the behaviour can be attributed to a conical ferromagnetic structure, as suggested by Hidaka *et. al.* [6] where there is a canting of the ferromagnetic structure, induced by the increasing relative strength of the antiferromagnetic interactions. This low temperature non-collinear structure has been confirmed by neutron diffraction measurements on $Cu_{0.09}Zn_{0.91}Cr_2Se_4$ reported in chapter 7 of this thesis and by similar experiments on $Cu_{0.15}Zn_{0.85}Cr_2Se_4$ reported by Hidaka *et. al.* [6]. Magnetic hysteresis is also observed in these compounds at 5 K which provided further evidence that the magnetic order at low temperature is not simply antiferromagnetic. It has been suggested by Groń *et. al.* that a spin glass state is found for $0.1 \leq x \leq 0.2$, but as there is evidence from the neutron diffraction experiments (reported in chapter 7 of this thesis) to suggest that there is a magnetically ordered structure below 20 K, then this cannot be the case here.

The fact that a paramagnetic state has not be achieved for these compounds below 400 K and the gradual decrease in magnetisation over a long temperature range indicate that there is considerable disorder and the behaviour is that of a glassy or blocked magnetic state. The neutron diffraction measurements on $Cu_{0.09}Zn_{0.91}Cr_2Se_4$ (reported in chapter 7) indicate that there is no long range ferromagnetic or antiferromagnetic order in zero applied field at 50 K in this sample. There is also a lack of consistency in the ordering temperatures of compounds in this series which may also be a result of disorder.

For compounds with $x \geq 0.92$, a transition to a paramagnetic state below 400 K can be identified by analysis of the $1/\chi$ versus temperature curves. With the exception of $ZnCr_2Se_4$, all compounds in this region of the series show some hysteresis at 5 K which suggests that the observed behaviour is not simply antiferromagnetic. Spin glass materials show magnetic hysteresis and therefore a spin glass structure would explain some of the observed magnetic properties. A spin glass structure has been suggested previously for compounds with $0.1 \leq x \leq 0.2$ [10] but not in this region of the series where a simple antiferromagnetic spiral structure was proposed. There is further evidence for a low temperature glassy structure from the neutron diffraction investigation of $Cu_{0.05}Zn_{0.95}Cr_2Se_4$ (reported in chapter 7 of this thesis) and from the aging experiments reported in this chapter, section 4.3.5. In addition, a splitting between the zero field cooled and field cooled magnetisation curves is seen below the transition temperature is seen for $0.99 \geq x \geq 0.97$, another indication of a spin glass magnetic structure. AC susceptibility measurements performed on $Cu_{0.05}Zn_{0.95}Cr_2Se_4$ (see section 4.3.4) find that there is a clear frequency dependence of the χ" peak, suggesting that this compound is a spin glass.

It is possible that the glassy magnetic structures found in the $Cu_{1-x}Zn_xCr_2Se_4$ series are partly a result of the synthesis methods used. As the compounds with $x \neq 0$ or 1 were quenched rapidly to low temperatures after firing, some chemical disorder may have been frozen into the samples which has resulted in the observed magnetic behaviour.

The values of θ_{cw} obtained for compounds with $x \geq 0.92$ are all positive and increase with decreasing x. This can be explained by the increasing strength of the ferromagnetic interactions as copper is added. These ferromagnetic interactions are enhanced by the double exchange mechanism which involves the hopping of electrons between the Cr^{3+} and Cr^{4+} ions which stabilises the ferromagnetic arrangement of spins. This mechanism is described in more detail in chapter 1, section 1.3.2 and chapter 2, section 2.3.5.2.3. As more copper is added to the $Cu_{1-x}Zn_xCr_2Se_4$ series, the concentration of Cr^{4+} increases and the double exchange mechanism becomes more prevalent. The values of θ_{cw} reported here are much lower (by about 150 K) than those reported by Krok *et. al.* [7]; this was also seen, although to a lesser extent, in $ZnCr_2Se_4$. The reasons for this are not clear; there may be a link with the synthesis conditions used but as it is not clear which synthesis conditions were used by Krok *et. al.* this cannot be pursued further.

Compounds in the $Cu_{1-x}Zn_xCr_2Se_4$ series doped with sulphur on the selenium site show some interesting variations in magnetic behaviour. In the $CuCr_2Se_{4-y}S_y$ series there is a decrease in Curie temperature with increasing sulphur content, in agreement with previous work by Ohbayashi *et. al.* [11]. The ferromagnetic interactions in $CuCr_2Se_4$ are thought to be 90 ° superexchange interactions taking place via the Se^{2-} ions (discussed in more detail in the introduction, section 1.2.2). As Se^{2-} is larger than S^{2-} (they have ionic radii of 198 and 184 pm respectively), replacing Se^{2-} with S^{2-} will result in a decrease in overlap of the Se/S *p* orbitals with the Cr *d* orbitals and this will weaken the ferromagnetic superexchange, leading to a decrease in T_C. The ferromagnetic transitions seen in these compounds are sharp, similar to that seen for $CuCr_2Se_4$.

In the $Cu_{0.30}Zn_{0.70}Cr_2Se_{4-y}S_y$ series a decrease in T_C is also seen with increasing sulphur content accompanied by a decrease in magnetisation of the whole temperature range. Interestingly, the low temperature transition (thought to be to a ferromagnetic spiral structure) seen in the $Cu_{1-x}Zn_xCr_2Se_4$ series where $0 < x \leq 0.8$ is not observed here. The ferromagnetic transitions take place over a wide temperature range as seen in the ferromagnetic compounds in the $Cu_{1-x}Zn_xCr_2Se_4$ series.

In the $Cu_{0.10}Zn_{0.90}Cr_2Se_{4-y}S_y$ series there is a decrease in magnetisation with increasing sulphur content and where $y \neq 0$ a transition to a paramagnetic state is seen below 400 K. θ_{cw} is positive for these compounds and decreases with increasing sulphur content. This indicates a change in the relative strengths of the ferromagnetic and antiferromagnetic interactions. A hysteresis effect is seen at 5 K in all compounds studied suggesting that the magnetic behaviour is not that of a simple antiferromagnet. In the magnetisation versus temperature plot of $Cu_{0.10}Zn_{0.90}Cr_2Se_2S_2$ a splitting of the field cooled and zero field cooled curves is seen below T_N which is indicative of spin glass behaviour.

The $Cu_{0.05}Zn_{0.95}Cr_2Se_{4-y}S_y$ and $ZnCr_2Se_{4-y}S_y$ series both show a decrease in magnetisation with increasing sulphur content. Where $y \neq 0$ there is a splitting of the field cooled and zero field curves below T_N and no low field hysteresis effect is seen at 5 K.

The values of θ_{cw} are positive in all compounds and decrease with increasing sulphur content. In both series the sulphur containing compounds have a lower T_N than the compounds containing selenium only, although there does not appear to be a correlation between the amount of sulphur present and the values of T_N.

It appears that, in general, the addition of sulphur to the $Cu_{1-x}Zn_xCr_2Se_4$ series results in a weakening of the ferromagnetic interactions resulting in a decrease in magnetism and, in the ferromagnetic compounds, a lowering of T_C. Where there is high zinc concentration ($x \geq 0.95$) there is a reduction in T_N with increasing sulphur content. This suggests that the weakening of the ferromagnetic interactions is resulting in a lowering of the transition temperature, a conclusion that has also been drawn from a study of compounds in the $Cu_{1-x}Zn_xCr_2Se_4$ series at high pressure, reported in chapter 6 of this thesis.

There is also evidence here, from the splitting of the zero field cooled and field cooled curves below T_N, that the addition of sulphur may lead to spin glass behaviour in these compounds, however, if this was the case we would also expect to see some magnetic hysteresis at low field and this has not been observed.

The $CuCr_2Se_{4-y}Br_y$ series is ferromagnetic over the entire composition range studied. There is a decrease in Curie temperature with increasing bromine content similar to the effect seen in the $CuCr_2Se_{4-y}S_y$ series, however, in this case the proportional effect of bromine addition is much greater. It was suggested for the $CuCr_2Se_{4-y}S_y$ series that the lowering of the Curie temperature is related to the smaller size of the S^{2-} ion which inhibits the ferromagnetic superexchange interaction. In the case of Br^- substitution, however, this cannot apply as the ionic radii of the Br^- and Se^{2-} ions are very similar (196 and 198 pm respectively).

The explanation for the decrease in T_C with bromine content is more likely to be due to the lower charge on the Br^- ion. In $CuCr_2Se_4$ the ferromagnetism is thought to be enhanced by the double exchange mechanism which occurs due to the mixed valency of the Cr ions. In $CuCr_2Se_4$ there are equal amounts of Cr^{3+} and Cr^{4+} present, which should maximise this effect. When Br^- is substituted for Se^{2-} it is likely that the Cr^{4+} will be reduced to form Cr^{3+} to balance the charge in the compound. Therefore the double exchange mechanism will be inhibited and the strength of the ferromagnetic interactions will decrease, lowering the T_C.

4.5 References

1. Sadykhov, R.Z., Guseinov, D.A., and Akhmedov, A.I., *Physics of the Solid State*, 1998. **40**(2): p. 252-253.
2. Okonska-Kozlowska, I., Jedrzejewska, I., and Wokulska, K., *J. Alloy. Compd.*, 1995. **219**(1): p. 100-102.
3. Juszczuk, S., Johansson, C., Hanson, M., and Gogolowicz, M., *Phys. Lett. A*, 1994. **192**(1): p. 429-434.
4. Juszczyk, S. and Gogolowicz, M., *J. Magn. Magn. Mater.*, 1993. **128**(1): p. 163-170.
5. Jendrzejewska, I., Mydlarz, T., Okonska-Kozlowska, I., and Heimann, J., *J. Magn. Magn. Mater.*, 1998. **186**: p. 381-385.
6. Hidaka, M., Tokiwa, N., Wai, T.T., Fujii, H., Ohoyama, K., Mizusima, S., Sakaurai, J., Ichikawa, F., and Itoh, K., *Phase Transit.*, 2002. **75**(3): p. 273-287.
7. Krok, J., Spalek, J., Juszczyk, S., and Warczewski, J., *Phys. Rev. B*, 1983. **28**(11): p. 6499-6509.
8. Plumier, R., *J. Appl. Phys.*, 1966. **37**(3): p. 964-965.
9. Nakatani, I., Nose, H., and Masumoto, K., *J. Phys. Chem. Solids*, 1978. **39**: p. 743-749.
10. Groń, T., Duda, H., and Warczewski, J., *Phys. Rev. B*, 1990. **41**(18): p. 12424.
11. Ohbayashi, K., Tominaga, Y., and Iida, S., *J. Phys. Soc. Jpn.*, 1968. **24**: p. 1173-1174.
12. Robbins, M., Baltzer, P.K., and Lopatin, E., *J. Appl. Phys.*, 1968. **39**(2): p. 662-666.
13. Lotgering, F.K., *Solid State Commun.*, 1964. **2**: p. 55.
14. Robbins, M., Lehmann, H.W., and White, J.G., *J. Phys. Chem. Solids*, 1967. **28**: p. 897.
15. Kanomata, T., Ido, H., and Kaneko, T., *J. Phys. Soc. Jpn.*, 1970. **29**(2): p. 332-335.
16. Khan, M.N., Venkatachalam, A., Ahmad, A., and Darshane, V.S., *J. Mater. Sci.*, 1990. **25**: p. 595-598.
17. Yamashita, O., Yamaguchi, Y., Nakatani, I., Watanabe, H., and Masumoto, K., *J. Phys. Soc. Japan*, 1979. **46**: p. 1145-1151.
18. Juszczuk, S., *J. Magn. Magn. Mater.*, 1988. **72**: p. 67-70.

19. Iikubo, S., Yasui, Y., Oda, K., Ohno, Y., Kobayashi, Y., Sato, M., and Kakurai, K., *J. Phys. Soc. Jpn.*, 2002. **71**(11): p. 2792-2799.
20. Plumier, R., *J. Phys-Paris*, 1966. **27**: p. 213-219.
21. Lotgering, F.K. and van Stapele, R.P., *J. Appl. Phys.*, 1968. **39**(2): p. 417-423.
22. Miyatani, K., Minematsu, K., Wada, K., and al., e., *J. Phys. Chem. Solids*, 1971. **32**(7): p. 1429-1434.
23. Yamashita, O., Yamauchi, H., Yamaguchi, Y., and Watanabe, H., *J. Phys. Soc. Jpn.*, 1979. **47**(2): p. 450-457.
24. Mydosh, J.A., *Spin glasses: an experimental introduction.* 1993, London: Taylor and Francis.
25. Wills, A.S., Dupuis, V., Vincent, E., Hammann, J., and Calemczuk, R., *Phys. Rev. B*, 2000. **62**(14): p. R9264-R9267.
26. van Stapele, R.P., *Sulphospinels.* Ferromagnetic Materials: a handbook on the properties of magnetically ordered substances, ed. E.P. Wohlfarth. Vol. 3. 1982, Amsterdam: North-Holland. 603-745.
27. Okonska-Kozlowska, I. and Krok, J., *Z. Anorg. Allg. Chem.*, 1978. **447**: p. 235.

Chapter 5 Electrical Transport Measurements

5.1 Introduction

The electrical properties of the $Cu_{1-x}Zn_xCr_2Se_4$ series are known to vary significantly with zinc concentration. $ZnCr_2Se_4$ is known to be a p-type semiconductor [1-4]; insulating behaviour has been observed at low temperature. [5] The p-type electrical conductivity has been explained by a concentration of zinc vacancies (which act as a double acceptor) that is higher than the concentration of selenium vacancies [6]. Groń *et. al.* found, from analysing conductivity versus temperature curves, that there were two activation energies for the conduction process[1] corresponding to two acceptor levels at different energies.

$CuCr_2Se_4$ shows p-type metallic behaviour [3, 7-9] that is thought to be connected to the double exchange mechanism that leads to the hopping of a t_{2g} electron between the Cr^{3+} and Cr^{4+} ions. This mechanism is described in detail in the introduction, section 1.3.2 and in the theory chapter, section 2.3.5.2.3. The relationship between ferromagnetic coupling and electrical conductivity, arising from the double exchange mechanism, was first realised by Zener [10] and is highly applicable to $CuCr_2Se_4$.

Studies of the electrical behaviour across the $Cu_{1-x}Zn_xCr_2Se_4$ series have found p-type conductivity across the whole series, with a transition from semiconducting to metallic at $x = 0.7$ [4]. Above $x = 0.7$ there is a large decrease in resistivity with increasing copper content which is attributed to the introduction of increasing amounts of Cr^{4+} into the system, leading to an increase in vacancy concentration. In addition, conduction facilitated by the hopping of electrons between the mixed valence chromium ions via the double exchange mechanism can occur when Cr^{4+} is present. Therefore, increasing the proportion of copper results in an increase in conductivity facilitated by both an increase in the number of carriers and the mobility of the carriers throughout the lattice.

The relationship between the double exchange mechanism and a colossal magnetoresistance (CMR) effect has previously been extensively studied for certain mixed valence manganates, such as the layered lanthanum perovskite manganates, as discussed in the introduction, 1.5.2.1. As the double exchange mechanism is known to operate in the $Cu_{1-x}Zn_xCr_2Se_4$ series, magnetoresistance measurements have been carried out to investigate the possibility of a CMR effect.

The phases chosen for the MR measurements were $ZnCr_2Se_4$, $Cu_{0.05}Zn_{0.95}Cr_2Se_4$, $Cu_{0.09}Zn_{0.91}Cr_2Se_4$ and $Cu_{0.25}Zn_{0.75}Cr_2Se_4$; these are representative of the 4 main types of magnetic behaviour observed in the series, namely antiferromagnetism, spin glass behaviour, conical ferromagnetism and ferromagnetism.

5.2 Experimental

Resistance measurements were performed using the electrical properties probe of an Oxford Instruments Maglab^{2000} instrument. Samples were pressed into pellets of approximately 0.8 mm thickness and sintered at their reaction temperature (see chapter 3), thermally quenching where appropriate. Copper wires were attached to the sample using gold paint in the appropriate configuration for a 4-probe resistance measurement, as described in chapter 2 of this thesis, section 2.43. The dimensions of the pellet were recorded accurately as was the distance, l, between the two inner wires. These were used to calculate the resistivity, ρ, using the relationship

$$\rho = \frac{RA}{l} \qquad \textbf{Equation 5.1}$$

where A is the cross-sectional area. The dimensions of the pellets were typically 0.8×4×2 mm. A constant current, I, was applied during the measurement, the value of which was varied according to the resistivity of the sample. For samples with high resistivity ($\approx 10^9$ ohms) a low current ($\approx 10^{-11}$ amps) was used; for samples with a lower resistivity (10^{-3} ohms) a higher current (10^{-3} amps) was used. In each case the highest current possible was passed through the sample to reduce the noise in the data.

Resistance versus temperature measurements were performed by cooling the sample to approximately 4 K at a fast rate (≈ 10 Kmin^{-1}) and then measuring the resistance while the sample was heated at a rate of 2 Kmin^{-1}. Where appropriate, fields were applied before cooling to give 'field cooled' resistance versus temperature measurements.

Magnetoresistance (MR) was calculated as a percentage using the formula

$$\mathrm{MR} = \frac{\rho(H) - \rho(0)}{\rho(0)} \times 100 \qquad \textbf{Equation 5.2}$$

where ρ(H) and ρ(0) are the resistivity at applied field (H) and zero field respectively.

5.3 Results

5.3.1 Resistivity of $ZnCr_2Se_4$

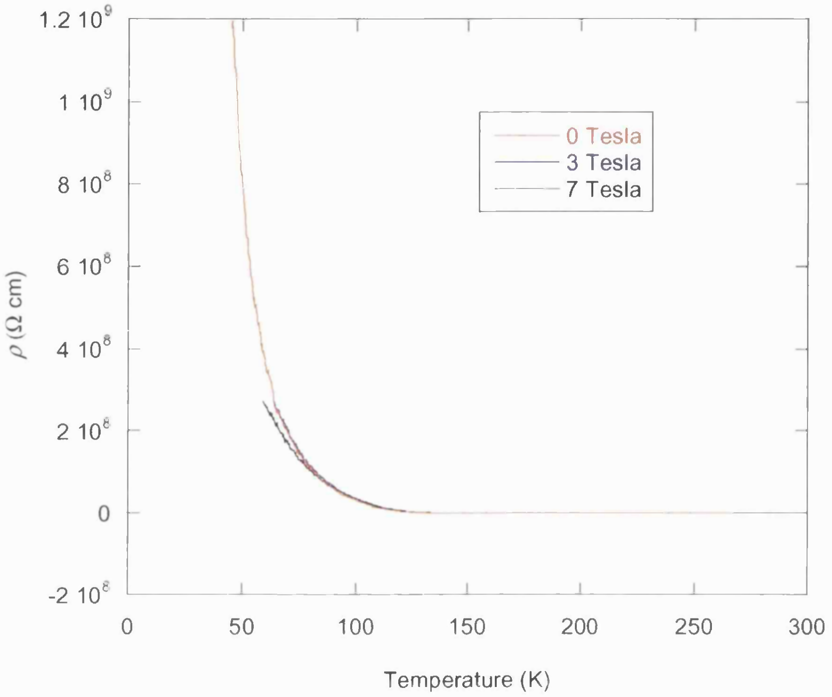

Figure 5.1 *$ZnCr_2Se_4$ Plot of resistivity vs. temperature at 0, 3 and 5 Tesla.*

Figure 5.1 shows resistivity versus temperature plots at 0, 3 and 7 Tesla for $ZnCr_2Se_4$; all plots show typical semiconducting behaviour. As the resistance of this compound was so high at low temperature it was not possible to measure the electrical properties below about 50 K, even using currents as small as 1×10^{-3} μA.

In order to confirm the semiconducting nature of $ZnCr_2Se_4$ a plot of $\ln(1/\rho)$ versus 1/T was drawn (figure 5.2). The expression to describe the behaviour of a semiconductor is

$$\sigma = \sigma_0 \exp^{-E_g/kT} \qquad \textbf{Equation 5.3}$$

where σ is the conductivity ($\sigma = 1/\rho$) and E_g is the band gap. Therefore plotting $\ln(1/\rho)$ versus 1/T should give a straight line with a gradient of E_g/k where semiconducting behaviour is observed.

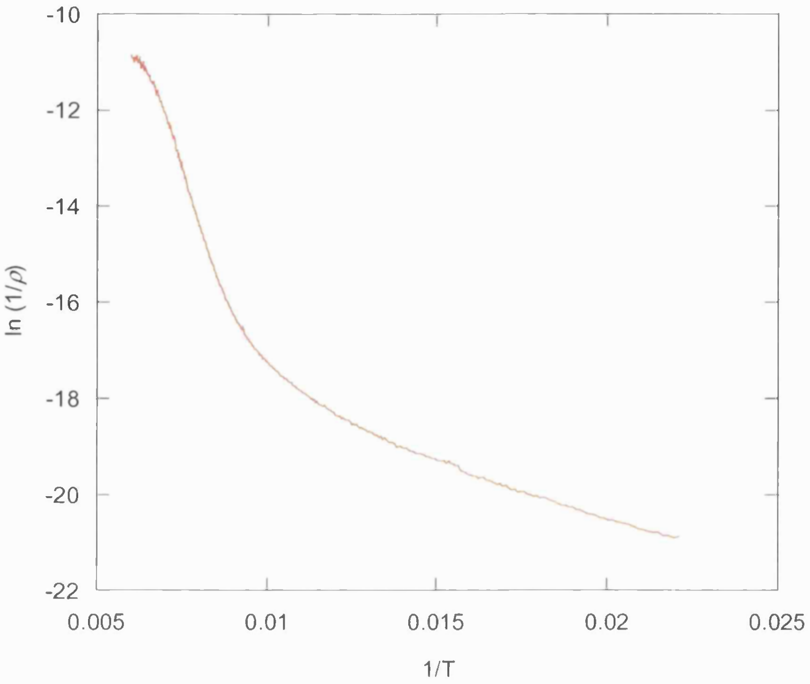

Figure 5.2 *$ZnCr_2Se_4$: Plot of ln (1/ρ) vs. 1/T at zero field.*

Figure 5.2 shows clearly two linear regions indicating that there are two semiconducting regions with different values of E_g, in agreement with the findings of Groń *et. al.* [1].

Fitting of the linear region at low temperature, between 45 and 80 K, gives a reasonable fit and an E_g of 0.044 eV; the high temperature region (110-150 K) gives a better linear fit and an E_g of 0.386 eV. These values compare reasonably well with the literature values of 0.056 and 0.2 eV respectively. Plots of these fits are shown in figures 5.3 and 5.4 for the low and high temperature range respectively.

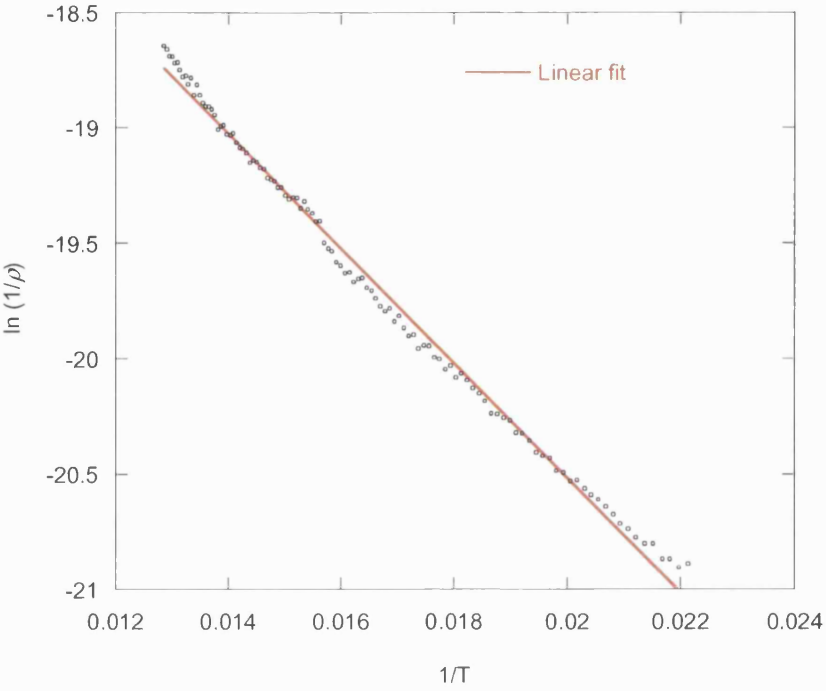

Figure 5.3 *ZnCr$_2$Se$_4$: Plot of ln(1/ρ) vs. 1/T in the temperature range 45→80 K.*

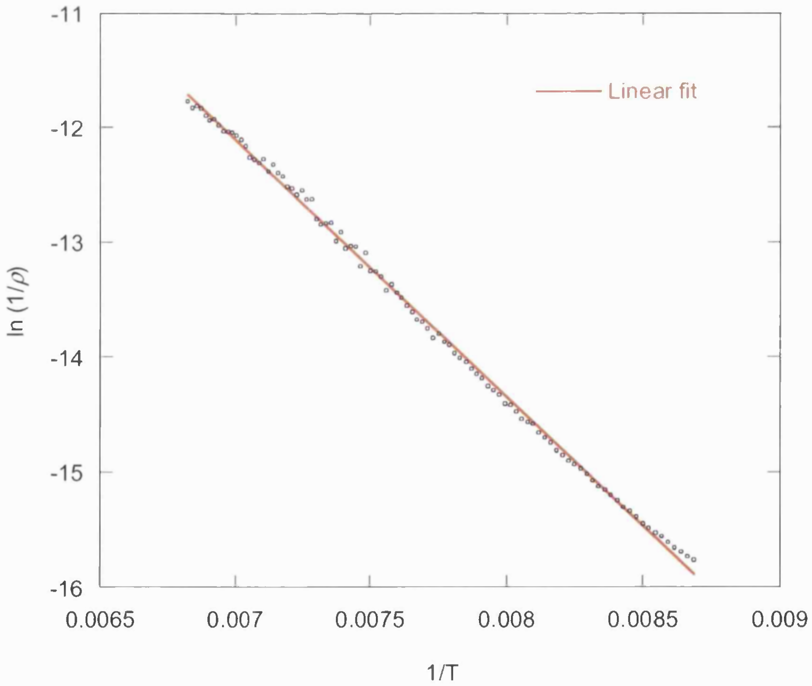

Figure 5.4 *ZnCr$_2$Se$_4$: Plot of ln(1/ρ) vs. 1/T in the temperature range 110→150 K.*

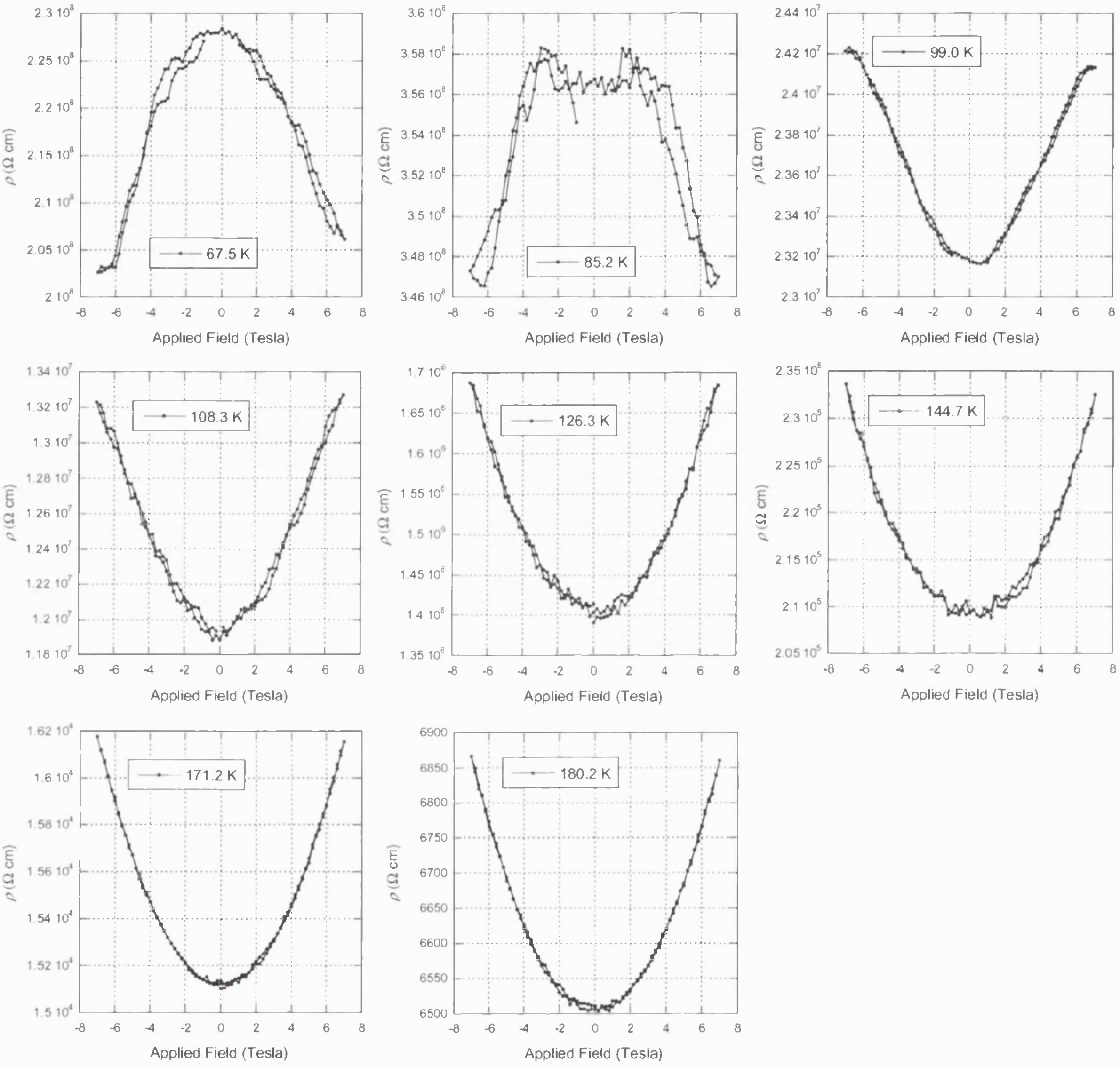

Figure 5.5 *$ZnCr_2Se_4$: Resistivity vs. field plots at temperatures from 67.5 – 180.2 K.*

As the resistance was so high at low temperature, reliable magnetoresistance values could not be obtained from the resistivity versus temperature plots as even a small inaccuracy in temperature could give a large error in resistivity. The magnetoresistance was therefore evaluated by measuring the resistivity while a field was applied from 0 → 7 → -7 → 0 Tesla at a series of fixed temperatures. The results are shown in figure 5.5.

At 67.5 K a negative magnetoresistance effect is seen of approximately 10 % at 7 Tesla. It is hard to define the values of magnetoresistance here very accurately as the data is fairly noisy due to the high resistance and small deviations from the set temperature result in large changes in resistivity.

At 85.2 K there appears to be a small positive magnetoresistance effect (approx 1.9 %) at low field (0 to 3 Tesla) followed by a larger negative magnetoresistance effect (5.2 %) at high field (3 to 7 Tesla). At 99.0 K and above, the magnetoresistance effect is positive and decreases with increasing temperature. Values of the magnetoresistance, normalised to field are plotted against applied field in figure 5.7; in temperatures below 100 K the MR effect a low field is proportionally much larger than at high field. At higher temperatures this effect is less pronounced. As the data is slightly noisy at some temperatures it is possible that the lower field values in figure 5.7 show features that are more a result of this noise than a real effect.

Figure 5.6 shows the resistivity against field plots at all temperatures studied plotted together on a logarithmic scale. The change in sign of the magnetoresistance can be seen as well as the rapid drop in zero field resistivity with temperature, corresponding to that seen in the resistivity versus temperature plot in figure 5.1.

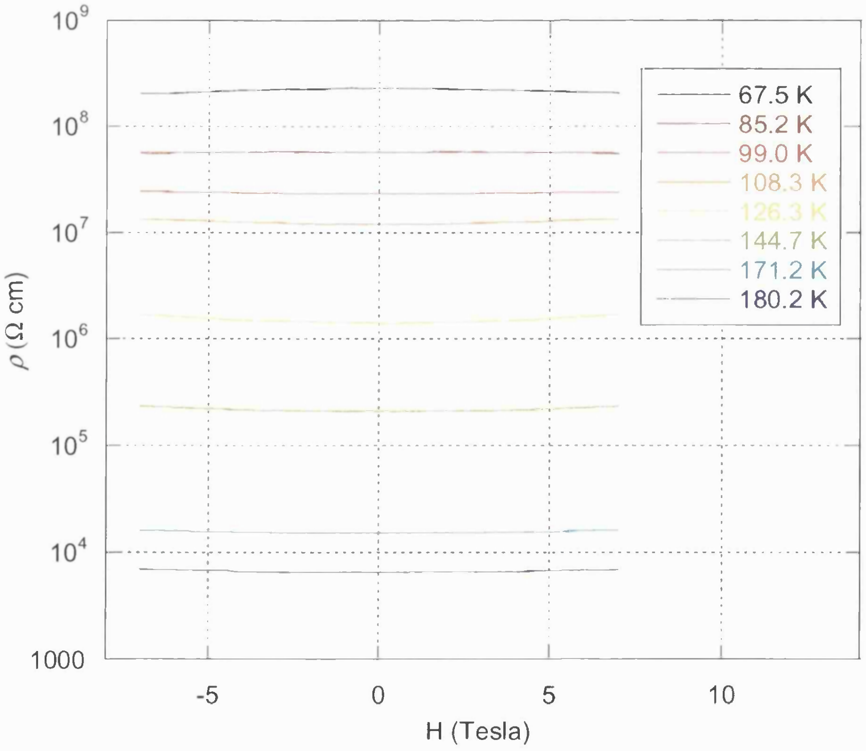

Figure 5.6 *$ZnCr_2Se_4$: Combined plot of resistivity vs. field at temperatures between 67.5 and 180.2 K.*

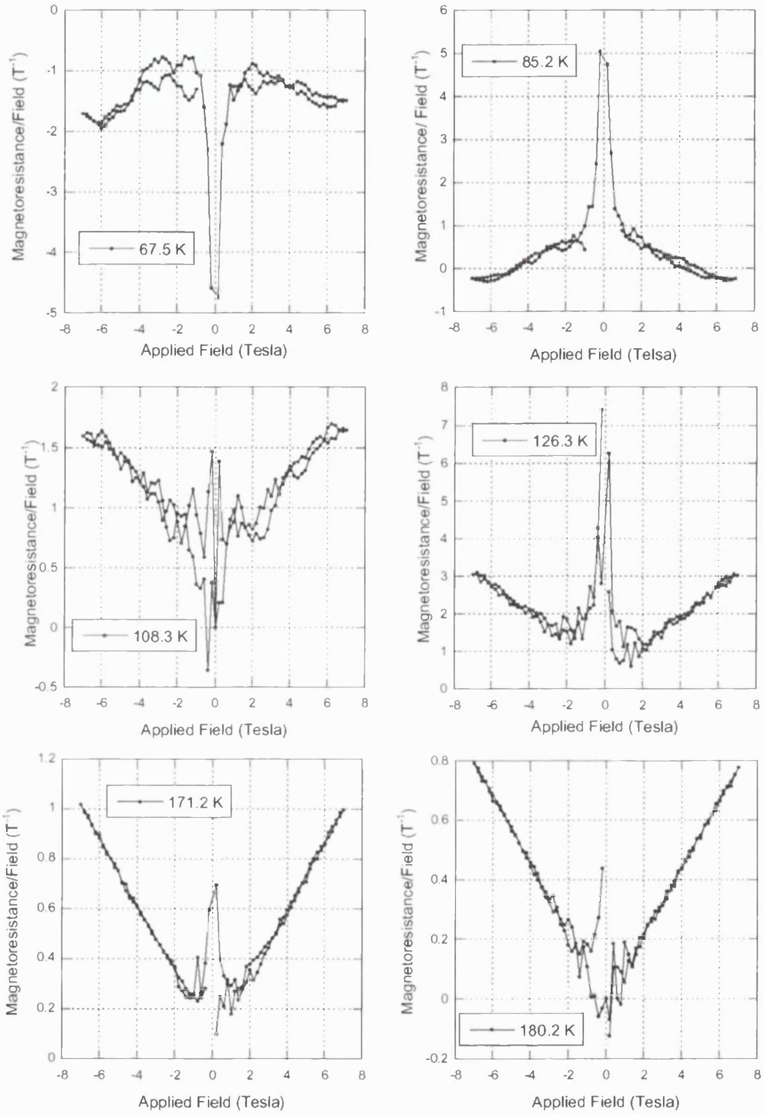

Figure 5.7 *ZnCr$_2$Se$_4$: Plots of magnetoresistance/field vs. field at temperatures between 67.5 and 180.2 K.*

5.3.2 Resistivity of $Cu_{0.05}Zn_{0.95}Cr_2Se_4$

Figures 5.8 and 5.9 show the resistivity versus temperature curves for $Cu_{0.05}Zn_{0.95}Cr_2Se_4$ at various applied fields. The behaviour appears to be semiconducting and a negative magnetoresistance effect can be clearly seen in the region below about 20 K. The values of resistivity are several orders of magnitude lower than observed for $ZnCr_2Se_4$ in agreement with previous observations on the resistivity of the $Cu_{1-x}Zn_xCr_2Se_4$ [1].

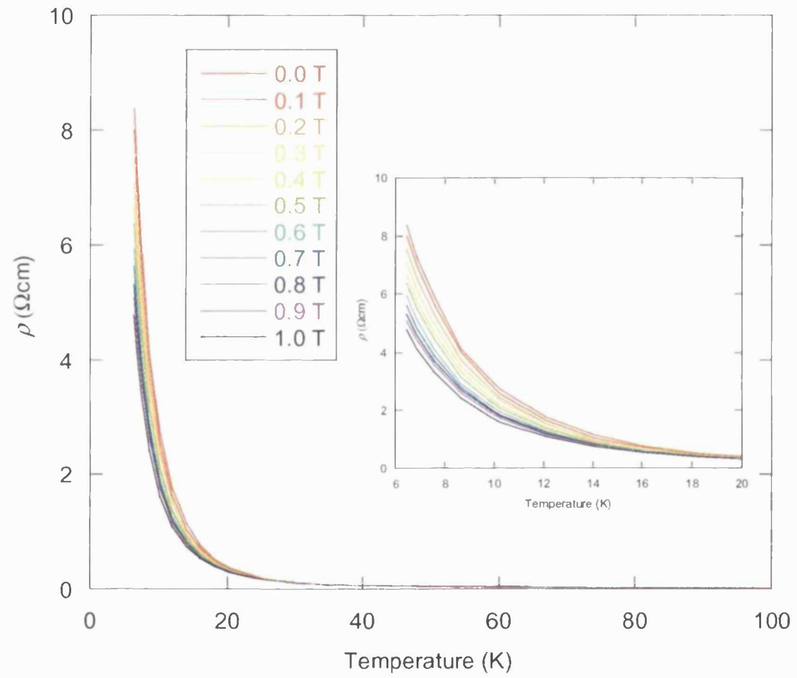

Figure 5.8 *$Cu_{0.05}Zn_{0.95}Cr_2Se_4$: Plot of resistivity vs. temperature in applied fields of 0 → 1 T with inset expansion of the region between 6 and 20 K*

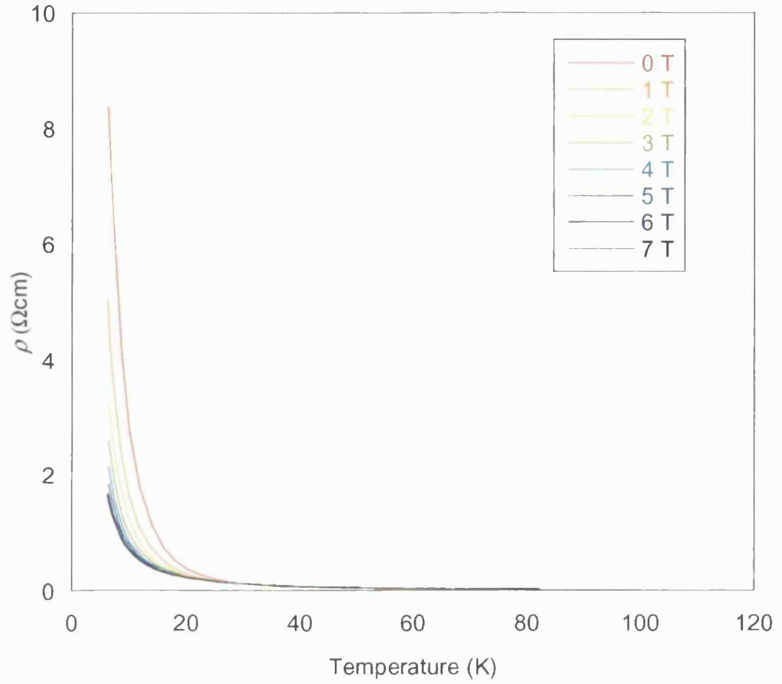

Figure 5.9 *$Cu_{0.05}Zn_{0.95}Cr_2Se_4$: Plot of resistivity vs. temperature in applied fields of 0 → 7 T*

To confirm the semiconducting behaviour of this compound, ln(1/ρ) was plotted against 1/T, which should give a straight line, as described in section 5.3.1.

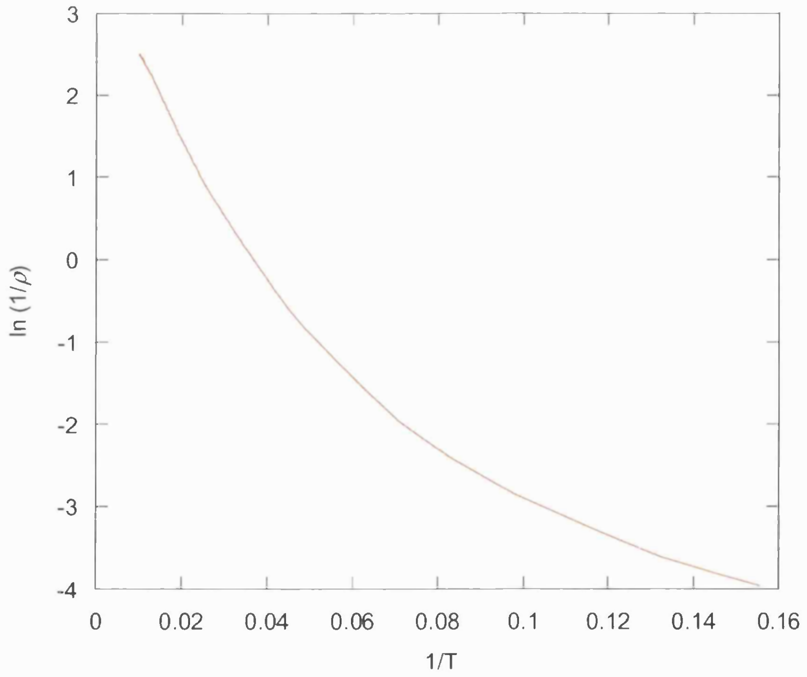

Figure 5.10 *$Cu_{0.05}Zn_{0.95}Cr_2Se_4$: Plot of ln(1/ρ) vs. 1/T for in the temperature range 4→100 K.*

Figure 5.10 shows that there are two approximately linear regions in the ln($1/\rho$) versus 1/T plot. In the low temperature region (0 → 25 K) as shown in figure 5.11 the data did not fit well to the semiconducting expression; a better, although not perfect, fit was achieved by applying Mott's expression for variable range hopping conduction [11]. For this conduction mechanism the resistivity is given by

$$\rho = \rho_0 \exp^{\left(-T_0/T\right)^{1/4}}$$ **Equation 5.4**

where a linear relationship is seen between ln($1/\rho$) and $1/(T^{1/4})$ as seen in figure 5.12.

In the high temperature region (40 → 100 K) a better fit was found to the semiconducting (figure 5.13) than the variable range hopping expression (figure 5.14).

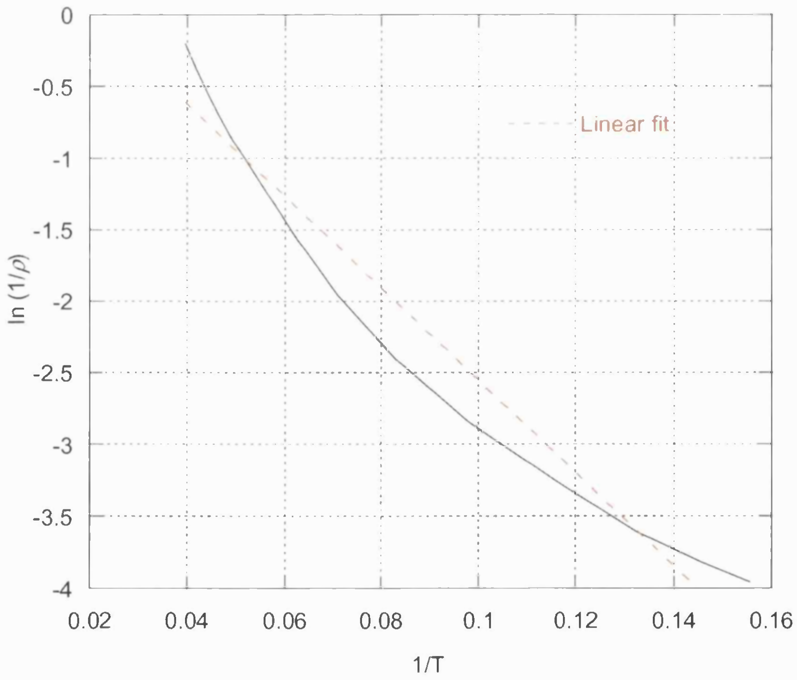

Figure 5.11 *$Cu_{0.05}Zn_{0.95}Cr_2Se_4$: Plot of ln(1/ρ) vs. 1/T in the temperature rage 4→25 K.*

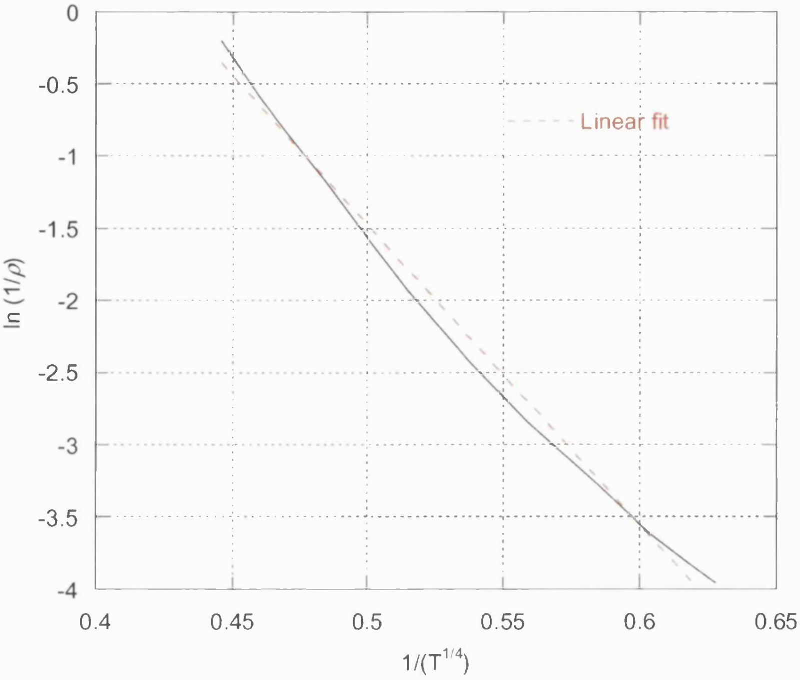

Figure 5.12 $Cu_{0.05}Zn_{0.95}Cr_2Se_4$: *Plot of* $ln(1/\rho)$ *vs.* $1/T^{1/4}$ *in the temperature range 4→25 K.*

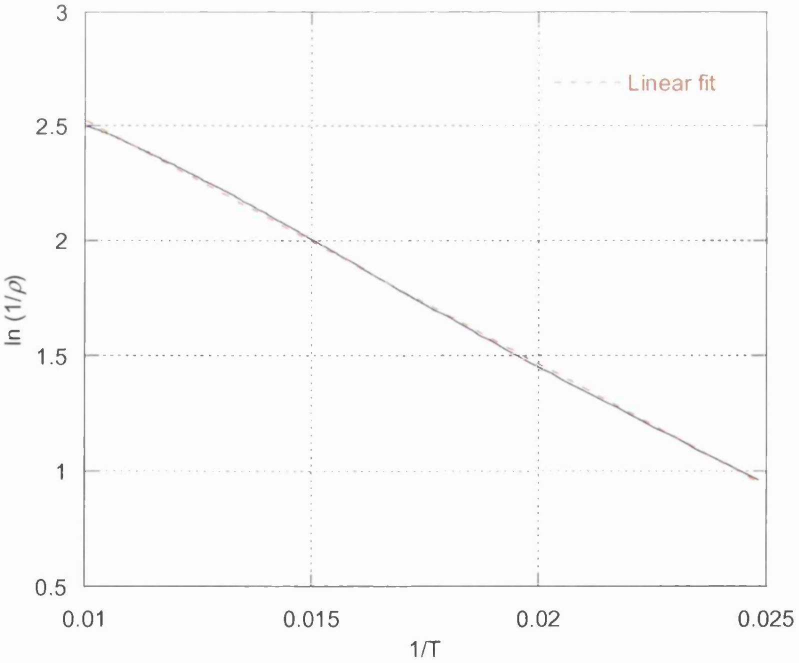

Figure 5.13 $Cu_{0.05}Zn_{0.95}Cr_2Se_4$: *Plot of* $ln(1/\rho)$ *vs.* $1/T$ *in the temperature range 40→100 K.*

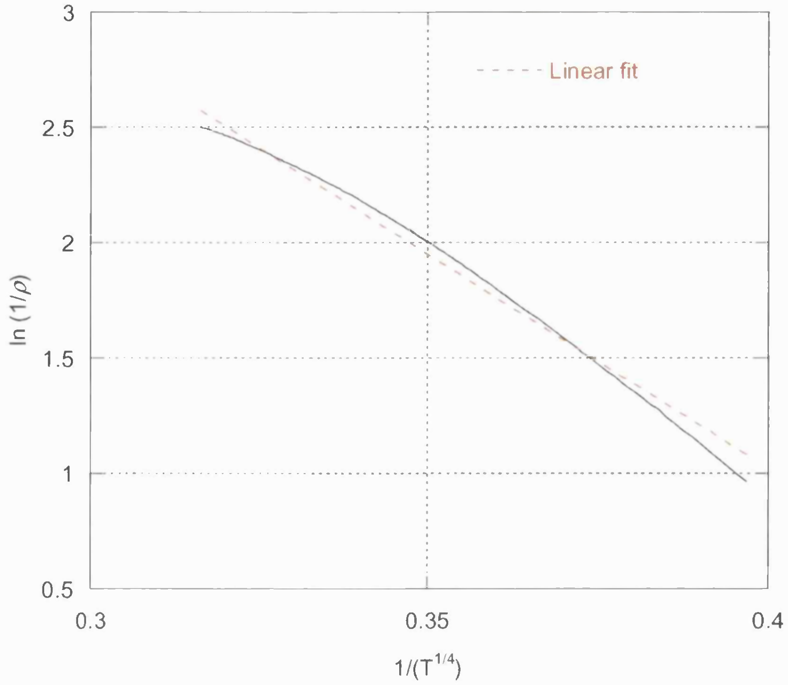

Figure 5.14 *$Cu_{0.05}Zn_{0.95}Cr_2Se_4$: Plot of ln(1/ρ) vs. $1/T^{1/4}$ in the temperature range 40→100 K.*

In an applied field the fit to the variable range hopping expression improves for the low temperature region and the high temperature; this effect increases with field and above $\mu_0 H$ = 4 Tesla the variable range hopping expression provides the best fit over the whole temperature range. The low and high temperature fits to the variable range hopping expression for $Cu_{0.05}Zn_{0.95}Cr_2Se_4$ at 7 Tesla are shown in figures 5.14 and 5.15; fits to the semiconducting expression are given in the appendix, section A.3.1, along with fits to the semiconducting and variable range hopping expressions of the resistivity in applied fields of 1, 2, 3, 4, 5, and 6 Tesla. Where the semiconducting expression gave the best fit in the high temperature region, values of E_g were extracted; 9.13, 8.53, 9.79 and 10.20 meV were obtained for applied fields of 0, 1, 2 and 3 Tesla respectively.

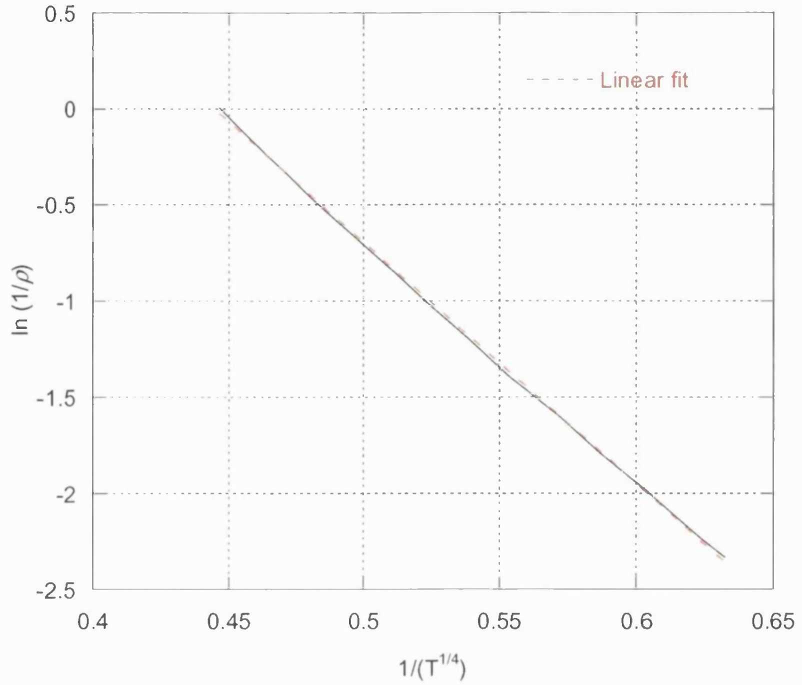

Figure 5.15 *$Cu_{0.05}Zn_{0.95}Cr_2Se_4$: Plot of ln(1/ρ) vs. $1/T^{1/4}$ in an applied field of 7 Tesla in the temperature range 4→25 K.*

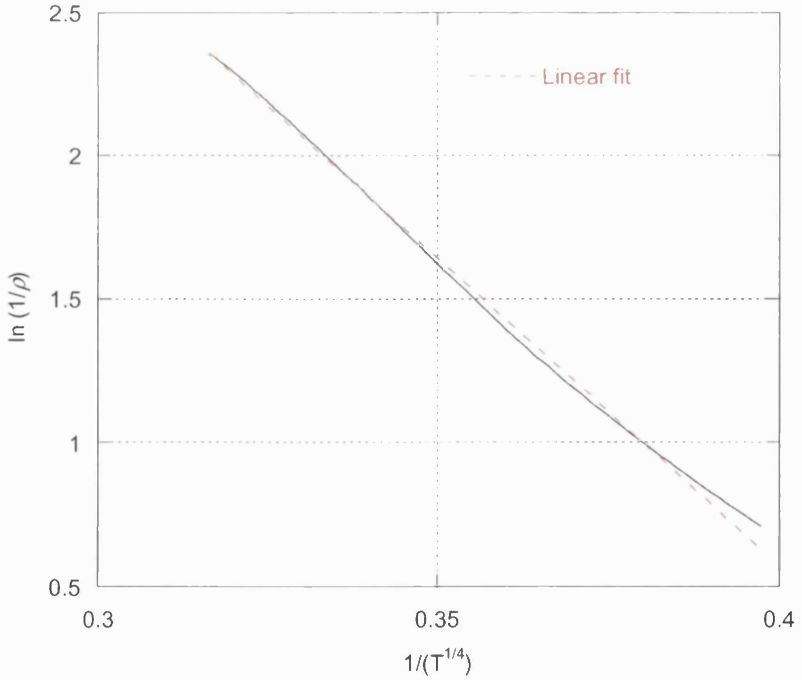

Figure 5.16 *$Cu_{0.05}Zn_{0.95}Cr_2Se_4$: Plot of ln(1/ρ) vs. $1/T^{1/4}$ in an applied field of 7 Tesla in the temperature range 40→100 K.*

Figures 5.17 and 5.18 show magnetoresistance versus temperature plots derived from the low and high field resistivity versus temperature measurements shown in figures 5.4 and 5.5. It can be seen here that there is a crossover between negative and positive magnetoresistance at approximately 35 K, which is not easily visible in the resistivity versus temperature measurements. This crossover corresponds to the temperature at which there is a change from variable range hopping to semiconducting behaviour in low fields.

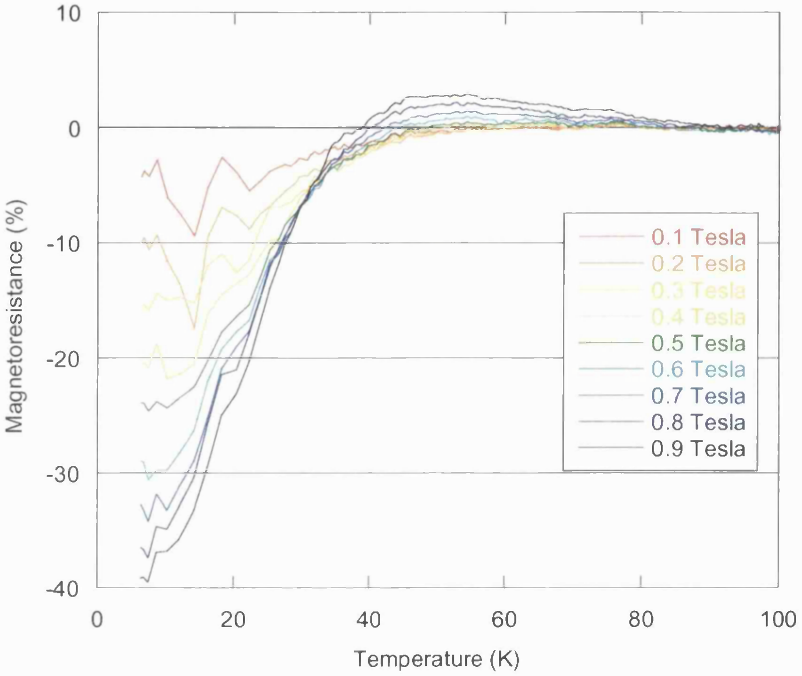

Figure 5.17 *$Cu_{0.05}Zn_{0.95}Cr_2Se_4$: Plot of low field magnetoresistance vs. temperature.*

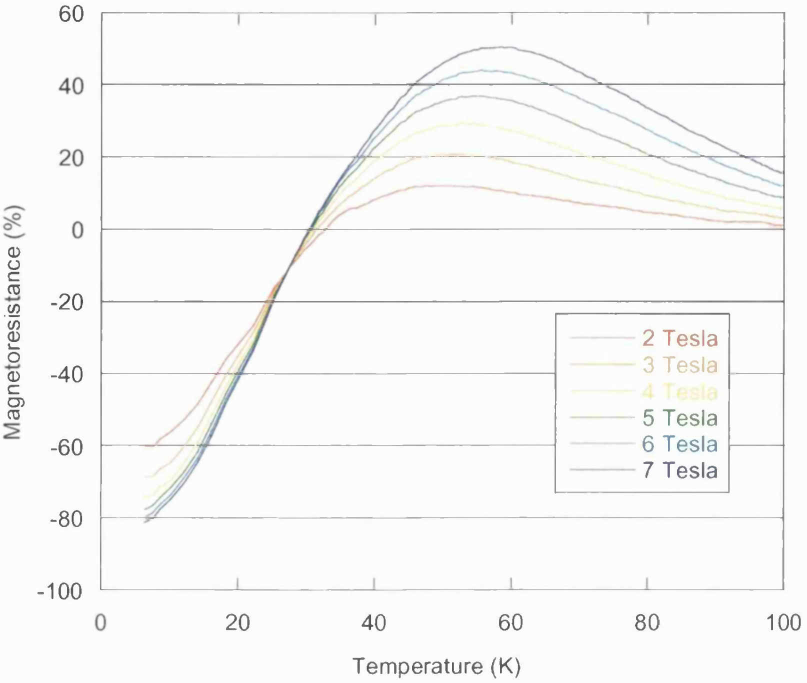

Figure 5.18 *$Cu_{0.05}Zn_{0.95}Cr_2Se_4$: Plot of high field magnetoresistance vs. temperature.*

In order to study the magnitude of the magnetoresistance effect and the crossover from a negative to positive effect, the resistivity was measured as a field was applied from 0 → 7 → -7 → 0 Tesla at a series of fixed temperatures. The results are shown in figures 5.19 and 5.19.

Figure 5.20 shows a negative magnetoresistance effect, decreasing with increasing temperature, from 3.2 to 22.5 K. At 27.0 K there is initially a negative MR effect at low field (0→1 T) followed by an increase of resistivity with field at higher fields. At 46.2 K and above there is positive magnetoresistance which decreases with increasing temperature. This behaviour corresponds to the magnetoresistance derived from the resistivity versus temperature plots.

Figure 5.17 shows the resistivity versus field data for all temperatures studied plotted together on a logarithmic scale; the crossover from negative to positive magnetoresistance can clearly be seen, as can the variation in zero field resistivity with temperature.

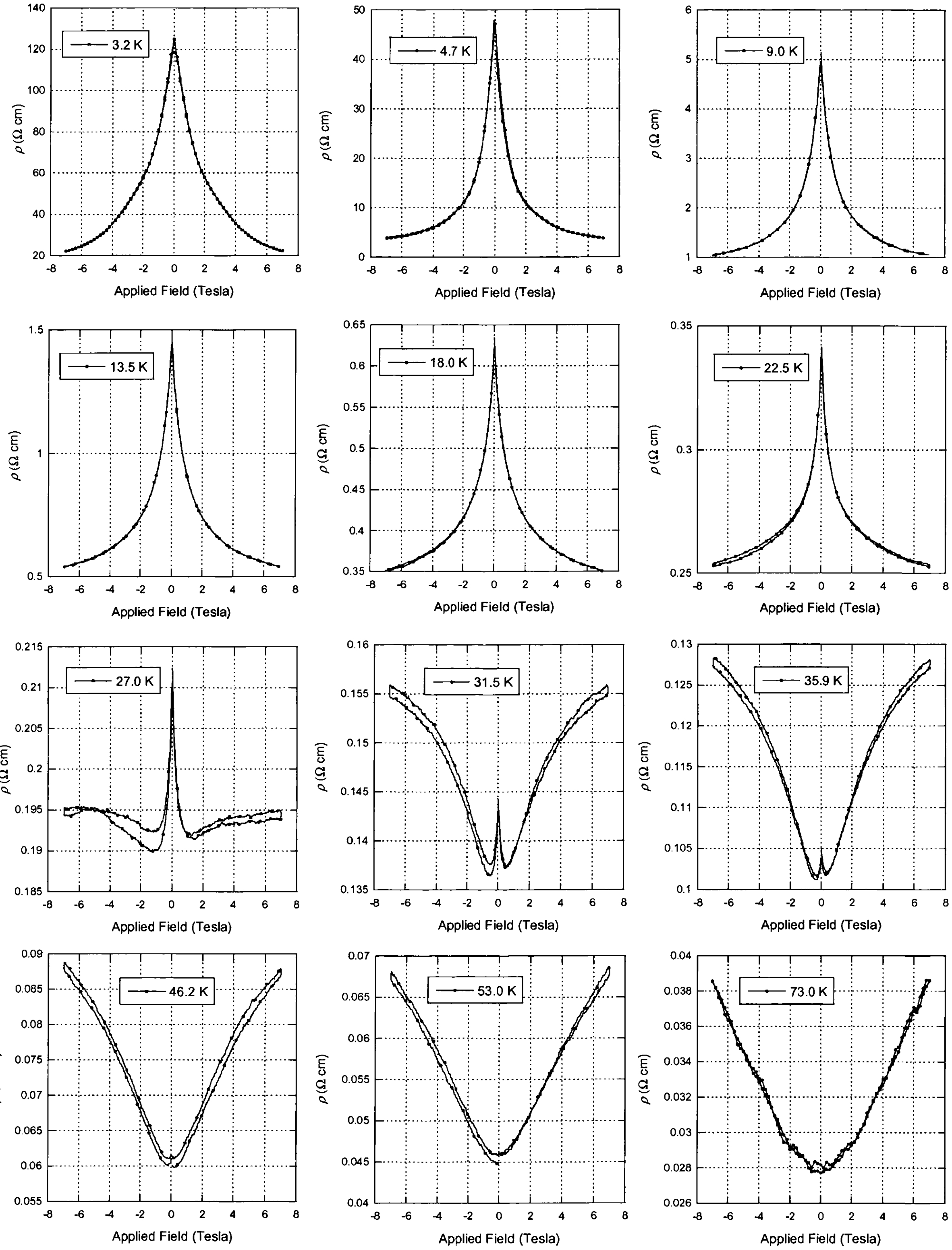

Figure 5.19 *$Cu_{0.05}Zn_{0.95}Cr_2Se_4$: Plots of resistivity vs. field at temperatures from 3.2 K to 73.0 K.*

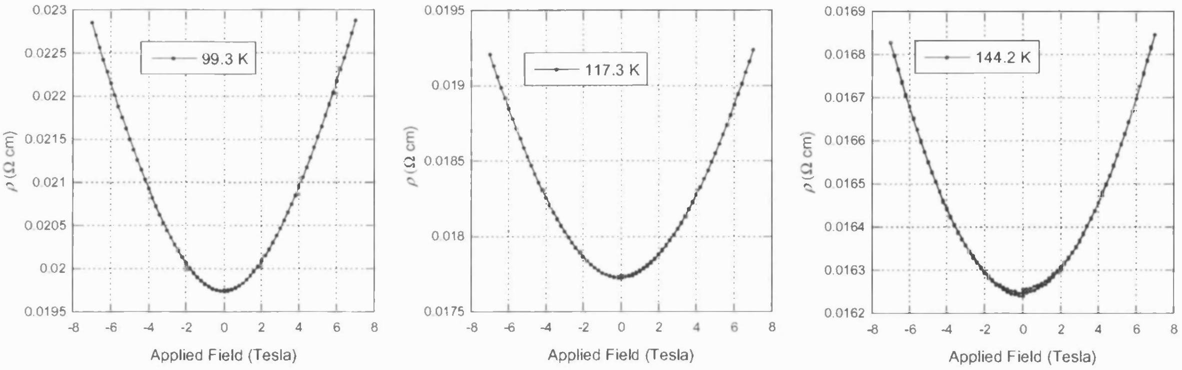

Figure 5.20 *$Cu_{0.05}Zn_{0.95}Cr_2Se_4$: Plots of resistivity vs. field at temperatures from 99.3 K to 144.2 K.*

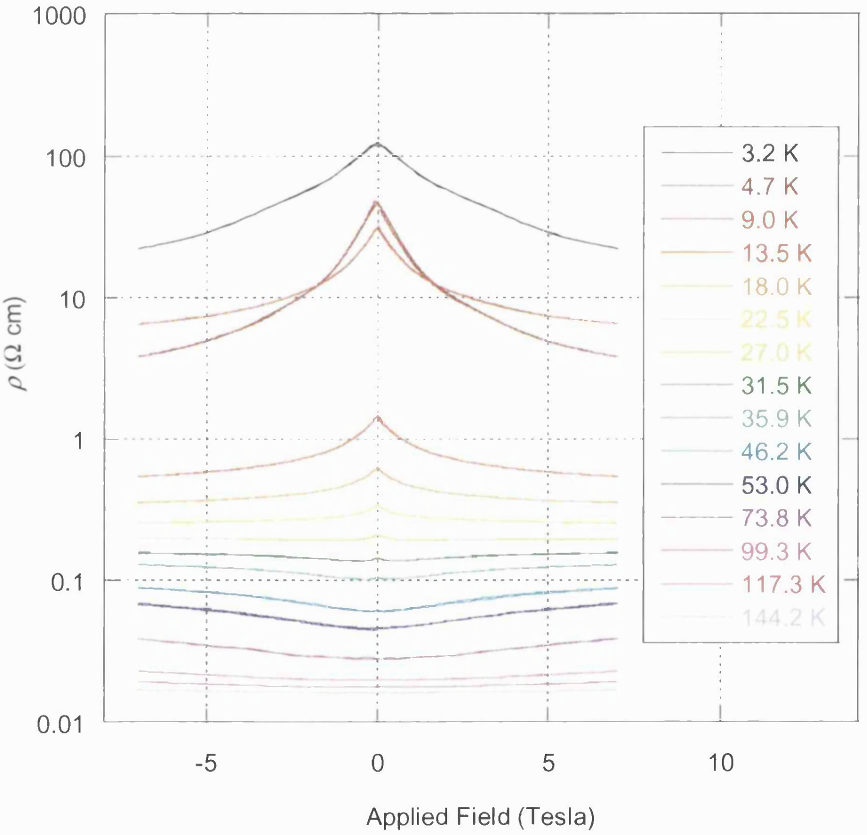

Figure 5.21 *$Cu_{0.05}Zn_{0.95}Cr_2Se_4$: Combined plot of resistivity vs. field at temperatures between 3.2 and 144.2 K.*

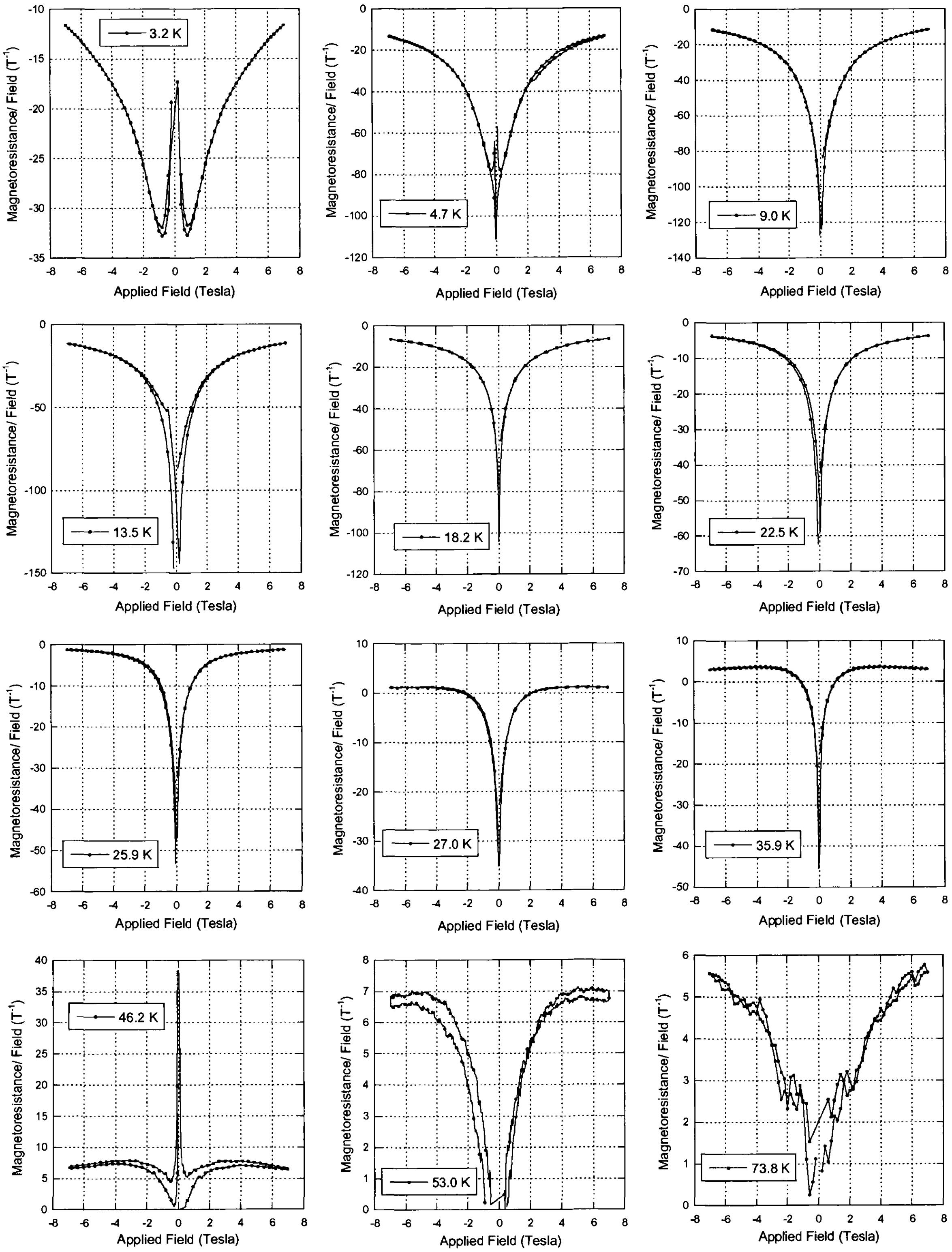

Figure 5.22 *$Cu_{0.05}Zn_{0.95}Cr_2Se_4$: Plots of magnetoresistance/field vs. field at temperatures between 3.2 and 73.8 K.*

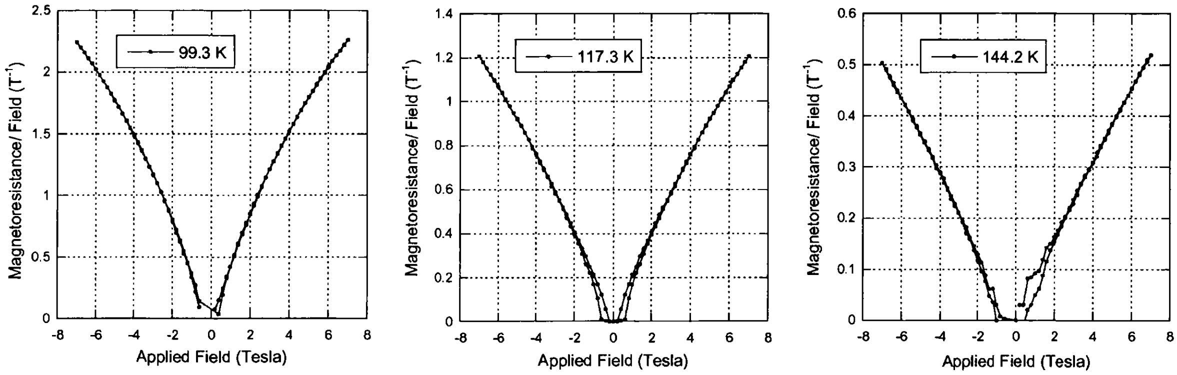

Figure 5.23 *$Cu_{0.05}Zn_{0.95}Cr_2Se_4$: Plots of magnetoresistance/field vs. field at temperatures between 99.3 and 144.2 K.*

Figures 5.18 and 5.19 show the magnetoresistance versus field at the temperatures studied, normalised to field. At 3.2 K the MR/H initially increases with field until a maximum at around 1 T and then decreases with field to 7 Tesla. From 4.7 to 46.2 K the magnetoresistance effect is proportionally larger at low field and above 46.2 K MR/H increases with increasing field.

The magnetoresistance effects seen here are much larger than those observed for the other compounds studied in the $Cu_{1-x}Zn_xCr_2Se_4$ series.

5.3.3 Resistivity of $Cu_{0.09}Zn_{0.91}Cr_2Se_4$

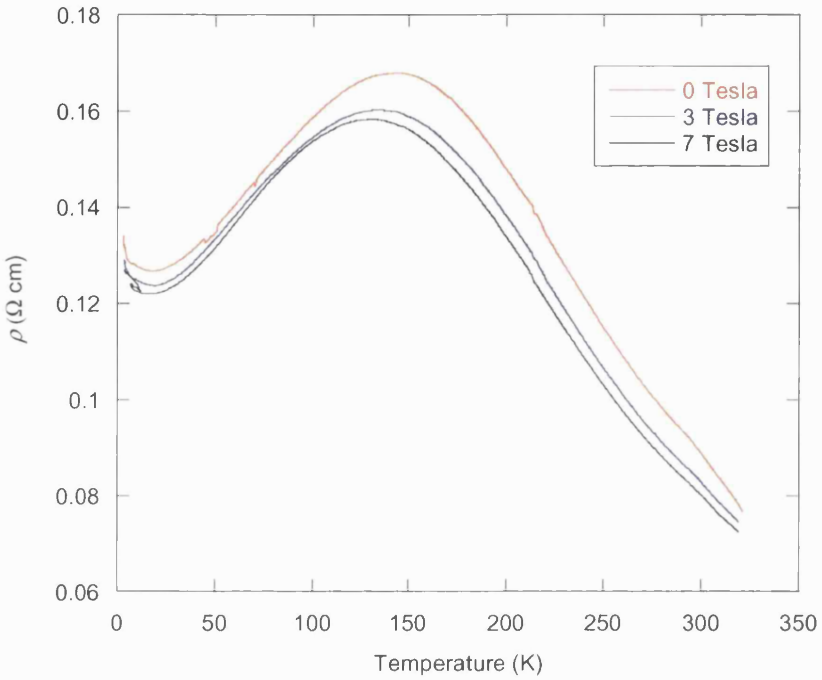

Figure 5.24 *$Cu_{0.09}Zn_{0.91}Cr_2Se_4$: Plot of resistivity vs. temperature at 0, 3 and 7 Tesla.*

Figure 5.24 shows resistivity versus temperature plots for $Cu_{0.09}Zn_{0.91}Cr_2Se_4$ at 0, 3 and 7 Tesla. After an initial decrease in resistivity with increasing temperature up to approximately 20 K there is an increase to about 150 K, followed by a decrease. This behaviour does not correspond to typical semiconducting or metallic behaviour and therefore is likely to arise from the presence of competing conduction mechanisms with varying influence at different temperatures. The values of the resistivity are approximately one order of magnitude less than those found for $Cu_{0.05}Zn_{0.95}Cr_2Se_4$, in keeping with the trend of a decrease in resistivity with the increase of copper in the series.

It appears from figure 5.24 that there is a negative magnetoresistance effect at all temperatures. This was investigated further by measuring the resistivity as a field is applied from 0 → 7 → -7 → 0 Tesla at a selection of fixed temperatures; the results are shown in figure 5.25.

At low temperature (4.6 → 22.6 K) there is a small negative magnetoresistance effect, which decreases with increasing temperature.

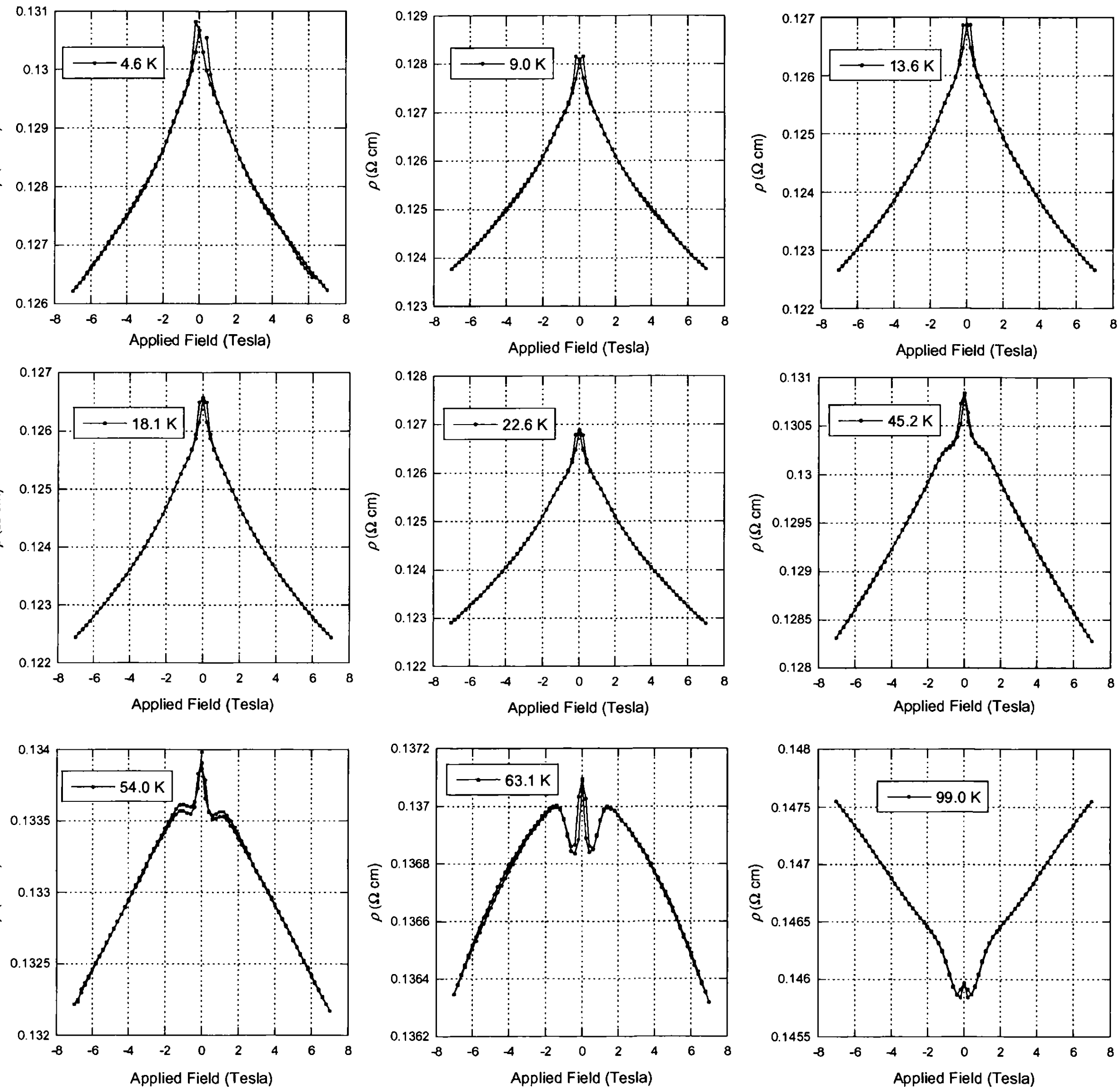

Figure 5.25 *$Cu_{0.09}Zn_{0.91}Cr_2Se_4$: Plots of resistivity vs. field at temperatures between 4.6 and 99.0 K*

At 45.2 K a shoulder appears in the resistivity versus field curve at around 0.4 Tesla which becomes more pronounced with increasing temperature to 63.1 K, where the resistance increases with field between 0.4 and 1.5 Tesla. This feature appears to be pre-empting a change to positive magnetoresistance as seen at 99.0 K. This change from negative to positive magnetoresistance mirrors that seen in $Cu_{0.05}Zn_{0.95}Cr_2Se_4$ and $ZnCr_2Se_4$, indicating that the mechanisms for magnetoresistance in these compounds are similar.

The change from negative to positive magnetoresistance is not seen in the resistivity versus temperature plots shown in figure 4.24. This is due to the fact that the resistivity versus temperature curves are influenced largely by the heating and cooling of the sample, thought to result in a reorganisation of ferromagnetic domains. This will be discussed in more detail in section 5.3.4 for $Cu_{0.25}Zn_{0.75}Cr_2Se_4$.

Figure 5.26 shows a plot of resistivity versus field for all temperatures studied. The change from negative to positive magnetoresistance can be seen, as well as the variation in zero field resistivity with temperature corresponding to the zero field resistivity versus temperature curve in figure 5.24.

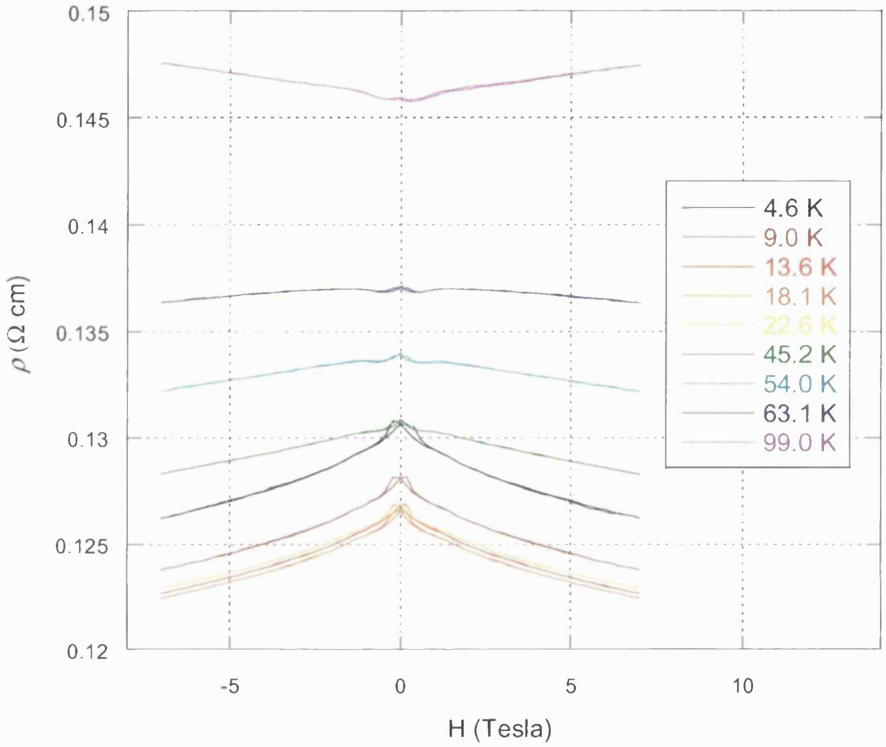

Figure 5.26 *$Cu_{0.09}Zn_{0.91}Cr_2Se_4$: Combined plot of resistivity vs. field at temperatures between 4.6 and 99.0 K*

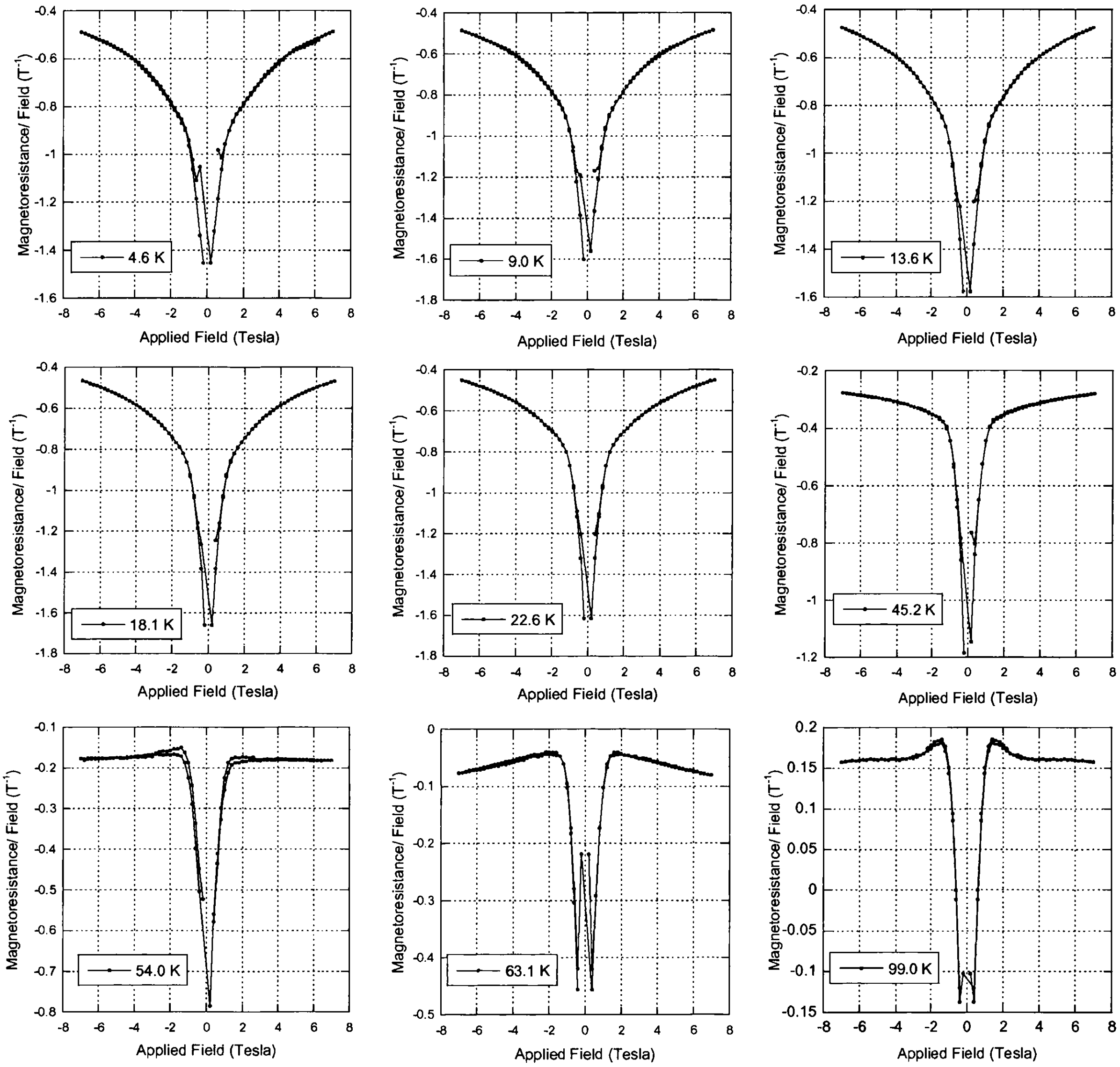

Figure 5.27 *$Cu_{0.09}Zn_{0.91}Cr_2Se_4$:Plots of magnetoresistance/field vs. field at temperatures from 4.6 to 99.0 K*

Figure 5.27 shows magnetoresistance versus field plots normalised to field. In general there seems to be a proportionally larger effect at low field than at higher fields. A negative magnetoresistance effect is seen up to 99.0 K, where there is a negative effect at low field (up to approx 0.7 T) and a positive effect at higher field. Overall the magnetoresistance effects are much smaller compared to those seen for $Cu_{0.05}Zn_{0.95}Cr_2Se_4$ and $ZnCr_2Se_4$.

5.3.4 Resistivity of $Cu_{0.25}Zn_{0.75}Cr_2Se_4$

Figure 5.28 shows the resistivity versus temperature of $Cu_{0.25}Zn_{0.75}Cr_2Se_4$ at 0, 0.5, 1, 3 and 7 Tesla. Between 0 and 20 K there is a decrease in resistivity with increasing temperature; above 20 K the behaviour appears to be typical of a metal with a metal insulator transition occurring at around 300 K for the 0 field measurement.

The values of the resistivity are several orders of magnitude smaller than seen for $Cu_{0.09}Zn_{0.91}Cr_2Se_4$ corresponding to the predicted drop in resistivity with increasing copper content across the series. These values are still much lower than those of most metals which typically have resistivities of around 10^{-7} Ωcm. Measurements of resistivity versus temperature in applied fields appear to show a large negative magnetoresistance effect across the whole temperature range, however the 3 T curve shows a lower resistance than the 7 T curve, which cast doubt on the integrity of these results.

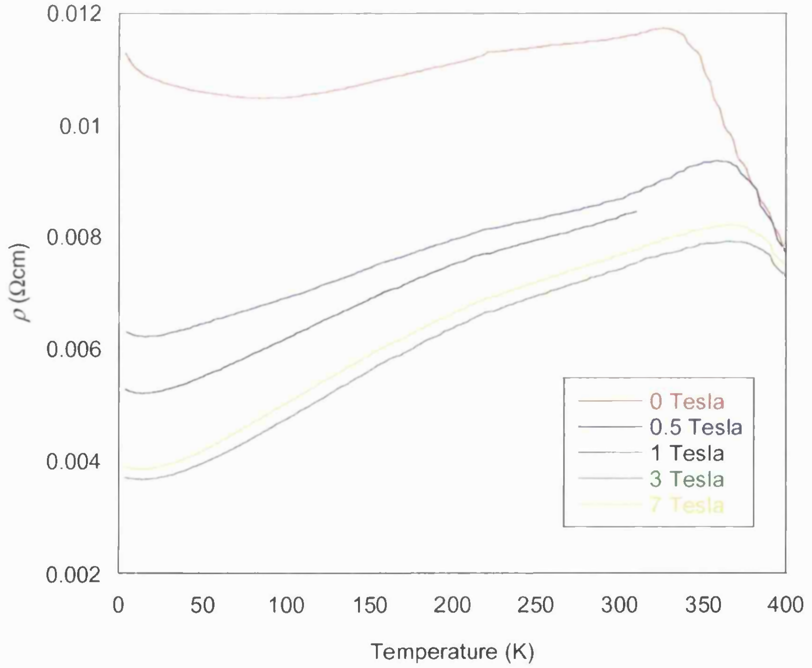

Figure 5.28 *$Cu_{0.25}Zn_{0.95}Cr_2Se_4$: Plot of resistivity vs. temperature in applied fields of 0, 0.5, 1, 3 and 7 Tesla*

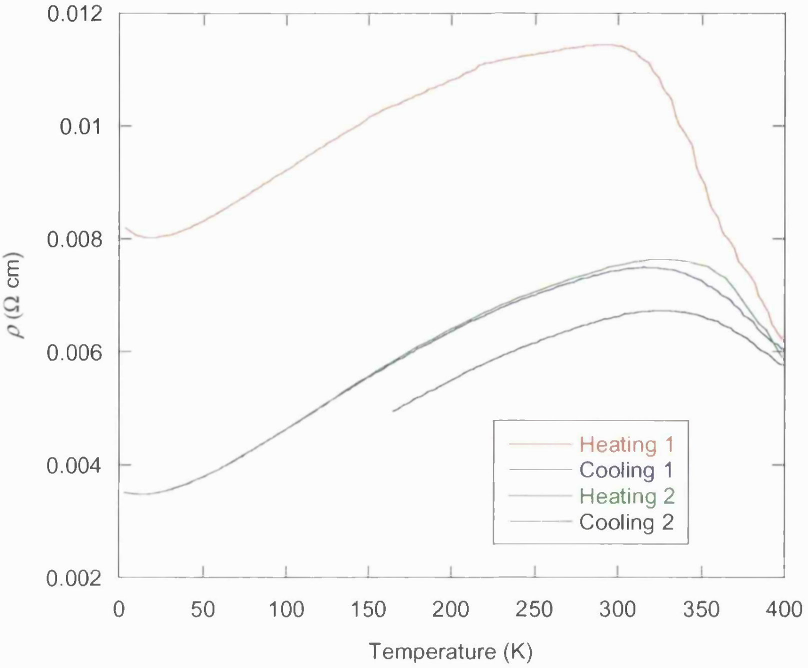

Figure 5.29 *$Cu_{0.25}Zn_{0.95}Cr_2Se_4$: Plot of resistivity vs. temperature in zero field during continuous heating and cooling cycles between 4 and 400 K.*

In order to confirm the reproducibility of the resistivity versus temperature data, the resistivity of a sample was measured during a heating and cooling cycle in zero field. The sample had not previously been exposed to large magnetic fields and the heating and cooling rate were both approximately 2 Kmin^{-1}; the results are shown in figure 5.29.

The sample was first cooled to approximately 4 K at a fast rate in zero field and then the resistivity measured as the temperature was increased at 2 Kmin^{-1} to 400 K (heating 1), to mirror the zero field measurement in figure 5.28. The behaviour shows consistency with the zero field measurement in figure 5.29, although the absolute values of resistivity are lower.

The resistivity was then measured as the sample was cooled at 2 Kmin^{-1} (cooling 1) and the results show significantly lower values of resistivity than the heating curve although the overall behaviour remains the same. On heating again (heating 2) there is no departure of the resistivity versus temperature curve from the first cooling curve at low temperature and a small difference above 150 K. The second cooling (cooling 2) shows a further drop in resistivity.

These results suggest a change in the domain structure of the material on heating to provide an easier path for the conduction electrons resulting in a lowering of the resistivity. This could be a change in the magnetic domains or the structural domains within the compounds; as both would have a significant effect on the magnetic properties it is not possible to ascertain from this data which is the most likely case. As the sample was quenched from a high temperature during synthesis, reorganisation of both structural and magnetic domains is likely on heating. The fact that there is relatively little change in resistivity at low temperature between the second cooling and heating indicates that this reorganisation of the domains only occurs at higher temperature which is to be expected.

We can therefore conclude that the resistivity versus temperature plots in various applied fields shown in figure 5.28 are not representative of a true bulk magnetoresistance effect but of the effect of cooling and heating cycles on the pressed powder sample. This phenomenon was also seen for $Cu_{0.09}Zn_{0.91}Cr_2Se_4$ in section 5.3.3. To enable the evaluation of the magnetoresistance effect in this compound we must refer to the resistivity versus field plots shown in figure 5.30.

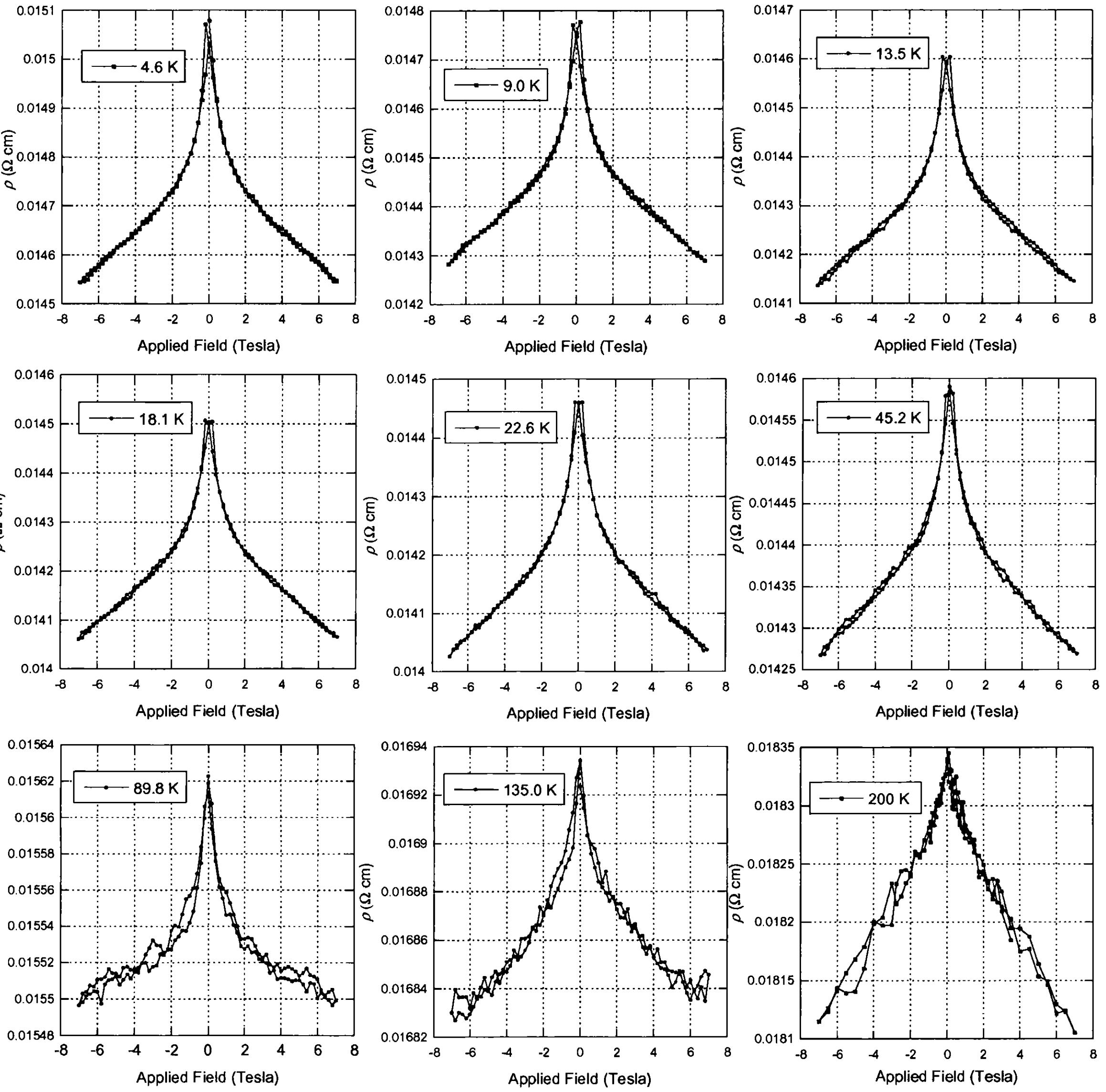

Figure 5.30 *$Cu_{0.25}Zn_{0.95}Cr_2Se_4$: Plots of resistivity vs. field at temperatures from 4.6 to 200 K.*

Figure 5.30 shows a small negative magnetoresistance effect at all temperatures studied, decreasing with increasing temperature. There is a slight hysteresis effect seen at low field for measurements up to 45.2 K. Figure 5.31 shows the resistance versus field plots for all temperatures measured; the varying degree of magnetoresistance effect can be seen as well as the variation of zero field resistivity with temperature corresponding to that seen in figure 5.29.

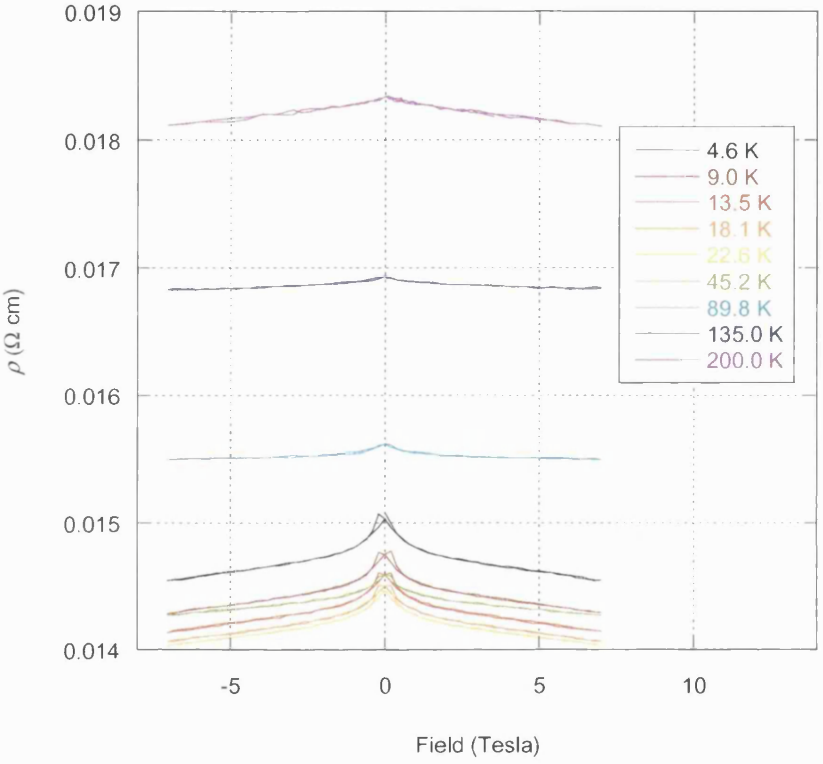

Figure 5.31 *$Cu_{0.25}Zn_{0.95}Cr_2Se_4$: Combined plot of resistivity vs. field at temperatures between 4.6 and 200 K.*

Figure 5.32 shows the magnetoresistance versus field plots, normalised to field. The magnetoresistance effect is much smaller than that seen for the other compounds studied in this series and decreases with increasing temperature. The MR effect is proportionally larger at low fields.

There is no evidence of a crossover from negative to positive magnetoresistance as seen for the other compounds studied in this series. It is possible that a crossover may occur at higher temperatures; several attempts were made to measure the resistivity versus field at temperatures above 200 K but all gave very noisy data and it was difficult to achieve temperature stability. The resistivity versus temperature curves do not suggest that there is a significant increase in magnetoresistance effect at temperatures near the metal insulator transition around 350 K as is seen in the CMR double exchange materials where changes in resistivity of several orders of magnitude are observed.

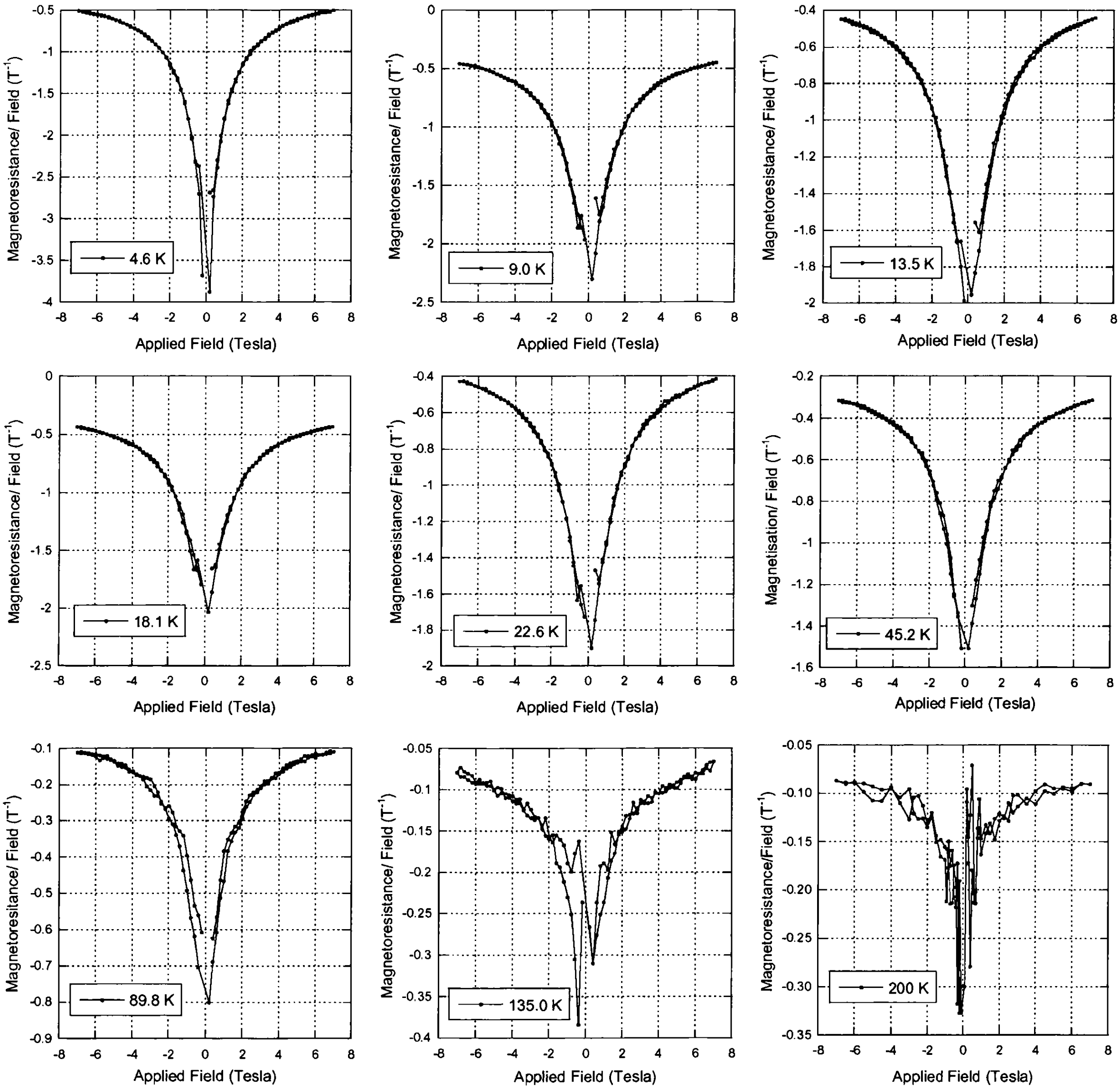

Figure 5.32 *$Cu_{0.25}Zn_{0.95}Cr_2Se_4$: Plot of magnetoresistance/field vs. field at temperatures between 4.6 and 200.0 K.*

5.4 Discussion

The electrical properties of the $Cu_{1-x}Zn_xCr_2Se_4$ series have been found to vary dramatically with x. $ZnCr_2Se_4$ is semiconducting with very high resistivity (10^9 Ωcm) at low temperature. Analysis of the resistivity versus temperature data suggests that there is thermally activated conduction involving two acceptor levels with different activation energies. This is in agreement with the findings of Groń *et. al* [1].

Magnetoresistance measurements have found a negative magnetoresistance at 67 K which changes gradually to a positive magnetoresistance effect at 99.0 K, corresponding to the change in activation energy of the semiconducting mechanism. This change of sign of the magnetoresistance suggests a change in conduction mechanism with temperature.

$Cu_{0.05}Zn_{0.95}Cr_2Se_4$ was also found to be semiconducting; the resistivity was several orders of magnitude lower than that of $ZnCr_2Se_4$. The lowering of the resistivity arises from the introduction of Cr^{4+} into the system which results in a greater number of vacancies and enhances the p-type conduction process. In addition, the presence of Cr^{4+} allows the double exchange mechanism to proceed, increasing the mobility of the carriers.

Analysis of the resistivity versus temperature data has revealed that there are two regimes of behaviour suggesting two different conduction mechanisms. At zero field, in the low temperature region (4-25 K), it was found that the resistivity was best described not by a simple semiconducting mechanism, but by the expression for variable range hopping (VRH) which is relevant to a situation where electrons near the fermi energy can tunnel between localised states. At higher temperature (40-200 K) conduction appears to occur via a typical semiconducting mechanism involving the thermal activation of carriers across a band gap. In an applied field an increasingly good fit is found to the VRH expression in the low temperature region; in the high temperature region the conduction mechanism appears to change from semiconducting to variable range hopping with increasing field.

The magnetoresistance effect in $Cu_{0.05}Zn_{0.95}Cr_2Se_4$ is much larger than that seen in $ZnCr_2Se_4$. There is a crossover from negative to positive magnetoresistance at approximately 40 K, consistent with the change in conduction mechanism from variable range hopping to semiconducting. A possible mechanism involves low temperature conduction via hopping of carriers between double exchange clusters which are likely to be present due to the known competition between ferromagnetic and antiferromagnetic interactions in this compound. Applying a field would result in an increase in the amount and size of these clusters, facilitating conduction and lowering the resistivity, hence giving a negative magnetoresistance effect. As the balance between the ferromagnetic and antiferromagnetic interactions is a delicate one in this compound (as demonstrated by the magnetic properties of high magnetisation and low field hysteresis effects) it is likely that only a small field would be needed to give a large MR effect as seen in the MR/H versus H plots.

There is also evidence from the neutron diffraction data (see chapter 7) that at zero field there is no long range ferromagnetic or antiferromagnetic order, and that the application of a magnetic field induces ferromagnetic ordering of the spins. This is consistent with the observation of a large MR effect at low temperature corresponding to the dramatic change in magnetic properties.

The mechanism for positive magnetoresistance in the high temperature region is less clear; a possible explanation is that the application of a magnetic field stabilises the ferromagnetic domains to such an extent that the energy of the chromium *d* electrons is lowered so far as to depopulate the conduction band; this is supported by the increase in band gap with field (1.07 meV from 0 to 3 Tesla) derived from the high temperature $\ln(1/\rho)$ versus 1/T plots. This would be consistent with a proportionally higher magnetoresistance effect at higher fields as the lowering in energy of the chromium band would be likely to increase with increasing field.

In $Cu_{0.09}Zn_{0.91}Cr_2Se_4$, the behaviour of the resistivity appears to be a result of a combination of competing interactions. Broadly speaking there appears to metallic behaviour below around 150 K, where the resistivity increases with temperature, and semiconducting behaviour above 150 K, where the resistivity decreases with temperature. The transition from a negative to positive MR effect does not seem to correspond to a change in the behaviour of the resistivity, although it is likely that the mechanisms for the MR effect are the same as those for $Cu_{0.05}Zn_{0.95}Cr_2Se_4$. The transition from a negative to a positive effect appears to occur over a much broader temperature range than for $Cu_{0.05}Zn_{0.95}Cr_2Se_4$; this would be consistent with the presence of competing conduction mechanisms whose influence over the bulk electronic behaviour changes over a wide temperature range. In the metallic region, the double exchange mechanism is likely to be dominant which is consistent with the negative magnetoresistance effect below 99 K; at higher temperatures increased thermal motion would give increased scattering of the spin polarised conduction electrons resulting in the double exchange mechanism breaking down.

The magnetoresistance effect is much smaller for $Cu_{0.09}Zn_{0.91}Cr_2Se_4$ than for $ZnCr_2Se_4$ and $Cu_{0.05}Zn_{0.95}Cr_2Se_4$ in both the positive and negative MR regimes. In the negative MR regime this would suggest that either a field cannot significantly increase the size of the ferromagnetic domains as the disorder in the system is too great, or that the ferromagnetic domains are already large and have reached a saturation point. Magnetisation measurements (reported in chapter 4) have found that $Cu_{0.09}Zn_{0.91}Cr_2Se_4$ has a higher magnetisation at 7 Tesla than $Cu_{0.05}Zn_{0.95}Cr_2Se_4$ so the first explanation seems unlikely. However the magnetisation of $Cu_{0.09}Zn_{0.91}Cr_2Se_4$ does not saturate until about 7 tesla so the second explanation would also appear to be invalid. Both explanations would also be inconsistent with the observed feature of a proportionally greater MR effect at lower field.

$Cu_{0.25}Zn_{0.75}Cr_2Se_4$ shows only a negative magnetoresistance effect, this is consistent with the compound being a double exchange ferromagnet over the whole temperature range studied. The MR effect observed here is smaller than that seen for all other compounds studied in this series which is consistent with $Cu_{0.09}Zn_{0.91}Cr_2Se_4$ showing a smaller effect than $Cu_{0.05}Zn_{0.95}Cr_2Se_4$. This reduction in MR effect corresponds to a decrease in resistivity of the samples. It may be that in $Cu_{0.09}Zn_{0.91}Cr_2Se_4$ and $Cu_{0.25}Zn_{0.75}Cr_2Se_4$ the conductivity at zero field is already high and that an increase in the size of the ferromagnetic domains induced by the application of a magnetic field cannot significantly increase the conductivity, hence resulting in a smaller MR effect. As it was not possible to measure the MR of $Cu_{0.25}Zn_{0.75}Cr_2Se_4$ accurately at high temperature it cannot be ruled out that a double exchange CMR effect may occur near T_C (~ 380 K). In the double exchange perovskite manganates the CMR effect is seen just above T_C where the application of a magnetic field re-aligns the spins of the manganese t_{2g} electrons, enabling an increase in conductivity. This mechanism is described in more detail in the introduction, section 1.5.2.1.

The magnetoresistance effects seen in the $Cu_{1-x}Zn_xCr_2Se_4$ series appear to differ greatly from those seen in the well known double exchange MR materials, such as $La_{1-x}Ca_xMnO_3$. In these compounds the MR effect is seen near to T_C only whereas the MR effects found here in the $Cu_{1-x}Zn_xCr_2Se_4$ series do not seem to centre around a magnetic transition. It is clear that the mechanism for the double exchange in these compounds differs from that of the CMR perovskites and does not relate to a metal insulator transition.

It has been suggested here that the large negative magnetoresistance effect in $Cu_{0.05}Zn_{0.95}Cr_2Se_4$ exists in a temperature range where conduction occurs via the variable range hopping mechanism. Magnetoresistance has been observed in variable range hopping conduction in many systems including CdSe [12], InP [13], Cu_2GeSe_3 [14] and Cr_2Se_{3-x} [15]. Both positive and negative effects have been observed as the VRH mechanism can apply to a variety of situations and no one mechanism of MR can be applied.

5.5 References

1. Groń, T., Duda, H., and Warczewski, J., *J. Phys-Paris*, 1988. **49**(12): p. 869.
2. Khan, M.N., Venkatachalam, A., Ahmad, A., and Darshane, V.S., *J. Mater. Sci.*, 1990. **25**: p. 595-598.
3. Krok-Kowalski, J., Warczewski, J., and Nikiforov, K., *J. Alloy. Compd.*, 2001. **315**: p. 62-67.
4. Groń, T., Duda, H., and Warczewski, J., *Phys. Rev. B*, 1990. **41**(18): p. 12424.
5. Groń, T., *Phil. Mag. B*, 1994. **70**: p. 121-132.
6. Watanabe, H., *J. Phys. Soc. Jpn.*, 1974. **37**: p. 140.
7. Tsurkan, V. and Radaustan, S.I., *Jpn. J. Appl. Phys.*, 1993. **32**(32-2): p. 313-315.
8. Lotgering, F.K. and van Stapele, R.P., *J. Appl. Phys.*, 1968. **39**(2): p. 417-423.
9. Robbins, M., Lehmann, H.W., and White, J.G., *J. Phys. Chem. Solids*, 1967. **28**: p. 897.
10. Zener, C., *Phys. Rev*, 1951. **82**: p. 403-405.
11. Mott, N.F. and Davis, E.A., *Electronic processes in non-crystalline materials*. The international series of monographs on physics, ed. W. Marshall and D.H. Wilkinson. 1971, Oxford: Clarendon Press.
12. Finlayson, D.M., *J. Phys.-Condes. Matter*, 1994. **6**(40): p. 8277-8283.
13. El Kaaouachi, A., Nafidi, A., and Biskupski, G., *Semicond. Sci. Technol.*, 2003. **18**(2): p. 69-74.
14. Marcano, G. and Marquez, R., *J. Phys. Chem. Solids*, 2003. **64**(9-10): p. 1725-1727.
15. Vaqueiro, P., Powell, A.V., Coldea, A.I., Steer, C.A., Marshall, I.M., Blundell, S.J., Singleton, J., and Ohtani, T., *Phys. Rev. B*, 2001. **64**: p. 132402-1-132402-4.

Chapter 6 High Pressure AC Susceptibility Measurements

6.1 Introduction

High-pressure studies of solid state materials can enable a unique insight into chemical interactions within the material whilst the chemical composition remains unchanged. Various properties of spinel compounds have been studied at high pressure.

Pressure induced phase transitions involving a Jahn-Teller type distortion from a cubic to tetragonal structure have been identified in some oxide spinels, such as $ZnMn_2O_4$, $NiMn_2O_4$ and $ZnTi_2O_4$[1-3]. This transition occurs at approximately 23 GPa. In the compound $CdCr_{2-x}Ga_xSe_4$ ($x = 0$, 0.06, and 0.12) a tetragonal distortion of the ambient pressure face centred cubic (fcc) unit cell is seen at applied pressures of 10 GPa. [4] It is suggested that a structural transition is observed at much lower applied pressures in selenide spinels than in oxide spinels due to the greater compressibility of these compounds. The zero-pressure bulk moduli of all the oxide spinels studied have been found to be approximately 200 GPa. The consistency in these values is thought to be due to the formation of a nearly close-packed fcc substructure by the oxygen ions which occupies most of the volume in the unit cell. Therefore the overall compressibility of these compounds is dictated primarily by the oxygen ions and it is reasonable to assume that the same principle may be applied to the selenide spinel compounds. The bulk modulus of the $CdCr_{2-x}Ga_xSe_4$ compounds studied is approximately 100 GPa, giving them a higher compressibility than the oxide spinels; this is also indicated by the lower ionicity and greater metallic character of the chemical bonding in the selenides.

As well as structural changes, other properties of spinel compounds have been found to show pressure dependence. The metal-insulator transition temperature of $CuIr_2S_4$ has been found to increase at a rate of 2.8 K per kbar (0.1 GPa) with the transition becoming less well defined at higher pressures [5]. No structural transition was observed to accompany these changes in transition temperature.

High-pressure studies of the Curie temperature of a selection of chalcogenide spinels have been carried out by Kanomata *et al.* [6-8] It was found that the pressure dependence of the T_C of the ferrimagnetic spinels (such as $FeCr_2S_4$ and $CoCr_2S_4$) is negative whereas that of the ferromagnetic spinels (such as $CdCr_2Se_4$ and $HgCr_2Se_4$) is positive. This phenomenon was attributed to the different types of interaction taking place within the compounds. In the case of the ferrimagnetic ACr_2S_4 compounds the strongest magnetic exchange interaction is a 125° A-S-B superexchange interaction between the nearest neighbour A (Fe, Co) and Cr ions. Therefore it is probable that this interaction is chiefly responsible for the pressure dependence of the Curie temperature as a change in the superexchange angle will significantly alter the magnitude of the exchange.

In the ferromagnetic chalcogenide spinels the magnetic behaviour is characterised by a combination of a near-neighbour ferromagnetic interaction and a distant neighbour antiferromagnetic superexchange interaction taking place between the Cr^{3+} ions. These interactions can also be considered in terms of a near neighbour ferromagnetic 90° Cr^{3+}-$X^{2-}Cr^{3+}$ superexchange interaction (where X is S or Se) and an antiferromagnetic exchange due to the direct overlap of the Cr^{3+} ion d-orbitals. This direct antiferromagnetic exchange increases rapidly with increasing Cr^{3+} orbital overlap and therefore this is thought to be the main influence in the pressure dependence of the Curie temperature in these compounds.

It is hoped that by studying the AC Susceptibility of compounds in the series $Cu_{1-x}Zn_xCr_2Se_4$ under high-pressure conditions it may be possible to learn more about the magnetic interactions taking place. As substitution of zinc for copper in the series results in an increase in lattice parameter, it may be expected that applying pressure would have an analogous effect on the magnetic properties as removing zinc from the structure. It may even be possible to induce the transition from ferromagnetism to antiferromagnetism (or vice versa) by applying pressure as well as by chemical substitution.

6.2 Experimental

All high-pressure measurements discussed in this chapter were carried out in the Physics Department of Washington University in St Louis, Missouri, using equipment belonging to the Schilling group. Experiments were carried out with the assistance of Takahiro Tomita and Professor James Schilling.

6.2.1 The Helium System

There are three basic methods of applying pressure in a system: hydrostatic pressure, uniaxial stress and quasihydrostatic pressure. Hydrostatic pressure can be applied using a liquid or gas as the pressure medium, resulting in compression of the sample without plastic deformation. Uniaxial stress, normally used for single crystals, can be achieved by subjecting the sample to a uniaxial compressive or tensile force, sufficiently small so as not to exceed the elastic limit of the material. The third method, quasihydrostatic pressure, uses a solid pressure medium that transmits both uniaxial and hydrostatic stress. This results in both plastic deformation and the introduction of defects into the sample.

In the case of AC susceptibility measurements, hydrostatic or uniaxial methods are normally used. Quasihydrostatic techniques are less suitable as embedding the coil system in a solid pressure medium can cause a change in geometry. This can effect the secondary-coil compensation and often results do not compare well with theoretical models. The hydrostatic method is normally the most desirable as no deformation of the sample occurs. The pressure generated by compression of a fluid is always hydrostatic and may remain nearly hydrostatic after the fluid has solidified below the melting point. As helium has the lowest melting point of any known fluid, it is possible to achieve purely hydrostatic measurements over a very wide temperature range. Although He-3 has a lower melting point at a given pressure than He-4 and would therefore make a more desirable pressure medium, it is rarely used due to the great expense.

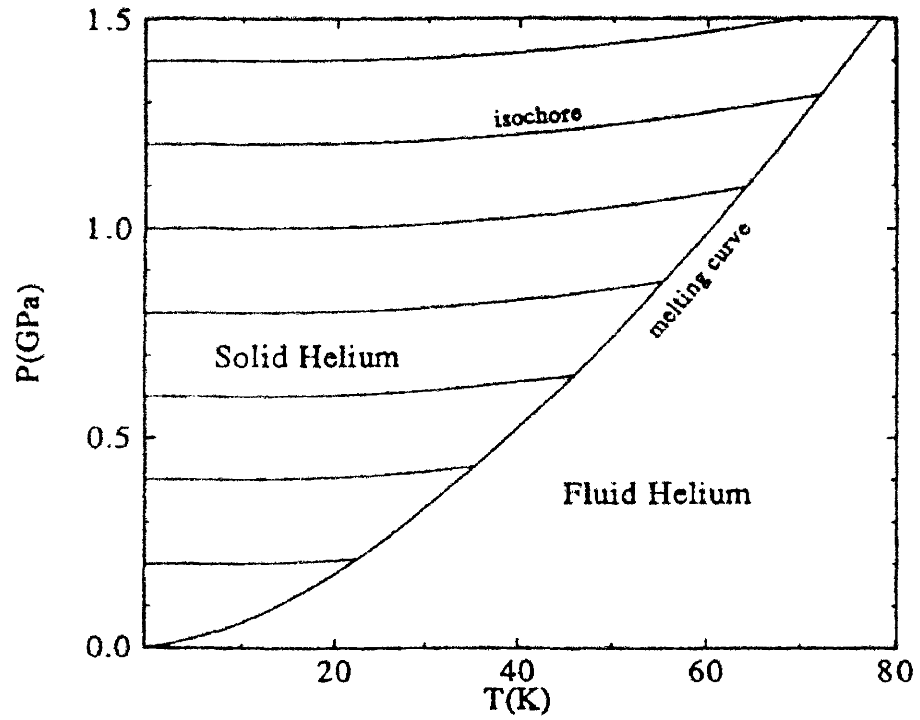

Figure 6.1 *The melting curve and isochores of solid He^4*

The melting curve and isochores for helium are shown in figure 6.1. Solid helium also exhibits a smaller pressure loss along an isochore from the freezing temperature than any other solid, due to the fact that most of the internal pressure in helium arises from zero point vibrations and hence is relatively insensitive to changes in temperature. [9]

6.2.2 The Helium-Gas Compressor System

Shown in figure 6.2 is a schematic diagram of the helium-gas compressor system, consisting of a 2-stage compressor unit which pressurizes helium inside a cylindrical autoclave.

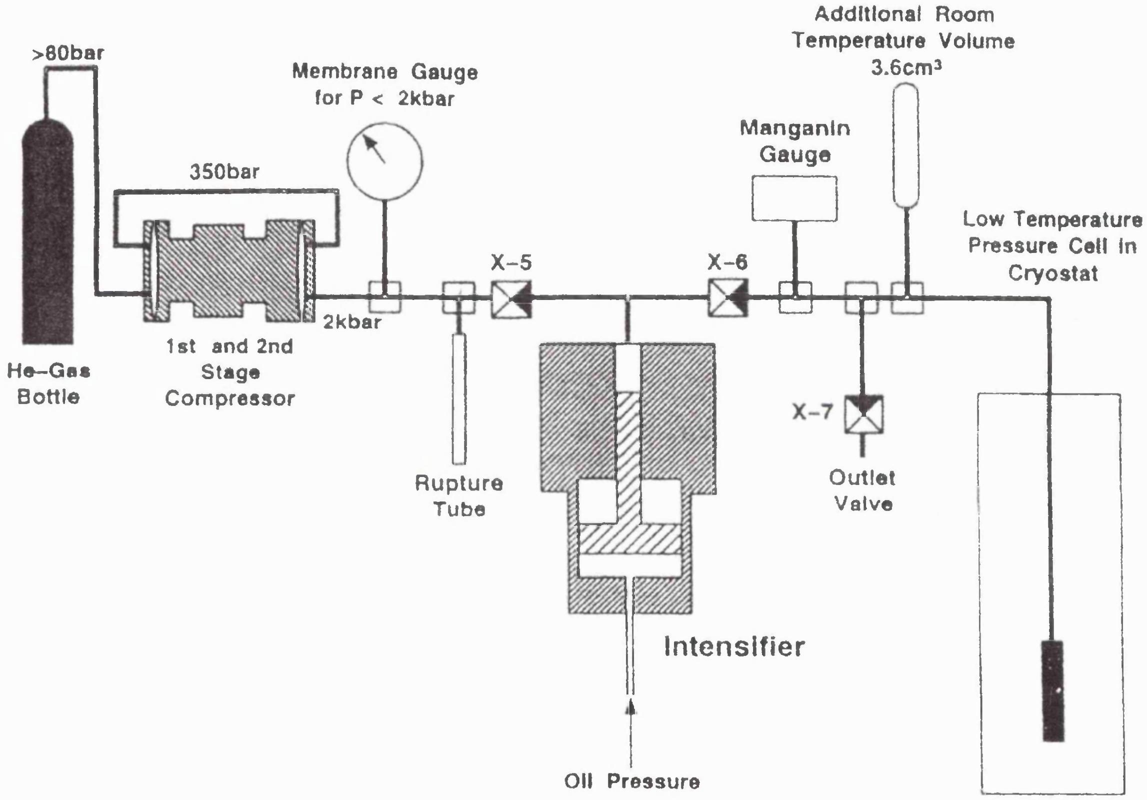

Figure 6.2 *Schematic diagram of the helium-gas compressor system*

Helium is fed into the 2-stage compressor, which generates a pressure of 0.17 GPa throughout the whole system after which valve X-5 is closed. The intensifier (driven by oil pressure) then compresses the helium further to a pressure of up to 1.4 GPa. The pressure is then transmitted to the pressure vessel via a flexible Cu-Be capillary with outer diameter 3 mm and inner diameter 0.3 mm. This enables the pressure cell to be placed in a variety of cryostats for temperature variation. A diagram of the pressure cell is shown in figure 6.3.

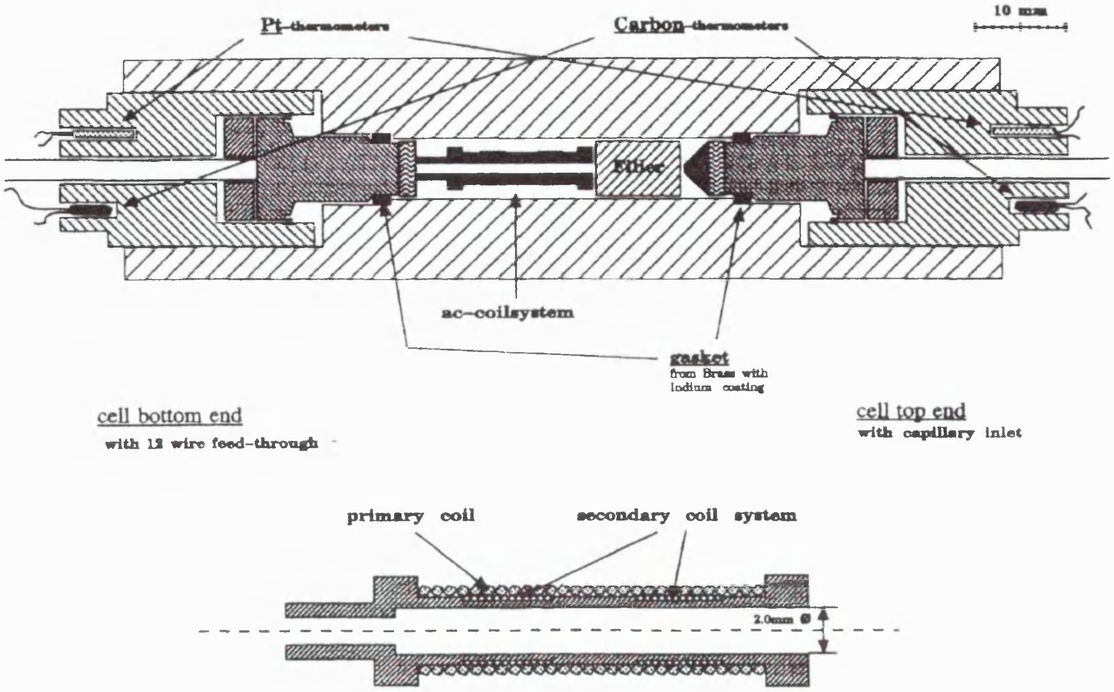

Figure 6.3 *Diagram of the Cu-Be pressure cell with enlargement of the AC coil system*

At the bottom end of the pressure cell there is a 12-wire reusable feed through which the electrical connections to the coil system are passed. Calibrated carbon and 100 Ω (RT) platinum resistors are mounted at both ends of the vessel to enable an accurate determination of the sample temperature throughout the measurement.

It is possible to change the pressure inside the Cu-Be vessel at any temperature or pressure at which the helium is liquid. At ambient pressures the helium remains fluid at all temperatures and at the maximum pressure for the system (1.4 GPa) the helium freezes at 75 K. Therefore it is possible to make hydrostatic pressure changes over a broad range of temperatures and pressures using this system.

When the helium has frozen, the conditions remain generally hydrostatic. Care must be taken to ensure that the helium freezes from the bottom of the pressure cell upwards so that the freezing helium is always in contact with the fluid helium. This avoids any non-uniform pressure changes as the helium contracts on freezing. Large pressure changes on freezing are partially avoided by the use of an additional room temperature volume (see figure 6.2) but as the volume is not infinite there remains a small change, in the case of this system less than 1%.

6.2.3 Low temperature

Low temperature was achieved using a closed cycle helium refrigerator. Helium is compressed to a pressure of 250 Psi and driven from the compressor to a 'coldhead' which is cooled by the rapid expansion of the helium gas. The helium is then returned to the compressor and the cycle is repeated. The coldhead is coupled to the sample chamber by a thick copper connection maintained under high vacuum. The sample tube is filled with helium gas to transmit cooling power to the pressure cell. Using this method, temperatures as low as 6.5 K can be easily achieved.

6.2.4 The AC Susceptibility Coil System

The AC susceptibility coil system used in this study consists of two compensated secondary coils each comprising of 485 turns of 30 μm diameter Cu wire, surrounded by the primary coil comprising of 740 turns of 60 μm diameter Cu wire. The sample is placed inside one of the secondary coils. A circuit diagram for the AC susceptibility and temperature measurement systems is shown in figure 6.4.

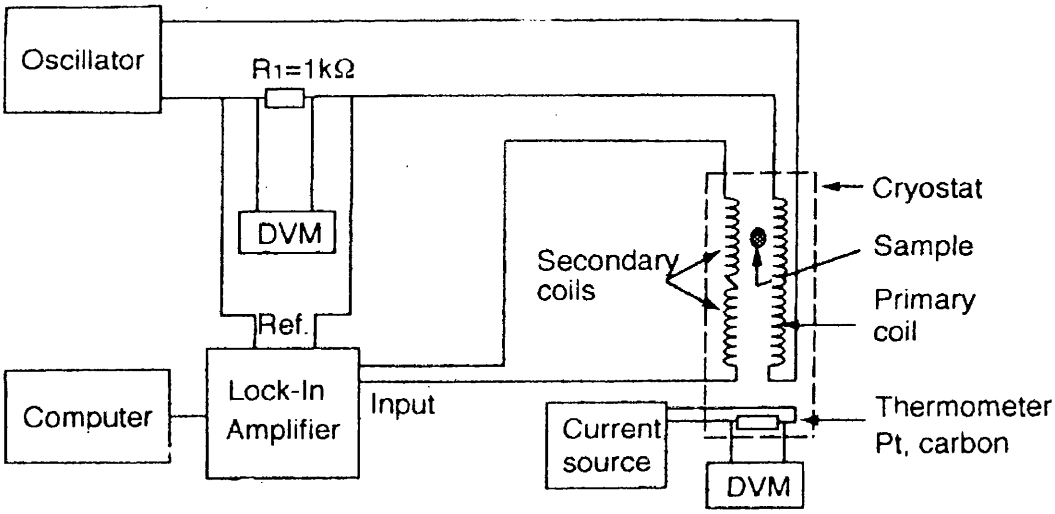

Figure 6.4 *Circuit diagram of the AC susceptibility and temperature measurement system*

An excitation current of several mA is generated through R_1 and the primary coil by a highly stable constant-current oscillator (Optimation Inc, model RCD-9). The signal from the compensated secondary coils is detected by the dual phase lock-in amplifier (Stanford

Research Model 530). The voltage drop across R_l serves as a reference voltage for the lock-in and allows an accurate determination of the excitation current. In order to obtain absolute values for χ' and χ'' the system must be calibrated by taking into account the exact geometry of the coil and the superconducting transition of a lead sphere. [10] This system has not been calibrated and therefore it is not possible to obtain specific values of susceptibility from the measurements, but as the accuracy of the calibration is only 10% it would not have been sufficient for this type of experiment anyway. The theory of the AC susceptibility technique is discussed in more detail in chapter 2 of this thesis, section 2.3.6.2.

6.3 Results

The AC susceptibility of samples from the series $Cu_{1-x}Zn_xCr_2Se_4$ was measured (where $x = 0.8$, 0.85, 0.90, 0.905, 0.91 and 0.92) at ambient pressure and applied pressures of up to 6 kbars. For all measurements a field of 5 gauss and a frequency of 200 Hz were used and the sensitivity of the lock-in amplifier was 500mV. After the high pressure measurements had been taken each sample was re-measured at ambient pressure to check the reproducibility of the ambient susceptibility curve.

6.3.1 Pressure Dependence of χ

Figures 6.5 to 6.11 show the temperature dependence of the AC susceptibility of compounds in the series $Cu_{1-x}Zn_xCr_2Se_4$ at ambient and applied pressures of up to 6 kbars. The χ' data only has been shown in all cases for clarity; no additional information was found from the χ'' curves.

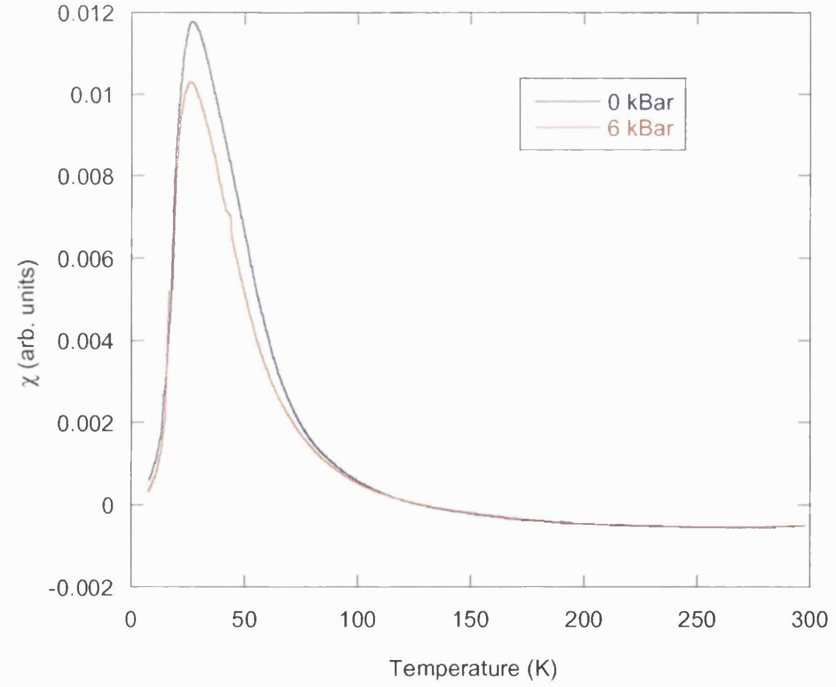

Figure 6.5 *AC susceptibility vs. temperature of* $Cu_{0.08}Zn_{0.92}Cr_2Se_4$ *at 0 and 6 kbar*

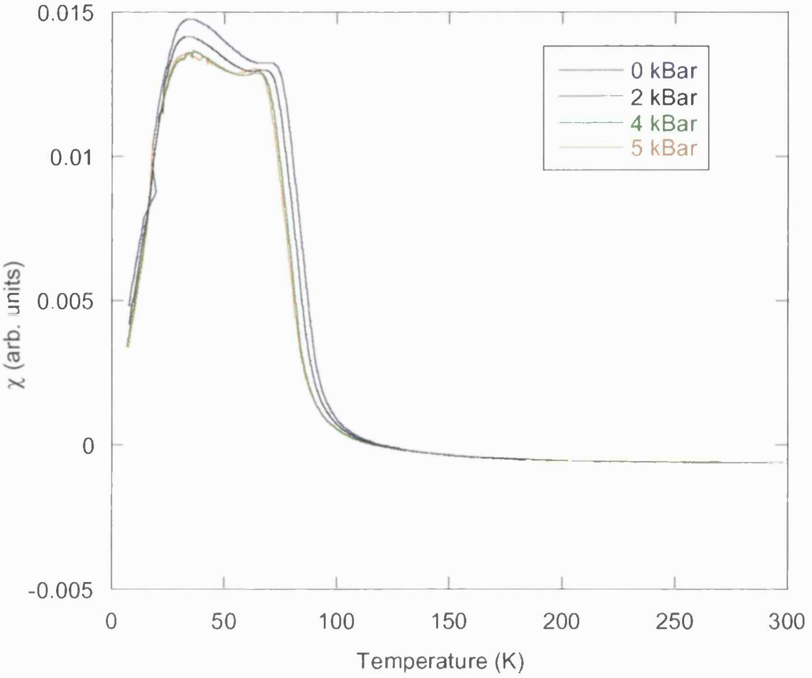

Figure 6.6 *AC susceptibility vs. temperature of* $Cu_{0.09}Zn_{0.91}Cr_2Se_4$ *at 0, 2, 4 and 5 kbar*

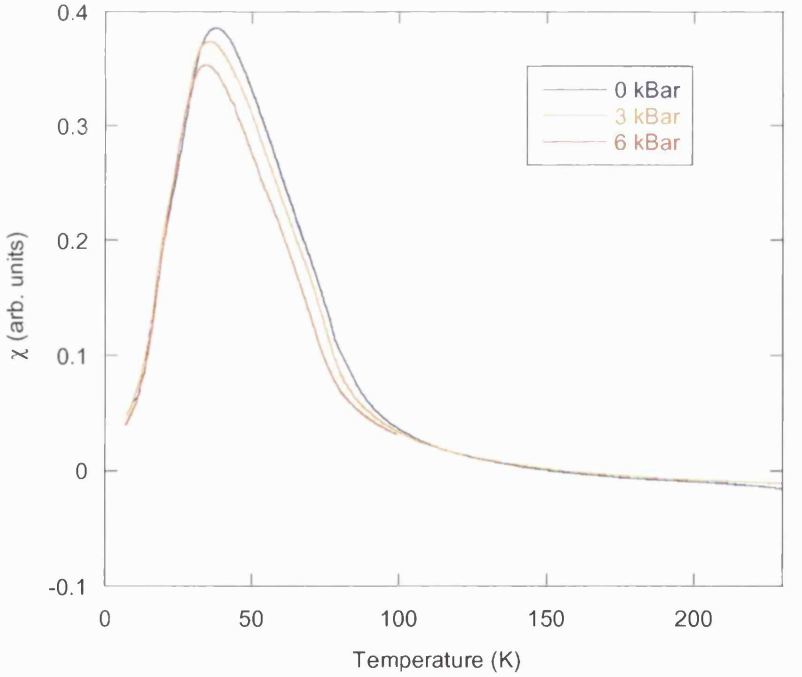

Figure 6.7 *AC susceptibility vs. temperature of* $Cu_{0.095}Zn_{0.905}Cr_2Se_4$ *at 0, 3 and 6 kbar*

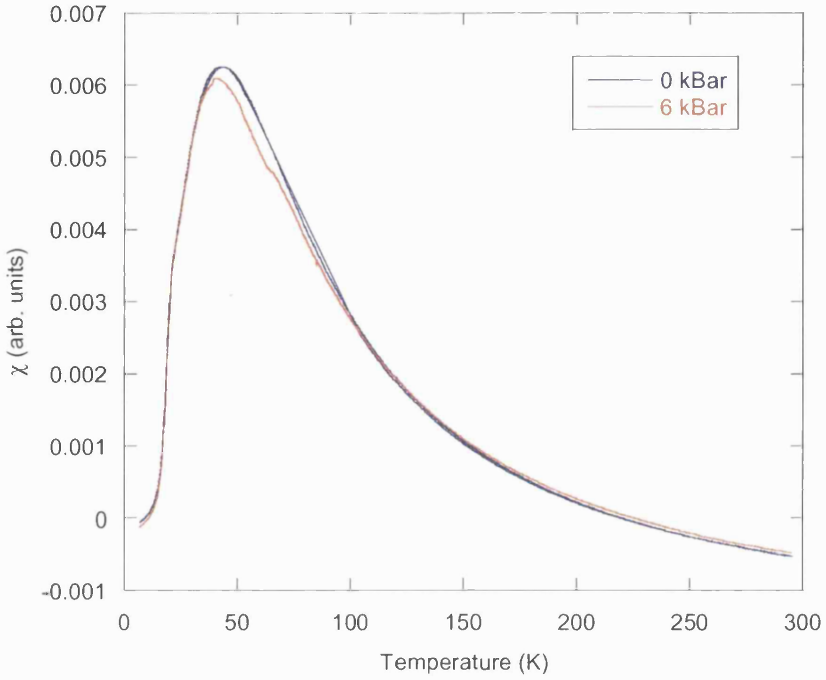

Figure 6.8 *AC susceptibility vs. temperature of* $Cu_{0.10}Zn_{0.90}Cr_2Se_4$ *at 0 and 6 kbar*

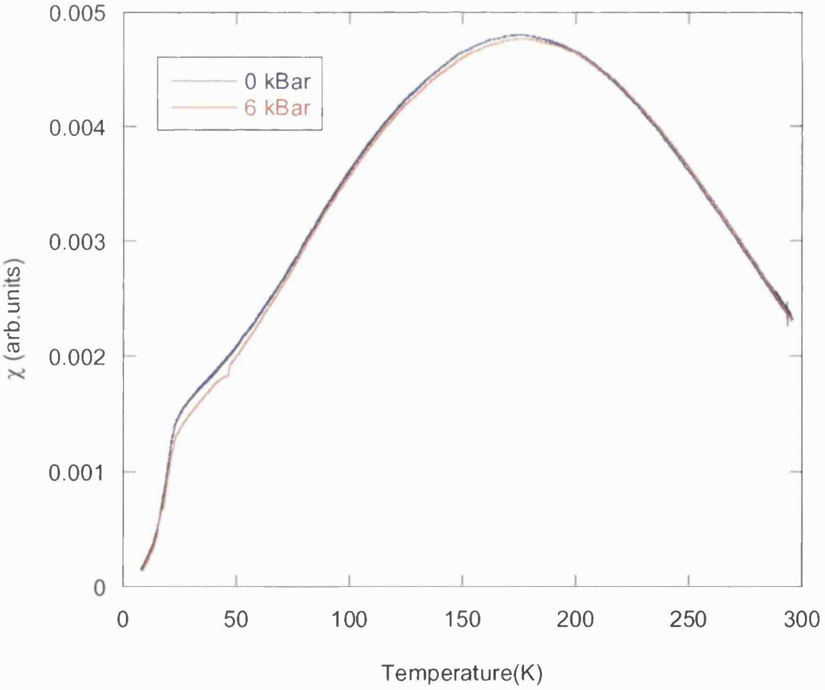

Figure 6.9 *AC susceptibility vs. temperature of* $Cu_{0.15}Zn_{0.85}Cr_2Se_4$ *at 0 and 6 kbar*

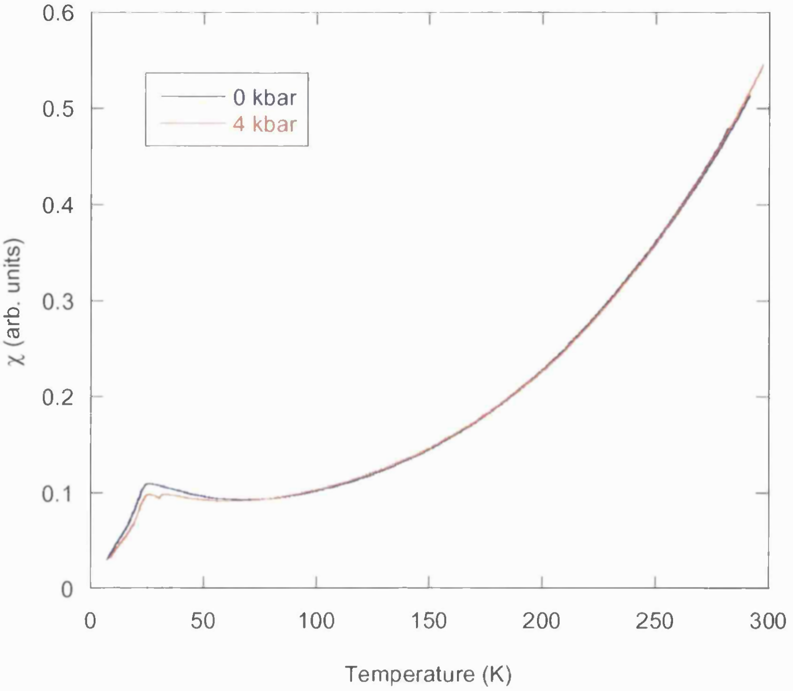

Figure 6.10 *AC susceptibility vs. temperature of* $Cu_{0.20}Zn_{0.80}Cr_2Se_4$ *at 0 and 4 kbar*

In all of the compounds studies there appears to be a reduction of the transition temperature and the magnitude of the susceptibility with increasing applied pressure. In the compounds $Cu_{0.20}Zn_{0.80}Cr_2Se_4$ and $Cu_{0.15}Zn_{0.85}Cr_2Se_4$ the low temperature transition is studied; this is thought to be a transition from a ferromagnetic to a non-collinear antiferromagnetic state and is also observed in the DC magnetisation measurements (see chapter 4 of this thesis).

In the χ' versus temperature plot of $Cu_{0.09}Zn_{0.91}Cr_2Se_4$ there is a second transition seen at around 80 K which was not observed in the DC magnetisation study of this compound, discussed in chapter 4 of this thesis. This behaviour resembles that seen in the AC measurements of $Cu_{0.05}Zn_{0.95}Cr_2Se_4$ where a second transition emerges in high frequency (10 kHz) when fields of over 100 Gauss are applied (see chapter 4 , section 4.3.4). However, as the measurements reported here were performed in low frequency (200 Hz) and low fields (5 Gauss), it is unclear why this second transition should appear in $Cu_{0.09}Zn_{0.91}Cr_2Se_4$. The lower temperature transition has been used here to study the effect of pressure to give consistency with the other compounds under investigation.

Figure 6.11 summarises the variation in transition temperature with applied pressure of the compounds investigated. The transition temperature was determined by differentiating χ with respect to temperature and taking the point where dχ/dT = 0. It was not possible to establish a transition temperature for $Cu_{0.15}Zn_{0.85}Cr_2Se_4$ in this manner as there is no maximum in the susceptibility at the transition temperature.

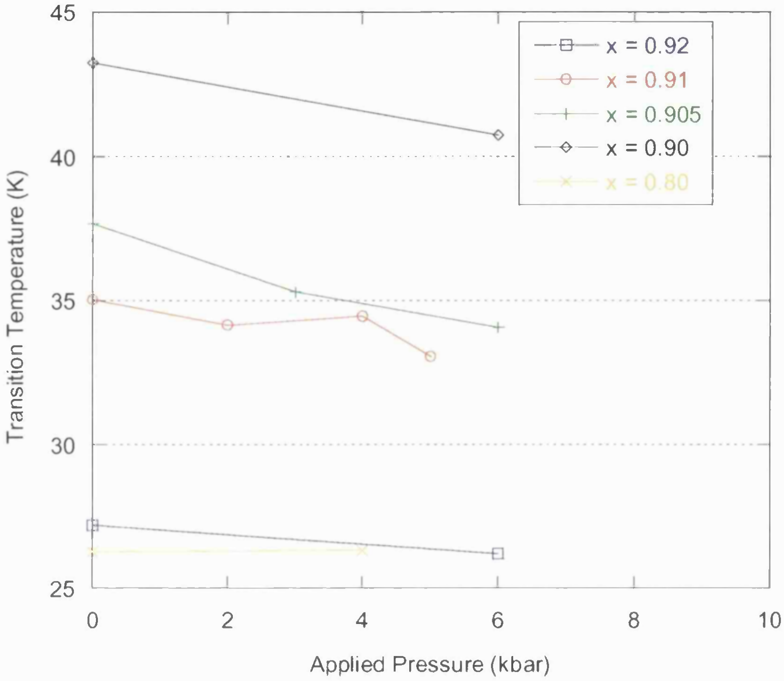

Figure 6.11 *Variation of transition temperature with applied pressure for compounds in the series* $Cu_{1-x}Zn_xCr_2Se_4$

It can be seen that, for all compounds studied, there is a reduction in transition temperature accompanied by a reduction in magnitude of the susceptibility around the transition temperature. This effect is much greater in compounds with $x \geq 0.9$, where the magnetic behaviour is predominantly antiferromagnetic. Figure 6.12 shows the variation of the transition temperature with composition and applied field for compounds in this region of the series.

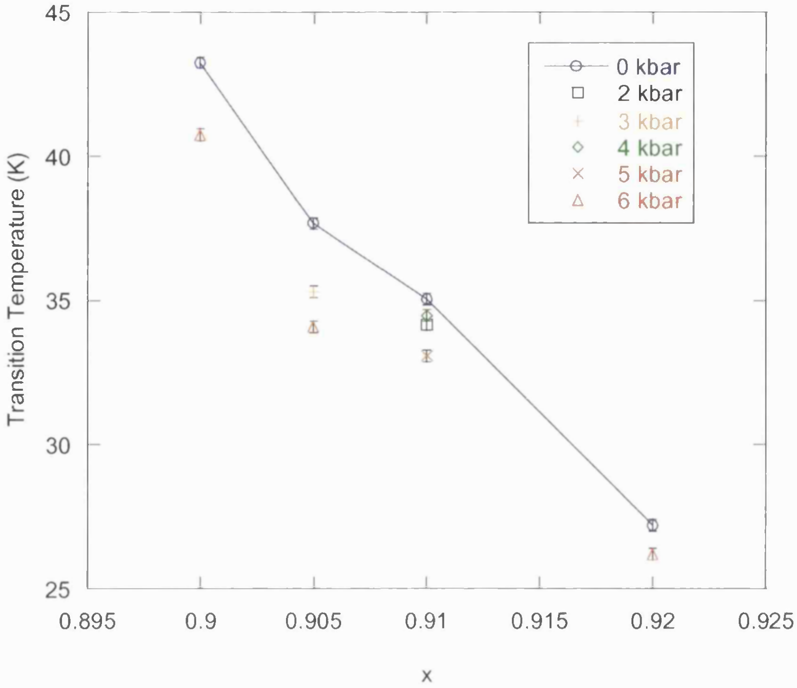

Figure 6.12 *Variation of transition temperature with composition and applied field for compounds in the series* $Cu_{1-x}Zn_xCr_2Se_4$

The results show an approximately linear relationship of composition with transition temperature. The decrease in transition temperature with applied pressure appears to be systematic with the exception of the 4 kbar measurement of $Cu_{0.09}Zn_{0.91}Cr_2Se_4$. This is likely to be due to the fact that the transition temperature in this compound coincided with the melting point of He^4 at 4 kbar. As discussed in section 6.2.2, heaters on the top and bottom of the pressure cell must be employed whilst the helium is melting or freezing to ensure a uniform pressure distribution. This process can unfortunately result in inaccurate temperature readings around the melting point and also lead to anomalies in the susceptibility curves. This can be seen quite clearly in the 4 kbar curves in figures 6.6 and 6.10. This effect can also be seen in some of the 6 kbar curves, but this is less problematic as the melting point of He^4 at 6 kbar is approximately 45 K which is well above the transition temperature for most of the compounds discussed in this chapter.

6.3.2 Pressure Dependence of χ^{-1}

Figures 6.13 to 6.16 show the χ^{-1} vs. temperature curves for samples with $x \geq 0.9$.

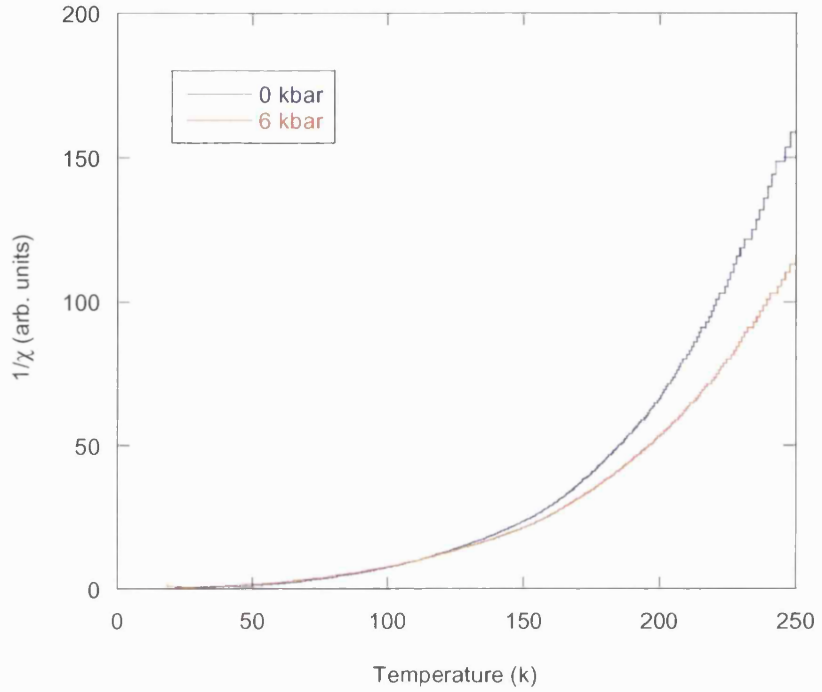

Figure 6.13 *Inverse susceptibility vs. temperature of* $Cu_{0.08}Zn_{0.92}Cr_2Se_4$ *at 0 and 6 kbar*

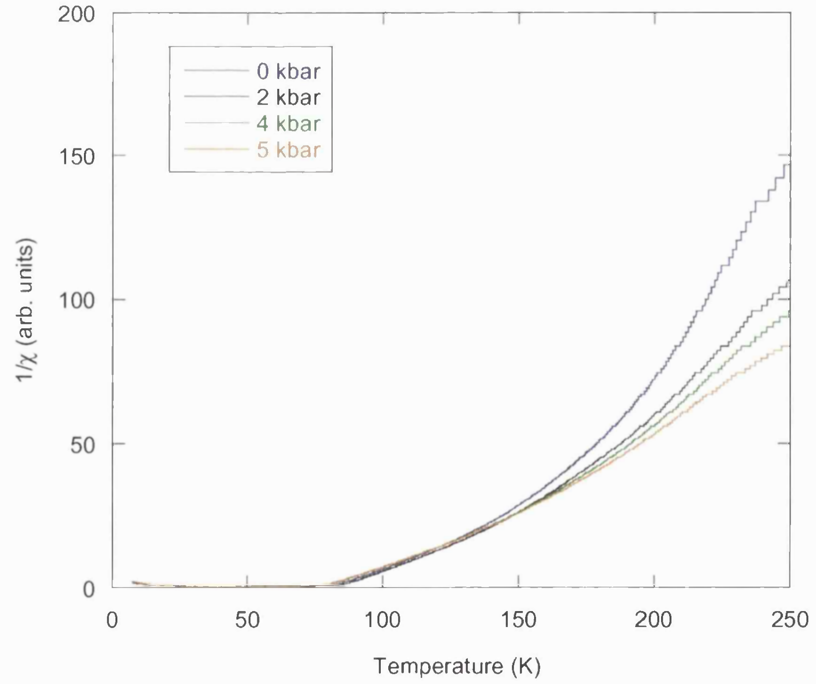

Figure 6.14 *Inverse susceptibility vs. temperature of* $Cu_{0.09}Zn_{0.91}Cr_2Se_4$ *at 0, 2, 4 and 5 kbar*

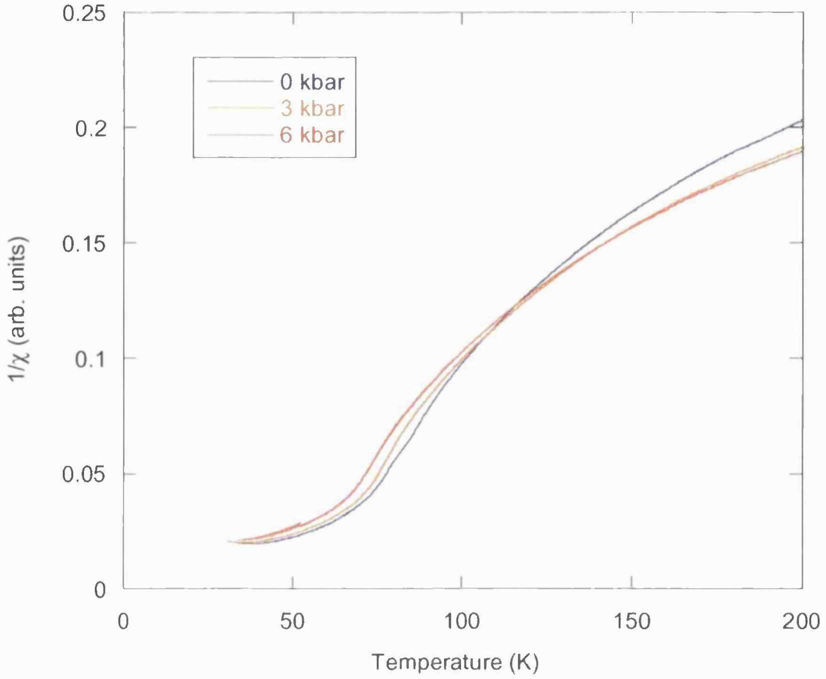

Figure 6.15 *Inverse susceptibility vs. temperature of* $Cu_{0.095}Zn_{0.905}Cr_2Se_4$ *at 0, 3 and 6 kbar*

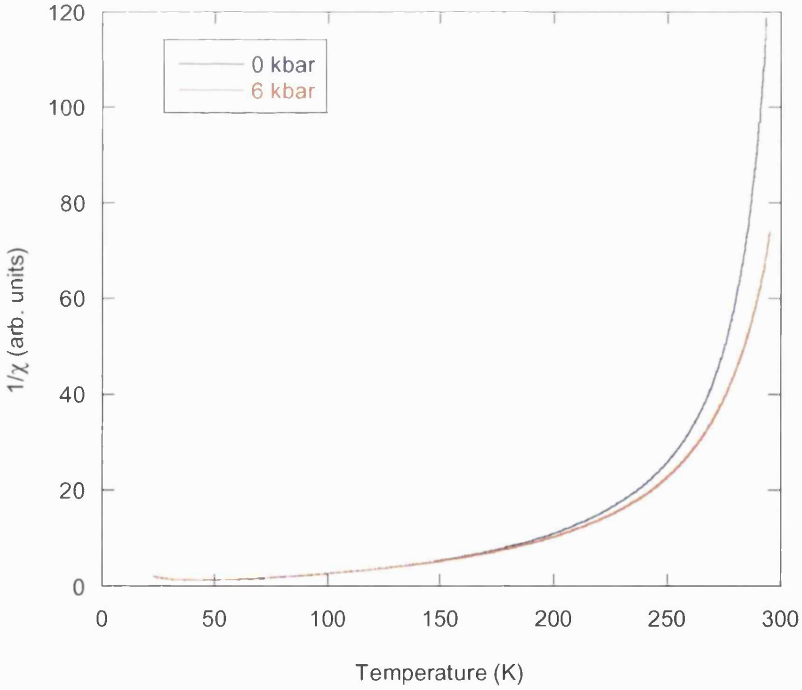

Figure 6.16 *Inverse susceptibility vs. temperature of* $Cu_{0.10}Zn_{0.90}Cr_2Se_4$ *at 0 and 6 kbar*

At ambient pressure, only $Cu_{0.08}Zn_{0.92}Cr_2Se_4$ showed a sufficient linear region in the $1/\chi$ versus temperature curve to be fitted to the Curie Law. This was also found from the

DC magnetisation measurements discussed in chapter 4. The fits of the linear regions of the curves to the curie law of are shown in figures 6.17 and 6.18.

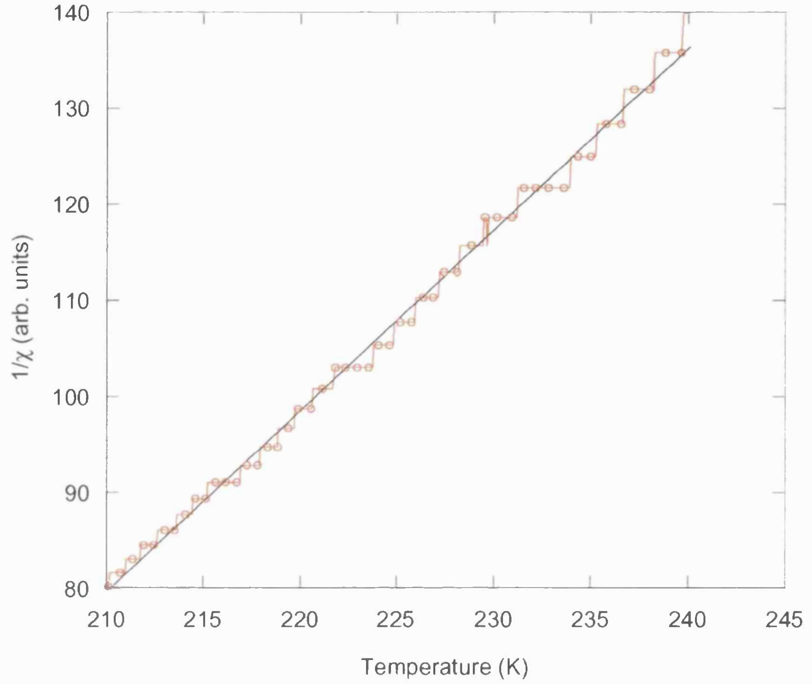

Figure 6.17 *Fit to the Curie law of data in the paramagnetic region of the 1/χ vs. temperature plot of* $Cu_{0.08}Zn_{0.92}Cr_2Se_4$ *at ambient pressure.*

The values of the Weiss constant, θ_{cw}, for $Cu_{0.08}Zn_{0.92}Cr_2Se_4$ in 0 and 6 kbar applied pressure were found to be 167.8(1) and 163.4(2) K respectively. The value at ambient pressure does not compare well with that derived from the DC measurements (358.4(3) K). However, the value obtained from the DC measurements was anomalously large and did not compare well with values reported in the literature. This inconsistency is likely to arise from the fact that only a small linear region was found in the 1/χ versus temperature plot in the temperature range studied and hence the fitting could have been inaccurate. The value of 167.8 K obtained here from the AC measurement is more consistent with the values of θ_{cw}, derived from the DC measurements, for the other compounds in the series with higher zinc concentration.

The lower value of θ_{cw} derived from the 6 kbar measurement indicates that the interactions are becoming more antiferromagnetic than ferromagnetic in character. This difference is small however and it should be considered that the linear region available for fitting was relatively small and therefore these values may not be very accurate.

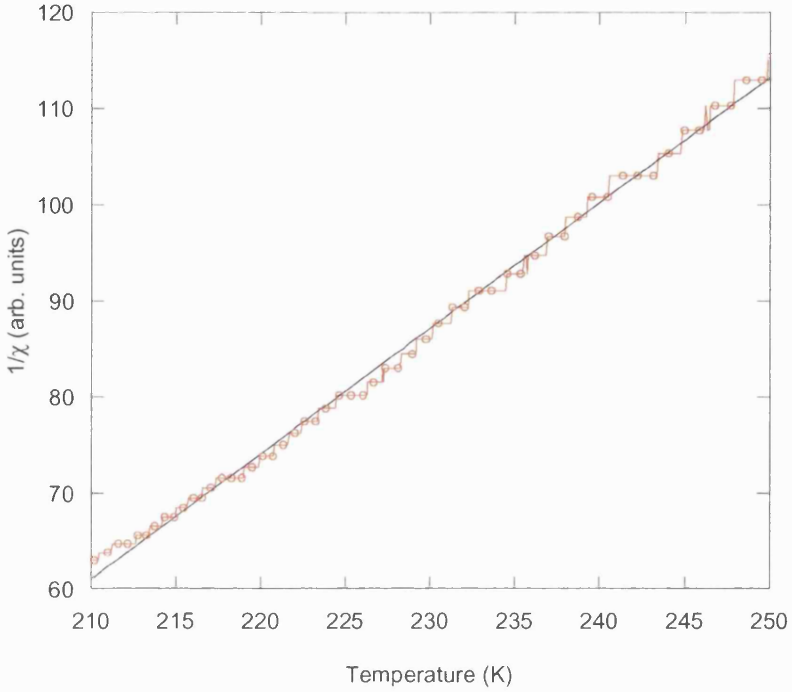

Figure 6.18 *Fit to the Curie law of data in the paramagnetic region of the 1/χ vs. temperature plot of* $Cu_{0.08}Zn_{0.92}Cr_2Se_4$ *in an applied pressure of 6 kbar*

6.4 Discussion

In order to interpret the effect of pressure on the transition temperatures of compounds in the $Cu_{1-x}Zn_xCr_2Se_4$ series, it is important to consider the magnetic interactions taking place between the chromium ions and their influence on the bulk magnetic properties of the series. The two main interactions that must be considered are the 90° ferromagnetic Cr-X-Cr superexchange interaction and the antiferromagnetic Cr-Cr direct exchange interaction. These interactions will be referred to as J_s (superexchange) and J_d (direct exchange) respectively throughout this discussion.

The properties of the $Cu_{1-x}Zn_xCr_2Se_4$ series depend on the relative strengths of the interactions J_s and J_d. Where $x = 1$, the bulk magnetic behaviour is predominantly antiferromagnetic, however, the positive value of the Weiss constant, θ_{cw}, and the spiral spin structure indicate that the ferromagnetic J_s interaction is not completely overcome and that the nearest neighbour interaction between the chromium ions is still positive, although small.

Where $x = 0$, the governing interaction is J_s and the behaviour is ferromagnetic. The magnetic properties of the compounds throughout the series are dictated by the relative strength of these interactions which, broadly speaking, vary with composition, J_d becoming stronger with increasing x. However, another factor influencing the relative strengths of J_d and J_s is the double exchange interaction which enhances the ferromagnetic J_s by the hopping of electrons between mixed valence Cr^{3+} and Cr^{4+} ions [11]. The mechanism of double exchange is described in more detail in chapter 2 of this thesis, section 2.3.5.2.3. Studying the magnetic properties of these compounds under varying pressure provides an opportunity to investigate the effect of changing the Cr-Cr distance whilst the composition, and hence the contribution of the double exchange, remains constant.

Application of pressure should shorten the Cr-Cr bond distance and hence strengthen J_d and the expense of J_s, leading to a decrease in ferromagnetic and an increase in antiferromagnetic character. This has been demonstrated by Kanomata *et. al.* who reported a lowering of the T_C of $CuCr_2Se_4$ with applied pressure [12] [6].

The results reported in this chapter, for compounds with $0.80 \leq x \leq 0.92$, show a decrease in the low temperature transition, T_N, with applied pressure. This would indicate that, although the overall order is antiferromagnetic, T_N is determined largely by the strength of the ferromagnetic nearest neighbour interaction which is weakened by the application of pressure.

Further support for these results comes from a study of magnetic properties of $ZnCr_2Se_4$ substituted randomly with Ga^{3+} [13]. This substitution resulted in a reduction of the lattice constant and hence a shorter Cr-Cr bond distance. It was found that there was a reduction in both T_N *and* θ_{cw} and it can therefore be considered that this substitution is analogous with the application of pressure.

6.5 References

1. Asbrink, S., Waskowska, A., Gerward, L., Olsen, J.S., and Talik, E., *Phys. Rev. B*, 1999. **60**(18): p. 12651-12656.
2. Asbrink, S., Waskowska, A., Olsen, J.S., and Gerward, L., *Phys. Rev. B*, 1998. **57**(9): p. 4972-4974.
3. Wang, Z.W., Saxena, S.K., and Zha, C.S., *Phys. Rev. B*, 2002. **66**(2): p. art. no.-024103.
4. Waskowska, A., Gerward, L., Olsen, J.S., and Malicka, E., *J. Phys.-Condes. Matter*, 2002. **14**(47): p. 12423-12431.
5. Oomi, G., Kagayama, T., Yoshida, I., Hagino, T., and Nagata, S., *J. Magn. Magn. Mater.*, 1995. **140**: p. 157-158.
6. Kanomata, T., Shirakawa, K., and Kaneko, T., *J. Phys. Soc. Jpn.*, 1983. **52**(4): p. 1387-1393.
7. Kanomata, T., Shirakawa, K., and Kaneko, T., *J. Phys. Soc. Jpn.*, 1985. **54**(1): p. 334-338.
8. Kanomata, T., Shirakawa, K., and Kaneko, T., *J. Magn. Magn. Mater.*, 1986. **54-7**: p. 1297-1298.
9. Spain, I.L. and Segall, S., *Cryogenics*, 1971: p. 26-36.
10. Schilling, J.S., Diederichs, J., Klotz, S., and Sieburger, R. *AC susceptibility studies of superconducting properties under high hydrostatic pressure.* in *Magnetic Susceptibility of Superconductors and Other Spin Systems.* 1991: Plenum Press, New York.
11. De Gennes, P.-G., *Phys. Rev.*, 1960. **118**(1): p. 141-154.
12. Kanomata, T., Ido, H., and Kaneko, T., *J. Phys. Soc. Jpn.*, 1970. **29**(2): p. 332-335.
13. Solanki, D., *Investigation of the synthesis and magnetic properties of selenide spinels.* 2002, University College London: London.

Chapter 7 Neutron Diffraction Measurements

7.1 Introduction

In order to gain further insight into the magnetic properties of the $Cu_{1-x}Zn_xCr_2Se_4$ series, neutron diffraction measurements have been carried out on a representative selection of compounds at a variety of temperatures and applied fields. The compounds chosen for study were $ZnCr_2Se_4$, $Cu_{0.05}Zn_{0.95}Cr_2Se_4$, $Cu_{0.09}Zn_{0.91}Cr_2Se_4$ and $Cu_{0.25}Zn_{0.75}Cr_2Se_4$ which have been shown from the magnetisation measurements to represent the four main types of magnetic behaviour seen in the series; namely antiferromagnetism, spin glass, canted ferromagnetism and ferromagnetism respectively. This same set of compounds was chosen for the electrical transport studies discussed in chapter 5.

$CuCr_2Se_4$ has been studied previously using both single crystal and powder neutron diffraction [1, 2]. The system has been found to be a collinear ferromagnet with the chromium ions contributing to the majority of the total magnetic moment. As the copper ion is in the 1+ oxidation state it has no unpaired electrons and therefore does not contribute to the magnetic moment of the compound.

Previous single crystal and powder neutron diffraction studies of $ZnCr_2Se_4$ have found it to have a helimagnetic or 'screw spin' structure below T_N, the propagation vector of which lies along the [001] axis [3-5]. The turning angle between the spins in the neighbouring [001] planes was established to be 42(1) °. Investigations of the magnetic structure in an applied field have found that a tilting of the spin rotation axis and a canting of the spins occurs towards the field direction [4]. Diffuse scattering has been observed above T_N around the (111) and (311) reflections which decreases with increasing temperature [5]. This was interpreted as a result of antiferromagnetic short range order along the [001] axis in the paramagnetic region just above T_N.

Hidaka *et. al.* have carried out powder neutron diffraction investigations on the $Cu_{1-x}Zn_xCr_2Se_4$ series where x = 0.85 and 0.70 at 2.5 and 40 K [5]. The study of $Cu_{0.15}Zn_{0.85}Cr_2Se_4$ at 2.5 K has revealed magnetic peaks corresponding to those resulting from the helical magnetic structure in $ZnCr_2Se_4$. These peaks were not visible at 40 K, suggesting that a transition from an antiferromagnetic spiral structure to a conical ferromagnetic structure occurs at some point between 2.5 and 40 K, as there is evidence of ferromagnetism at room temperature from magnetisation measurements. At 40 K, some magnetic diffuse scattering was observed and attributed to the existence of short range antiferromagnetic interactions, like those seen in $ZnCr_2Se_4$, in the conical ferromagnetic phase.

$Cu_{0.15}Zn_{0.85}Cr_2Se_4$ was also measured at 350 and 430 K to study the ferromagnetic to paramagnetic transition [5]. No difference was found between the two diffraction patterns and no diffuse scattering was observed at either temperature leading to the conclusion that the short range antiferromagnetic order was not present and that the conical ferromagnetism was not long range. Studies of $Cu_{0.30}Zn_{0.70}Cr_2Se_4$ found similar results [5], the only difference being a slightly increased value of T_N; the value of the incommensurate ordering vector, Q, was found to be 0.470 for $x = 0$, 0.85 and 0.70.

In a more recent study, Ikubo *et. al* have carried out powder neutron diffraction studies of the $Cu_{1-x}Zn_xCr_2Se_4$ series for $x = 0.3$, 0.5 and 0.7 at 7 K, room temperature and 420 K [6]. For all compounds at low temperature, magnetic satellite peaks are observed close to the (111) reflection, as seen in the previous studies of $ZnCr_2Se_4$ and they proposed that this was due to a low temperature conical structure. The ferromagnetic chromium moment was extracted using Rietveld refinement (assuming that the moments have a collinear structure) for all temperatures. There was a significant decrease in moment in all cases between room temperature and 420 K suggesting a transition from a ferromagnetic to a paramagnetic state.

7.2 Experimental

Neutron diffraction experiments were carried out on GEM instrument at the ISIS Pulsed Neutron Facility at Rutherford Appleton Laboratory, Didcot. Here the time of flight technique is used, as described in the Chapter 2, section 2.2.4. This instrument has a relatively long flight path, L, of 17 m which gives high resolution. The detectors are in 7 banks, all comprising of ZnS scintillators. Figure 7.1 shows a schematic diagram of the detectors in the GEM instrument.

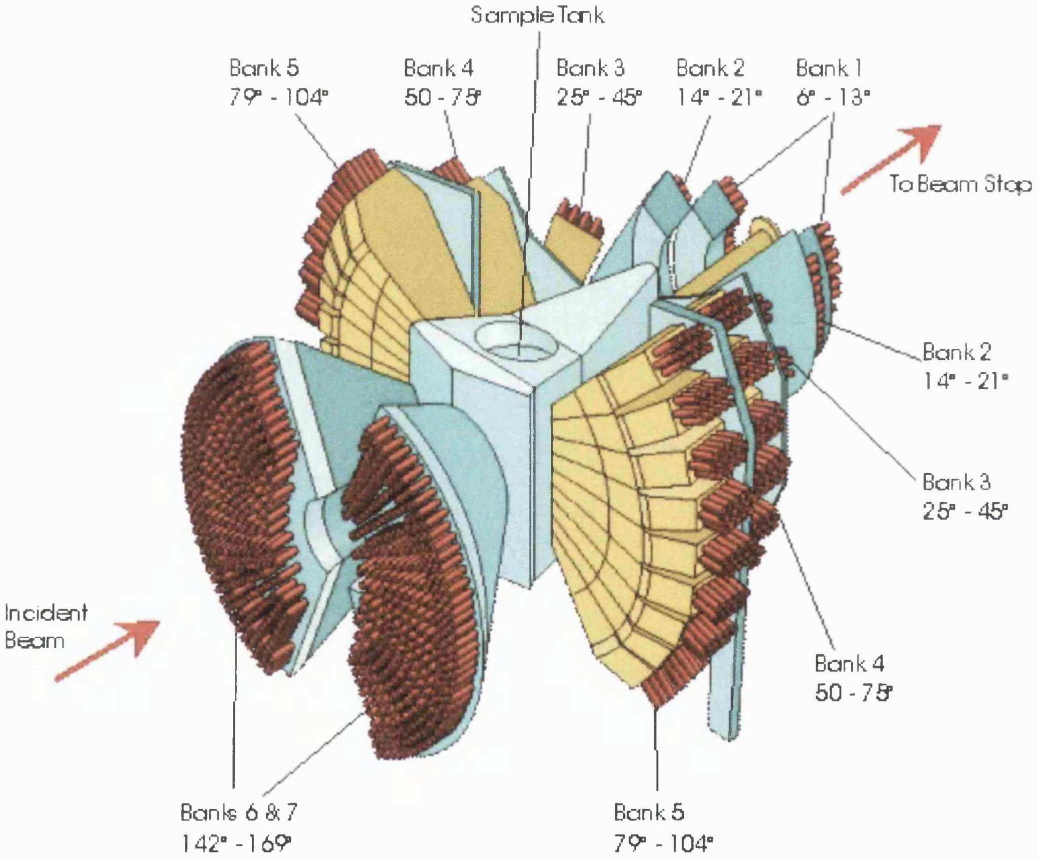

Figure 7.1 *Schematic diagram of the GEM instrument, showing the position of the detector banks. Taken from* [7]

Each sample was pressed into several pellets of 10 mm diameter and approximately 3 mm thickness before being placed into a cylindrical vanadium can, diameter 10 mm. Approximately 7 g of sample was used in each case to ensure the maximum amount of sample intercepted the beam. Silica wool was packed into the can over the sample to prevent any movement when the field was applied.

Experiments were performed in a cryostat with a temperature range of 2 to 300 K and capable of applying fields of up to 8 Tesla. A counting time of 2-3 hours was used for each data set.

7.3 Results

For each of the compounds studied, the powder neutron diffraction pattern was measured at zero field and a selection of applied fields between 0.01 and 8 Tesla at a series of temperatures relevant to the known magnetic transitions. It was found that the majority of the magnetic and structural information was contained in data from detector bank 3 which covers the angle $25\ ^{\circ} \leq 2\theta \leq 45\ ^{\circ}$ and the d-spacing range 0.3-8.3 Å. When using a high resolution diffractometer such as GEM one would normally expect to obtain very high quality diffraction data from all detector banks after 2-3 hours collection time. In this case however, the data from many of the banks contained extra peaks resulting from the sample environment apparatus which overlapped with both structural and magnetic peaks from the sample. In addition, the sample rod which was used to lower the sample into the beam was not quite straight which resulted in the sample not being positioned correctly in the centre of the beam, leading to a decrease in the number of counts and hence data of poor statistical quality. This situation was improved slightly by rotating the sample rod to optimise the position of the sample but this process was very time consuming as data had to be collected for at least 30 minutes between each rotation to evaluate the improvement in data quality; therefore only a limited improvement in statistics could be achieved for each sample. It was decided to carry out the refinements using only data from bank 3 (which contains the majority of the magnetic and structural information and no peaks due to the sample containment apparatus) as there was no additional information to be gained from a multi-bank refinement.

It was possible to deduce qualitatively, from examination of the diffraction patterns, information on the nature of the magnetic interactions within each sample. It also proved possible to determine the magnitude of the ferromagnetic moment on the chromium ions by Rietveld refinement, using the program GSAS [8]. In order to do this the magnetic structure was assumed to be collinear, with the chromium moments aligned ferromagnetically along one of the equivalent crystallographic axis. Although this is a gross approximation for the samples studied, which are thought to have an antiferromagnetic spiral or canted ferromagnetic structure, the results enable an evaluation of the effect of an applied field on the magnetic properties and a comparison with the magnetisation results presented in chapter 4 of this thesis.

In some cases, peaks resulting from the incommensurate antiferromagnetic spiral structure can clearly be identified in the diffraction patterns. These cannot be indexed by the GSAS program as it does not contain the facility for refining incommensurate magnetic structures. Other refinement programs, such as Fullprof [9] , are able to model incommensurate magnetic structures, however, a further complication arises when studying neutron powder diffraction in applied magnetic fields. As the sample consists of many tiny crystallites of different size in arranged in a random orientation, their individual responses to an applied magnetic field will be different and an infinite number of magnetic structures will be represented in the diffraction pattern. In order to interpret the data using Rietveld refinement, one approach is to assume that the magnetic structure is the same for every crystallite. This is reasonable for ferromagnetic structures where the moment is expected to align parallel to the applied field. In the case of the antiferromagnetic spiral structure this approximation cannot be used and therefore Rietveld refinement is not able to solve the magnetic structure in this way. Therefore only a simple, qualitative interpretation of the data is possible for compounds with the incommensurate antiferromagnetic structure.

As in all neutron diffraction patterns, the intensity of the magnetic peaks decreases rapidly from large to small d-spacing and therefore the majority of the information on the magnetic structure is contained in the large d-spacing region of the pattern. Unfortunately, this region of the pattern also has a relatively high noise to signal ratio which has made the identification and refinement of the magnetic peaks difficult. Data from bank 2, which covers the d-spacing range 0.5-15 Å, also contains the magnetic peaks but there was no improvement in the signal to noise ratio here.

The problems experienced in refining the intensities in the powder X-ray diffraction data, discussed in chapter 3 of this thesis, were not found in the refinement of the neutron diffraction patterns. This is consistent with the theory that the intensity problems were due to a preferred orientation effect, created when the crystallites in the powder sample become aligned when the powder is packed into the sample holder with the flat surface of a glass slide. In the powder neutron diffraction measurement the sample is placed in a cylindrical sample can and the neutrons probe the bulk of the sample rather than surface and therefore the preferred orientation effect does not occur.

7.3.1 Neutron diffraction of $ZnCr_2Se_4$

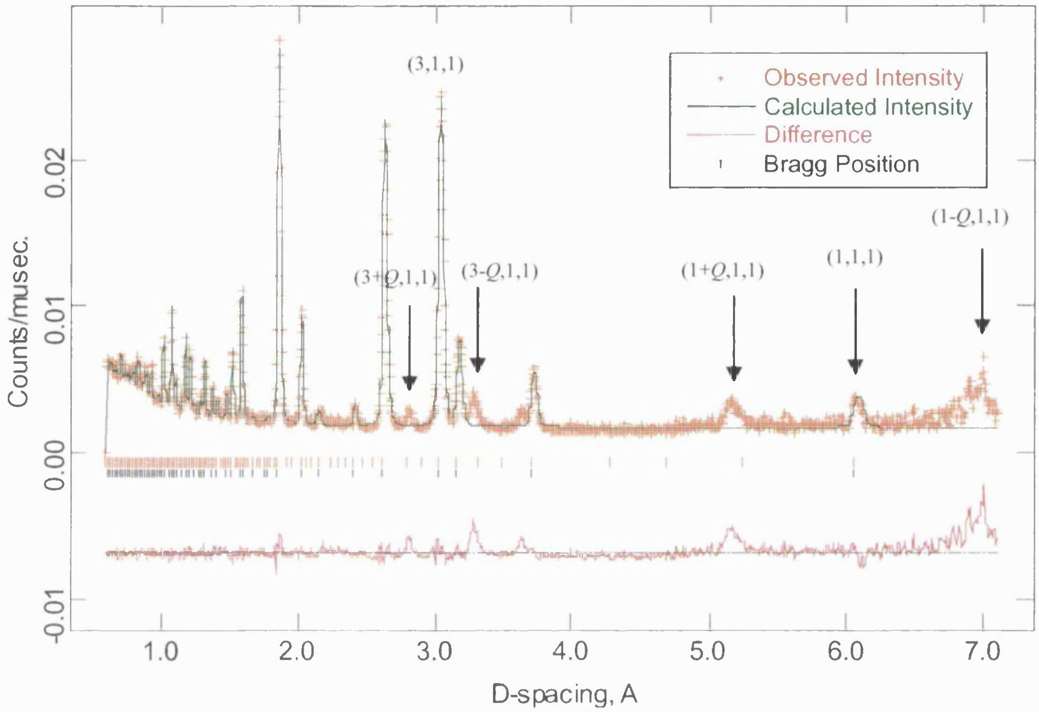

Figure 7.2 *Rietveld refinement of the powder neutron diffraction pattern of* $ZnCr_2Se_4$ *at 2K, showing the observed, calculated and difference intensity plots*

The neutron diffraction pattern of $ZnCr_2Se_4$ was recorded at 2, 20 and 30 K in zero applied field and at 2 K in applied fields of 0, 1, 3, and 8 Tesla.

Figure 7.2 shows a refinement of the neutron diffraction pattern of $ZnCr_2Se_4$ at 2K in zero applied field. The antiferromagnetic peaks can clearly be seen as the satellite reflections to the (111) and (311) reflections. The value of Q was found to be 0.468, using the equation

$$\frac{1}{d}=\sqrt{\frac{h^2+k^2+l^2}{a^2}}$$

Equation 7.1

Figure 7.3 shows an expanded area of the diffraction patterns of $ZnCr_2Se_4$ at 2, 20 and 30 K. The antiferromagnetic peaks disappear between 20 and 30 K, which is consistent with $T_N = 24$ K. It is difficult to assess whether there is any diffuse scattering around the (111) and (311) reflections as reported by Hidaka *et. al.* [5] as the signal to noise ratio is rather high in that region of the pattern. Attempts at subtracting the 30 K data from the 2 K data to reveal the magnetic peaks were also unsuccessful as the high levels of noise obscured the small antiferromagnetic reflections.

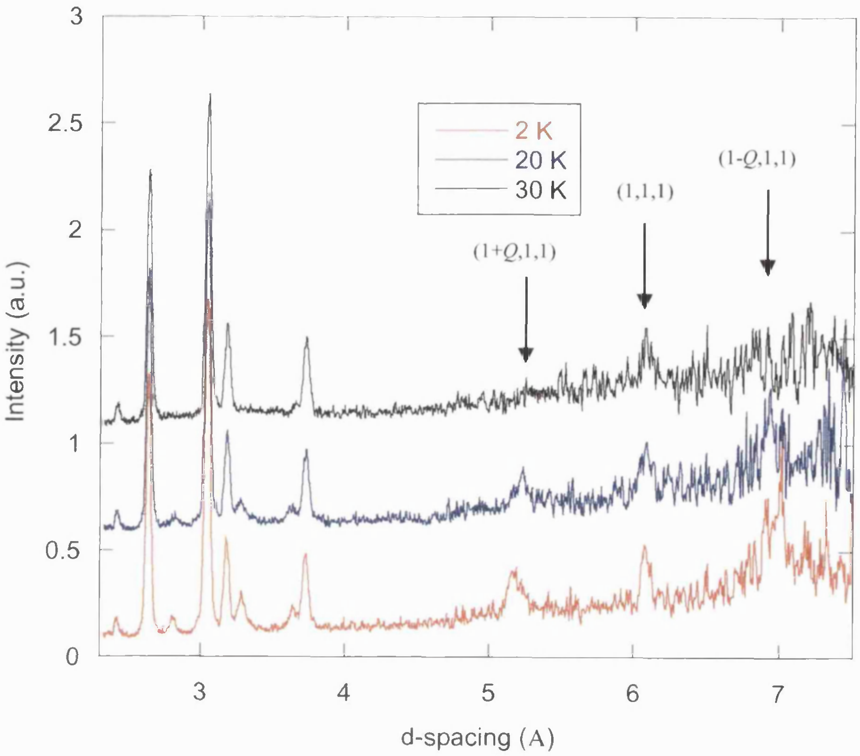

Figure 7.3 *Section of the neutron diffraction pattern of* $ZnCr_2Se_4$ *at 2, 20 and 30 K in zero applied field.*

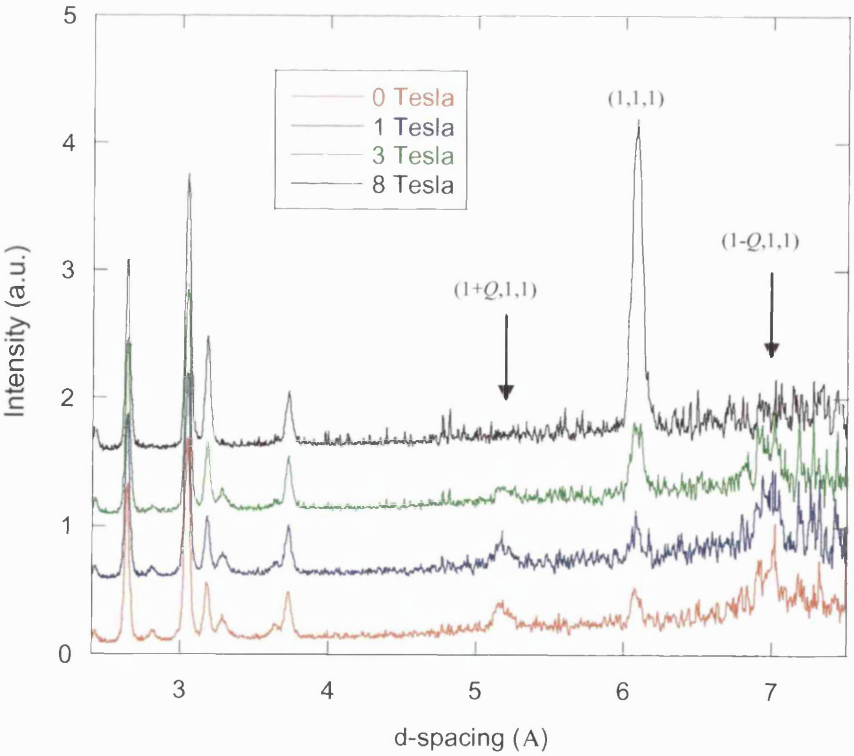

Figure 7.4 *Section of the neutron diffraction pattern of* $ZnCr_2Se_4$ *at 2 K in applied fields of 0, 1 3 and 8 tesla.*

Figure 7.4 shows the neutron diffraction patterns of $ZnCr_2Se_4$ at 2 K in applied fields of 0, 1, 3 and 8 Tesla. Due to the large noise to signal ratio at higher d-spacing it is difficult to discern any difference between the 0 and 1 Tesla patterns, but the 3 and 8 Tesla plots clearly show a significant increase in the intensity of the (111) reflection and a reduction in the intensity of the antiferromagnetic satellite reflections. The increase in the intensity of the (111) reflection suggests that an increased ferromagnetic component of the magnetism is being introduced in the presence of an applied magnetic field. In high fields (8 Tesla) the long range antiferromagnetic spiral structure appears to be destroyed totally as the satellite peaks to the (111) and (311) reflections are no longer present.

Rietveld refinements of the patterns in 1, 3 and 8 Tesla have been carried out. The magnetic model was included as a second phase, using lattice parameters derived from the 2 K, 0 Tesla refinement, and P1 symmetry. The model that gave the best fit to the data is ferromagnetic with the moment aligned along one of the equivalent crystallographic axes, arbitrarily z. The results of these refinements are given in table 7.1; plots of the refinements are given in the appendix, section A.4.1 .

Temperature, (K)	**Applied Field, (T)**	**μ_B per Cr**	**Lattice Parameter, a, (Å)**	χ^2	R_{wp}
2	0	0.00*	10.5073(3)	3.915	9.11
2	1	0.13(7)	10.482(1)	2.796	9.31
2	3	0.95(6)	10.4819(2)	2.892	8.26
2	8	2.8*	10.482(3)	2.072	7.32
20	0	0.00*	10.498(6)	2.050	8.01
30	0	0.00*	10.5054(4)	1.504	6.86

Table 7.1 *Magnetic moment, lattice parameter and goodness of fit values obtained from the Rietveld refinement of powder neutron diffraction patterns of $ZnCr_2Se_4$ in a selection of temperatures and applied fields.*

The results of the Rietveld refinements show that the moment increases with applied field at 2 K. The goodness of fit values are higher than would normally be satisfactory in these refinements; this is due to the presence of the antiferromagnetic reflections which can not be modelled by the GSAS program and the high signal to noise ratio of the data at

---

* In this case the best fit to the data was achieved by manually adjusting the magnitude of the moment

high d-spacing. It was not possible to exclude the antiferromagnetic reflections from the refinement as they overlap partially with some of the structural peaks. In the 8 Tesla refinement, the best fit to the data was achieved by manually adjusting the size of the moment.

There were problems in all cases refining the peak shape as it was not described well by the functions given in the GSAS program. As the main purpose of these refinements was to extract the magnitude of the ferromagnetic moment, the information for which is contained chiefly in the intensity of the (111) peak, this problem with the peak shape is only significant where it prevents the accurate determination of the intensity of the (111) peak. Other potential errors in determining the size of the moment arise from the large signal to noise ratio of the data in the high d-spacing region of the pattern which creates difficulty in fitting the height of the background and the shape of the (111) peak correctly. It should be considered, therefore, that the error in the moment given by the GSAS program may be smaller than the actual error.

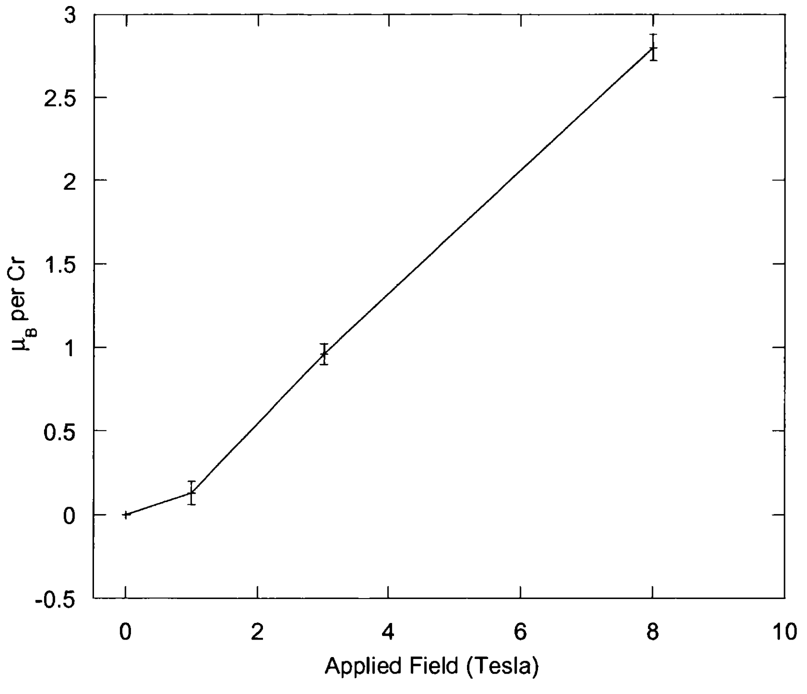

Figure 7.5 *Plot of refined moment vs. applied field for* $ZnCr_2Se_4$ *at 2 K.*

Figure 7.5 shows a plot of moment (in μ_B per Cr) versus applied field at 2 K for $ZnCr_2Se_4$. Within error, there appears to be an approximately linear increase of moment with applied field; this is in accordance with the magnetisation versus field measurement reported in chapter 4, page 130. The magnetisation measurement was carried out at 5 K and gave a moment of approximately 2.5 μ_B per Cr at 7 Tesla, where the magnetisation appeared to have saturated.

For the zero field neutron diffraction patterns at 2, 20 and 30 K the best fit to the data was achieved by setting the moment to zero μ_B per Cr. Attempts were made to refine a value for the moment in each case but this resulted in unstable refinements and gave no improvement to the fit. It was therefore not possible to estimate an error in these values.

7.3.2 Neutron diffraction of $Cu_{0.05}Zn_{0.95}Cr_2Se_4$

The neutron diffraction pattern of $Cu_{0.05}Zn_{0.95}Cr_2Se_4$ was measured at 2 and 60 K in applied fields of 0, 1 and 3 Tesla. Figure 7.6 shows a section of the neutron diffraction patterns of $Cu_{0.05}Zn_{0.95}Cr_2Se_4$ at 2 and 60 K. The antiferromagnetic satellite peaks seen in $ZnCr_2Se_4$ at low temperature are not seen here; for comparison figure 7.7 shows a section of the diffractions patterns for $ZnCr_2Se_4$ and $Cu_{0.05}Zn_{0.95}Cr_2Se_4$ at 2 K.

It can be seen in figures 7.6 and 7.7 that there appears to be some diffuse scattering around the (111) and (311) peaks in the 2 K measurement which is indicative of short range magnetic order. This has been observed by Hidaka *et. al.* at low temperature in their studies of $ZnCr_2Se_4$ and $Cu_{0.15}Zn_{0.85}Cr_2Se_4$ [5].

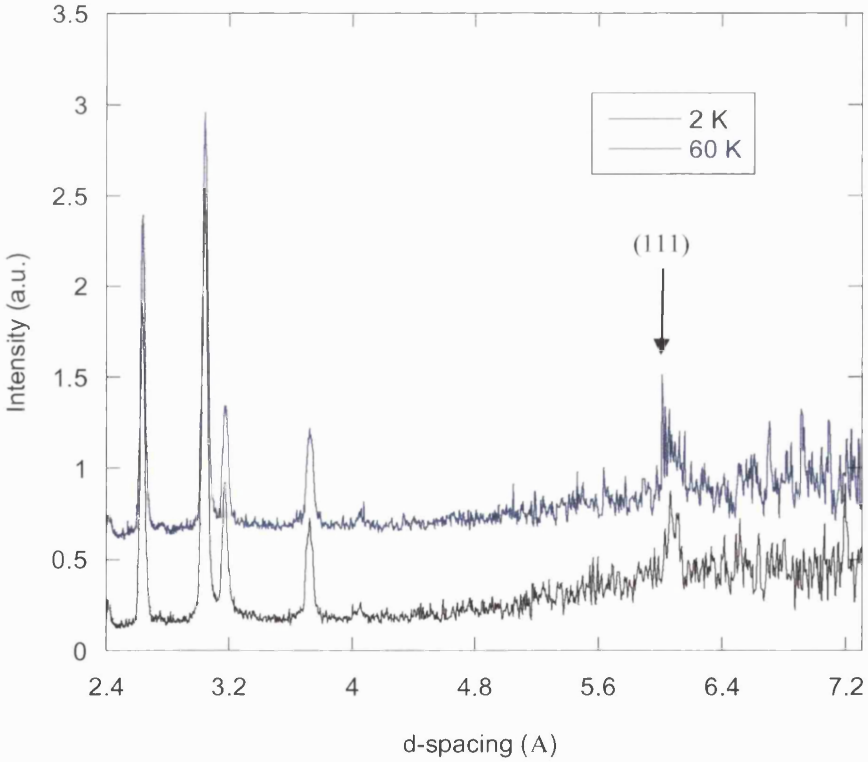

Figure 7.6 *Section of the neutron diffraction pattern of $Cu_{0.05}Zn_{0.95}Cr_2Se_4$ at 2 and 60 K.*

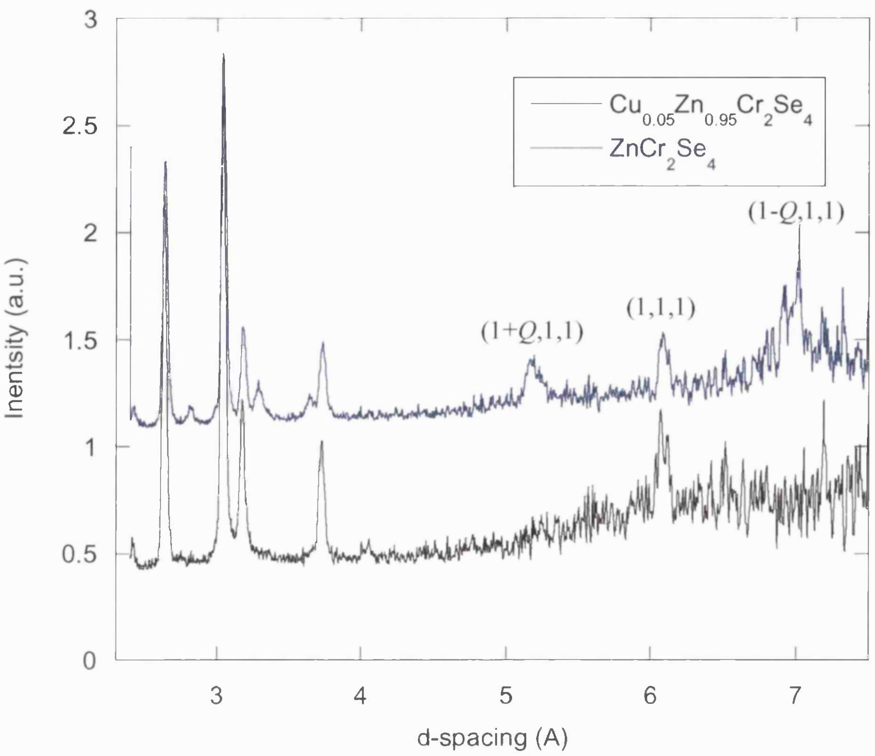

Figure 7.7 *Section of the neutron diffraction patterns of* $Cu_{0.05}Zn_{0.95}Cr_2Se_4$ *and* $ZnCr_2Se_4$ *at 2 K.*

Figure 7.8 shows the neutron diffraction patterns of $Cu_{0.05}Zn_{0.95}Cr_2Se_4$ at 2 K in applied fields of 0, 1 and 3 Tesla. There is a significant increase in the intensity of the (111) peak with field, indicative of an increasing ferromagnetic moment. By visual examination of the diffraction patterns it is clear that the effect of an applied magnetic field of 1 tesla in increasing the ferromagnetic moment in $Cu_{0.05}Zn_{0.95}Cr_2Se_4$ is much greater than in $ZnCr_2Se_4$. In order to investigate this quantitively, Rietveld refinement of the neutron diffraction patterns was carried out, as for $ZnCr_2Se_4$, with a ferromagnetic component along the *z* axis. The results are given in table 7.2 (page 242) and figure 7.11 (page 243).

Figure 7.9 shows a section of the neutron diffraction patterns of $Cu_{0.05}Zn_{0.95}Cr_2Se_4$ at 60 K in applied fields of 0, 1 and 3 Tesla. There is an increase in the intensity of the (111) peak with increasing field, the magnitude of which appears less at 1 Tesla than in the 2 K measurement. The magnitude of the ferromagnetic moment induced by the application of these fields was assessed by Rietveld refinement, as for the 2 K patterns. The results are given in table 7.2 and figure 7.11. A plot of the 2 K, 0 Tesla refinement is shown in figure 7.10; plots of the refinements for all other measured neutron diffraction patterns of $Cu_{0.05}Zn_{0.95}Cr_2Se_4$ are given in the appendix, section A.4.2.

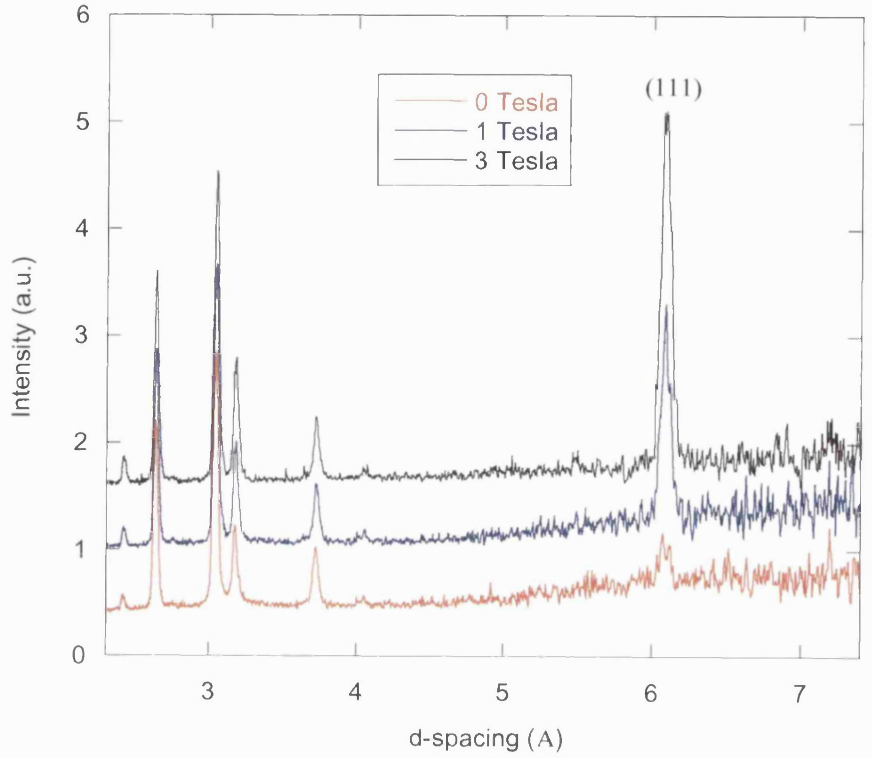

Figure 7.8 *Section of the neutron diffraction patterns of* $Cu_{0.05}Zn_{0.95}Cr_2Se_4$ *at 2 K in applied fields of 0, 1 and 3 T.*

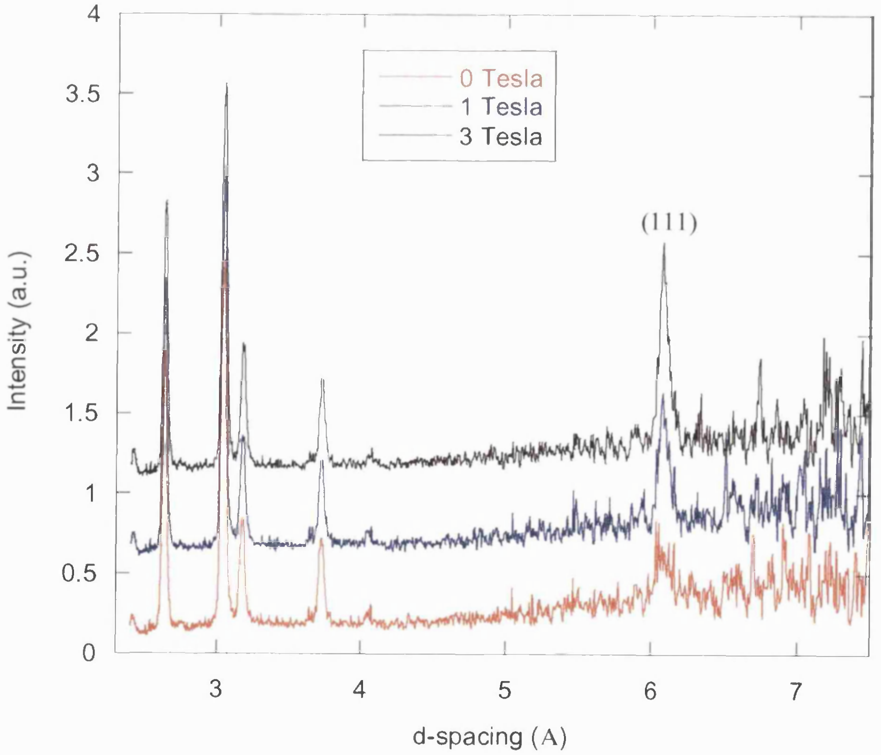

Figure 7.9 *Section of the neutron diffraction patterns of* $Cu_{0.05}Zn_{0.95}Cr_2Se_4$ *at 60 K in applied fields of 0, 1 and 3 T.*

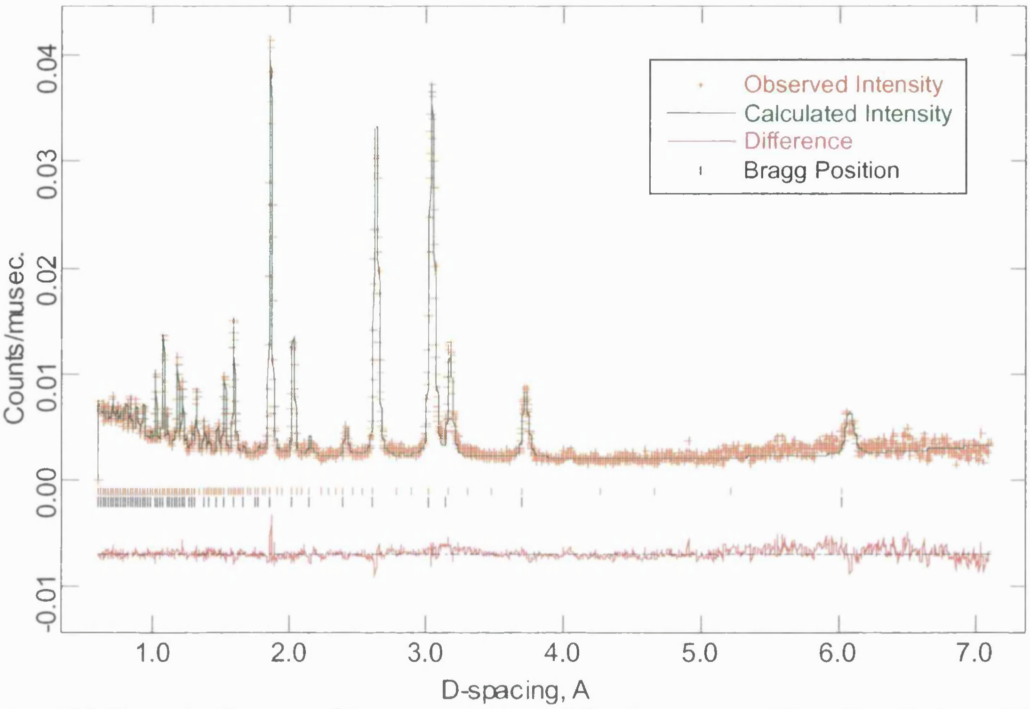

Figure 7.10 *Rietveld refinement of the powder neutron diffraction pattern of* $Cu_{0.05}Zn_{0.95}Cr_2Se_4$ *at 2 K, showing the observed, calculated and difference intensity plots.*

Temperature, (K)	Applied Field, (T)	μ_B per Cr	Lattice Parameter, a, (Å)	χ^2	R_{wp}
2	0	0.00 *	10.4667(5)	1.725	7.42
2	1	1.50*	10.471(3)	1.624	7.84
2	3	1.75*	10.477(4)	1.498	7.53
60	0	0.00*	10.470(2)	1.427	7.36
60	1	0.65(3)	10.463(2)	1.514	7.58
60	3	0.95*	10.468(2)	1.514	7.61

Table 7.2 *Magnetic moment, lattice parameter and goodness of fit values obtained from the Rietveld refinement of powder neutron diffraction patterns of* $Cu_{0.05}Zn_{0.95}Cr_2Se_4$ *in a selection of temperatures and applied fields.*

Table 7.2 shows the results of the Rietveld refinements of the neutron diffraction patterns of $Cu_{0.05}Zn_{0.95}Cr_2Se_4$ at 2 and 60 K in applied fields of 0, 1 and 3 Tesla. Figure 7.11 shows a plot of moment (in μ_B per Cr) versus applied field at 2 and 60 K. In some cases the best fit to the data was achieved by manually adjusting the magnitude of the moment. The errors quoted for the refined parameters are those given by the GSAS

---

[*] In this refinement the best fit to the data was achieved by manually adjusting the magnitude of the moment.

program, the errors for the manually adjusted parameters shown in figure 7.11 were estimated by inspection. The goodness of fit parameters obtained from the refinements are above normally acceptable levels. This is due to a combination of factors, namely the problems experienced in correctly fitting the peak profiles, the high noise to signal ratios at high angle and in the case of the 2 K, 0 Tesla experiment, the presence of diffuse magnetic scattering at high angle.

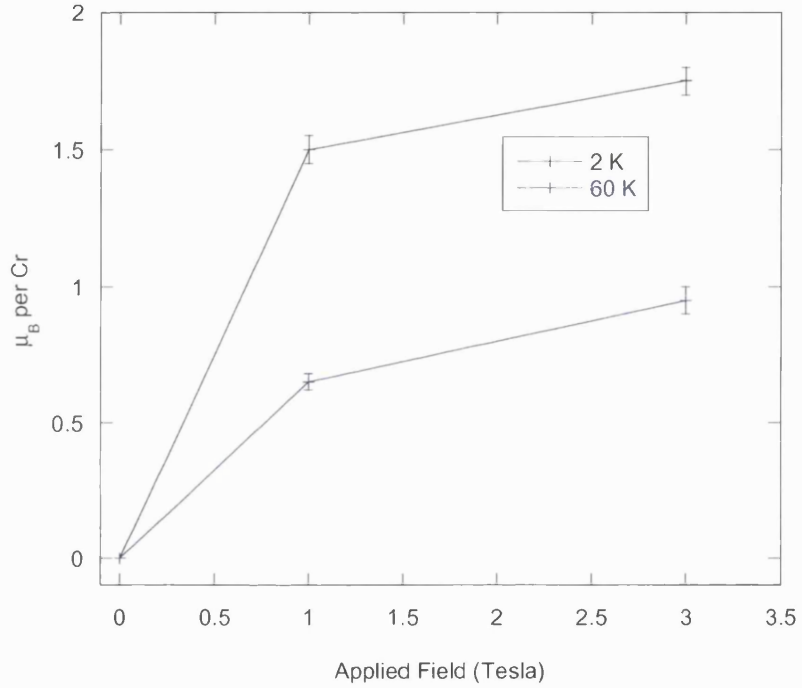

Figure 7.11 *Plot of refined moment vs. applied field for* $Cu_{0.05}Zn_{0.95}Cr_2Se_4$ *at 2 and 60 K.*

Figure 7.11 shows the variation in refined magnetic moment with applied field at 2 and 60 K. It can be seen that there is a proportionally greater increase of moment in an applied field of 1 Tesla than in 3 Tesla in both 2 and 60 K. This is in agreement with the magnetisation versus temperature measurements carried out at 5 K for $Cu_{0.05}Zn_{0.95}Cr_2Se_4$, reported in chapter 4, page 129. The magnetisation versus field of $Cu_{0.05}Zn_{0.95}Cr_2Se_4$ was also recorded at 60 K for comparison with the neutron diffraction data; the results are shown in the appendix, section A.4.2. For both temperatures, the values of the moment derived from the Rietveld refinement are approximately 0.5 μ_B lower than those obtained from the magnetisation measurements.

For the zero field neutron diffraction patterns at 2 and 60 K the best fit to the data was achieved by setting the moment to zero μ_B per Cr. Attempts were made to refine a value for the moment in each case but this resulted in unstable refinements and gave no improvement to the fit. It was therefore not possible to estimate an error in these values.

The lattice parameter increases between 2 and 60 K in zero applied field from 10.4667(5) to 10.470(2) Å as would be expected from thermal expansion. The value of the lattice parameter at room temperature, taken from the Rietveld refinements of the X-ray powder diffraction patterns reported in chapter 3 is 10.490(1) Å. At 2 K, the refinements show a small increase in lattice parameter with applied field (~ 0.003 Å per Tesla). This could be due to a positive magnetostriction effect due to the enhancing of the ferromagnetic interactions within the lattice as has been reported previously by Kusz *et. al.* for compounds in the $Cu_{1-x}Zn_xCr_2Se_4$ series where $0.8 \leq x \leq 0$ [10]. However, the data seems of insufficient quality to judge this effect accurately. During the refinement process, correlations of the profile parameters with the lattice parameters occurred when the (111) peak was small and this may have lead to inaccuracies in the refined lattice parameter.

At 60 K, the refined lattice parameter decreases slightly with the application of 1 Tesla and then increases again in an applied field of 3 Tesla. As for the 2 K measurements, this result is probably due to inaccuracies in the refinement and is unlikely to represent the true situation.

7.3.3 Neutron diffraction of $Cu_{0.09}Zn_{0.91}Cr_2Se_4$

Neutron diffraction patterns of $Cu_{0.09}Zn_{0.91}Cr_2Se_4$ were measured at 2, 15, 25, 50 and 150 K in zero field and also in an applied field of 5 Tesla at 2 and 50 K. Figure 7.12 shows a section of the diffraction patterns at all temperatures measured. Antiferromagnetic satellite reflections are clearly visible in the 2 and 15 K patterns at around 5.2 and 6.9 Å as seen in $ZnCr_2Se_4$; above this temperature these reflections are not present, suggesting that a transition from an antiferromagnetic spiral structure to a ferromagnetic or paramagnetic state has occurred.

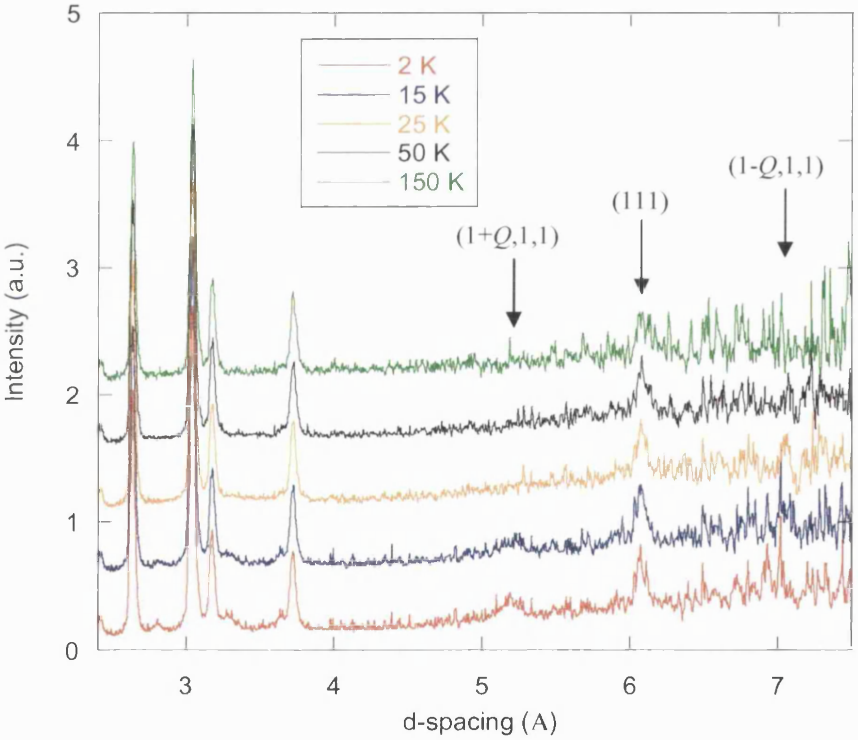

Figure 7.12 *Section of the neutron diffraction pattern of $Cu_{0.09}Zn_{0.91}Cr_2Se_4$ at 2, 15, 25, 50 and 150 K.*

Figures 7.13 and 7.14 show a section of the neutron diffraction patterns of $Cu_{0.09}Zn_{0.91}Cr_2Se_4$ in applied fields of 0 and 5 Tesla at 2 and 50 K respectively. At 2 K, there is a significant increase in the intensity of the (111) reflection accompanied by a reduction in the intensity of the antiferromagnetic satellite peaks when a field of 5 Tesla is applied. A similar increase in intensity of the (111) peak is seen in a field of 5 Tesla at 50 K. Rietveld refinement has been carried out, as for $ZnCr_2Se_4$ and $Cu_{0.05}Zn_{0.95}Cr_2Se_4$, to obtain the magnitude of the moment on the Cr ions. The results of these refinements are given in table 7.3, page 248.

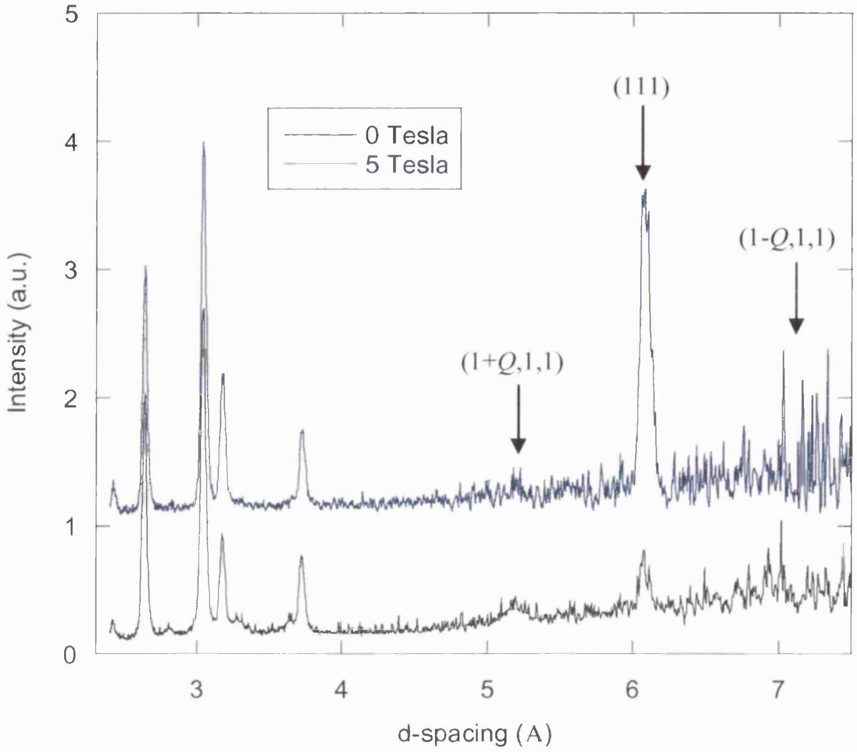

Figure 7.13 *Section of the neutron diffraction pattern of* $Cu_{0.09}Zn_{0.91}Cr_2Se_4$ *at 2 K in applied fields of 0 and 5 T.*

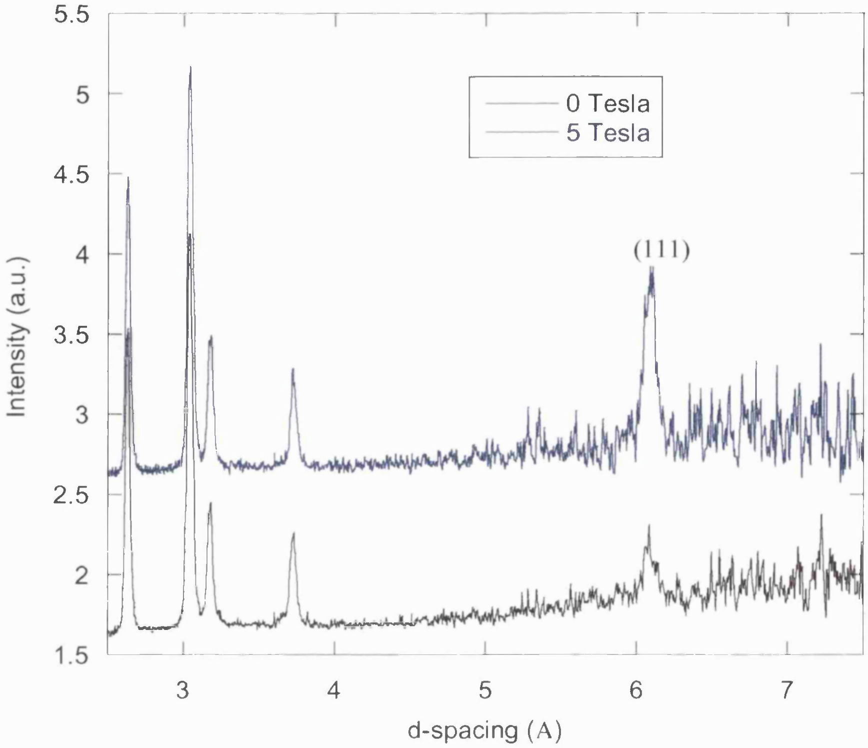

Figure 7.14 *Section of the neutron diffraction pattern of* $Cu_{0.09}Zn_{0.91}Cr_2Se_4$ *at 50 K in applied fields of 0 and 5 T.*

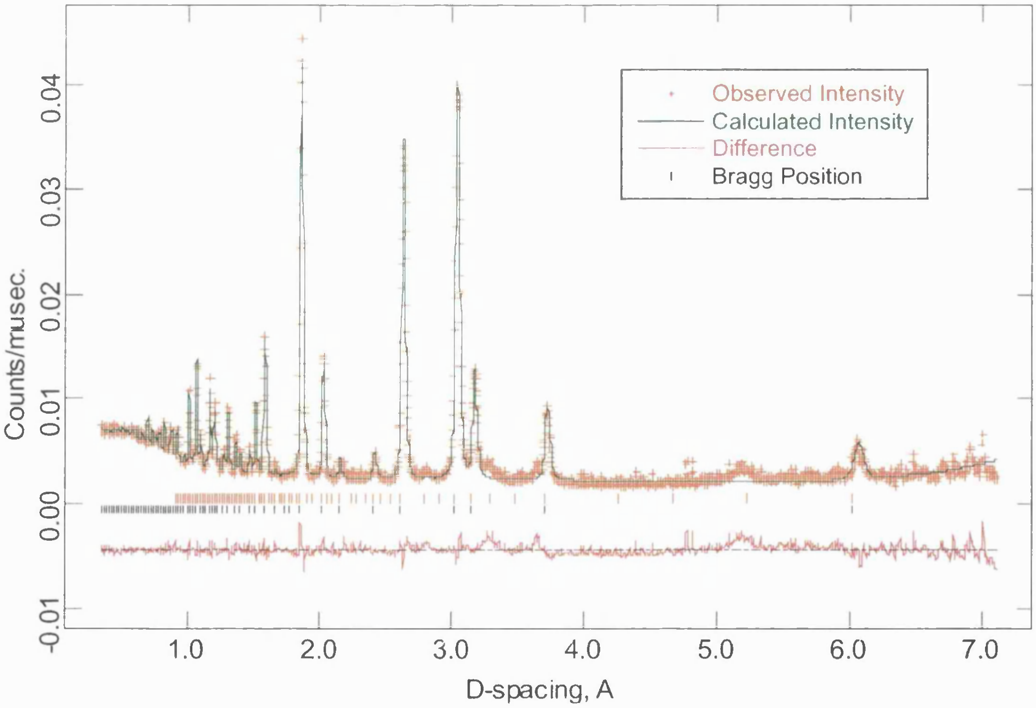

Figure 7.15 *Rietveld refinement of the powder neutron diffraction pattern of* $Cu_{0.09}Zn_{0.91}Cr_2Se_4$ *at 2K, showing the observed, calculated and difference intensity plots.*

Temperature, (K)	**Applied Field, (T)**	**μ_B per Cr**	**Lattice Parameter, a, (Å)**	χ^2	R_{wp}
2	0	0.86(7)	10.467(1)	3.589	7.24
2	5	3.06(8)	10.465(1)	1.037	8.18
15	0	0.3(1)	10.467(2)	2.413	6.63
25	0	0.000*	10.4608(9)	1.796	5.78
50	0	0.000*	10.4608(9)	1.551	5.42
50	5	2.07(7)	10.467(1)	1.067	7.64
150	0	0.000*	10.463(1)	1.086	6.98

Table 7.3 *Magnetic moment, lattice parameter and goodness of fit values obtained from the Rietveld refinement of powder neutron diffraction patterns of* $Cu_{0.09}Zn_{0.91}Cr_2Se_4$ *in a selection of temperatures and applied fields.*

Figure 7.15 shows a plot of the Rietveld refinement of the powder neutron diffraction pattern of $Cu_{0.09}Zn_{0.91}Cr_2Se_4$ at 2 K in zero applied field. Plots of the Rietveld refinements of all other patterns recorded for $Cu_{0.09}Zn_{0.91}Cr_2Se_4$ are given in the appendix, section A.4.3. The results of these refinements are given on table 7.3 and figure 7.16 shows the variation of moment (in μ_B per Cr) with applied field at 2 and 50 K. The errors given in the table are those given by the GSAS program.

---

* In this refinement the best fit to the data was achieved by manually adjusting the magnitude of the moment.

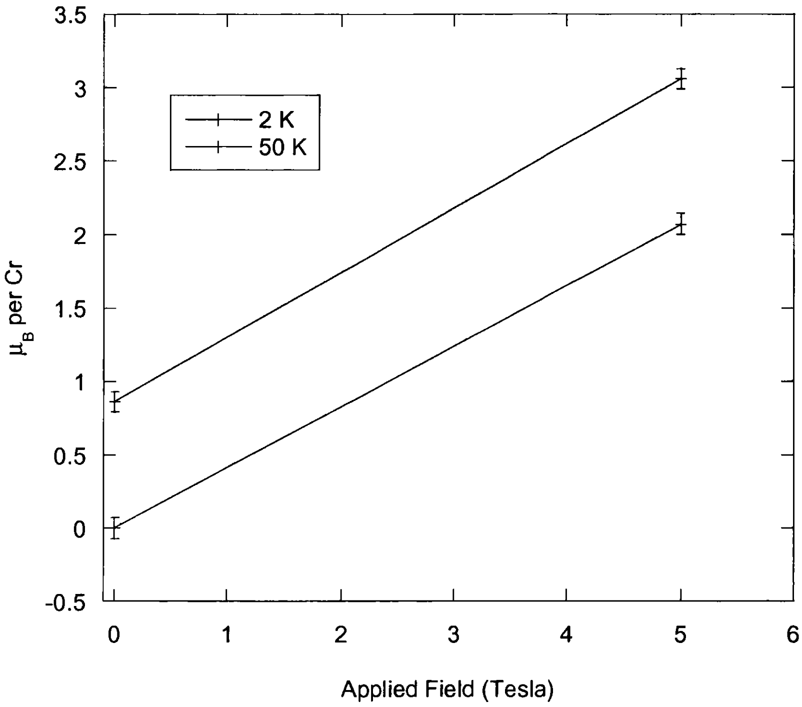

Figure 7.16 *Plot of refined moment vs. applied field for* $Cu_{0.09}Zn_{0.91}Cr_2Se_4$ *at 2 and 50 K.(The line is shown as a guide)*

Figure 7.16 shows that there is, within error, approximately the same increase in moment with an applied field of 5 Tesla at 50 K as there is at 2 K. The magnitude of the moment at 2 K in 5 Tesla is approximately 3 μ_B per Cr which is slightly larger than the value of 2.5 μ_B per Cr obtained from the magnetisation versus field measurements at 5 K reported in chapter 4, figure 4.12, page 129.

Unlike in the $ZnCr_2Se_4$ and $Cu_{0.05}Zn_{0.95}Cr_2Se_4$ refinements, it was possible to refine a non-zero moment in $Cu_{0.09}Zn_{0.91}Cr_2Se_4$ at zero applied field and 2 K. The refined moment decreased from 0.87 to 0.3 μ_B per Cr between 2 and 15 K; at temperatures of 25 K and above the best fit to the data was achieved with a moment of 0 μ_B per Cr. The refined values are considerably higher (nearly 10 times) than the values obtained in the 100 gauss magnetisation versus temperature measurement reported in chapter 4, figure 4.4, page 120. The 100 Gauss magnetisation versus temperature plot shows a rise in magnetisation from 2 to 25 K followed by a decrease in higher temperatures whereas the values of the magnetisation derived from the neutron experiments show a decrease from 2 K. This disparity between the values of the moment derived from neutron diffraction and those from the magnetisation measurements is also seen in $Cu_{0.25}Zn_{0.75}Cr_2Se_4$ and has been reported previously by Ikubo *et. al.* [6]. This phenomenon will be considered in more detail in the discussion section of this chapter.

The refined lattice parameters do not seem to correlate to either temperature or field, which is likely to be a consequence of the poor peak shape fitting at high d-spacing. The room temperature value of the lattice parameter, obtained from the Rietveld refinement of X-ray powder diffraction data reported in chapter 3 is 10.4847(7) Å.

7.3.4 Neutron diffraction of $Cu_{0.25}Zn_{0.75}Cr_2Se_4$

Powder neutron diffraction patterns of $Cu_{0.25}Zn_{0.75}Cr_2Se_4$ were recorded at 5, 15, 25 and 50 K in zero applied field and at 5 K in 0.01, 0.1, 1, 5 and 8 Tesla and at 50 K in 5 Tesla. Figure 7.17 shows a section of the neutron powder diffraction patterns at 5, 15, 25 and 50 K in zero applied field. Due to the high noise to signal ratio at high d-spacing it is not possible to judge conclusively if there are any antiferromagnetic satellite reflections present or if there is a significant reduction in the intensity of the (111) reflection with increasing temperature.

Figure 7.18 shows a section of the neutron powder diffraction pattern of $Cu_{0.25}Zn_{0.75}Cr_2Se_4$ at 5 K in applied fields of 0, 0.01, 0.1, 1 5, and 8 Tesla. There is a significant increase in the intensity of the (111) peak with applied field, indicative of an increase in the size of the ferromagnetic moment on the chromium ion. A similar effect is seen in figure 7.19 which shows a section of the neutron diffraction patterns at 50 K in 0 and 5 Tesla. Rietveld refinement was carried out on all patterns to obtain the size of the ferromagnetic moment on the chromium ion in each case; the results are given in table 7.4, page 253.

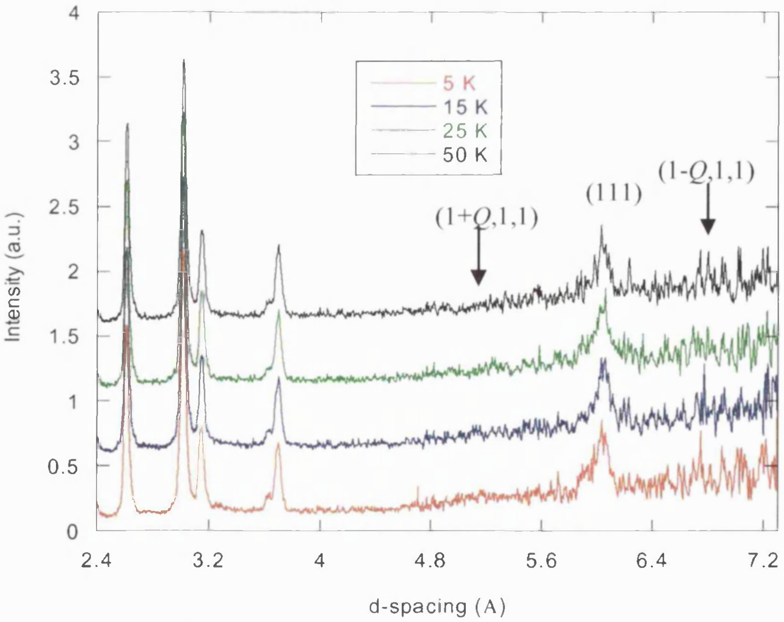

Figure 7.17 *Section of the neutron diffraction pattern of* $Cu_{0.25}Zn_{0.75}Cr_2Se_4$ *at 5, 15, 25 and 50 K.*

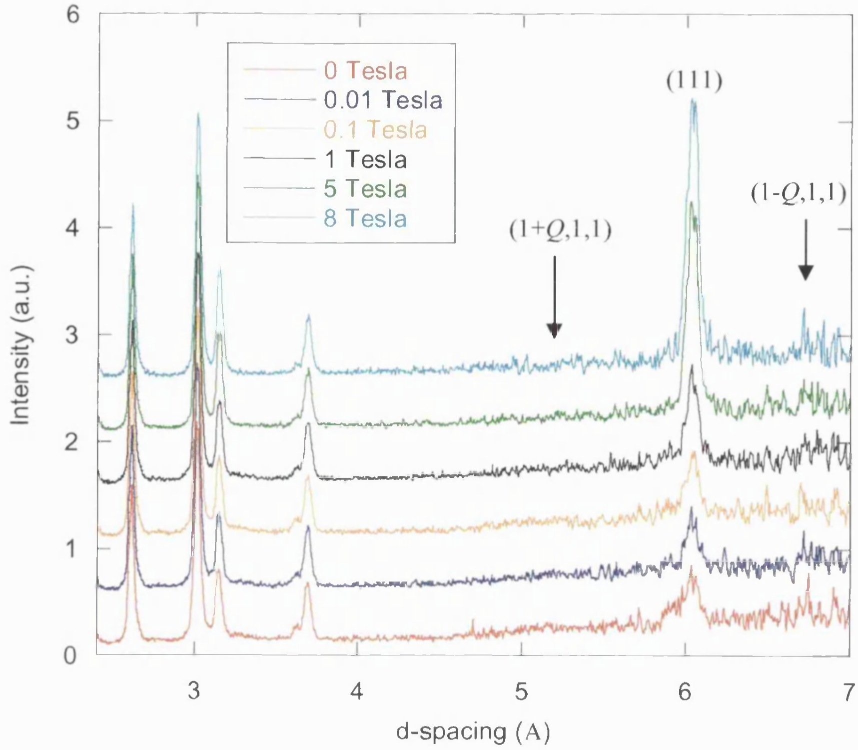

Figure 7.18 *Section of the neutron diffraction pattern of* $Cu_{0.25}Zn_{0.75}Cr_2Se_4$ *at 5 K in applied fields of 0, 0.01, 0.1, 1, 5 and 8 T.*

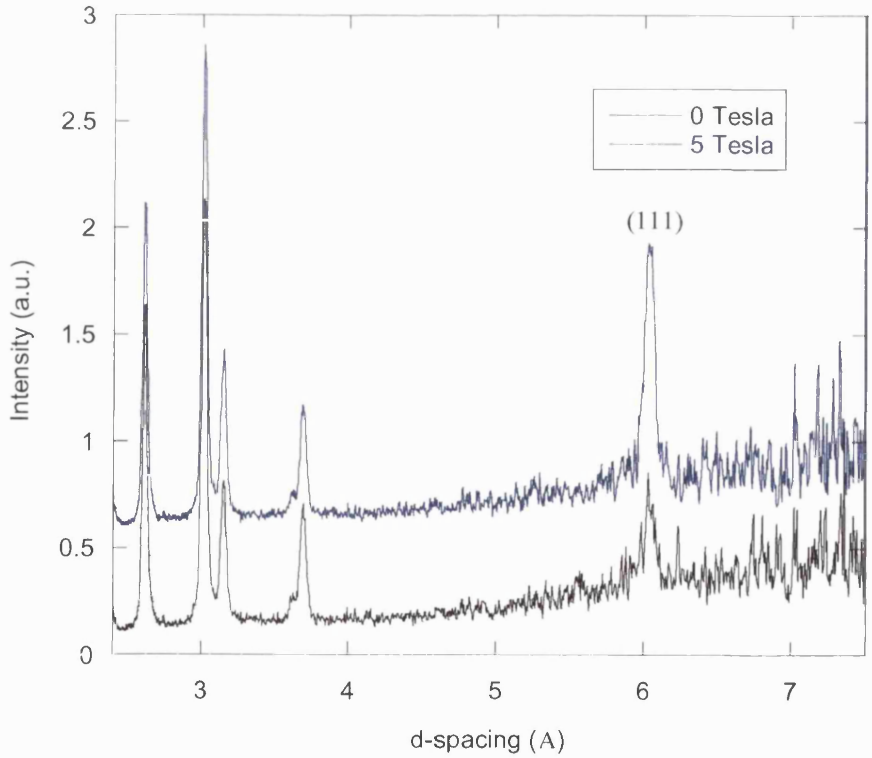

Figure 7.19 *Section of the neutron diffraction pattern of Cu0.25Zn0.75Cr2Se4 at 50 K in applied fields of 0 and 5 T.*

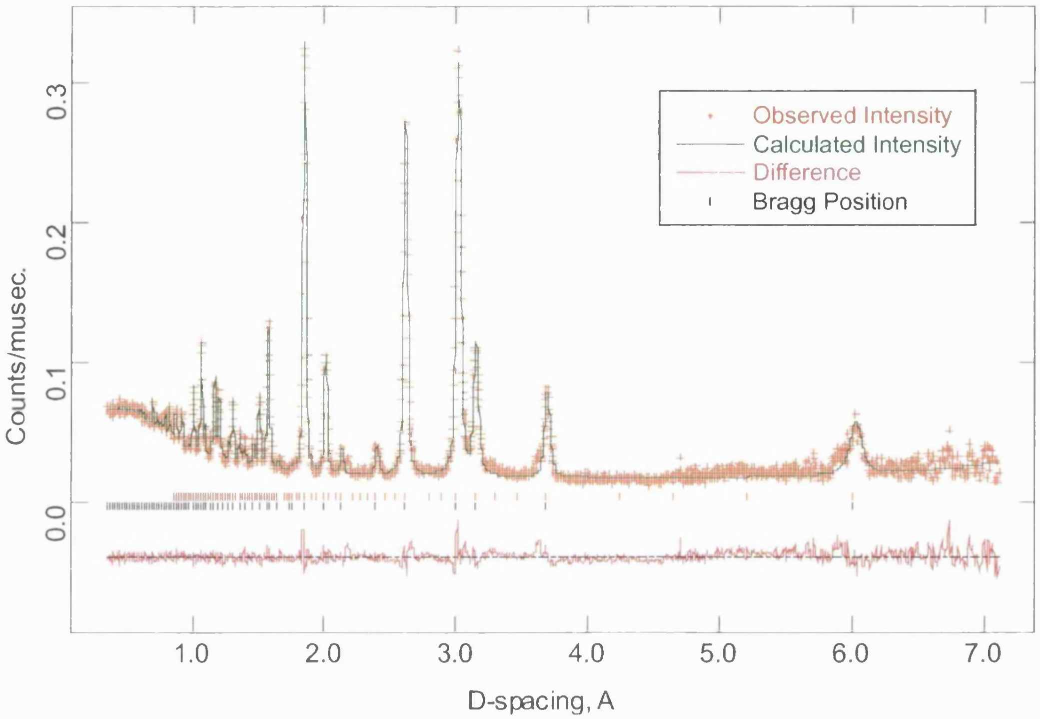

Figure 7.20 *Rietveld refinement of the powder neutron diffraction pattern of* $Cu_{0.25}Zn_{0.75}Cr_2Se_4$ *at 2K, showing the observed, calculated and difference intensity plots.*

Temperature, (K)	Applied Field, (T)	μ_B per Cr	Lattice Parameter, a, (Å)	χ^2	R_{wp}
5	0	1.41(6)	10.4341(2)	1.950	6.31
5	0.01	1.41(6)	10.4402(2)	1.884	6.18
5	0.1	1.50(5)	10.4403(2)	1.947	6.38
5	1	1.56(3)	10.4392(2)	1.999	6.48
5	5	2.51*	10.4371(2)	1.993	6.19
5	8	3.14(3)	10.4350(2)	1.514	6.71
15	0	1.50(7)	10.441(1)	1.624	5.81
25	0	1.54(6)	10.4400(2)	1.899	6.09
50	0	0.84(6)	10.439(1)	1.528	5.67
50	5	2.22(4)	10.4318(2)	1.614	6.42

Table 7.4 *Magnetic moment, lattice parameter and goodness of fit values obtained from the Rietveld refinement of powder neutron diffraction patterns of* $Cu_{0.25}Zn_{0.75}Cr_2Se_4$ *in a selection of temperatures and applied fields.*

Figure 7.20 shows a plot of the Rietveld refinement of $Cu_{0.25}Zn_{0.75}Cr_2Se_4$ at 5 K in zero applied field. Plots of the refinements of all other patterns recorded for $Cu_{0.25}Zn_{0.75}Cr_2Se_4$

---

* In this refinement the best fit to the data was achieved by manually adjusting the magnitude of the moment.

are given in the appendix, section A.4.4. The results of the refinements are shown in table 7.4. The errors quoted are those given in the GSAS program.

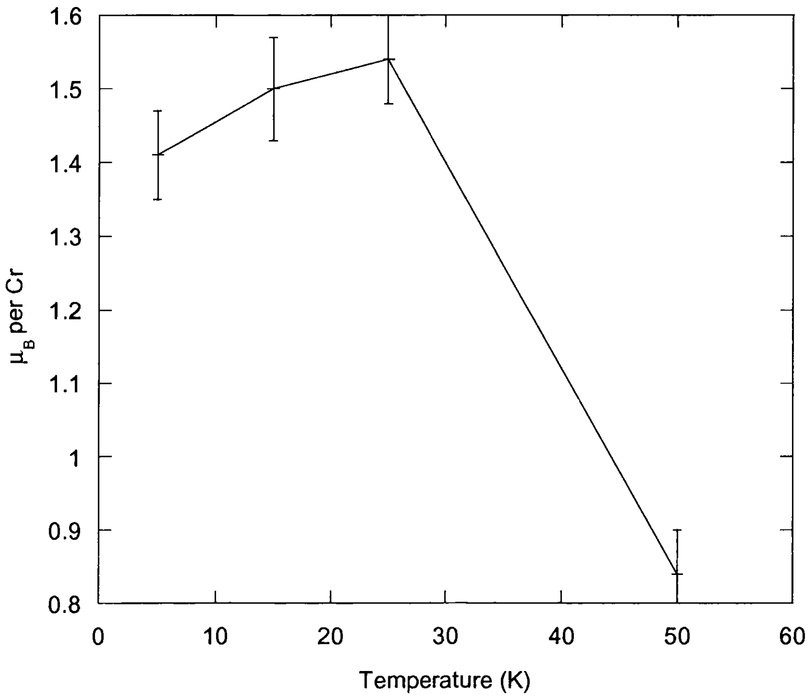

Figure 7.21 *Plot of refined moment vs. temperature for* $Cu_{0.25}Zn_{0.75}Cr_2Se_4$ *in zero applied field.*

Figure 7.21 shows the variation of the refined ferromagnetic chromium moment with temperature. The variation of the size of the moment with temperature agrees well with that seen in the magnetisation versus temperature curves presented in chapter 4, page 118, figure 4.2, however, the values are much larger. The maximum value of the magnetisation, which occurs at approximately 25 K, in the magnetisation versus temperature curves is about 0.33 μ_B per Cr, which is a fifth of the value obtained at 30 K from the refinements of the neutron diffraction data. This feature was also seen for $Cu_{0.09}Zn_{0.91}Cr_2Se_4$ and will be discussed in more detail in the discussion section of this chapter.

This phenomenon is not seen in the 'in field' values of the ferromagnetic moment obtained from the refinements; the values of the moment obtained in 1, 5 and 8 Tesla agree well with the values obtained from the magnetisation versus field measurements, presented in chapter 4, page 129, figure 4.12. Figure 7.22 shows the variation of refined moment with applied field at 5 and 50 K. It is difficult to identify a clear trend in the behaviour of the moment at low field at 5 K as the errors are large compared with the variation in the values. In addition, the poor quality of the data at high d-spacing makes accurate determination of small changes in the value of the moment difficult, as the change in intensity of the (111) peak is slight.

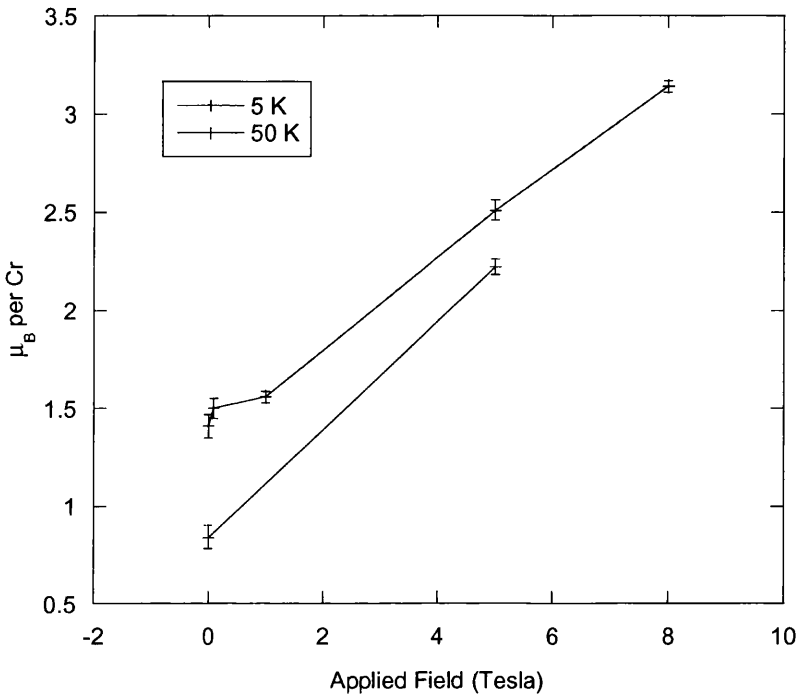

Figure 7.22 *Plot of refined moment vs. applied field for* $Cu_{0.25}Zn_{0.75}Cr_2Se_4$ *at 5 and 50 K.*

The refined lattice parameters are also recorded in table 7.4; there appears to be no clear correlation with either temperature or applied field. It must be concluded that the data is not of sufficient quality to give an accurate determination of subtle changes in the lattice parameter. The value of the lattice parameter obtained from the Rietveld refinement of room temperature X-ray powder diffraction data, presented in chapter 3, was 10.4596(6) Å.

7.4 Discussion

Analysis of the powder neutron diffraction refinements has revealed some interesting features in the magnetic behaviour of the $Cu_{1-x}Zn_xCr_2Se_4$ series.

Analysis of the neutron diffraction patterns of $ZnCr_2Se_4$ in zero applied field at low temperature has shown that there satellite peaks to the (111) and (311) reflections which correspond to an antiferromagnetic spiral structure, in agreement with previously reported work on the neutron diffraction of $ZnCr_2Se_4$ [4, 5]. The peaks are not seen above 20 K, indicating that a transition to a paramagnetic state has occurred; this is concurrent with the results of the magnetometry experiments reported in chapter 4.

The neutron diffraction experiments performed in applied fields reveal an increase in the intensity of the (111) peak corresponding to the emergence of an ordered ferromagnetic moment on the chromium ions. In high fields (8 Tesla) the antiferromagnetic peaks disappear altogether; this suggests that the application of a high field is aligning the chromium moments in the spiral structure towards the direction of the field and hence driving them into ferromagnetic order. The variation of the refined magnetic moment with applied field corresponds well to that of the magnetic moment obtained from the magnetisation measurements in both behaviour and magnitude.

The neutron diffraction measurements performed on $Cu_{0.05}Zn_{0.95}Cr_2Se_4$ have shown that there are no antiferromagnetic peaks visible at low temperature. This indicates that there is no long range antiferromagnetic order in the magnetic structure, supporting the conclusions drawn from the magnetisation data (see chapter 4) and various literature reports [11] that this compound has a glassy magnetic structure.

The neutron diffraction experiments performed in an applied field show an increase in the intensity of the (111) peak with an increase in the applied field. This increase was proportionally much greater than observed for $ZnCr_2Se_4$, indicating that the chromium moments in $Cu_{0.05}Zn_{0.95}Cr_2Se_4$ are more easily rotated towards an applied field than in $ZnCr_2Se_4$. The behaviour of the chromium moment with field in $Cu_{0.05}Zn_{0.95}Cr_2Se_4$ corresponds to that seen in the magnetisation versus field measurements. The driving of the magnetic structure into a ferromagnetically ordered state from a glassy state is consistent with the findings of a large, negative magnetoresistance effect at low temperature as reported in chapter 5. The proposed mechanism for this magnetoresistance effect involves the formation of ferromagnetic double exchange clusters in the presence of an applied field which facilitate conduction by increasing the mobility of the conduction electrons.

The neutron diffraction measurements performed on $Cu_{0.09}Zn_{0.91}Cr_2Se_4$ reveal peaks due to the antiferromagnetic spiral structure at low temperature in zero applied field. This shows that there is ordered magnetism at low temperature here unlike in $Cu_{0.05}Zn_{0.95}Cr_2Se_4$. The satellite peaks are not visible above 15 K indicating that there has been a transition to a ferromagnetic state or paramagnetic state. The results of the magnetisation measurements on this compound have revealed that this transition is not to a simple paramagnetic state (see chapter 4, section 4.3.1.1) so we can assume that the transition is to a ferromagnetic state.

The neutron diffraction measurements performed in an applied field of 5 Tesla reveal an increase in the chromium moment of approximately the same magnitude at 2 and 50 K, showing that an aligned, rather than a disordered state is reached above 15 K. This increase in moment appears to be proportionally greater than is seen with applied field for $Cu_{0.05}Zn_{0.95}Cr_2Se_4$ and $ZnCr_2Se_4$ although a direct comparison cannot be made as these compounds were not measured in 5 Tesla.

The neutron diffraction measurements performed on $Cu_{0.25}Zn_{0.75}Cr_2Se_4$ do not show any clear antiferromagnetic peaks at low temperature although the noise in the data makes it difficult to confirm this. Neutron diffraction experiments by Ikubo *et. al.* [6]on $Cu_{0.3}Zn_{0.7}Cr_2Se_4$ have shown antiferromagnetic peaks at low temperature and the magnetisation versus temperature measurements reported in chapter 4 of this thesis do show a transition at approximately 20 K which was thought to correspond to a transition to an incommensurate spiral antiferromagnetic spiral structure.

The response of the refined magnetic moment to an applied field at 5 K compares well with that found from the magnetisation versus temperature measurements reported in chapter 4.

Where it was possible to refine the zero field chromium moments at various temperatures, it was found that a significantly larger value of the moment was derived from the neutron diffraction measurements than from the 100 Gauss magnetisation versus field measurements, reported in chapter 4. This effect has been observed previously in a study by Ikubo *et. al.* of $Cu_{0.7}Zn_{0.3}Cr_2Se_4$ and $Cu_{0.5}Zn_{0.5}Cr_2Se_4$ [6].

They compared the values of the Cr moment derived from neutron diffraction experiments in zero field with those derived from magnetisation measurements recorded in a field of 1 Tesla over a temperature range of 5 to 400 K. It was found that the values obtained from the neutron diffraction measurements were approximately 20 percent higher than the values obtained from the magnetisation measurements over the whole temperature range. The explanation for this phenomenon arises from the difference in the way that the moment is measured by neutron diffraction and DC magnetometry.

In the magnetometry measurements, the magnetisation of the whole sample is measured, typically over a length scale of a few millimetres. The neutron diffraction measurement measures the moment over a length scale of approximately 10,000 Å. If there are many ferromagnetic domains present in the sample, at low field these domains will not all be aligned relative to each other. In the magnetometry measurement, the value obtained for the moment is reduced by a cancelling effect of the moments in misaligned ferromagnetic domains. In neutron diffraction, the length scale of the measurement is small enough to measure the moment of each domain independently and therefore the value of the moment obtained is higher than that from the magnetometry measurement. This effect is not seen in high fields (above ~1 Tesla) as the ferromagnetic domains have been aligned towards the field and therefore the magnetometry value of the moment is not reduced.

For all the samples studied, some general observations should be made concerning the accuracy of the refined values of the chromium moment. As mentioned previously, the majority of the magnetic scattering is seen at high d-spacing and consequently most of the information on the size of the ferromagnetically ordered moment is contained in the intensity of the (111) peak. There was considerable difficulty in refining the peak shape correctly in all refinements carried out and often these problems gave rise to correlations between the size of the chromium moment and the peak profile parameters. There were also difficulties in fitting the background correctly at high d-spacing due to the high signal to noise ratio.

Where the moment is large (*i.e.* in high applied fields), the intensity of the (111) peak is also large and therefore errors in the magnitude of the moment arising from poor peak shape modelling and a badly fitting background are relatively small. However, when the (111) peak is small (*i.e.* at zero field and small applied fields) these errors become much more significant and should be taken into consideration.

In this study, there did not appear to be any significant correlation between the structural lattice parameters and applied field or temperature. This is likely to be due to the problems experienced in refining the peak shape correctly which, as the peak shape was not symmetrical, could have led to the peak positions being inaccurately determined which in turn would cause inaccuracies in the lattice parameter. For all the compounds studied the lattice parameters seemed to compare reasonably with the lattice parameters obtained from the room temperature X-ray diffraction experiments, taking into account thermal expansion.

It is unfortunate that more accurate values of the lattice parameters could not be obtained from the refinements as there have been literature reports of a magnetostriction effect in compounds in this series. Kusk *et.al.* measured the lattice parameter of a selection of ferromagnetic compounds from the $Cu_{1-x}Zn_xCr_2Se_4$ series in the temperature range 100-500 K and compared the results with theoretical values of the lattice parameter, calculated using the Grüneisen-Debye theory [10].

They found a good agreement of the theoretical and calculated values at high temperature, in the paramagnetic region, but at lower temperatures, where the compounds are ferromagnetically ordered, they observed a spontaneous positive magnetostriction effect. It would be interesting to investigate this further for both the ferromagnetic and antiferromagnetic compounds in the $Cu_{1-x}Zn_xCr_2Se_4$ series and to study what effect an applied field may have on the magnetostriction. These experiments would best be performed using X-ray rather than neutron diffraction techniques as this would eliminate the magnetic scattering from the patterns, simplifying the refinement process and enabling a more accurate determination of the lattice parameter.

7.5 References

1. Robbins, M., Lehmann, H.W., and White, J.G., *J. Phys. Chem. Solids*, 1967. **28**: p. 897.
2. Yamashita, O., Yamaguchi, Y., Nakatani, I., Watanabe, H., and Masumoto, K., *J. Phys. Soc. Japan*, 1979. **46**: p. 1145-1151.
3. Akimitsu, J., Siratori, K., Shirane, G., Iizumi, M., and Watanabe, T., *J. Phys. Soc. Jpn.*, 1978. **44**(1): p. 172-180.
4. Plumier, R., *J. Appl. Phys.*, 1966. **37**(3): p. 964-965.
5. Hidaka, M., Tokiwa, N., Wai, T.T., Fujii, H., Ohoyama, K., Mizusima, S., Sakaurai, J., Ichikawa, F., and Itoh, K., *Phase Transit.*, 2002. **75**(3): p. 273-287.
6. Iikubo, S., Yasui, Y., Oda, K., Ohno, Y., Kobayashi, Y., Sato, M., and Kakurai, K., *J. Phys. Soc. Jpn.*, 2002. **71**(11): p. 2792-2799.
7. *http://www.isis.rl.ac.uk/disordered/gem/gem_home.htm*
8. Larson, A.C. and Von Dreele, R.B., *General Structural Analysis System*. 1998, University of California.
9. Rodriguez-Carvajal, J., *Fullprof*. 2003.
10. Kusz, J., Juszczyk, S., and Warczewski, J., *J. Appl. Crystallogr.*, 1988. **21**: p. 898-901.
11. Groń, T., Duda, H., and Warczewski, J., *Phys. Rev. B*, 1990. **41**(18): p. 12424.

Chapter 8 Conclusions and future work

8.1 Conclusions

The aim of the work reported in this thesis was to investigate fully the magnetic and electronic properties of the $Cu_{1-x}Zn_xCr_2Se_4$ series to attain an understanding of the electronic interactions occurring within the compounds. The focus of the work was on the region of the series with $x \geq 0.8$. In addition, the magnetism of the $Cu_{1-x}Zn_xCr_2Se_{4-y}S_y$ and $CuCr_2Se_{4-y}Br_y$ series has been studied to show how the nature of the X-site species can effect the Cr-Cr interactions.

Compounds in the $Cu_{1-x}Zn_xCr_2Se_4$ series, where $1 \geq x \geq 0$, were successfully prepared using standard solid state synthesis methods. It was found that there was limited solubility in the series where $x \leq \sim 0.9$ which could be partially overcome by quenching the reaction mixture after firing. Compounds in the $Cu_{1-x}Zn_xCr_2Se_{4-y}S_y$ and $CuCr_2Se_{4-y}Br_y$ series were also prepared; solubility in these series was limited to $y \leq 2$ and $y \leq 0.75$ respectively.

The magnetic properties of all compounds prepared were investigated by DC SQUID magnetometry. In the $Cu_{1-x}Zn_xCr_2Se_4$ series it was found that there was a change in magnetic behaviour across the series. Compounds with $0 < x \leq 0.8$ are ferromagnetic with high T_C values that decrease with increasing x; the ferromagnetic transitions occur over a broad temperature range. In these compounds a low temperature peak is seen in the magnetisation curves at around 20 K corresponding to a transition to a conical ferromagnetic structure at low temperature.

For compounds with $0.80 < x \leq 0.91$, a conical ferromagnetic structure exists; this has been confirmed for $Cu_{0.09}Zn_{0.91}Cr_2Se_4$ by means of powder neutron diffraction measurements which show evidence for a low temperature incommensurate spiral spin structure. The magnitude of the magnetisation of these compounds at low temperature is typical of that of a ferromagnet, indicating that the spiral structure has a strong ferromagnetic component. There is a maximum in the magnetisation versus temperature curve at approximately 20 K, followed by a gradual decrease in magnetisation with increasing temperature. The neutron diffraction measurements show that the ordered conical structure is not present at 50 K; however, the magnetisation results show that a simple paramagnetic state has not been reached below 400 K. Therefore it is likely that a glassy or blocked magnetic state exists above 20 K.

In compounds where $0.92 \leq x < 1.00$, there is evidence to show that a spin glass magnetic state may exist below 20 K. Neutron diffraction studies of $Cu_{0.05}Zn_{0.95}Cr_2Se_4$ have shown there to be no long range ordered magnetism below 20 K and AC susceptibility measurements have revealed a frequency dependence of the χ" peak, indicative of glassy magnetic behaviour.

$ZnCr_2Se_4$ was found to be antiferromagnetic with an ordered spiral spin structure below 24 K. There was no evidence for a glassy magnetic state at low temperature in this compound. The magnetic properties of compounds in the $Cu_{1-x}Zn_xCr_2Se_4$ series reported in this thesis agree well with those found in previous studies by other authors [1-4].

The magnetic properties of the $Cu_{1-x}Zn_xCr_2Se_4$ series can be explained in terms of the relative strengths of the Cr-Cr ferromagnetic and antiferromagnetic exchange interactions. The ferromagnetic interactions are strengthened by the double exchange mechanism. As the double exchange mechanism can only occur when there is Cr^{4+} present and the addition of Cu^+ to the system produces Cr^{4+}, it follows that the ferromagnetic interactions are strengthened with decreasing x. At $x = 1$, the ferromagnetic interactions are relatively weak (although they are still strong enough to give a positive value of θ_{cw}) and $ZnCr_2Se_4$ is an antiferromagnet with a spiral spin structure. Here, the nearest neighbour chromium spins are ferromagnetically aligned (hence the positive θ_{cw}) but the overall order is antiferromagnetic. As Cu^+ is introduced into the system, the double exchange mechanism can start to operate, increasing the strength of the ferromagnetic interactions. This leads to a canting of the spins in the antiferromagnetic spiral structure, leading to an increase in the magnetisation of the compounds and increasing, positive values of θ_{cw}. This also appears to lead to magnetic disorder in some compounds with large values of x (*e.g.* $x = 0.95$). When a field is applied to these compounds, long range ferromagnetic order is induced.

With increasing copper content, the ferromagnetic interactions are strengthened. At low temperature a conical ferromagnetic structure exists and at high temperature the structure is collinear. It has been found that the ordering temperature for the low temperature conical ferromagnetic structure is dependent on the relative strengths of the ferromagnetic and antiferromagnetic near neighbour interactions. High pressure AC susceptibility measurements have shown that decreasing the Cr-Cr bond distance (hence strengthening the antiferromagnetic direct exchange interaction relative to the ferromagnetic super exchange interaction) resulted in a lowering of the ordering temperature of the conical magnetic structure (T_N). Analogous behaviour was seen in the $Cu_{1-x}Zn_xCr_2Se_{4-y}S_y$ series where increasing the sulphur content (hence weakening the ferromagnetic superexchange interaction due to the smaller ionic radius of S^{2-} compared with Se^{2-}) resulted in a decrease in T_N.

Magnetoresistance measurements have been carried out on four representative compounds from the $Cu_{1-x}Zn_xCr_2Se_4$ series, namely $ZnCr_2Se_4$ (an antiferromagnet with a spiral spin structure), $Cu_{0.05}Zn_{0.95}Cr_2Se_4$ (a compound with a glassy magnetic structure that orders ferromagnetically in an applied field), $Cu_{0.09}Zn_{0.91}Cr_2Se_4$ (a conical ferromagnet) and $Cu_{0.25}Zn_{0.75}Cr_2Se_4$ (a collinear ferromagnet with a low temperature conical ferromagnetic structure). It was found that the resistivity of these compounds decreased dramatically with decreasing x, consistent with the double exchange mechanism increasing the mobility of the carriers.

The magnetoresistance effect in compounds with $x = 1$, 0.95 and 0.91 showed a crossover from a negative effect at low temperature to a positive effect at higher temperature. In $Cu_{0.05}Zn_{0.95}Cr_2Se_4$ this change in behaviour was found to correspond to a change in conduction mechanism from variable range hopping (VRH, below ~ 30 K) to semiconducting (above ~ 40 K). In the VRH conduction regime it is proposed that the mechanism for magnetoresistance involves the double exchange mechanism. It is likely that clusters of ferromagnetically ordered spins exist in $Cu_{0.05}Zn_{0.95}Cr_2Se_4$ due to the competition that exists between the ferromagnetic and antiferromagnetic near neighbour interactions. Applying a field increases the extent of these ferromagnetic clusters and this in turn increases the mobility of the conduction electrons via the double exchange mechanism.

The mechanism for the positive magnetoresistance in the semiconducting conduction regime is less clear. It is possible that the application of a field stabilises the ferromagnetic domains to such an extent that the chromium *d* electrons are lowered in energy and the conduction band is depopulated. $Cu_{0.25}Zn_{0.75}Cr_2Se_4$ is metallic and only small, negative magnetoresistance is seen over the whole temperature range studied (4-200 K).

In conclusion, the magnetic and electronic properties of the $Cu_{1-x}Zn_xCr_2Se_4$ series appear to be dictated primarily by the relative strengths of the nearest neighbour ferromagnetic and antiferromagnetic exchange interactions. The magnetic behaviour in all regions of the series represents a compromise between ferromagnetic and antiferromagnetic behaviour. The double exchange mechanism plays an important role in the strengthening of the ferromagnetic interactions and is also responsible for a negative magnetoresistance effect observed across the series.

8.2 Future Work

The work reported in this thesis has revealed many interesting properties of the $Cu_{1-x}Zn_xCr_2Se_4$ series which provide scope for much further investigation.

The magnetoresistance measurements performed on compounds from the $Cu_{1-x}Zn_xCr_2Se_4$ series with high zinc concentration ($x \geq 0.9$) have revealed some interesting effects including a large negative MR effect and a crossover to positive MR at higher temperatures. However the measurements carried out on $Cu_{0.25}Zn_{0.75}Cr_2Se_4$ showed only a small positive effect below 200 K. It cannot be ruled out from these measurements that double exchange CMR effect, as seen in the perovskite manganates, may occur near the T_C (~ 380 K). It would be useful to measure the MR effect of this compound and other ferromagnetic compounds from this series at high temperatures (~ 200- 500 K) to investigate the possibility of a high temperature CMR effect. In order to obtain accurate MR measurements it may be necessary to use samples with greater homogeneity than the pressed powder pellets, such as single crystals or thin films. It may also be interesting to re-examine the MR effect in the high zinc compounds using single crystal or thin film samples which may provide a greater insight into the mechanisms for the observed properties.

In some compounds in the $Cu_{1-x}Zn_xCr_2Se_4$ series with $x \geq 0.9$ a possible spin glass phase was identified. It would be interesting to investigate this further using a variety of techniques, such as muon spin relaxation (μSR), Mössbauer spectroscopy and specific heat experiments which can all provide further insight into the magnetic behaviour of glassy materials.

The high pressure AC susceptibility measurements, reported in chapter 6, provided an insight into the changes in magnetic behaviour with changing Cr-Cr distance. It would be useful to carry out some high pressure X-ray diffraction experiments to complement this work by providing an indication of how the lattice parameter changes with applied pressure.

The neutron diffraction experiments reported in chapter 7 were not able to provide an insight into magnetostriction effects in compounds in the $Cu_{1-x}Zn_xCr_2Se_4$ series. High resolution diffraction experiments in a series of applied fields could be carried out to investigate this further.

8.3 References

1. Iikubo, S., Yasui, Y., Oda, K., Ohno, Y., Kobayashi, Y., Sato, M., and Kakurai, K., *J. Phys. Soc. Jpn.*, 2002. **71**(11): p. 2792-2799.
2. Juszczuk, S., Johansson, C., Hanson, M., and Gogolowicz, M., *Phys. Lett. A*, 1994. **192**(1): p. 429-434.
3. Juszczyk, S. and Gogolowicz, M., *J. Magn. Magn. Mater.*, 1991. **92**(1): p. 388-396.
4. Khan, M.N., Venkatachalam, A., Ahmad, A., and Darshane, V.S., *J. Mater. Sci.*, 1990. **25**: p. 595-598.

Chapter 9 Appendix

A.1 1 Rietveld refinements of compounds in the series $Cu_{1-x}Zn_{2x}Cr_2Se_4$

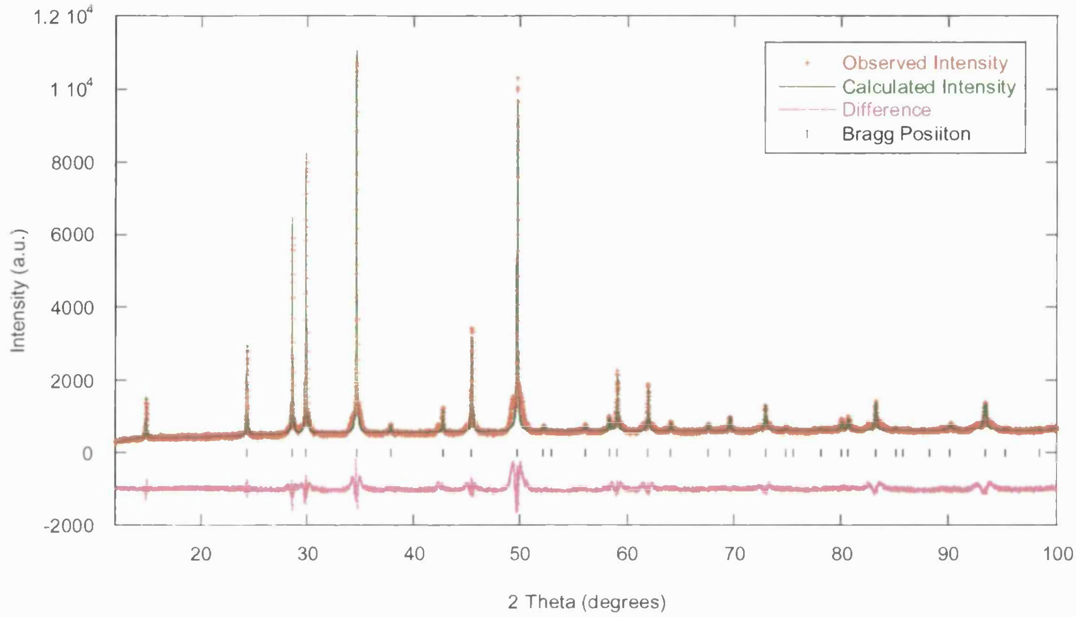

Figure 9.1 *Rietveld refinement of the powder X-ray diffraction pattern of* $Cu_{0.75}Zn_{0.25}Cr_2Se_4$ *showing the observed, calculated and difference intensity plots.*

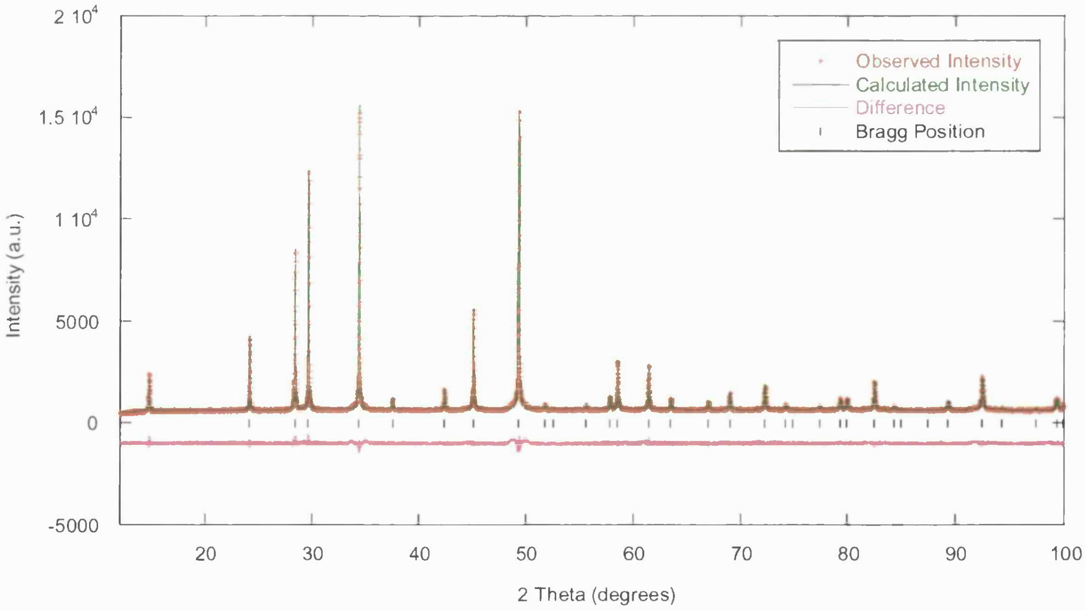

Figure 9.2 *Rietveld refinement of the powder X-ray diffraction pattern of* $Cu_{0.25}Zn_{0.75}Cr_2Se_4$ *showing the observed, calculated and difference intensity plots.*

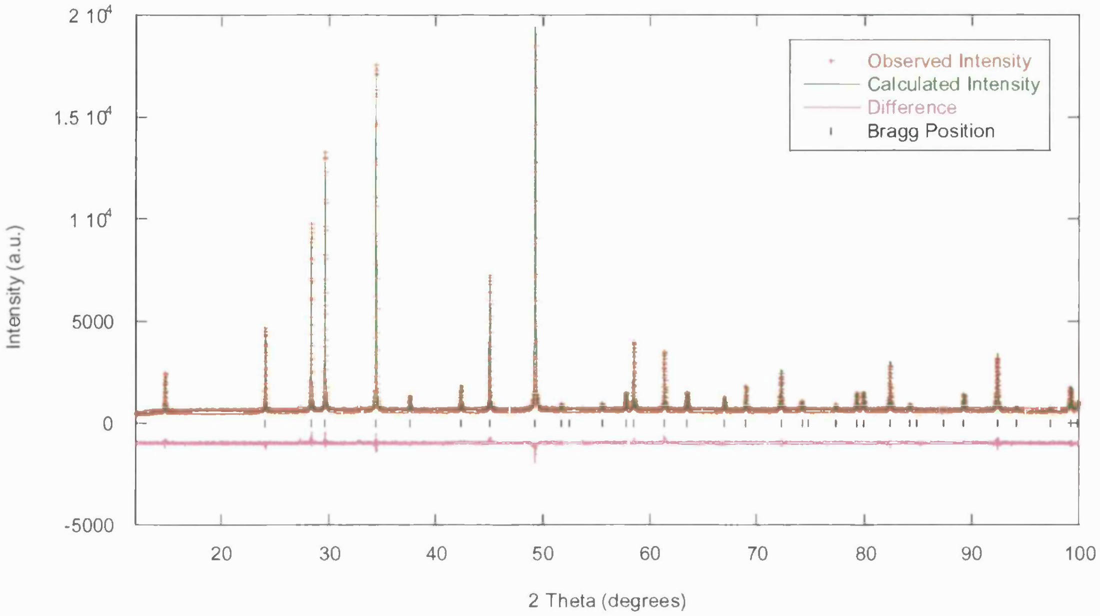

Figure 9.3 *Rietveld refinement of the powder X-ray diffraction pattern of* $Cu_{0.20}Zn_{0.80}Cr_2Se_4$ *showing the observed, calculated and difference intensity plots.*

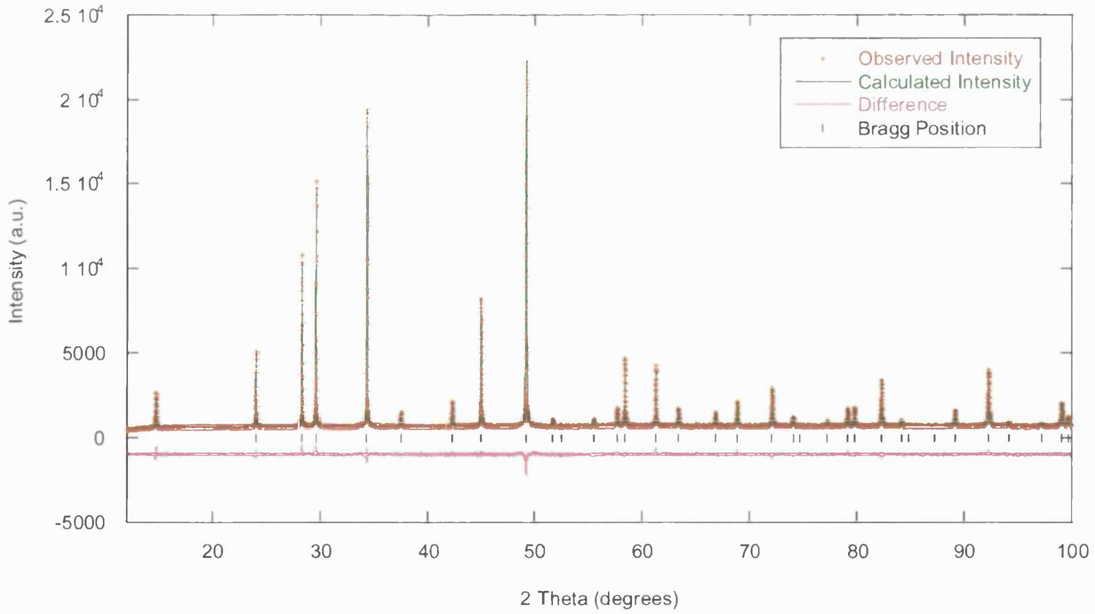

Figure 9.4 *Rietveld refinement of the powder X-ray diffraction pattern of* $Cu_{0.15}Zn_{0.85}Cr_2Se_4$ *showing the observed, calculated and difference intensity plots.*

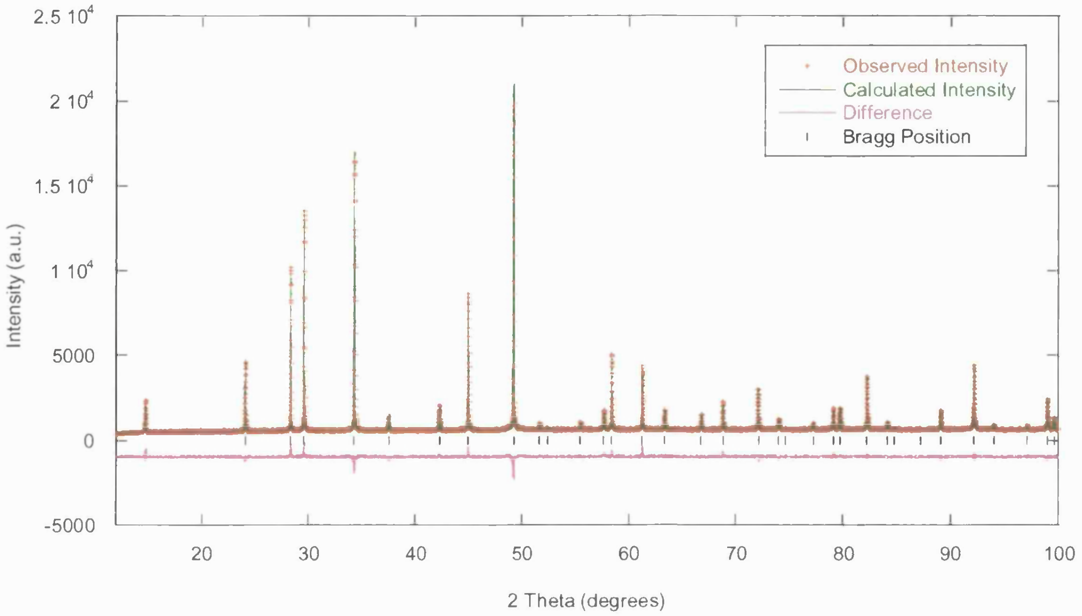

Figure 9.5 *Rietveld refinement of the powder X-ray diffraction pattern of* $Cu_{0.10}Zn_{0.90}Cr_2Se_4$ *showing the observed, calculated and difference intensity plots.*

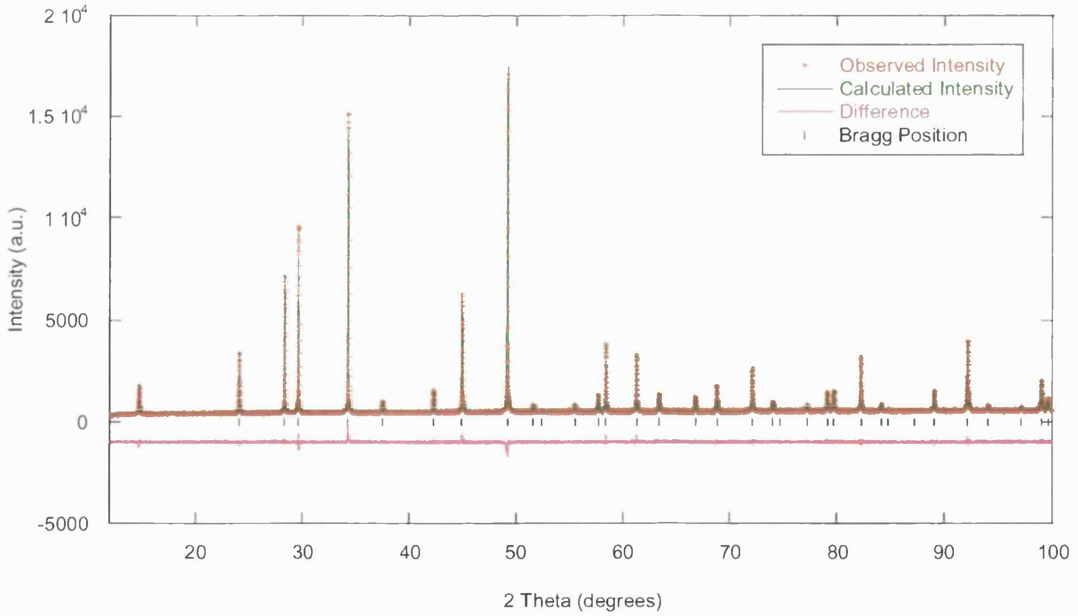

Figure 9.6 *Rietveld refinement of the powder X-ray diffraction pattern of* $Cu_{0.095}Zn_{0.905}Cr_2Se_4$ *showing the observed, calculated and difference intensity plots.*

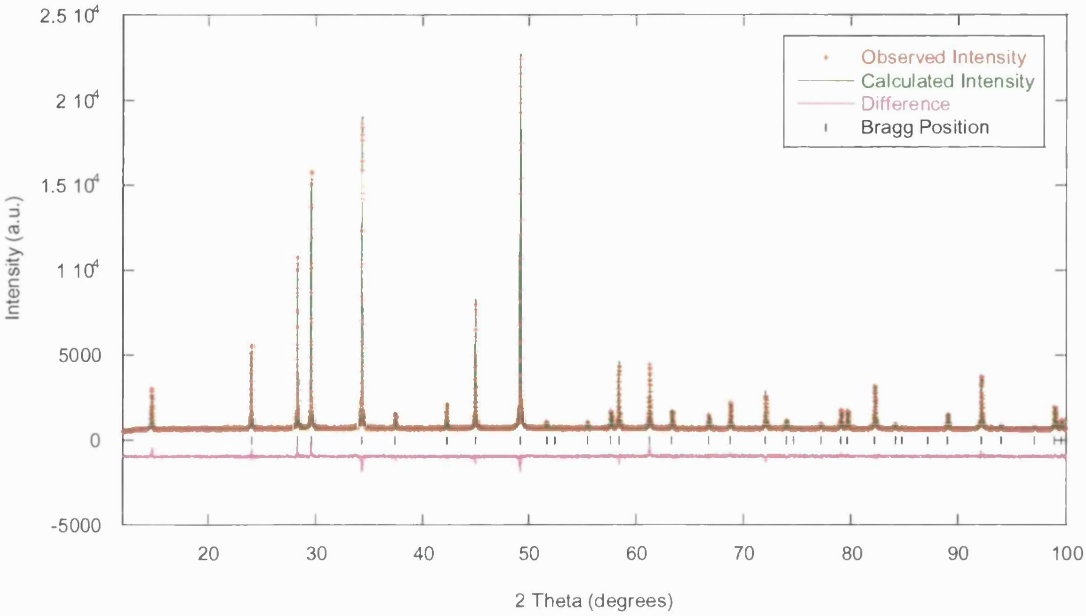

Figure 9.7 *Rietveld refinement of the powder X-ray diffraction pattern of* $Cu_{0.09}Zn_{0.91}Cr_2Se_4$ *showing the observed, calculated and difference intensity plots.*

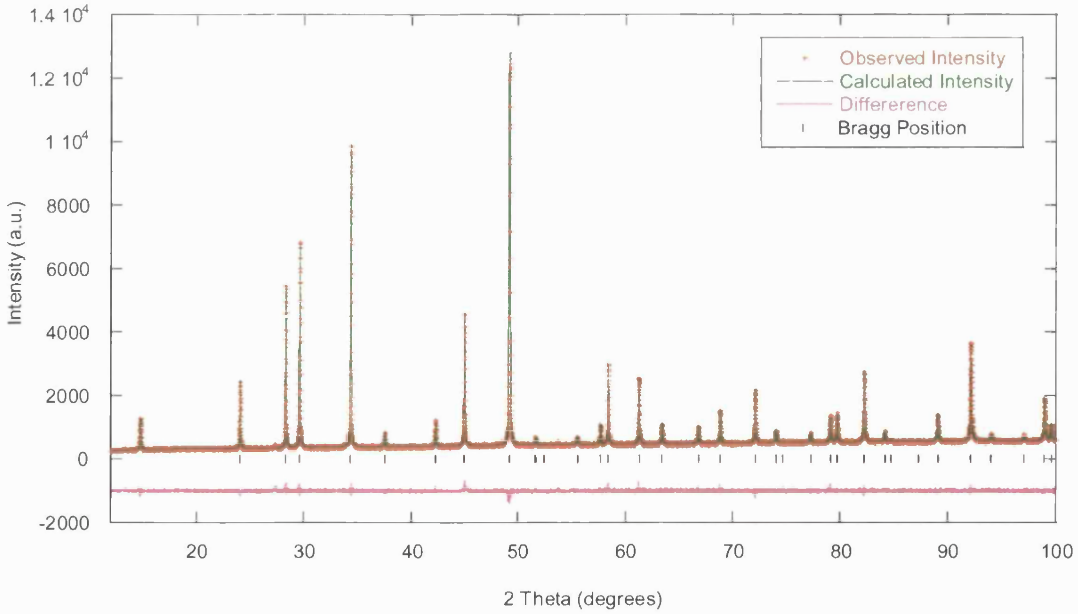

Figure 9.8 *Rietveld refinement of the powder X-ray diffraction pattern of* $Cu_{0.08}Zn_{0.92}Cr_2Se_4$ *showing the observed, calculated and difference intensity plots.*

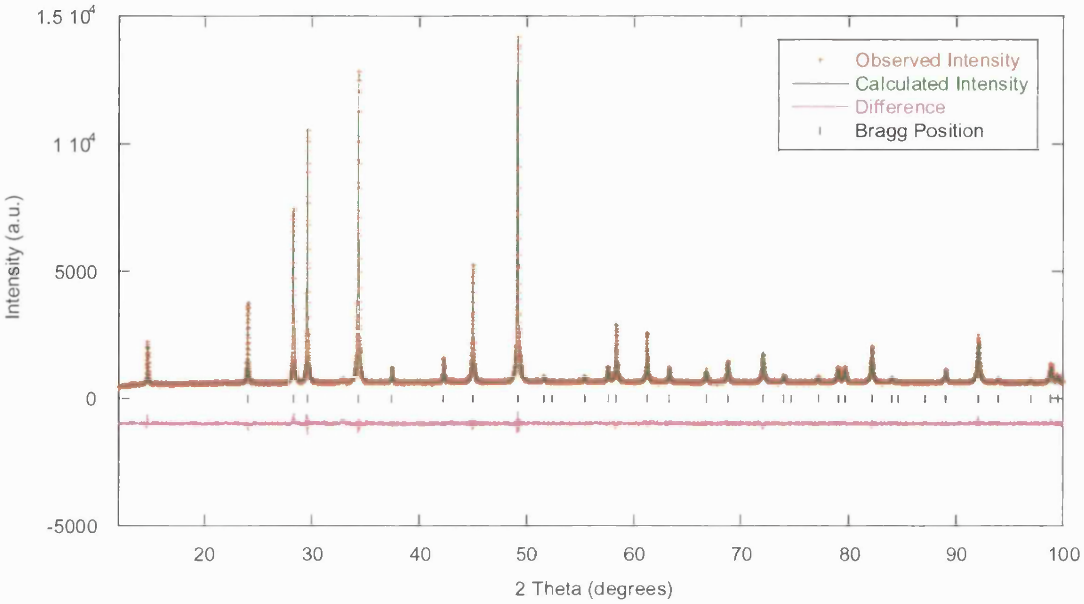

Figure 9.9 *Rietveld refinement of the powder X-ray diffraction pattern of* $Cu_{0.05}Zn_{0.95}Cr_2Se_4$ *showing the observed, calculated and difference intensity plots.*

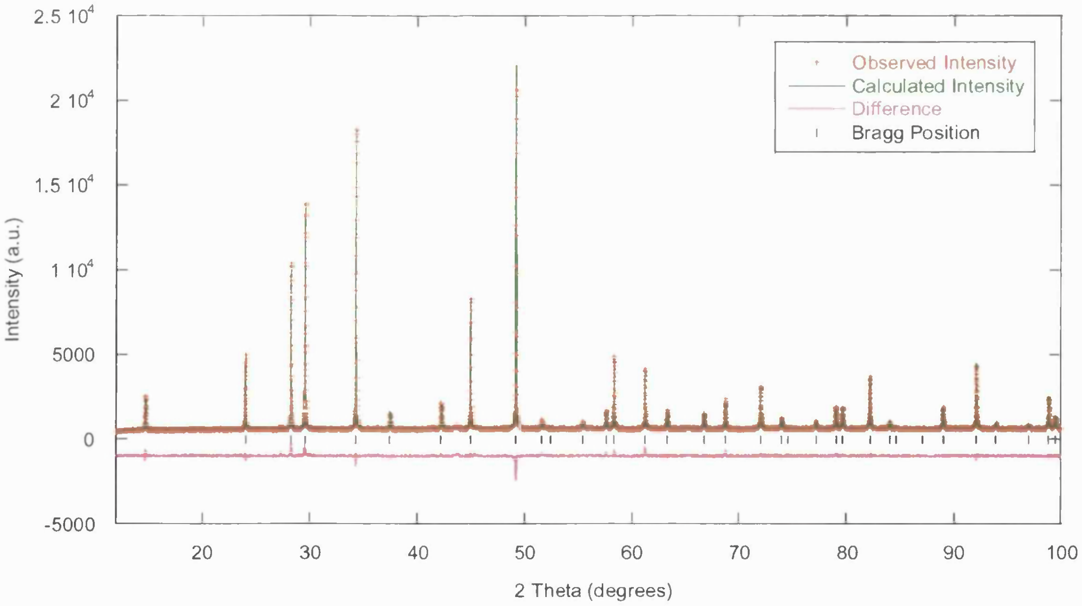

Figure 9.10 *Rietveld refinement of the powder X-ray diffraction pattern of* $Cu_{0.04}Zn_{0.96}Cr_2Se_4$ *showing the observed, calculated and difference intensity plots.*

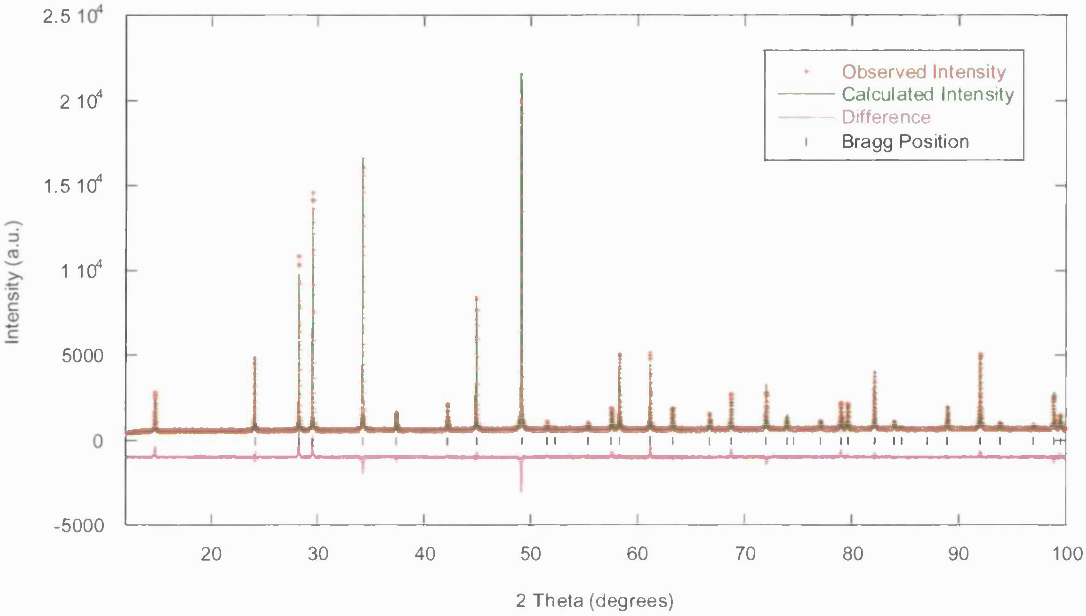

Figure 9.11 *Rietveld refinement of the powder X-ray diffraction pattern of* $Cu_{0.03}Zn_{0.97}Cr_2Se_4$ *showing the observed, calculated and difference intensity plots.*

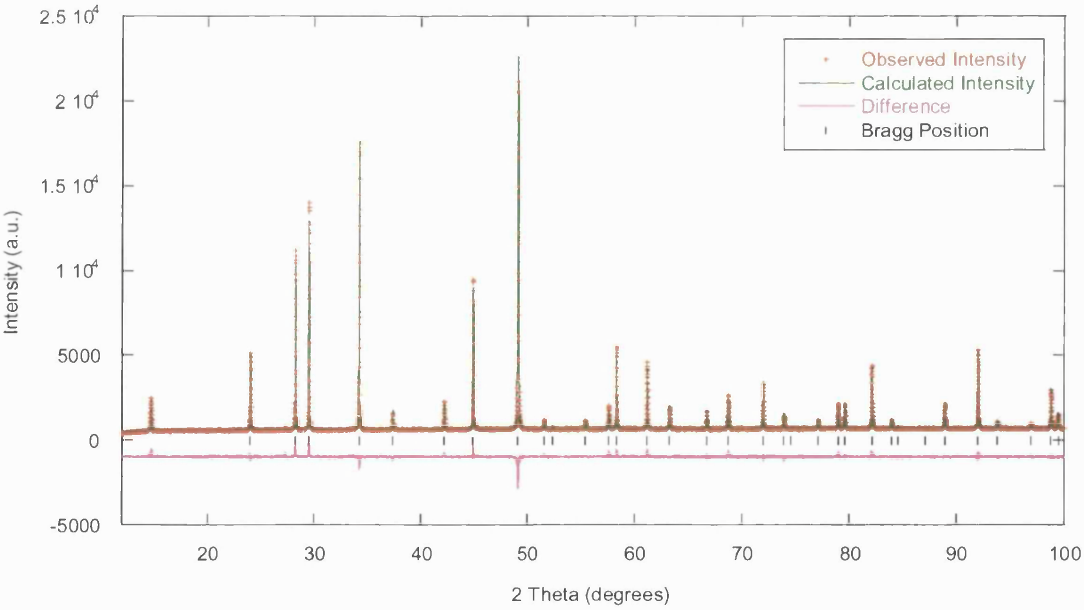

Figure 9.12 *Rietveld refinement of the powder X-ray diffraction pattern of* $Cu_{0.01}Zn_{0.99}Cr_2Se_4$ *showing the observed, calculated and difference intensity plots.*

A.1 2 Rietveld refinements of compounds in the series $Cu_{1-x}Zn_xCr_2Se_{4-y}S_y$

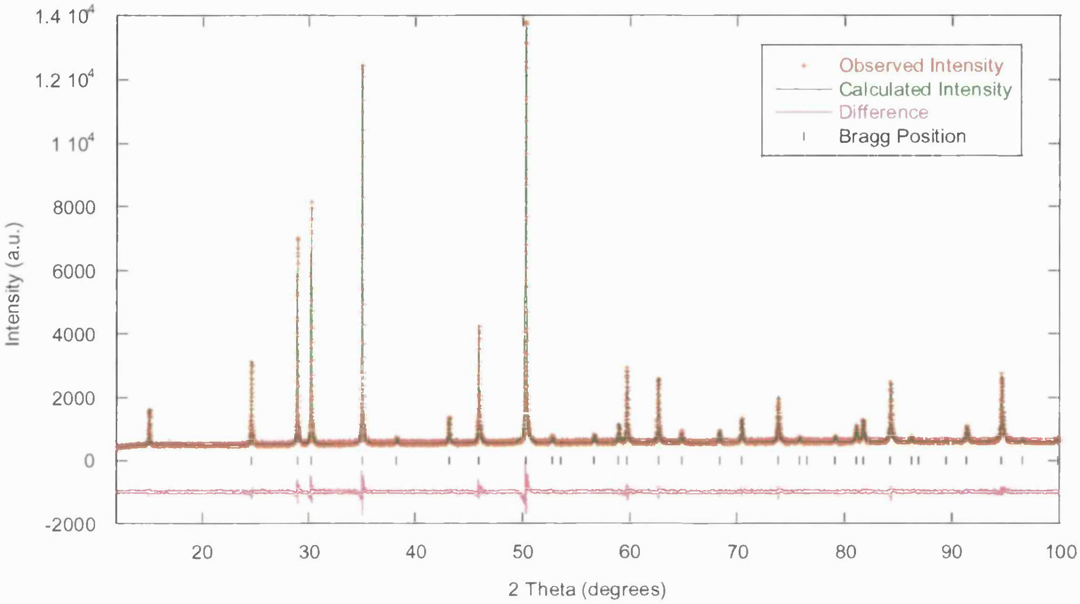

Figure 9.13 *Rietveld refinement of the powder X-ray diffraction pattern of* $CuCr_2Se_{3.5}S_{0.5}$ *showing the observed, calculated and difference intensity plots.*

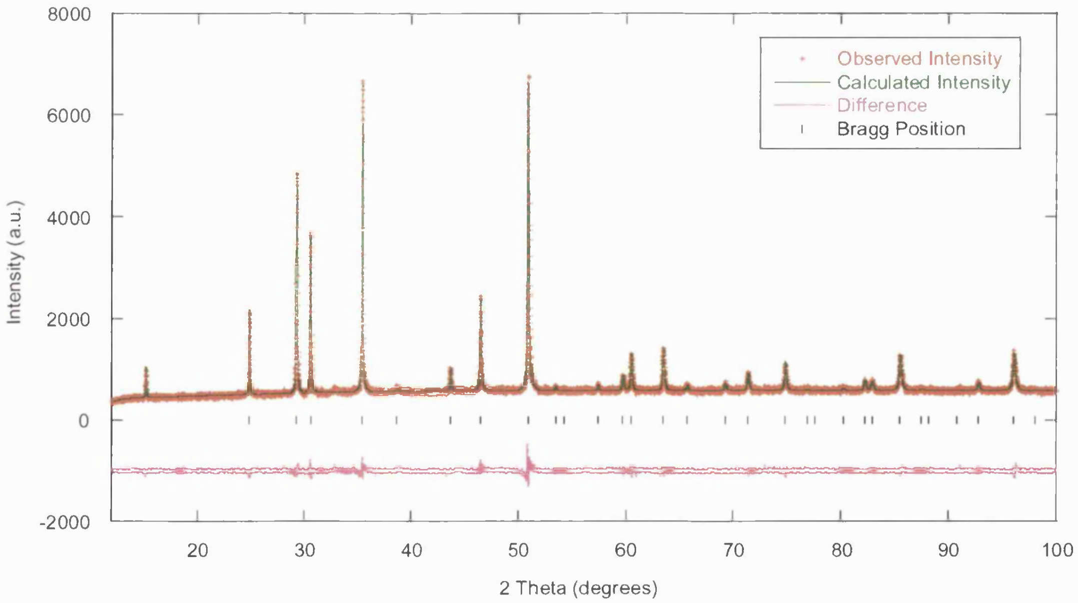

Figure 9.14 *Rietveld refinement of the powder X-ray diffraction pattern of* $CuCr_2Se_{2.5}S_{1.5}$ *showing the observed, calculated and difference intensity plots.*

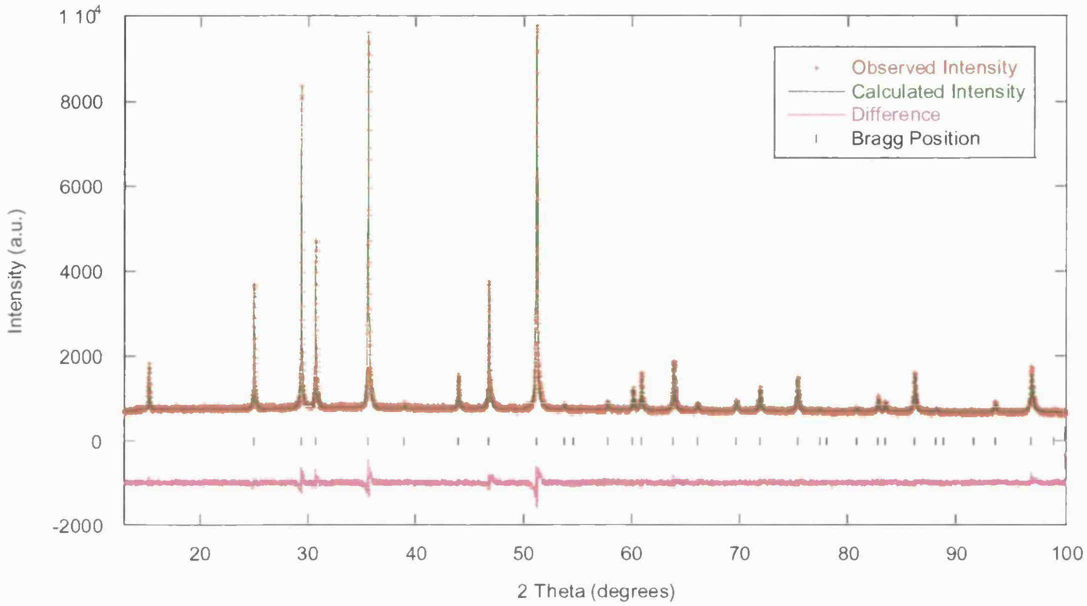

Figure 9.15 *Rietveld refinement of the powder X-ray diffraction pattern of* $CuCr_2Se_{2.0}S_{2.0}$ *showing the observed, calculated and difference intensity plots.*

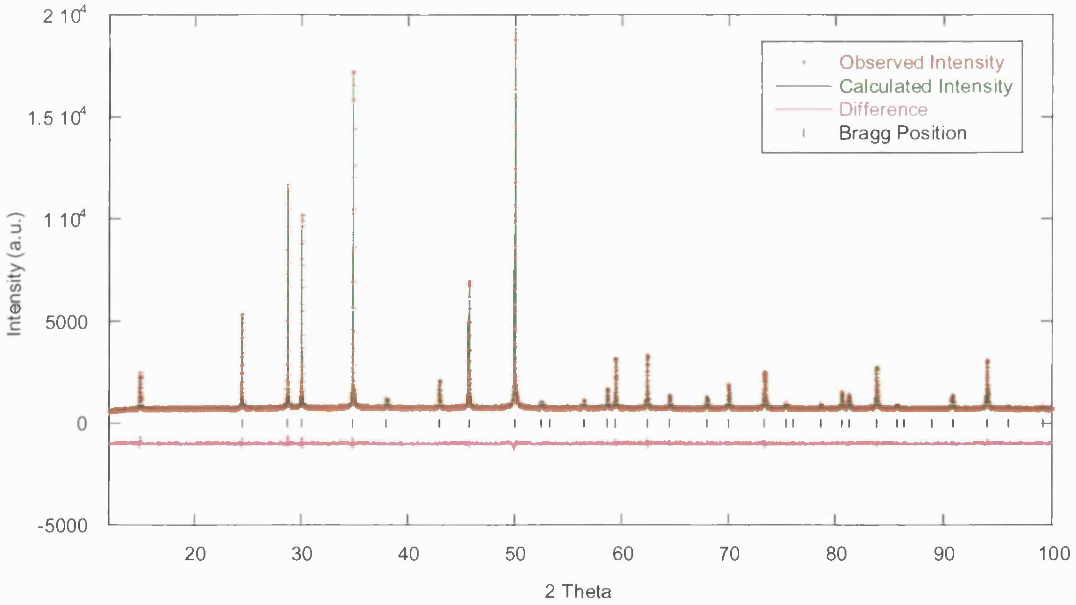

Figure 9.16 *Rietveld refinement of the powder X-ray diffraction pattern of* $Cu_{0.30}Zn_{0.70}Cr_2Se_{3.0}S_{1.0}$ *showing the observed, calculated and difference intensity plots.*

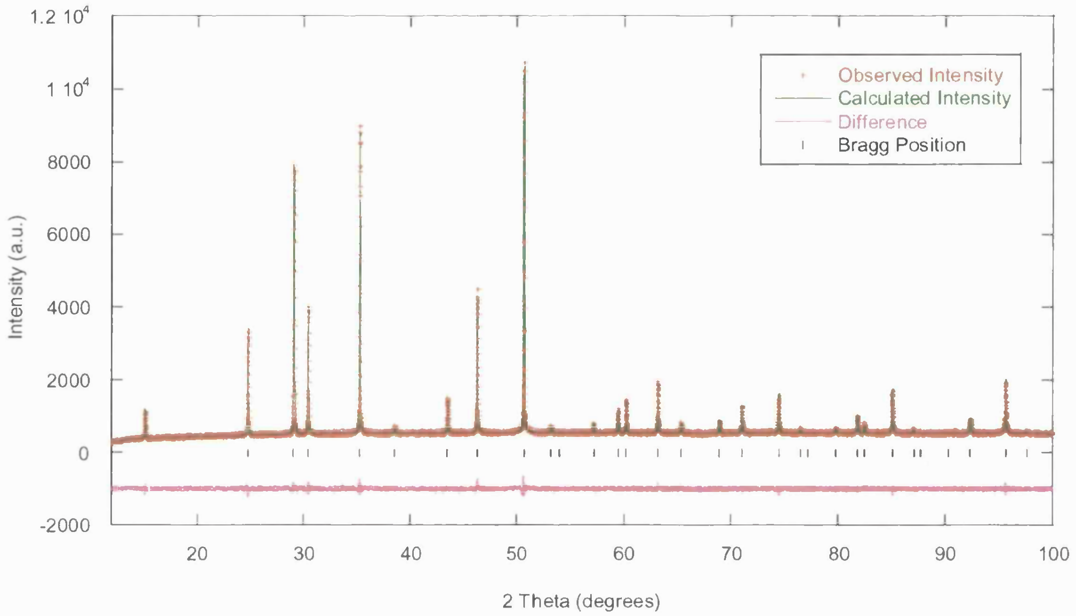

Figure 9.17 *Rietveld refinement of the powder X-ray diffraction pattern of* $Cu_{0.30}Zn_{0.70}Cr_2Se_{2.0}S_{2.0}$ *showing the observed, calculated and difference intensity plots.*

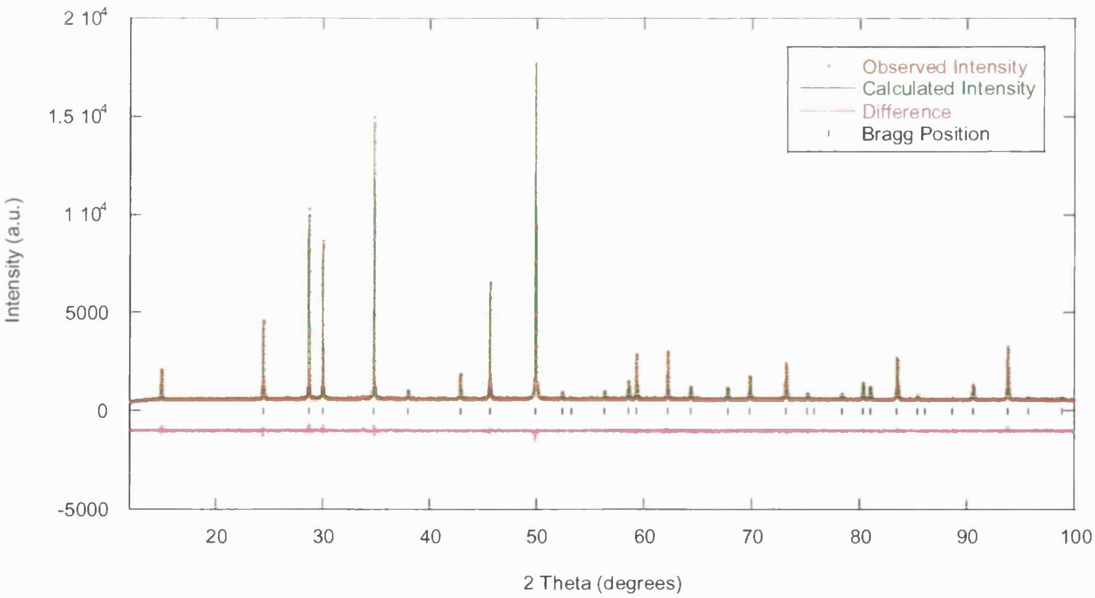

Figure 9.18 *Rietveld refinement of the powder X-ray diffraction pattern of* $Cu_{0.10}Zn_{0.90}Cr_2Se_{3.0}S_{1.0}$ *showing the observed, calculated and difference intensity plots.*

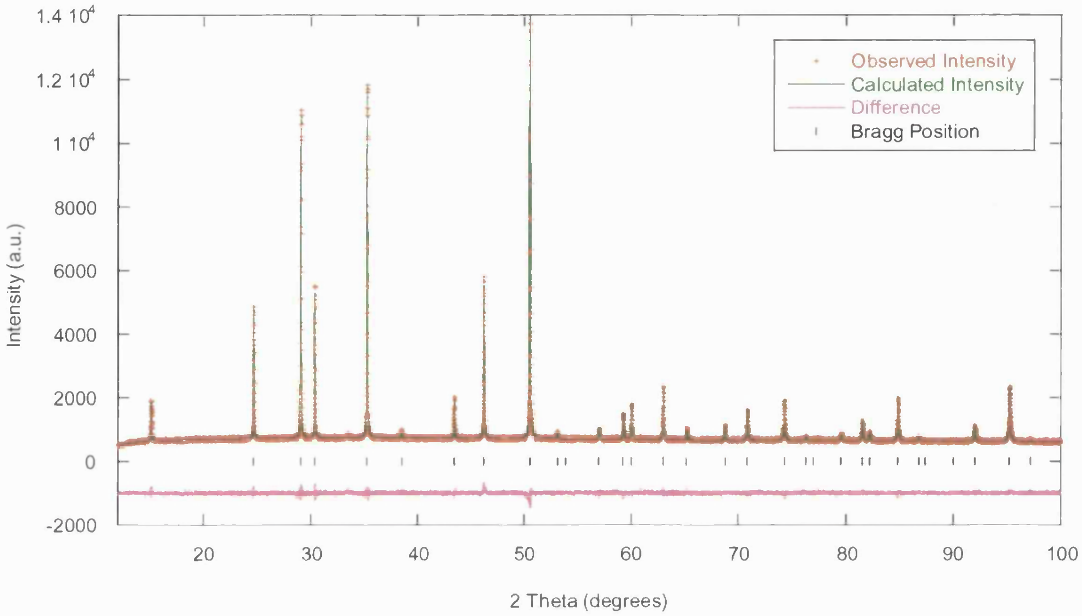

Figure 9.19 *Rietveld refinement of the powder X-ray diffraction pattern of* $Cu_{0.10}Zn_{0.90}Cr_2Se_{2.0}S_{2.0}$ *showing the observed, calculated and difference intensity plots.*

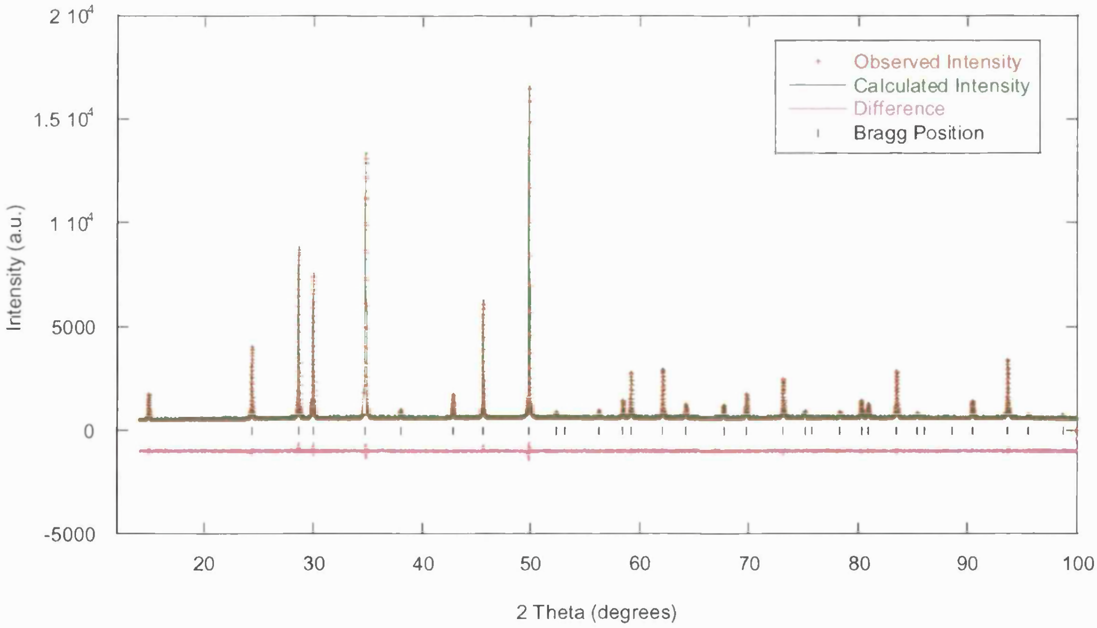

Figure 9.20 *Rietveld refinement of the powder X-ray diffraction pattern of* $Cu_{0.05}Zn_{0.95}Cr_2Se_{3.0}S_{1.0}$ *showing the observed, calculated and difference intensity plots.*

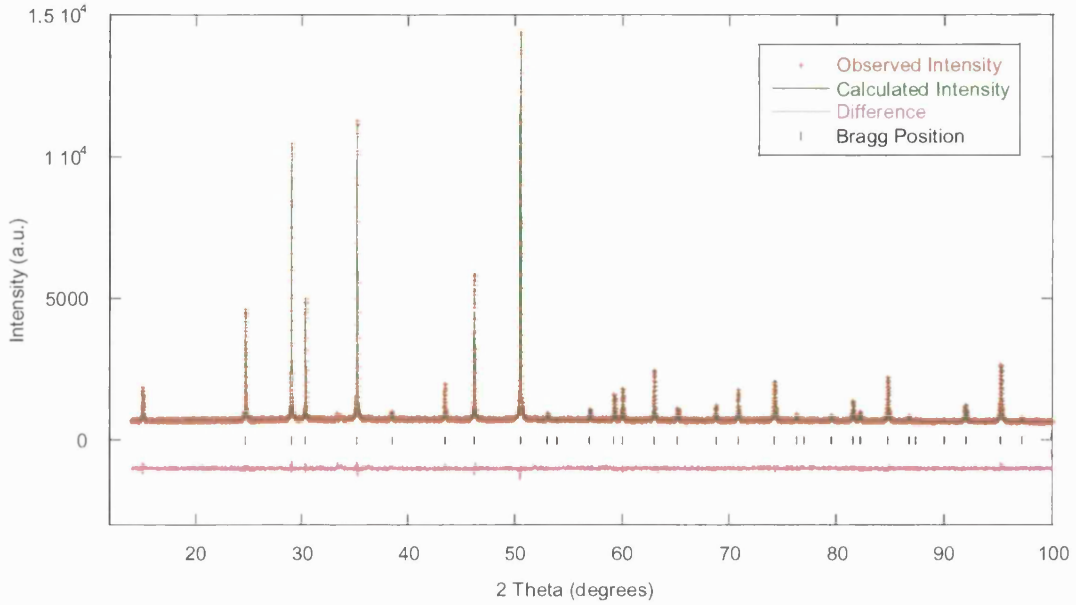

Figure 9.21 *Rietveld refinement of the powder X-ray diffraction pattern of* $Cu_{0.05}Zn_{0.95}Cr_2Se_{2.0}S_{2.0}$ *showing the observed, calculated and difference intensity plots.*

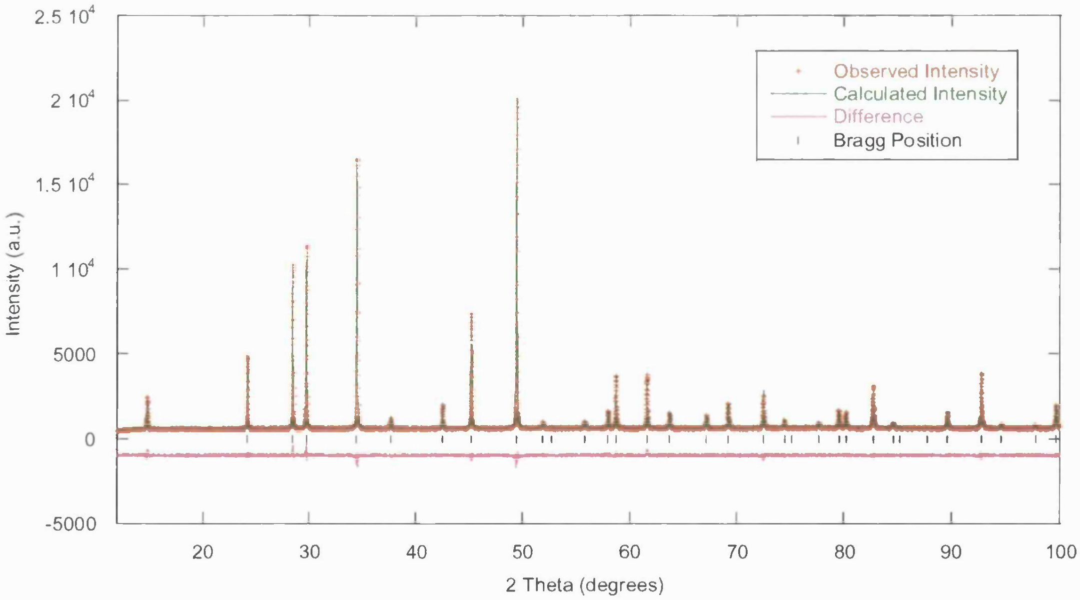

Figure 9.22 *Rietveld refinement of the powder X-ray diffraction pattern of* $ZnCr_2Se_{3.5}S_{0.5}$ *showing the observed, calculated and difference intensity plots.*

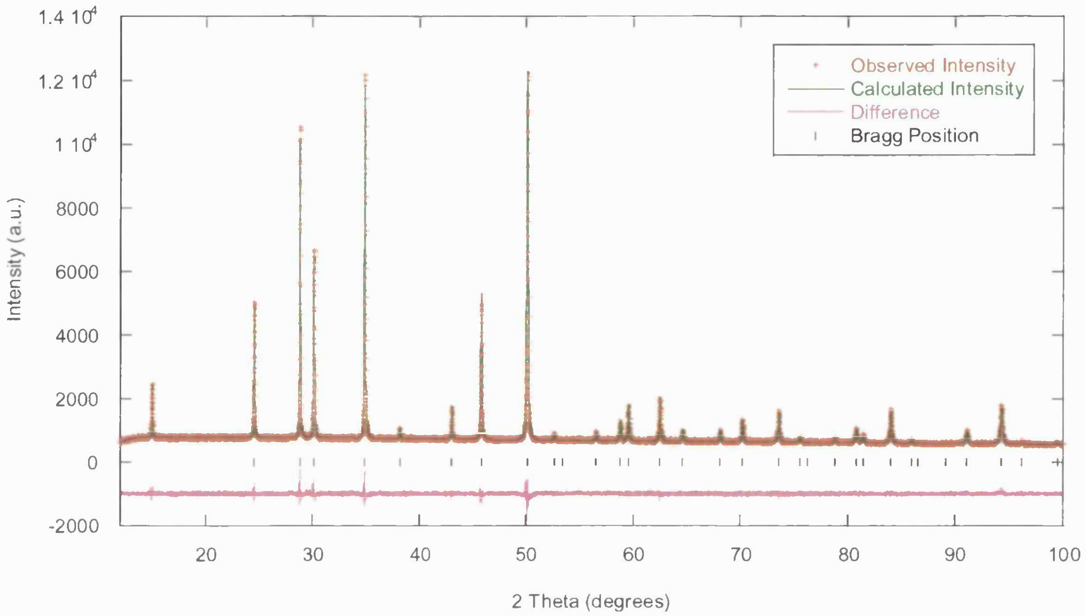

Figure 9.23 *Rietveld refinement of the powder X-ray diffraction pattern of* $ZnCr_2Se_{2.5}S_{1.5}$ *showing the observed, calculated and difference intensity plots.*

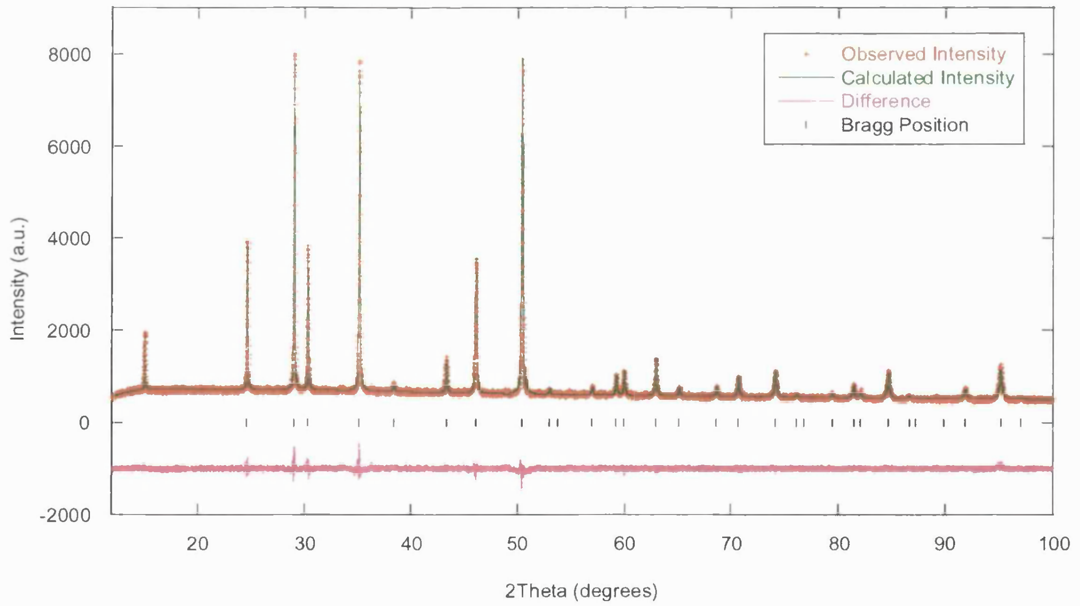

Figure 9.24 *Rietveld refinement of the powder X-ray diffraction pattern of* $ZnCr_2Se_{2.0}S_{2.0}$ *showing the observed, calculated and difference intensity plot*

A.1 3 Rietveld refinements of compounds in the series $CuCr_2Se_{4-y}Br_y$

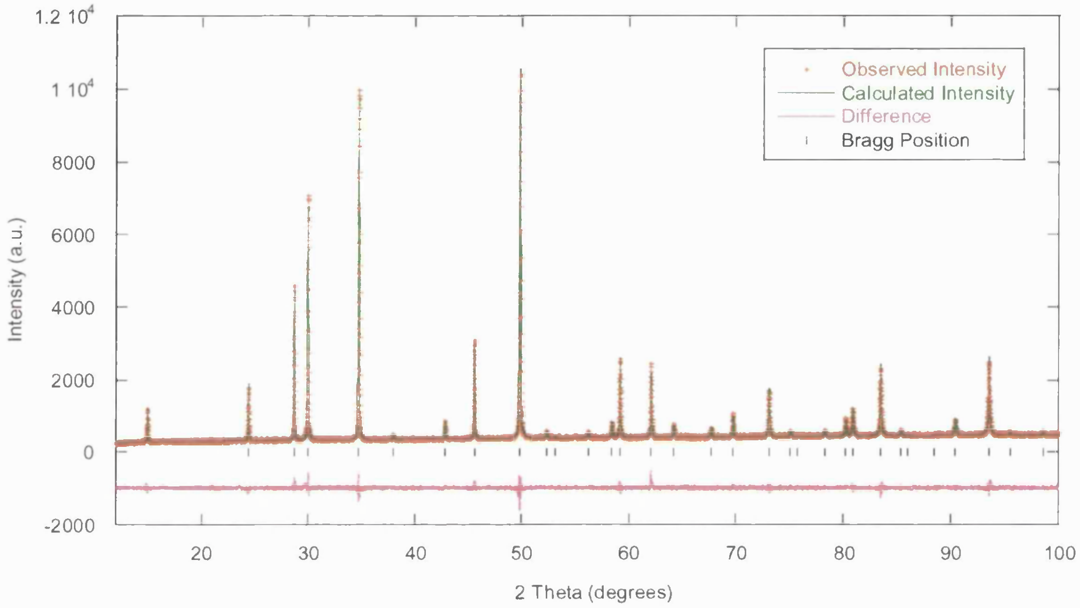

Figure 9.25 *Rietveld refinement of the powder X-ray diffraction pattern of* $CuCr_2Se_{3.50}Br_{0.50}$ *showing the observed, calculated and difference intensity plots.*

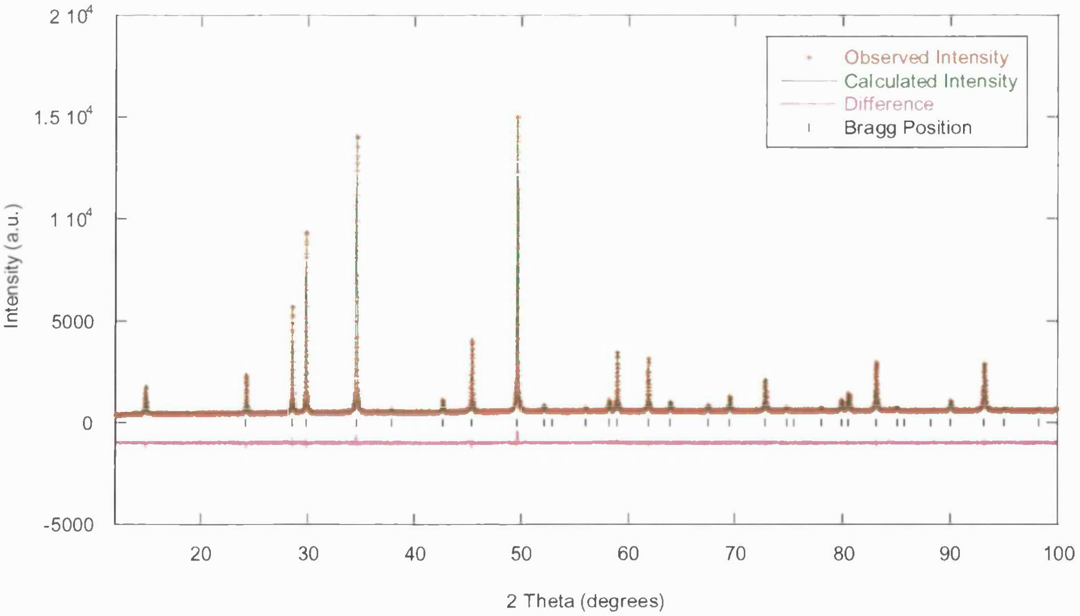

Figure 9.26 *Rietveld refinement of the powder X-ray diffraction pattern of* $CuCr_2Se_{3.75}Br_{0.25}$ *showing the observed, calculated and difference intensity plots.*

A.2 χ versus temperature fits

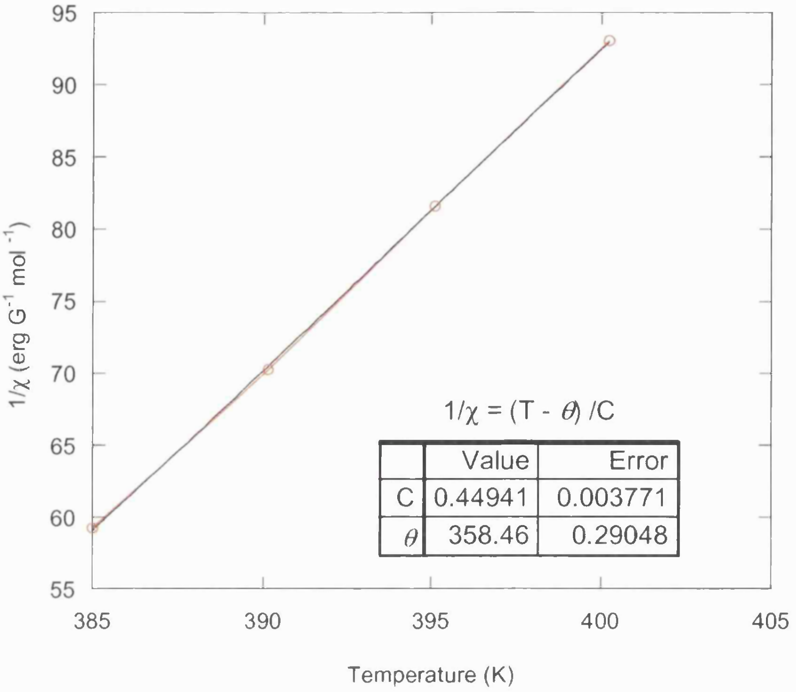

$1/\chi = (T - \theta) / C$

	Value	Error
C	0.44941	0.003771
θ	358.46	0.29048

Figure 9.27 *Fit to the Curie law of data in the paramagnetic region of the* $1/\chi$ *vs. temperature plot of* $Cu_{0.08}Zn_{0.92}Cr_2Se_4$

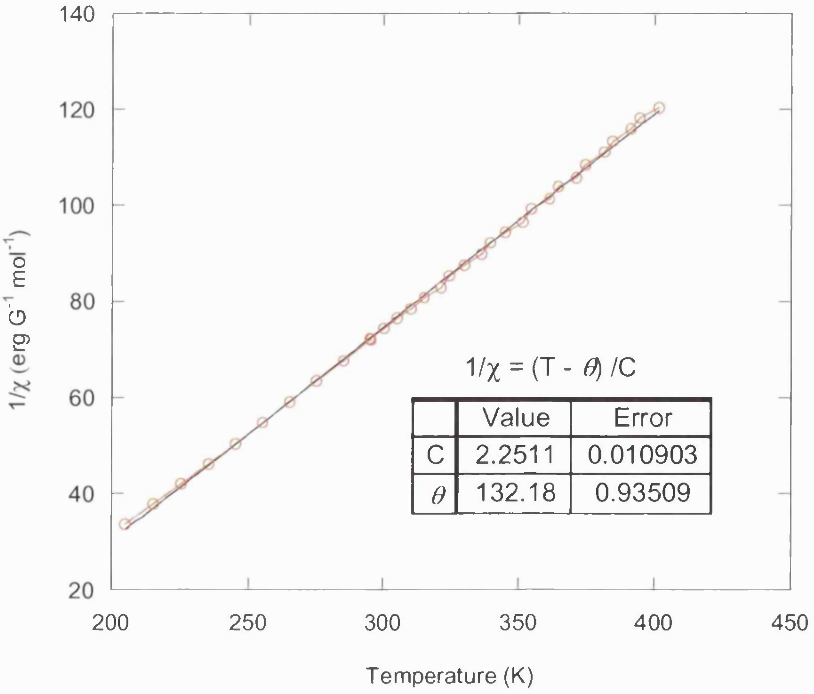

$1/\chi = (T - \theta) / C$

	Value	Error
C	2.2511	0.010903
θ	132.18	0.93509

Figure 9.28 *Fit to the Curie law of data in the paramagnetic region of the* $1/\chi$ *vs. temperature plot of* $Cu_{0.07}Zn_{0.93}Cr_2Se_4$

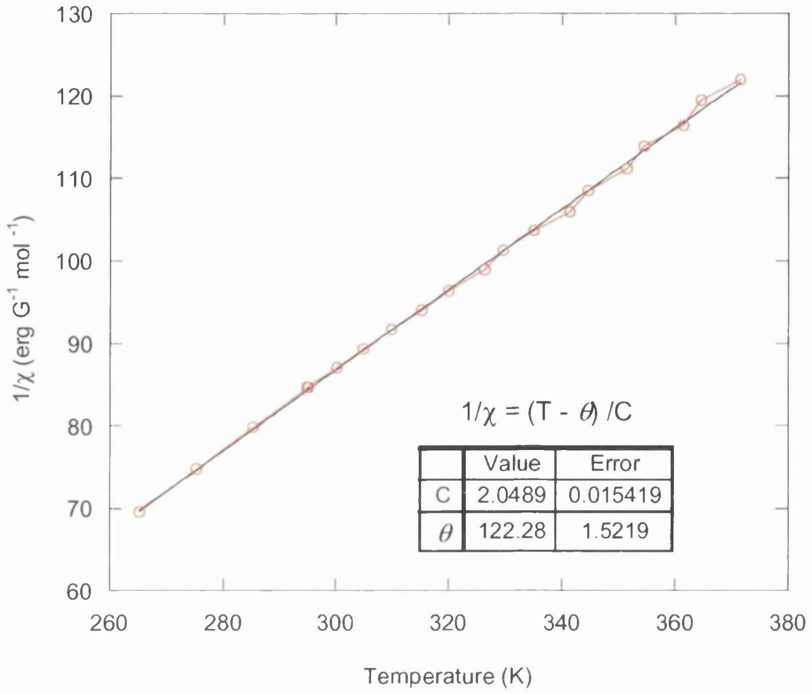

Figure 9.29 *Fit to the Curie law of data in the paramagnetic region of the 1/χ vs. temperature plot of* $Cu_{0.05}Zn_{0.95}Cr_2Se_4$

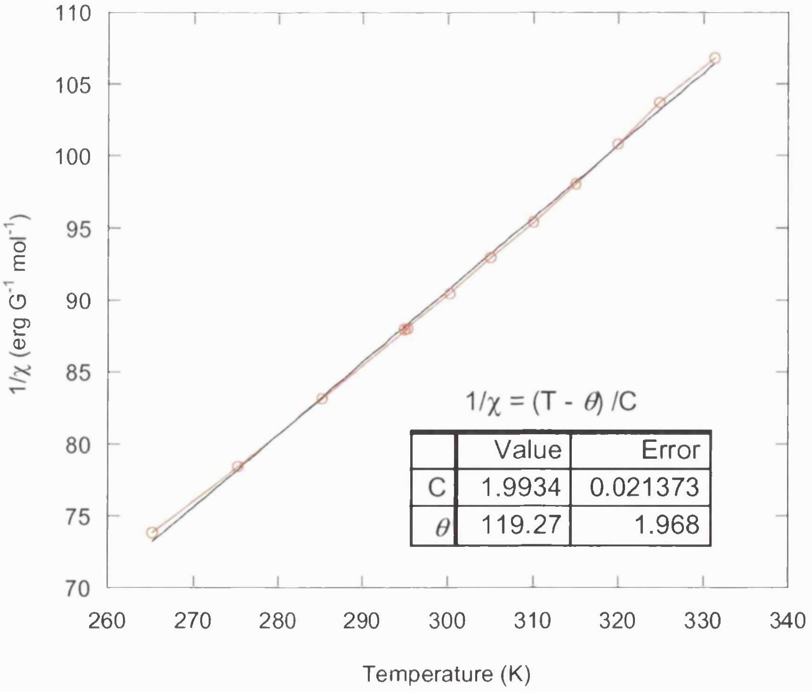

Figure 9.30 *Fit to the Curie law of data in the paramagnetic region of the 1/χ vs. temperature plot of* $Cu_{0.03}Zn_{0.97}Cr_2Se_4$

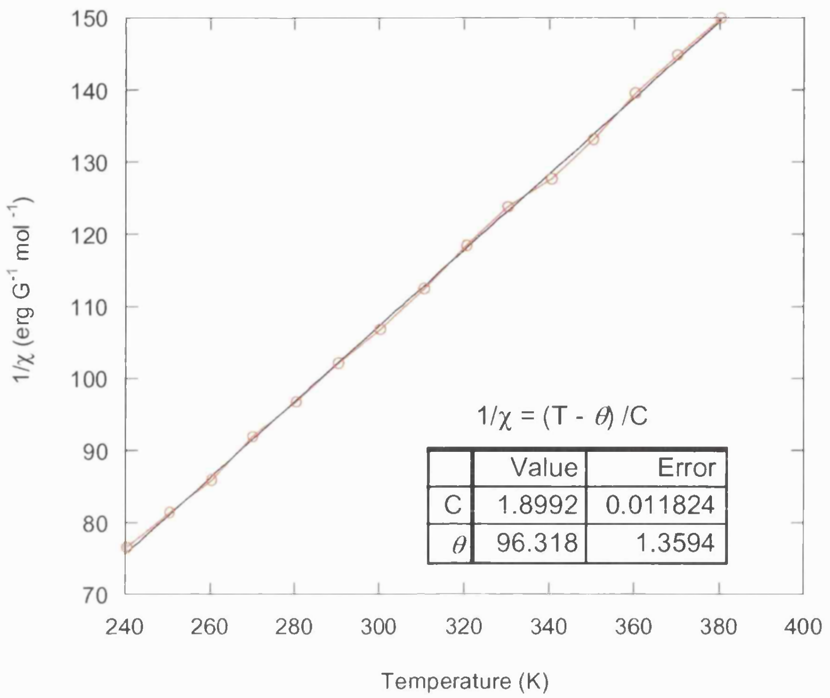

$1/\chi = (T - \theta)/C$

	Value	Error
C	1.8992	0.011824
θ	96.318	1.3594

Figure 9.31 *Fit to the Curie law of data in the paramagnetic region of the 1/χ vs. temperature plot of* $Cu_{0.01}Zn_{0.99}Cr_2Se_4$

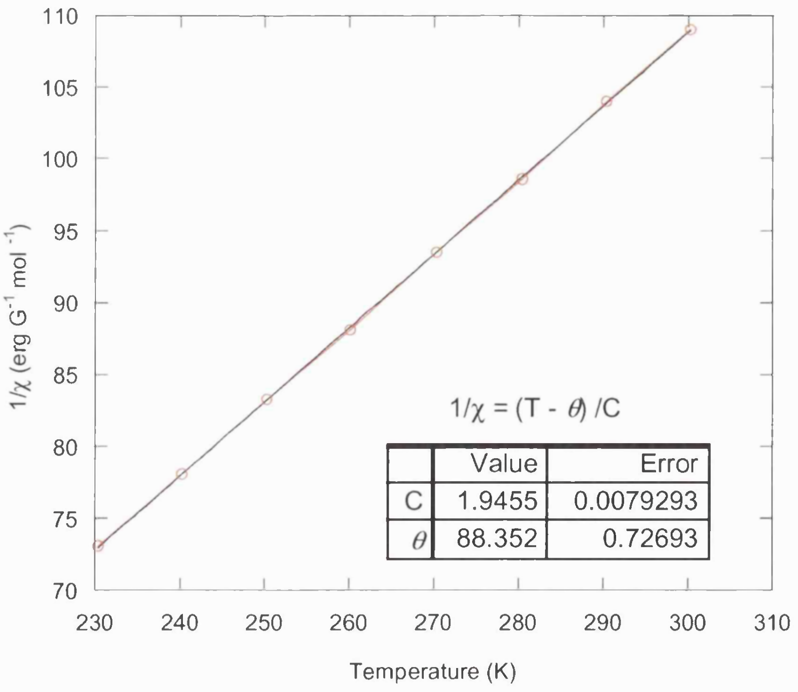

$1/\chi = (T - \theta)/C$

	Value	Error
C	1.9455	0.0079293
θ	88.352	0.72693

Figure 9.32 *Fit to the Curie law of data in the paramagnetic region of the 1/χ vs. temperature plot of* $ZnCr_2Se_4$.

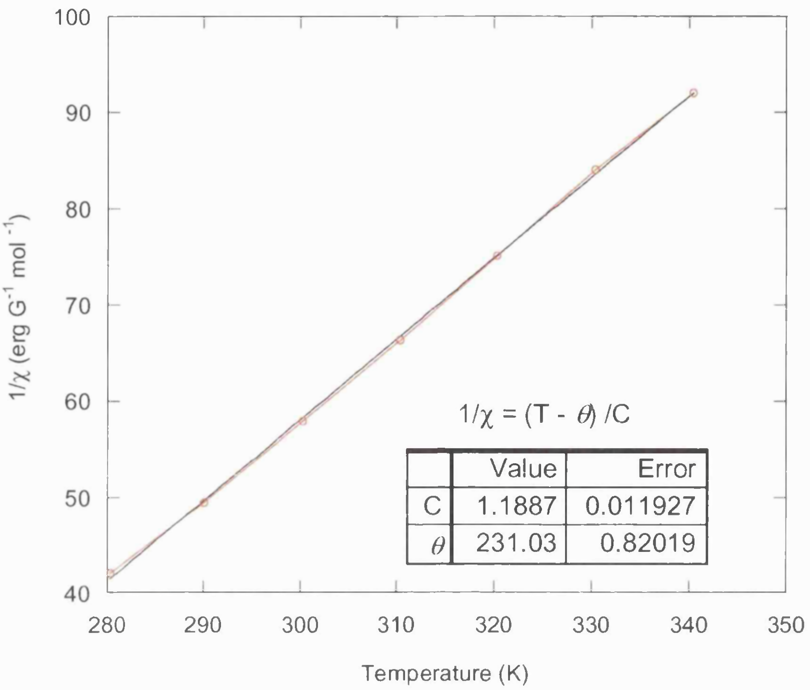

	Value	Error
C	1.1887	0.011927
θ	231.03	0.82019

Figure 9.33 *Fit to the Curie law of data in the paramagnetic region of the 1/χ vs. temperature plot of* $Cu_{0.1}Zn_{0.9}Cr_2Se_3S$.

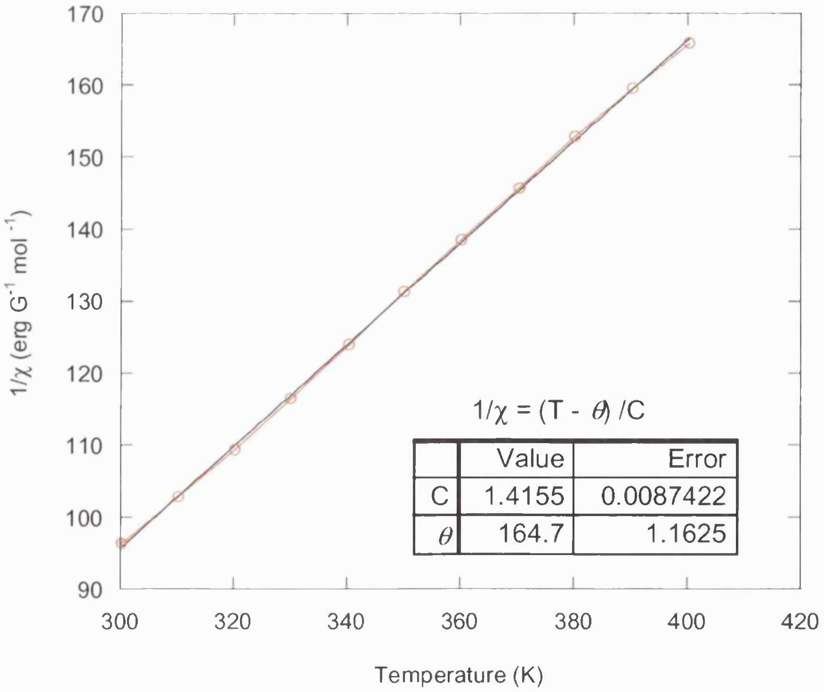

	Value	Error
C	1.4155	0.0087422
θ	164.7	1.1625

Figure 9.34 *Fit to the Curie law of data in the paramagnetic region of the 1/χ vs. temperature plot of* $Cu_{0.1}Zn_{0.9}Cr_2Se_2S_2$.

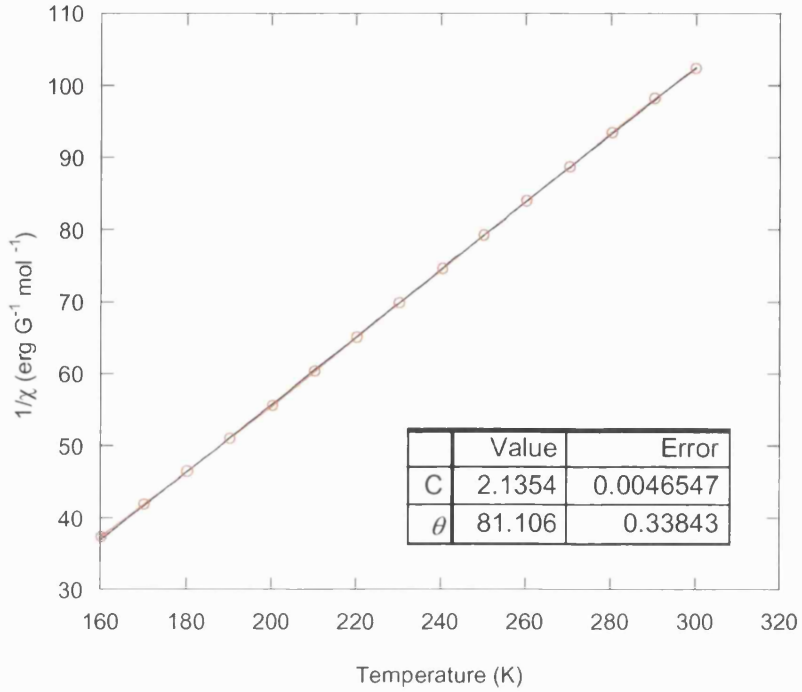

Figure 9.35 *Fit to the Curie law of data in the paramagnetic region of the $1/\chi$ vs. temperature plot of* $Cu_{0.05}Zn_{0.95}Cr_2Se_3S$.

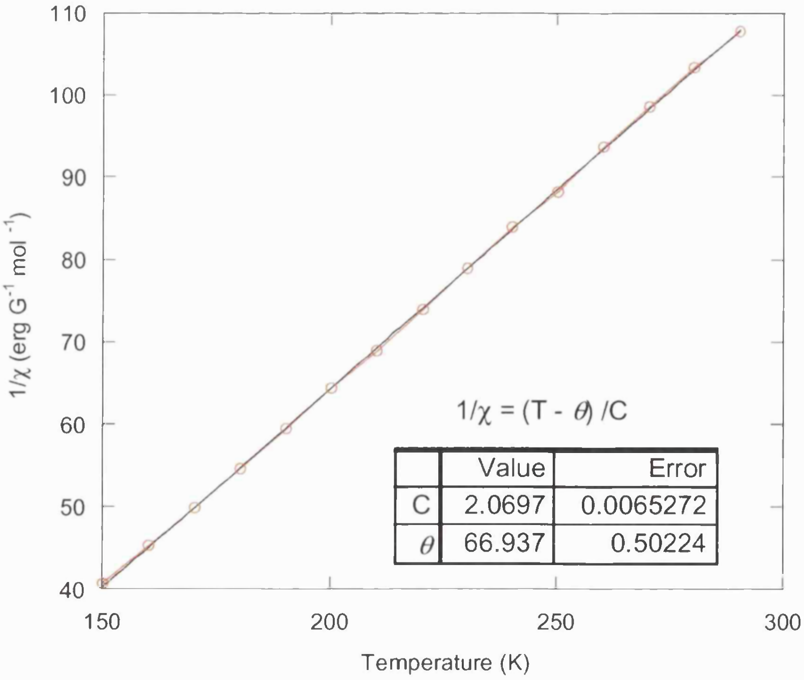

Figure 9.36 *Fit to the Curie law of data in the paramagnetic region of the $1/\chi$ vs. temperature plot of* $Cu_{0.05}Zn_{0.95}Cr_2Se_2S_2$.

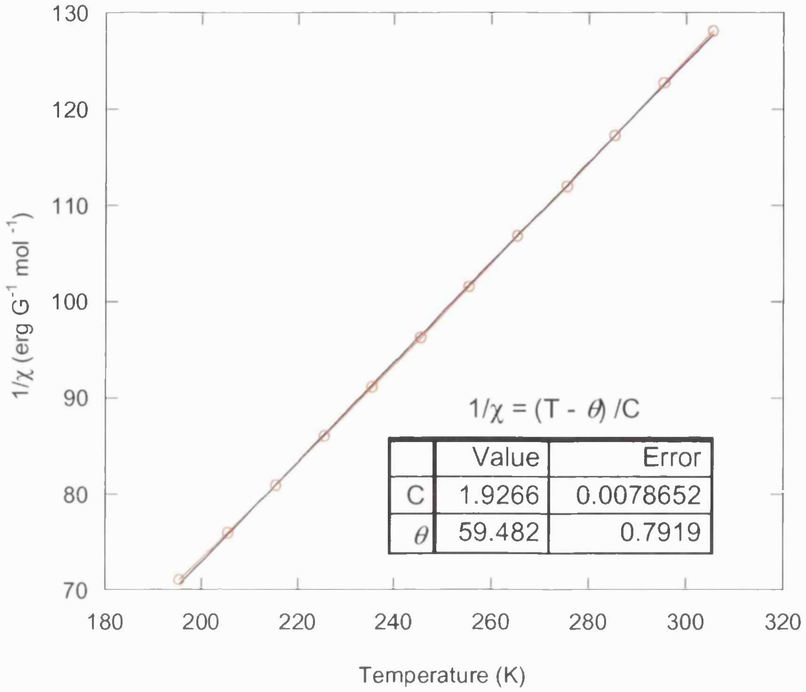

Figure 9.37 *Fit to the Curie law of data in the paramagnetic region of the 1/χ vs. temperature plot of* $ZnCr_2Se_{3.5}S_{0.5}$.

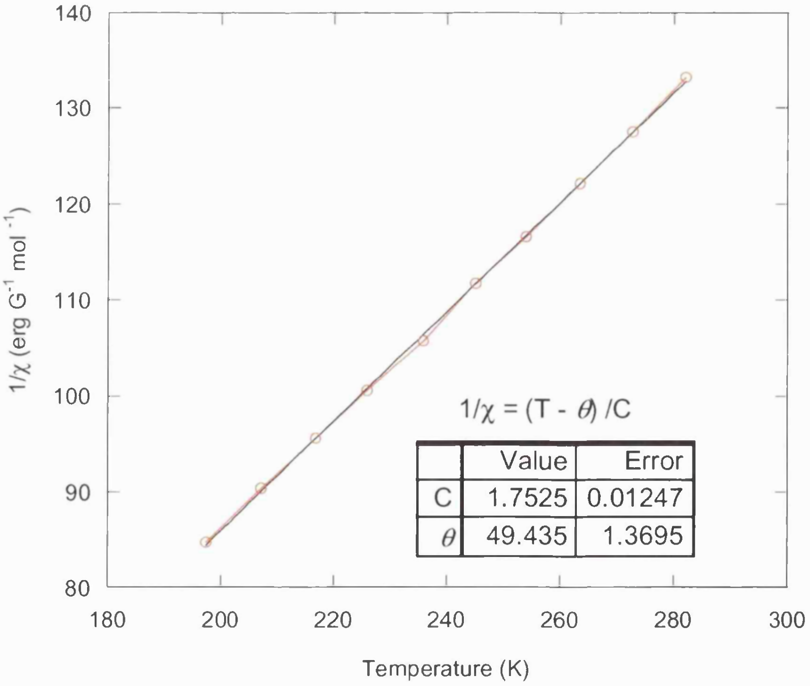

Figure 9.38 *Fit to the Curie law of data in the paramagnetic region of the 1/χ vs. temperature plot of* $ZnCr_2Se_{3.0}S_{1.0}$.

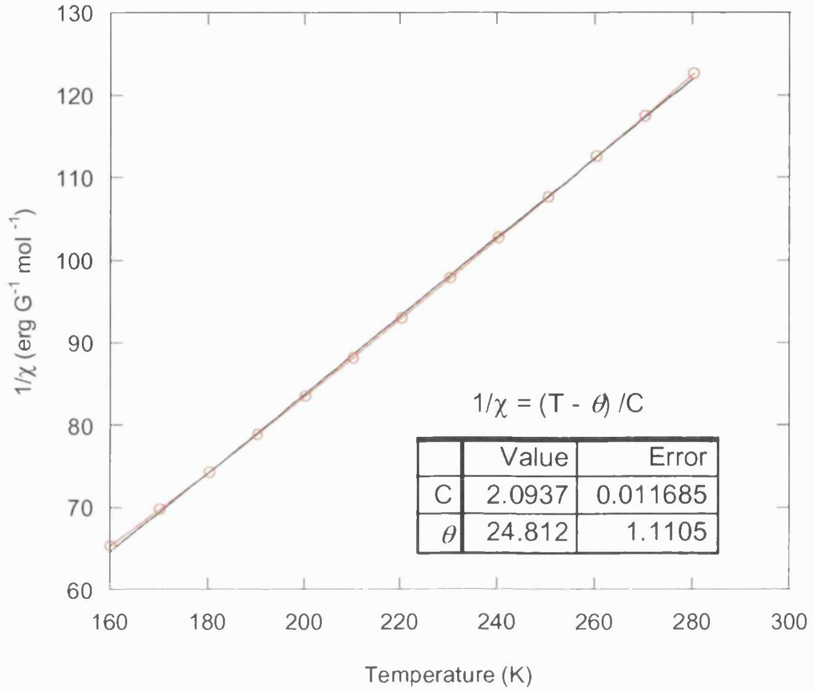

Figure 9.39 *Fit to the Curie law of data in the paramagnetic region of the* $1/\chi$ *vs. temperature plot of* $ZnCr_2Se_{2.5}S_{1.5}$.

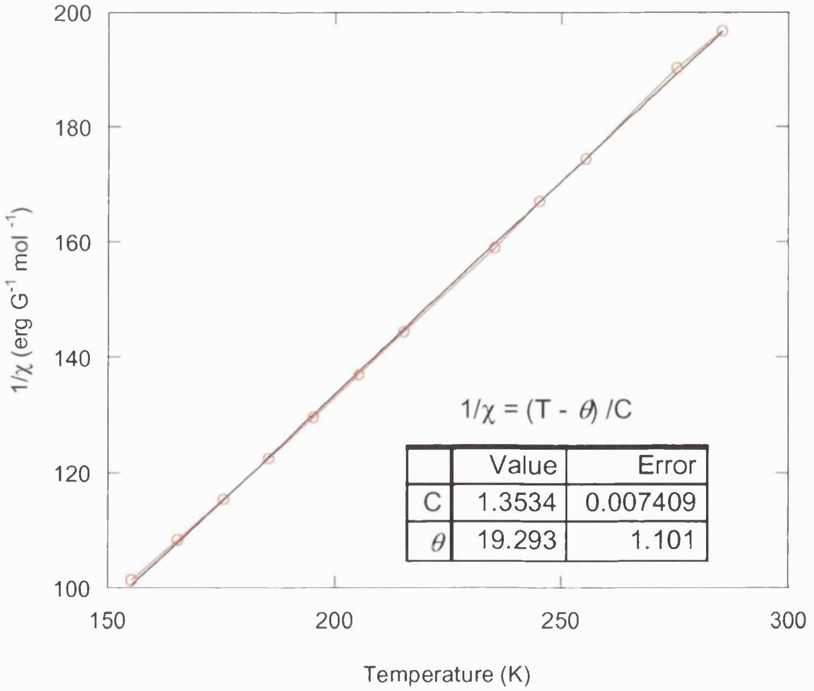

Figure 9.40 *Fit to the Curie law of data in the paramagnetic region of the* $1/\chi$ *vs. temperature plot of* $ZnCr_2Se_{2.0}S_{2.0}$.

A.3 Resistivity versus temperature fits

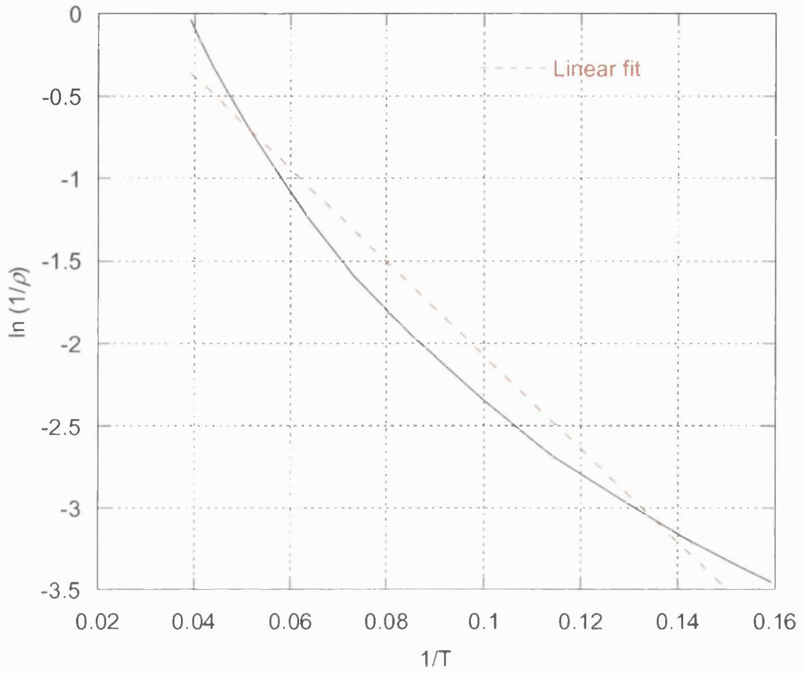

Figure 9.41 *Plot of ln(1/ρ) vs. 1/T for* $Cu_{0.05}Zn_{0.95}Cr_2Se_4$ *in an applied field of 1 Tesla in the temperature range 4→25 K.*

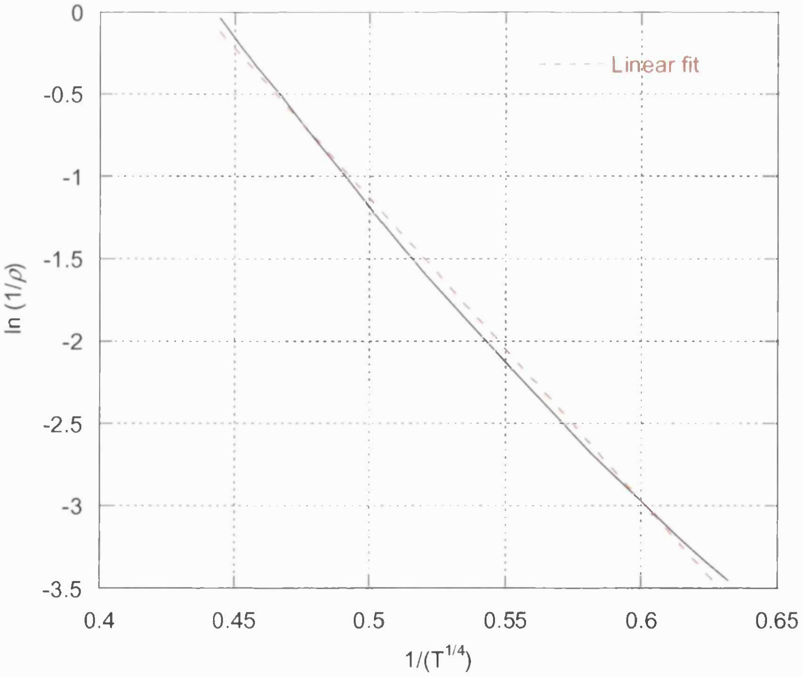

Figure 9.42 *Plot of ln(1/ρ) vs.* $1/T^{1/4}$ *for* $Cu_{0.05}Zn_{0.95}Cr_2Se_4$ *in an applied field of 1 Tesla in the temperature range 4→25 K.*

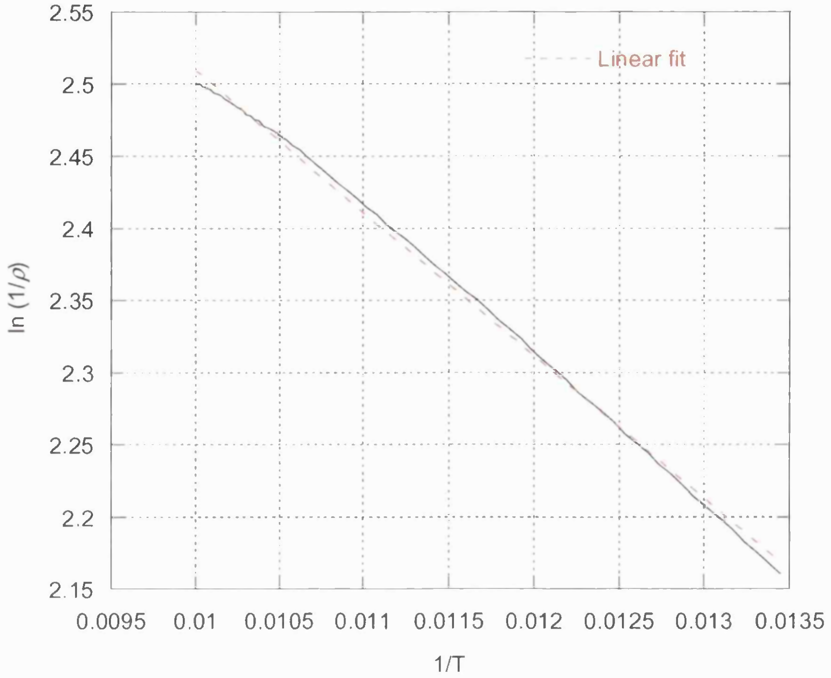

Figure 9.43 *Plot of ln(1/ρ) vs. 1/T for* $Cu_{0.05}Zn_{0.95}Cr_2Se_4$ *in an applied field of 1 Tesla in the temperature range 40→100 K.*

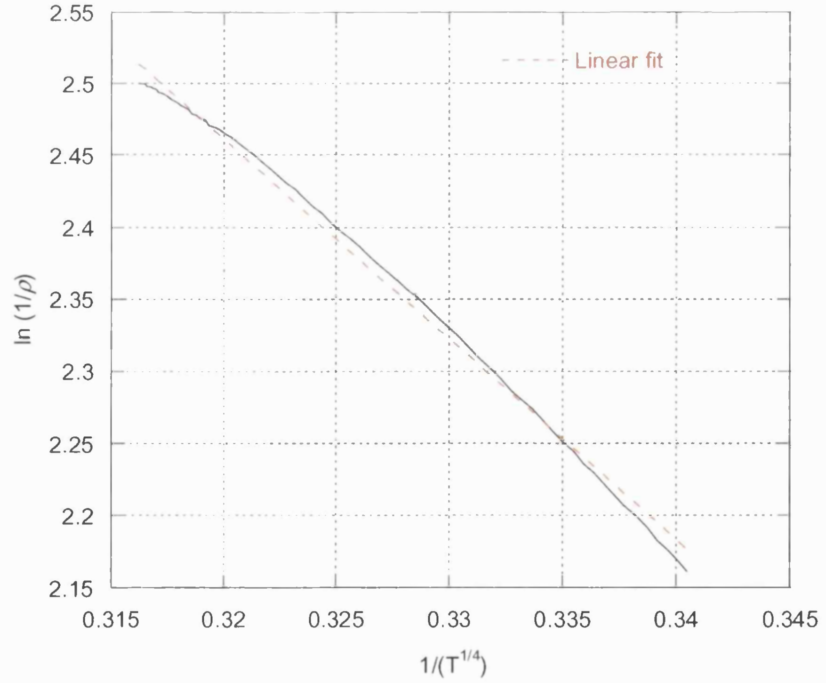

Figure 9.44 *Plot of ln(1/ρ) vs.* $1/T^{1/4}$ *for* $Cu_{0.05}Zn_{0.95}Cr_2Se_4$ *in an applied field of 1 Tesla in the temperature range 40→100 K.*

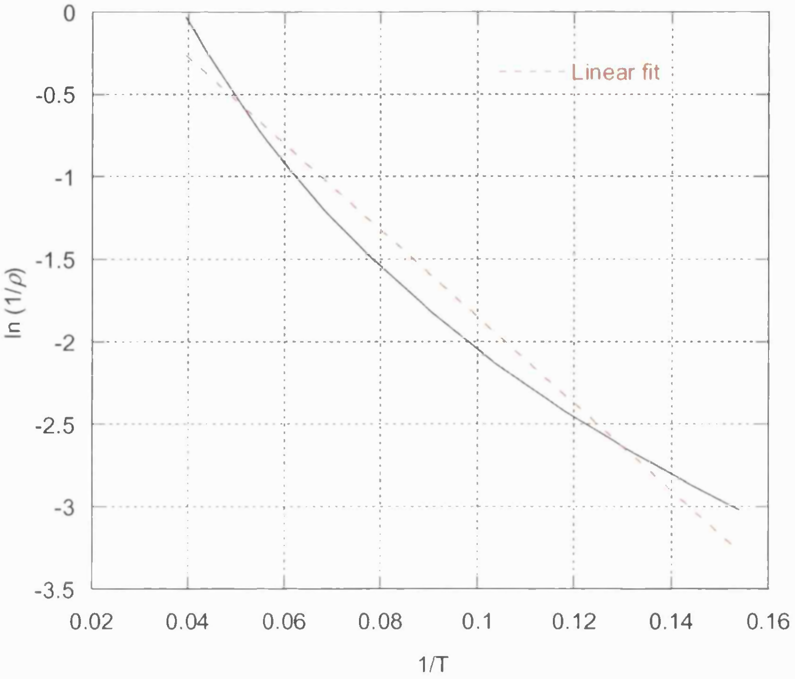

Figure 9.45 *Plot of* $ln(1/\rho)$ *vs.* $1/T$ *for* $Cu_{0.05}Zn_{0.95}Cr_2Se_4$ *in an applied field of 2 Tesla in the temperature range 4→25 K.*

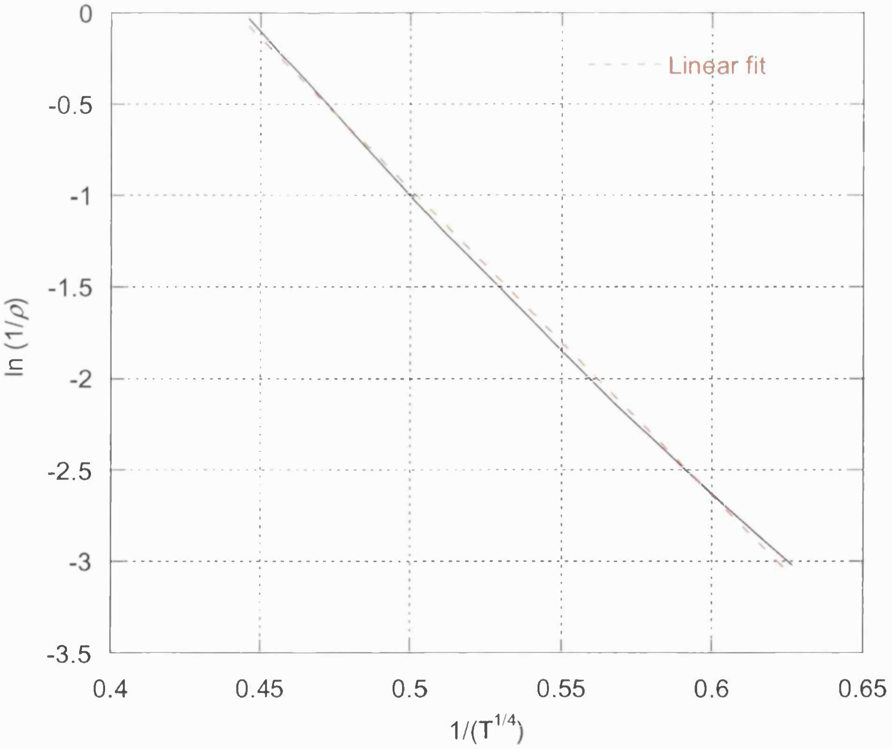

Figure 9.46 *Plot of* $ln(1/\rho)$ *vs.* $1/T^{1/4}$ *for* $Cu_{0.05}Zn_{0.95}Cr_2Se_4$ *in an applied field of 2 Tesla in the temperature range 4→25 K.*

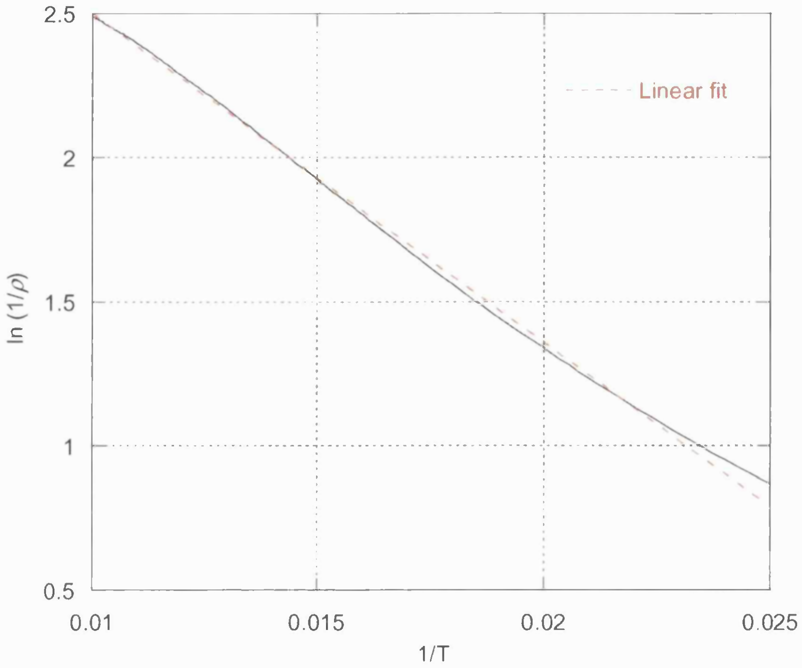

Figure 9.47 *Plot of ln(1/ρ) vs. 1/T for* $Cu_{0.05}Zn_{0.95}Cr_2Se_4$ *in an applied field of 2 Tesla in the temperature range 40→100 K.*

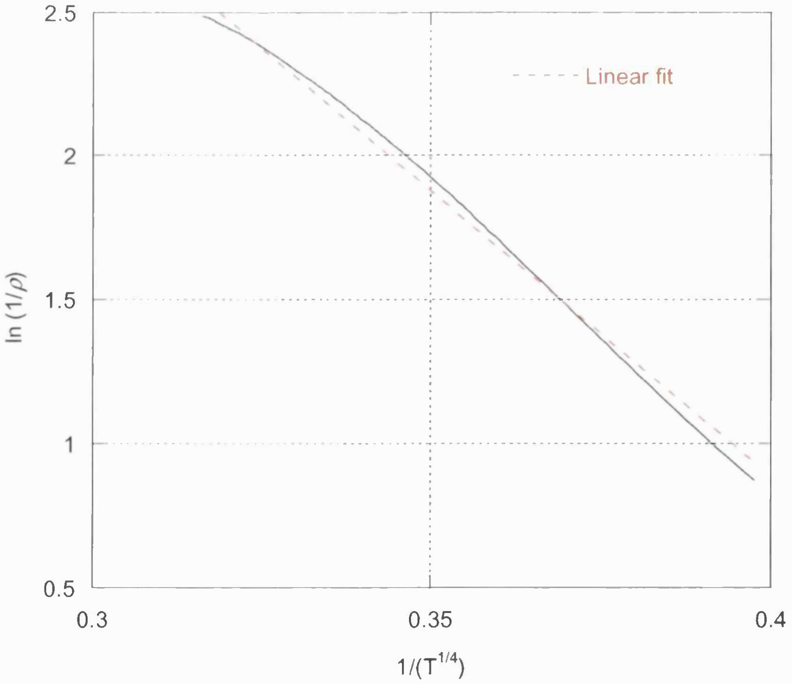

Figure 9.48 *Plot of ln(1/ρ) vs.* $1/T^{1/4}$ *for* $Cu_{0.05}Zn_{0.95}Cr_2Se_4$ *in an applied field of 2 Tesla in the temperature rage 40→100 K.*

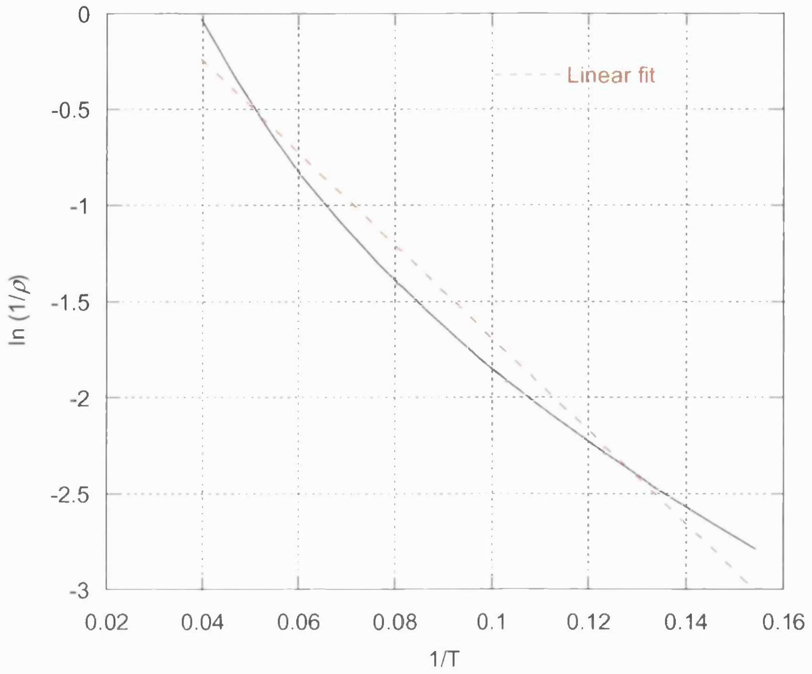

Figure 9.49 *Plot of ln(1/ρ) vs. 1/T for* $Cu_{0.05}Zn_{0.95}Cr_2Se_4$ *in an applied field of 3 Tesla in the temperature range 4→25 K.*

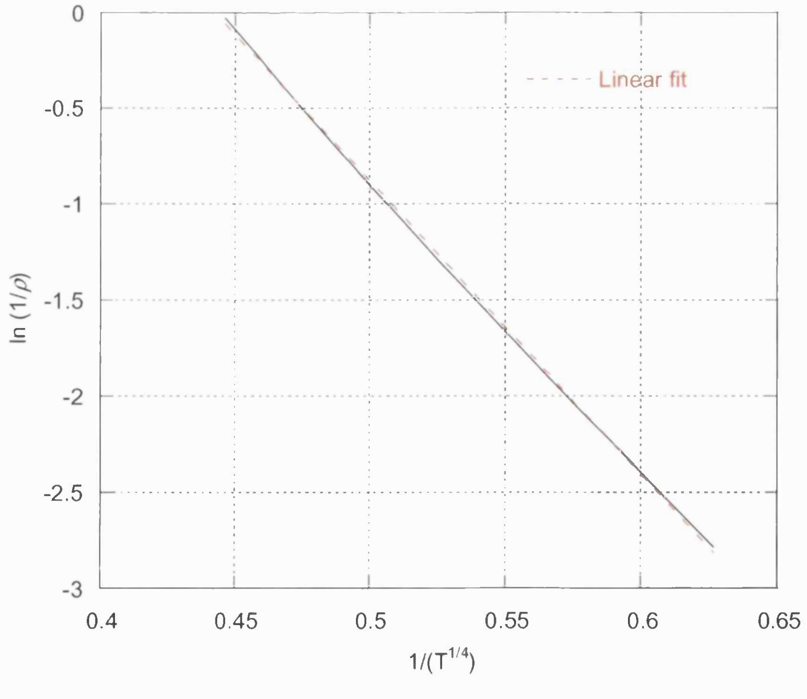

Figure 9.50 *Plot of ln(1/ρ) vs.* $1/T^{1/4}$ *for* $Cu_{0.05}Zn_{0.95}Cr_2Se_4$ *in an applied field of 3 Tesla in the temperature range 4→25 K.*

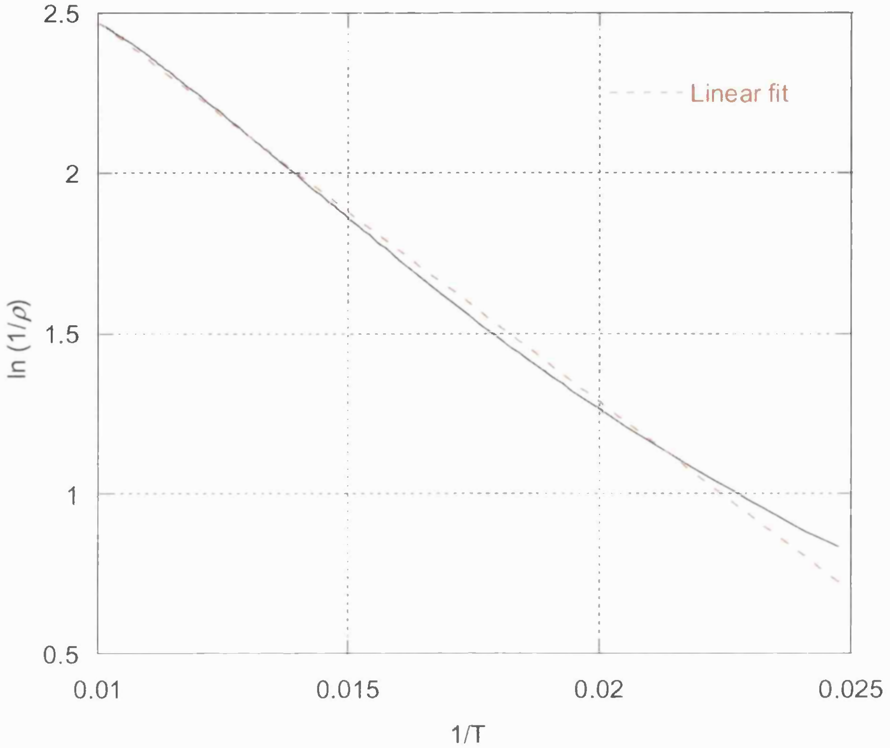

Figure 9.51 *Plot of ln(1/ρ) vs. 1/T for* $Cu_{0.05}Zn_{0.95}Cr_2Se_4$ *in an applied field of 3 Tesla in the temperature range 40→100 K.*

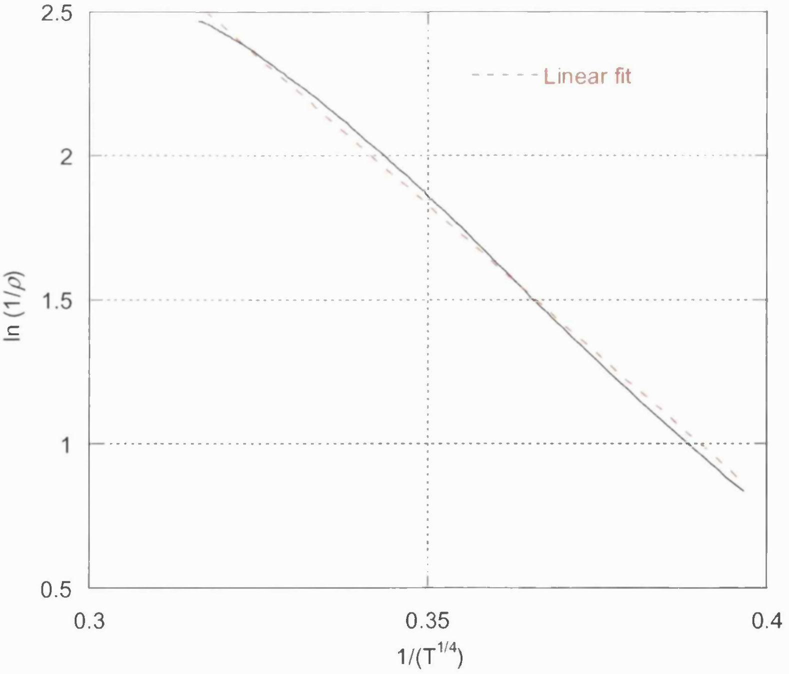

Figure 9.52 *Plot of ln(1/ρ) vs.* $1/T^{1/4}$ *for* $Cu_{0.05}Zn_{0.95}Cr_2Se_4$ *in an applied field of 3 Tesla in the temperature range 40→100 K.*

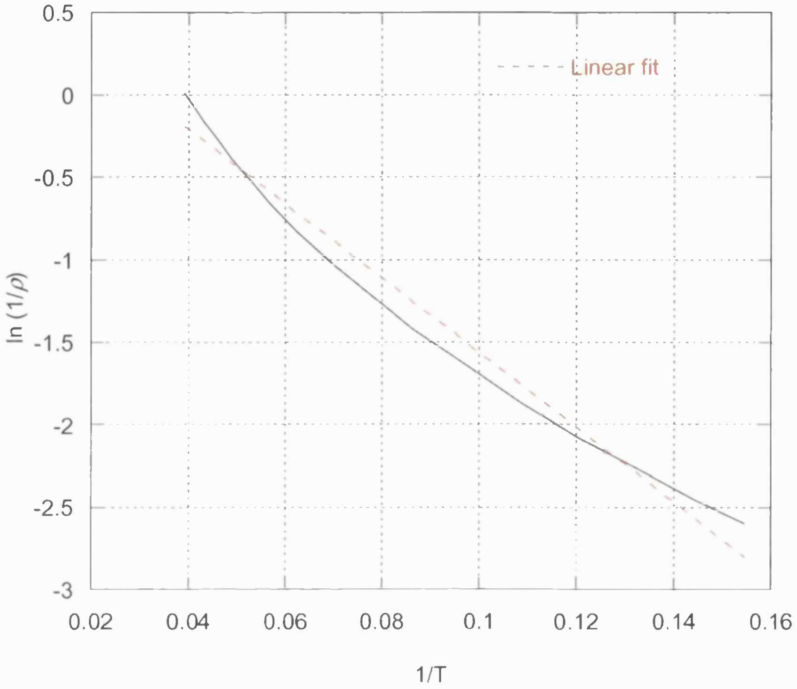

Figure 9.53 *Plot of ln(1/ρ) vs. 1/T for* $Cu_{0.05}Zn_{0.95}Cr_2Se_4$ *in an applied field of 4 Tesla in the temperature range 4→25 K.*

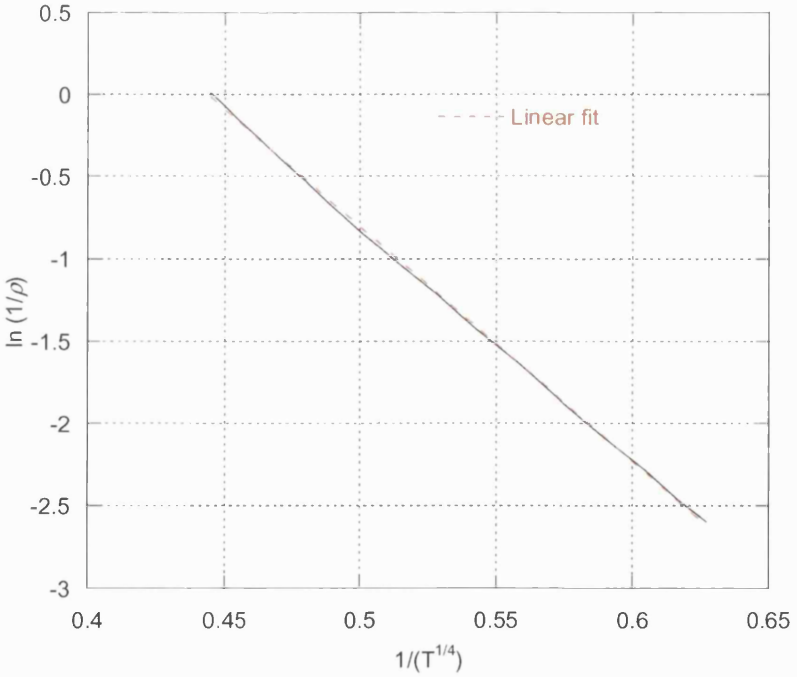

Figure 9.54 *Plot of ln(1/ρ) vs.* $1/T^{1/4}$ *for* $Cu_{0.05}Zn_{0.95}Cr_2Se_4$ *in an applied field of 4 Tesla in the temperature range 4→25 K.*

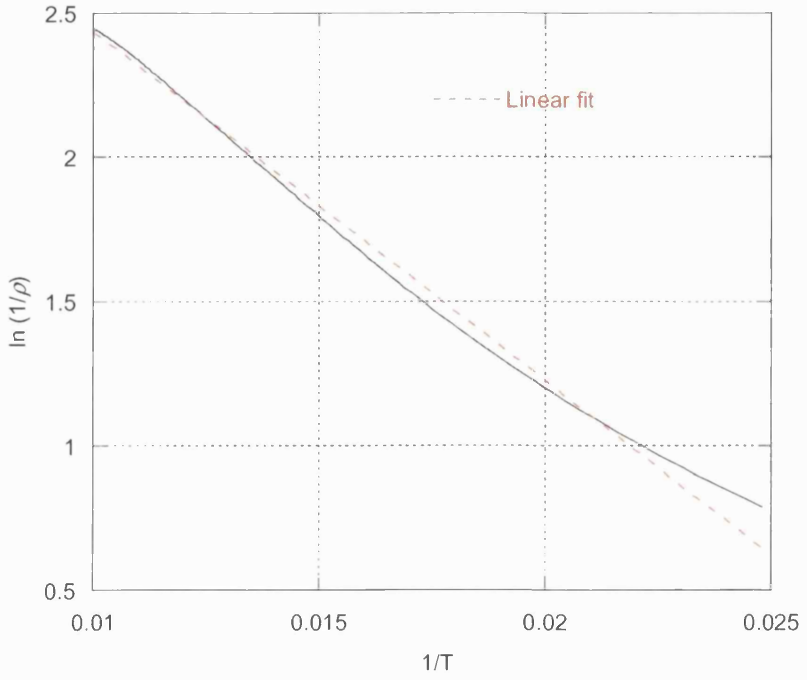

Figure 9.55 *Plot of* $ln(1/\rho)$ *vs.* $1/T$ *for* $Cu_{0.05}Zn_{0.95}Cr_2Se_4$ *in an applied field of 4 Tesla in the temperature range 40→100 K.*

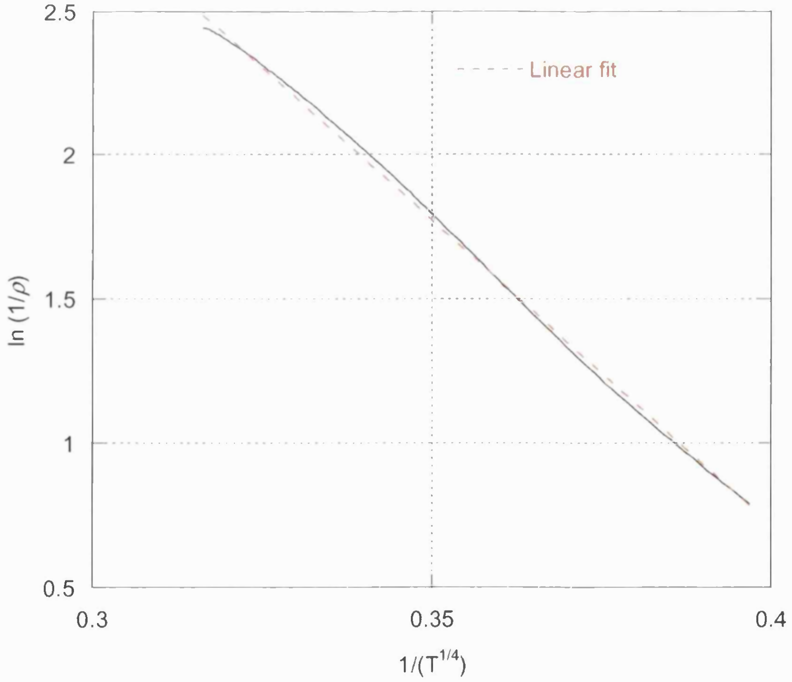

Figure 9.56 *Plot of* $ln(1/\rho)$ *vs.* $1/T^{1/4}$ *for* $Cu_{0.05}Zn_{0.95}Cr_2Se_4$ *in an applied field of 4 Tesla in the temperature range 40→100 K.*

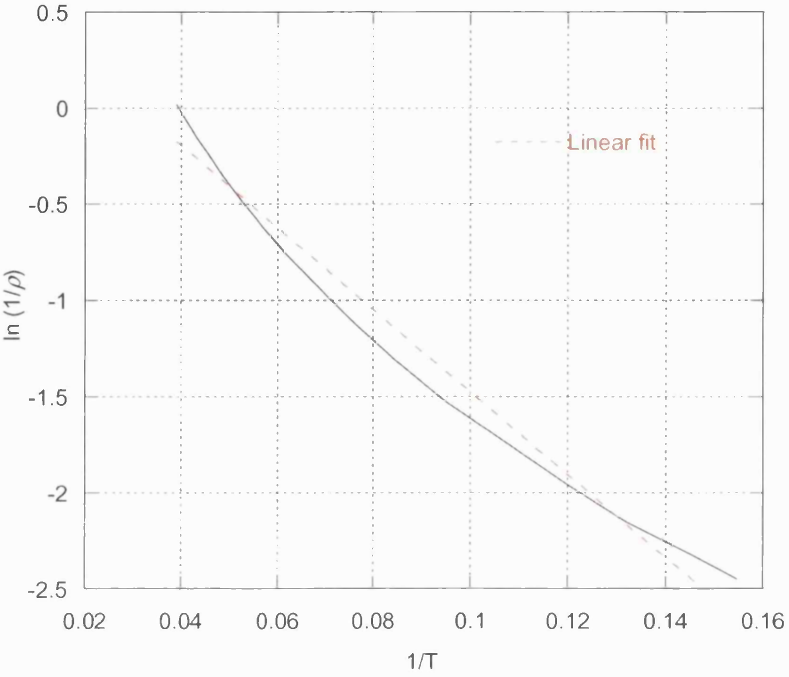

Figure 9.57 *Plot of* $ln(1/\rho)$ *vs.* $1/T$ *for* $Cu_{0.05}Zn_{0.95}Cr_2Se_4$ *in an applied field of 5 Tesla in the temperature range 4→25 K.*

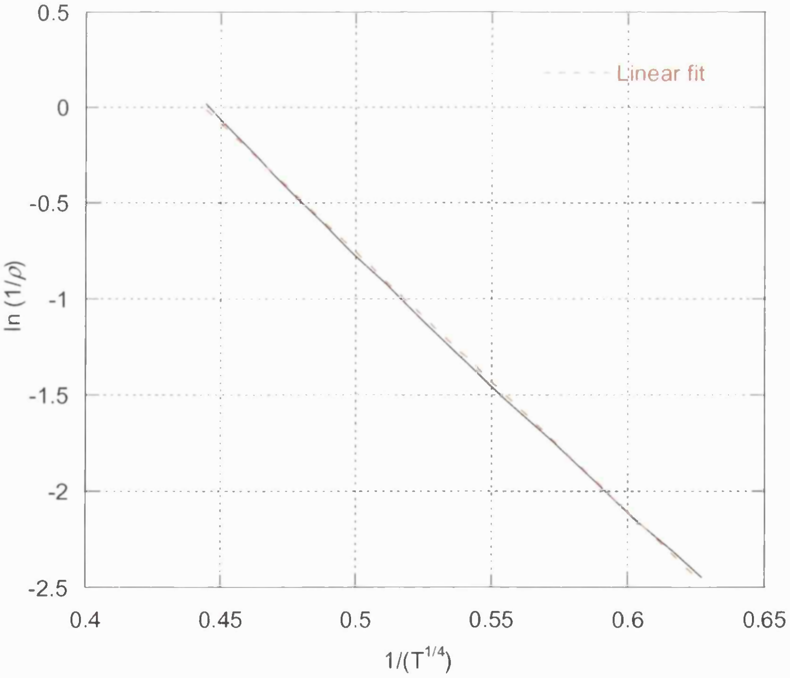

Figure 9.58 *Plot of* $ln(1/\rho)$ *vs.* $1/T^{1/4}$ *for* $Cu_{0.05}Zn_{0.95}Cr_2Se_4$ *in an applied field of 5 Tesla in the temperature range 4→25 K.*

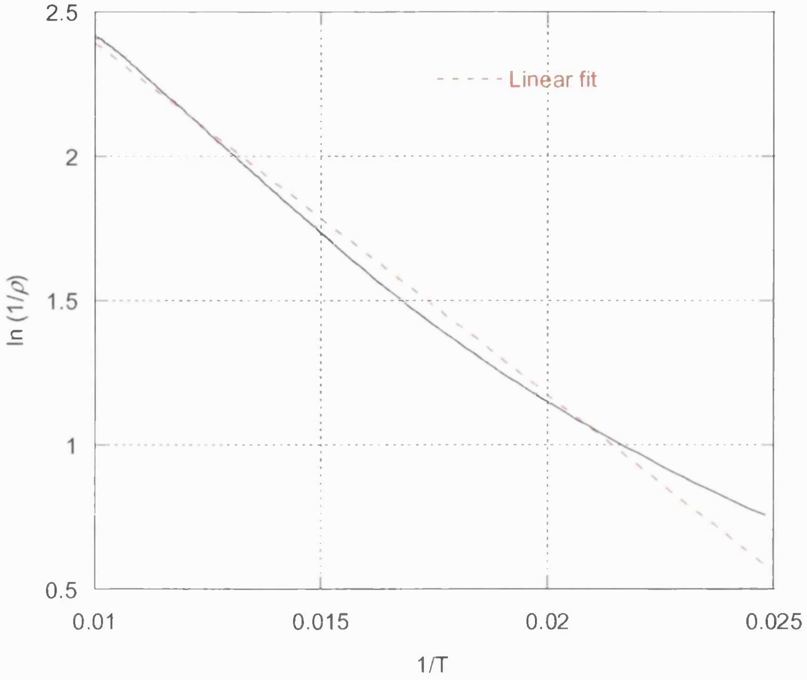

Figure 9.59 *Plot of* $ln(1/\rho)$ *vs.* $1/T$ *for* $Cu_{0.05}Zn_{0.95}Cr_2Se_4$ *in an applied field of 5 Tesla in the temperature range 40→100 K.*

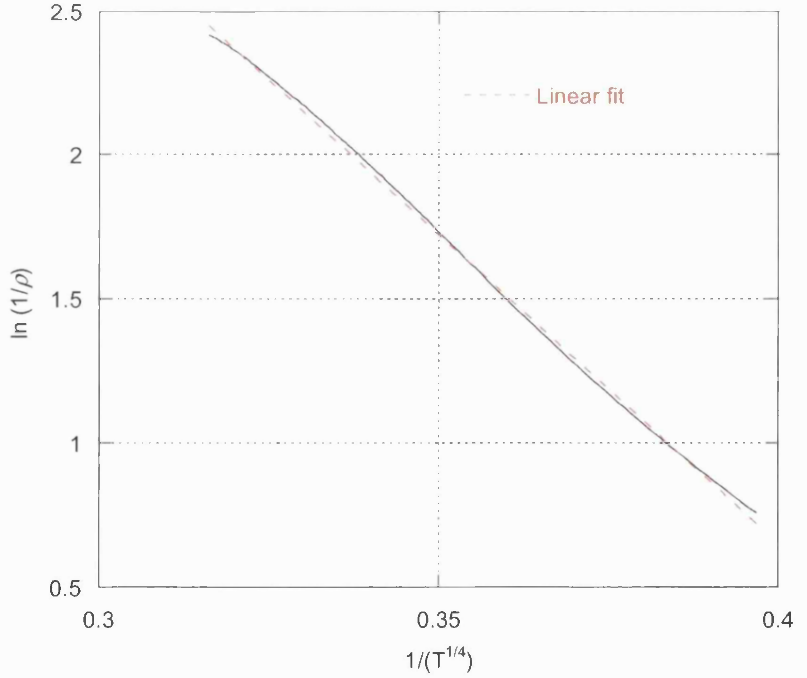

Figure 9.60 *Plot of* $ln(1/\rho)$ *vs.* $1/T^{1/4}$ *for* $Cu_{0.05}Zn_{0.95}Cr_2Se_4$ *in an applied field of 5 Tesla in the temperature range 40→100 K.*

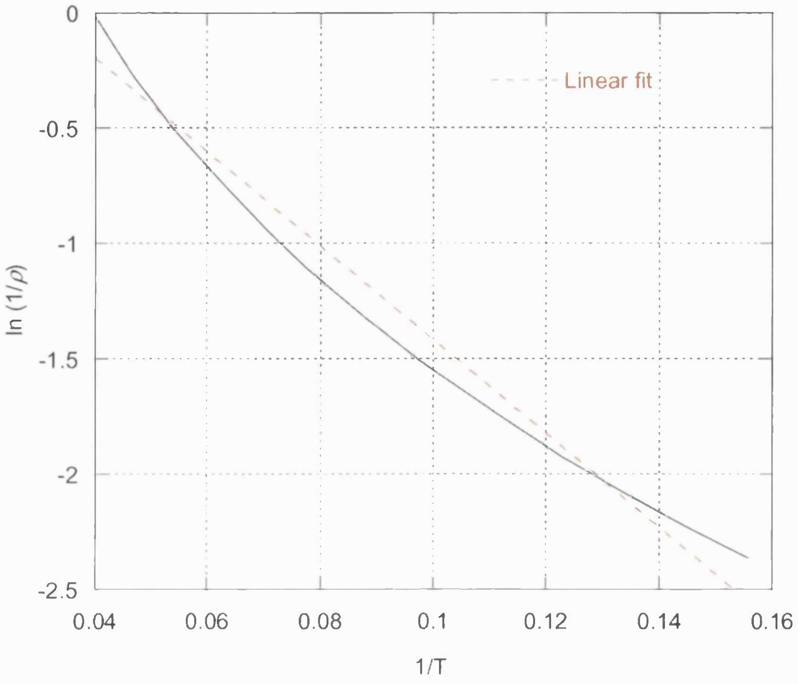

Figure 9.61 *Plot of* $\ln(1/\rho)$ *vs.* $1/T$ *for* $Cu_{0.05}Zn_{0.95}Cr_2Se_4$ *in an applied field of 6 Tesla in the temperature range 4→25 K.*

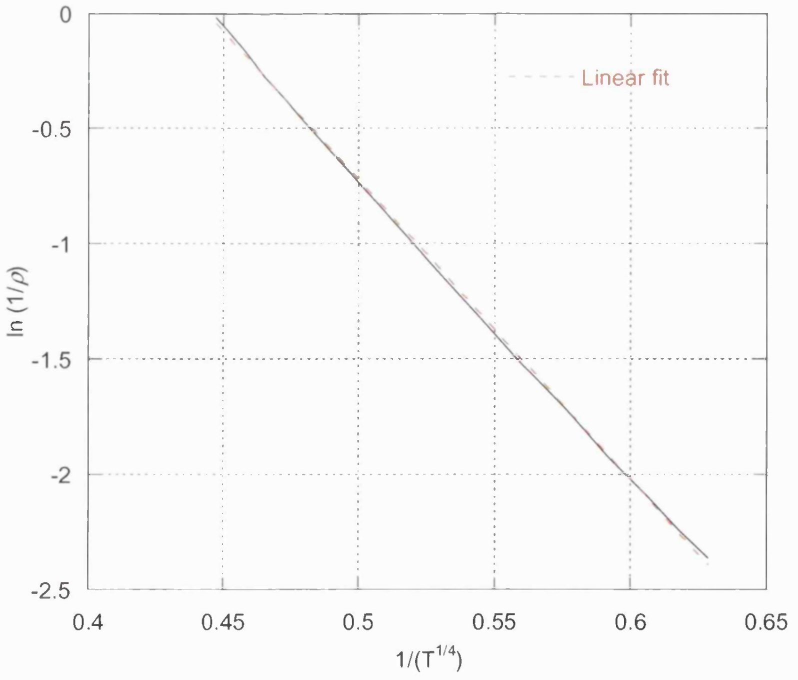

Figure 9.62 *Plot of* $\ln(1/\rho)$ *vs.* $1/T^{1/4}$ *for* $Cu_{0.05}Zn_{0.95}Cr_2Se_4$ *in an applied field of 6 Tesla in the temperature range 4→25 K.*

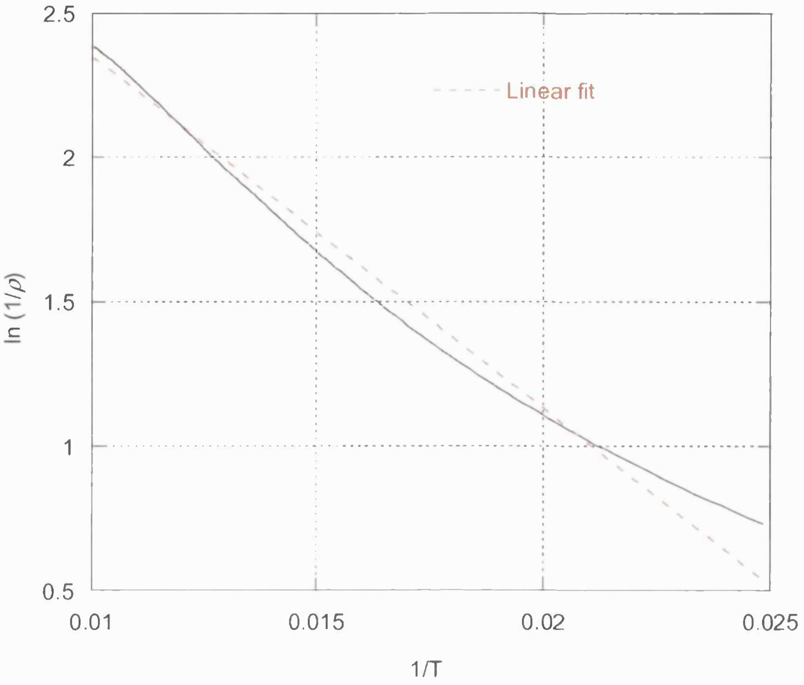

Figure 9.63 *Plot of* $\ln(1/\rho)$ *vs.* $1/T$ *for* $Cu_{0.05}Zn_{0.95}Cr_2Se_4$ *in an applied field of 6 Tesla in the temperature range 40→100 K.*

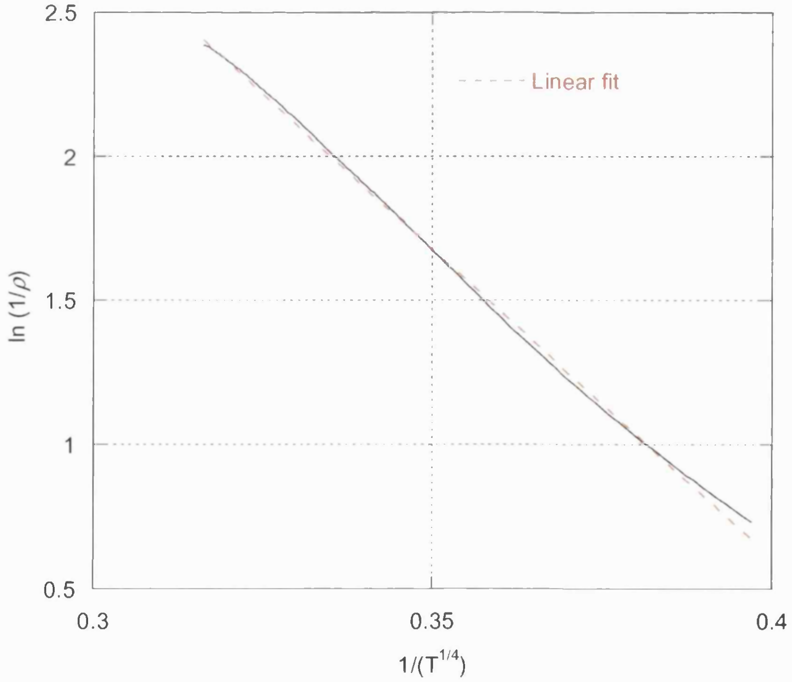

Figure 9.64 *Plot of* $\ln(1/\rho)$ *vs.* $1/T^{1/4}$ *for* $Cu_{0.05}Zn_{0.95}Cr_2Se_4$ *in an applied field of 6 Tesla in the temperature range 40→100 K.*

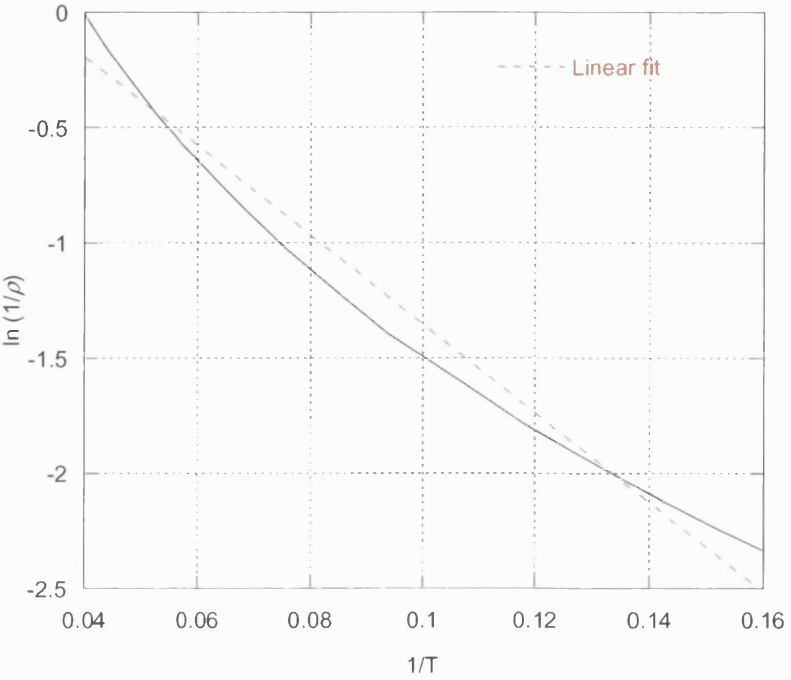

Figure 9.65 *Plot of ln(1/ρ) vs. 1/T for* $Cu_{0.05}Zn_{0.95}Cr_2Se_4$ *in an applied field of 7 Tesla in the temperature range 4→25 K.*

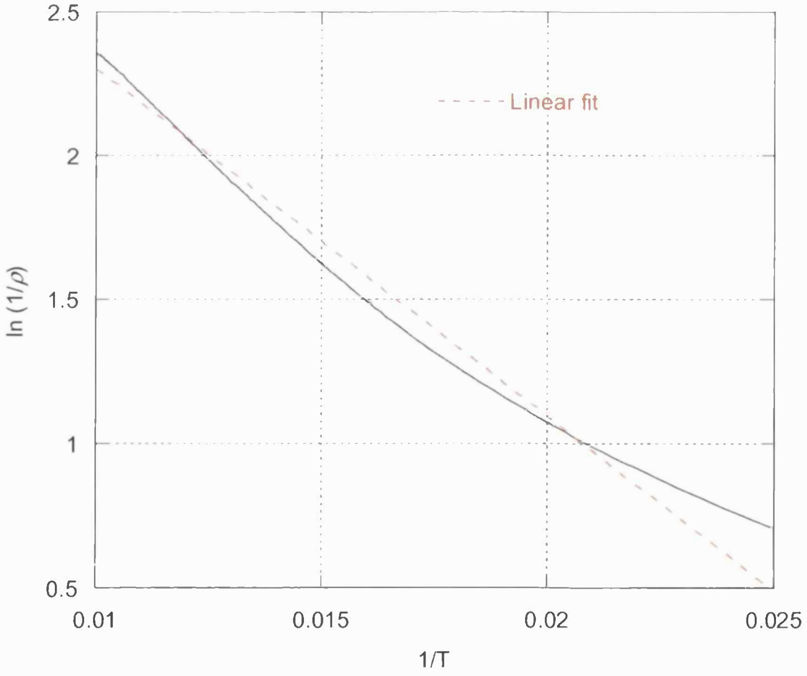

Figure 9.66 *Plot of ln(1/ρ) vs. 1/T for* $Cu_{0.05}Zn_{0.95}Cr_2Se_4$ *in an applied field of 7 Tesla in the temperature range 40→100 K.*

A.4 Neutron Diffraction Experiments

A.4.1 $ZnCr_2Se_4$

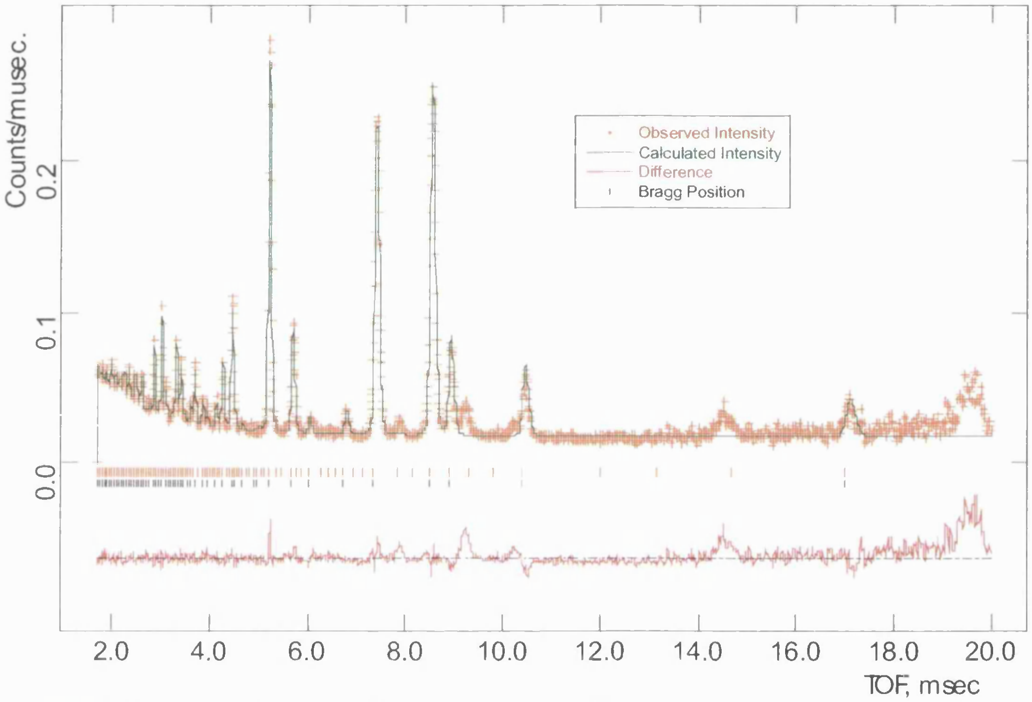

Figure 9.67 *Rietveld refinement of the powder neutron diffraction pattern of $ZnCr_2Se_4$ at 2K in an applied field of 1 Tesla, showing the observed, calculated and difference intensity plots.*

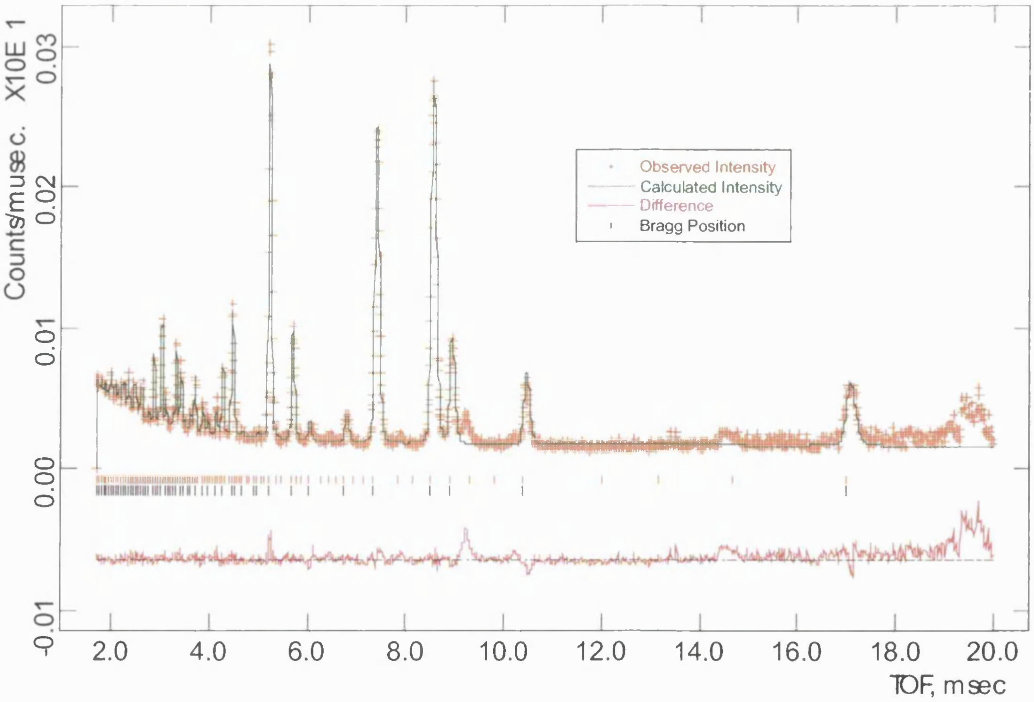

Figure 9.68 *Rietveld refinement of the powder neutron diffraction pattern of $ZnCr_2Se_4$ at 2K in an applied field of 1 Tesla, showing the observed, calculated and difference intensity plots.*

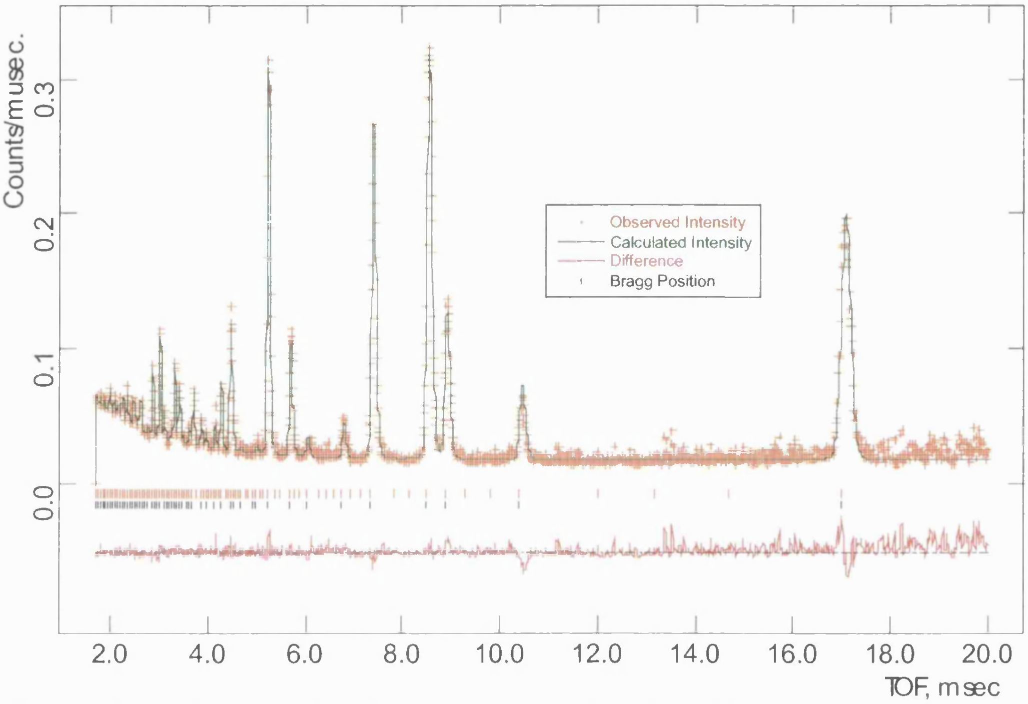

Figure 9.69 *Rietveld refinement of the powder neutron diffraction pattern of* $ZnCr_2Se_4$ *at 2K in an applied field of 8 Tesla, showing the observed, calculated and difference intensity plots.*

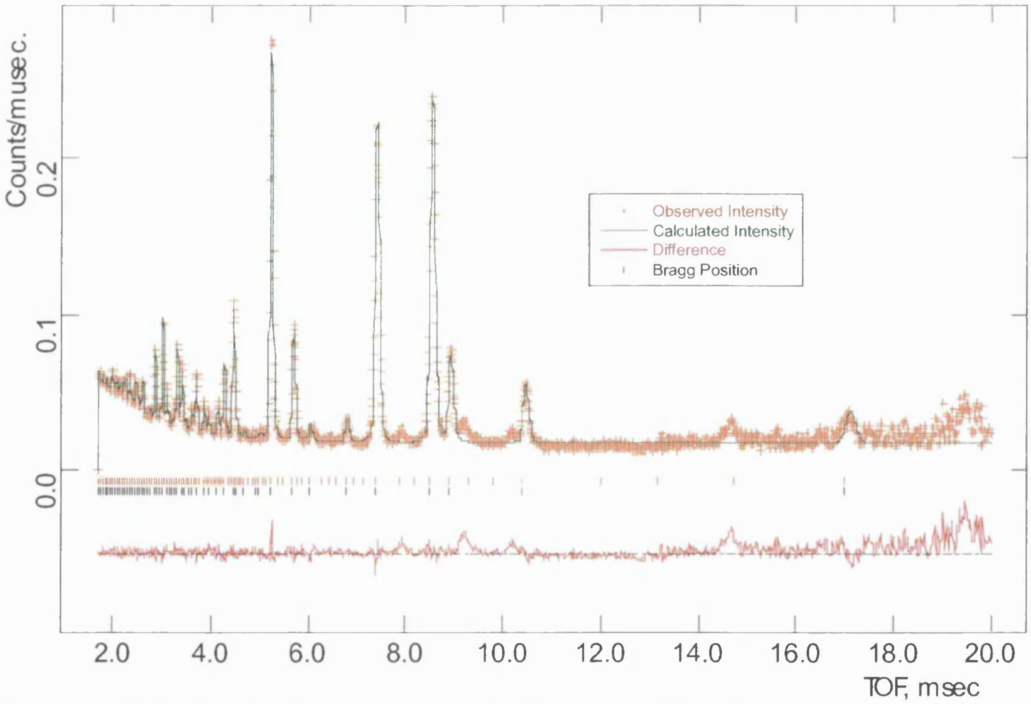

Figure 9.70 *Rietveld refinement of the powder neutron diffraction pattern of* $ZnCr_2Se_4$ *at 20K, showing the observed, calculated and difference intensity plots.*

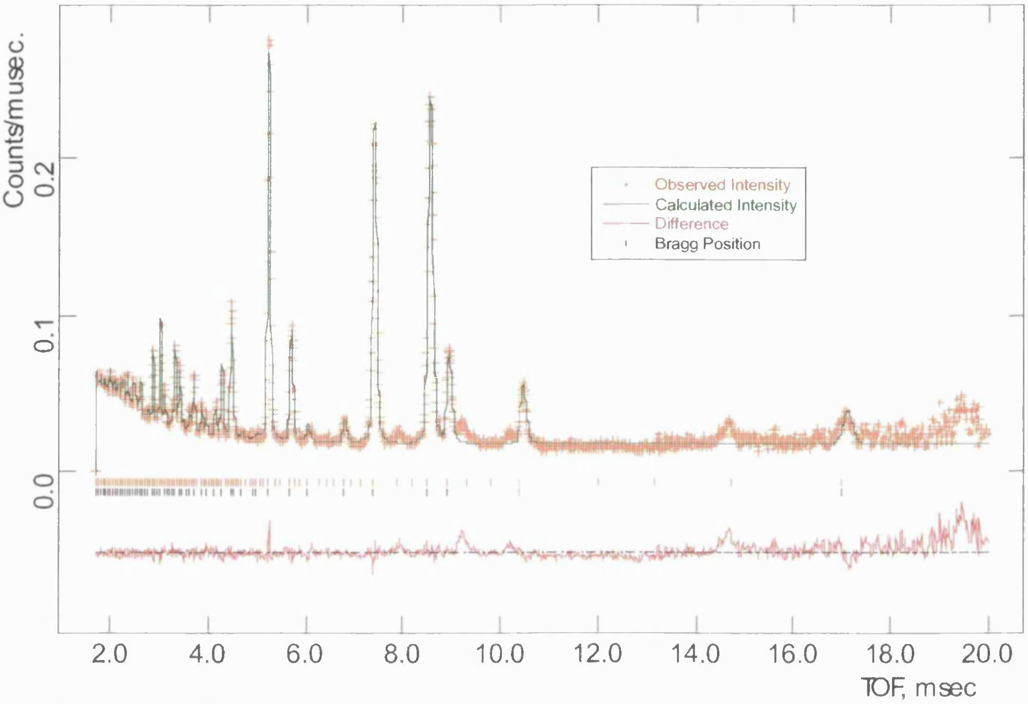

Figure 9.71 *Rietveld refinement of the powder neutron diffraction pattern of $ZnCr_2Se_4$ at 30K, showing the observed, calculated and difference intensity plots.*

A.4.2 $Cu_{0.05}Zn_{0.95}Cr_2Se_4$

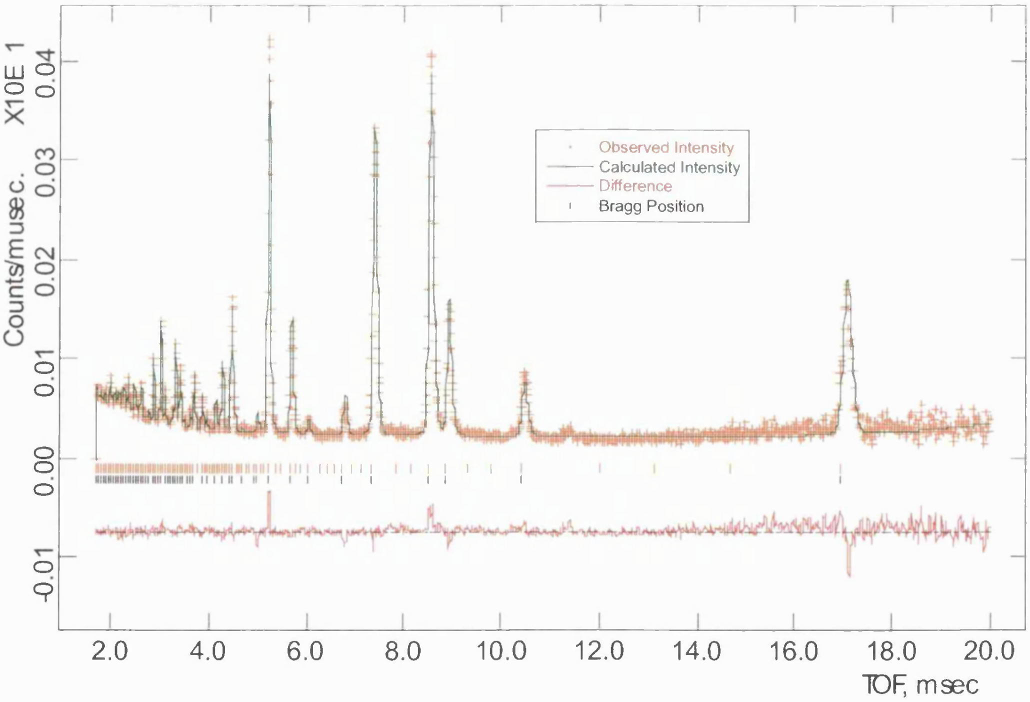

Figure 9.72 *Rietveld refinement of the powder neutron diffraction pattern of $Cu_{0.05}Zn_{0.95}Cr_2Se_4$ at 2K in an applied field of 1 Tesla, showing the observed, calculated and difference intensity plots.*

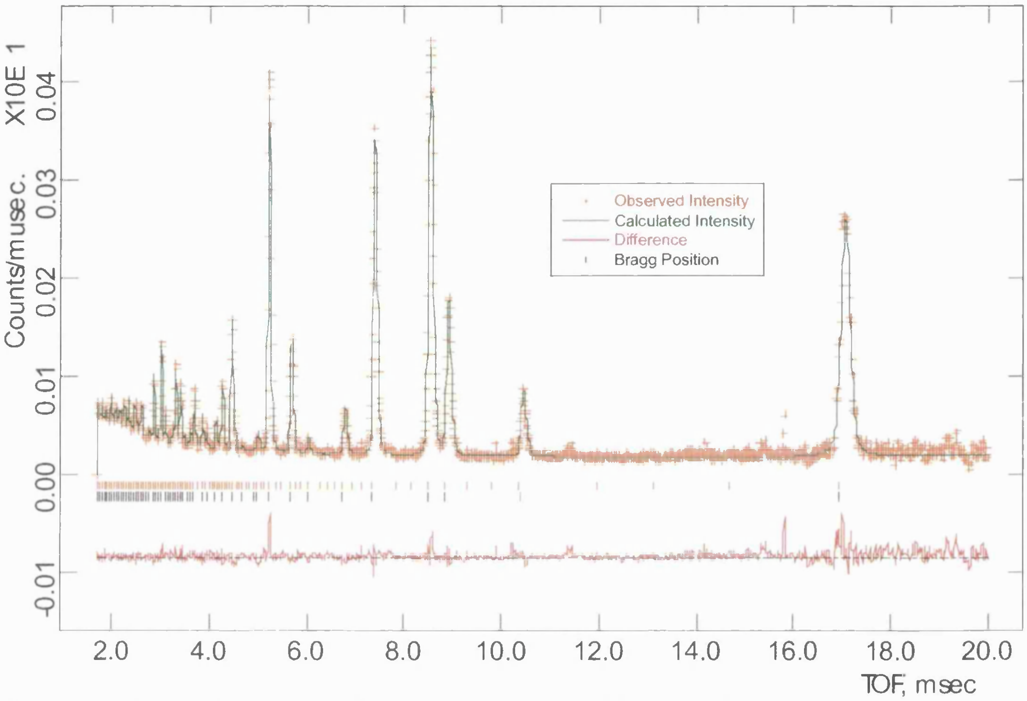

Figure 9.73 *Rietveld refinement of the powder neutron diffraction pattern of* $Cu_{0.05}Zn_{0.95}Cr_2Se_4$ *at 2K in an applied field of 3 Tesla, showing the observed, calculated and difference intensity plots.*

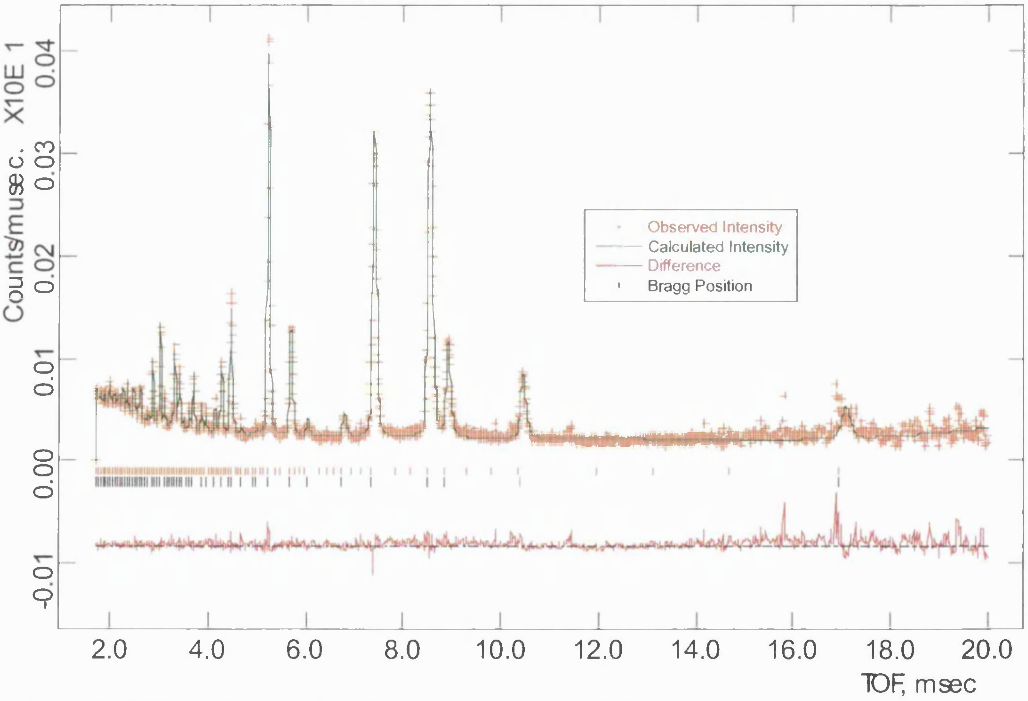

Figure 9.74 *Rietveld refinement of the powder neutron diffraction pattern of* $Cu_{0.05}Zn_{0.95}Cr_2Se_4$ *at 60 K,, showing the observed, calculated and difference intensity plots.*

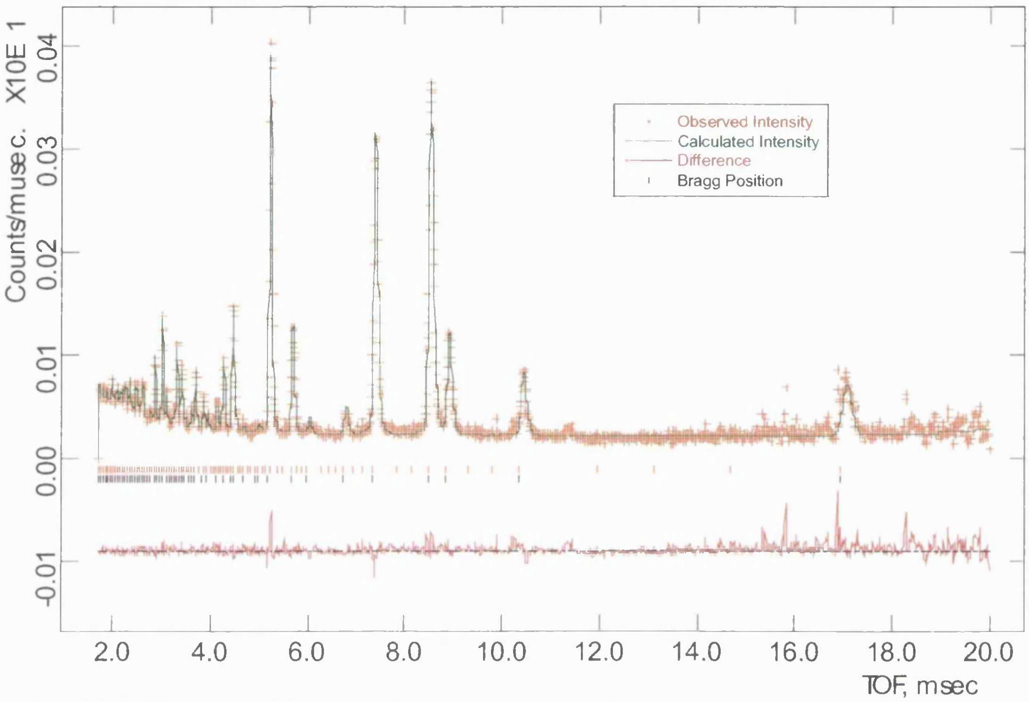

Figure 9.75 *Rietveld refinement of the powder neutron diffraction pattern of* $Cu_{0.05}Zn_{0.95}Cr_2Se_4$ *at 60K, showing the observed, calculated and difference intensity plots.*

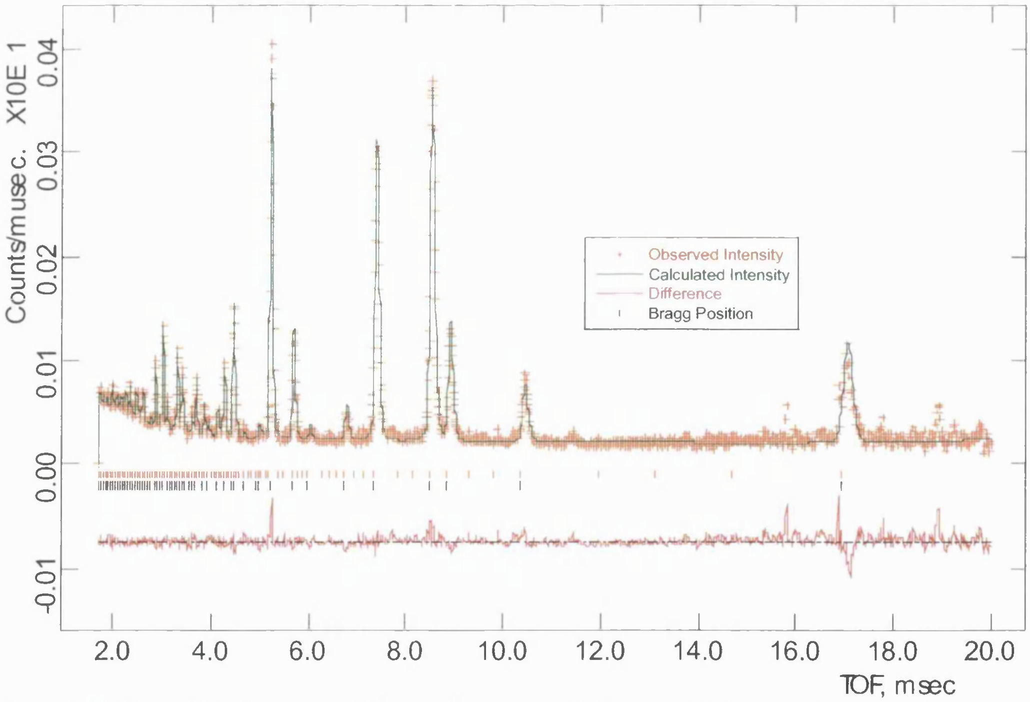

Figure 9.76 *Rietveld refinement of the powder neutron diffraction pattern of* $Cu_{0.05}Zn_{0.95}Cr_2Se_4$ *at 60K in an applied field of 3 Tesla, showing the observed, calculated and difference intensity plots.*

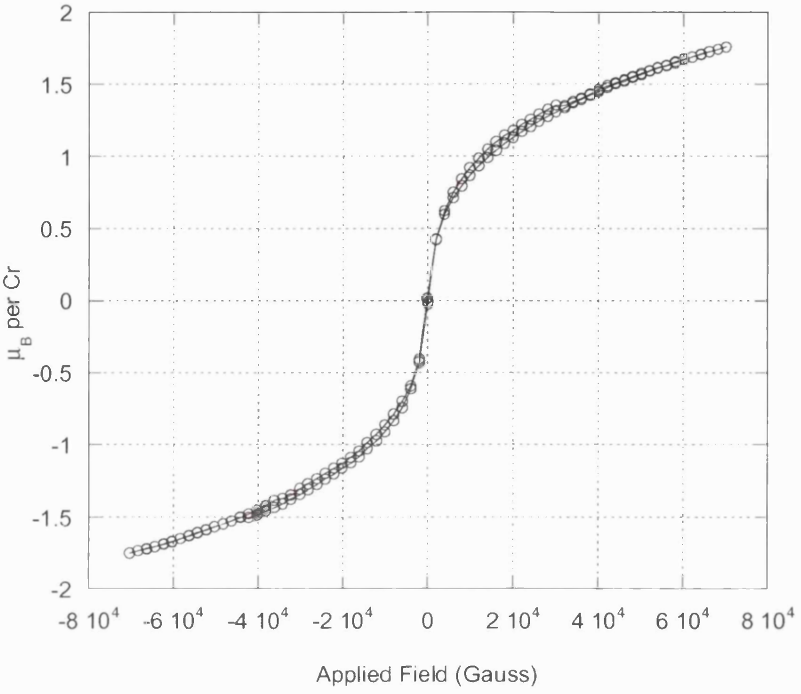

Figure 9.77 *Magnetisation vs. field of* $Cu_{0.05}Zn_{0.95}Cr_2Se_4$ *at 60 K.*

A.4.3 $Cu_{0.09}Zn_{0.91}Cr_2Se_4$

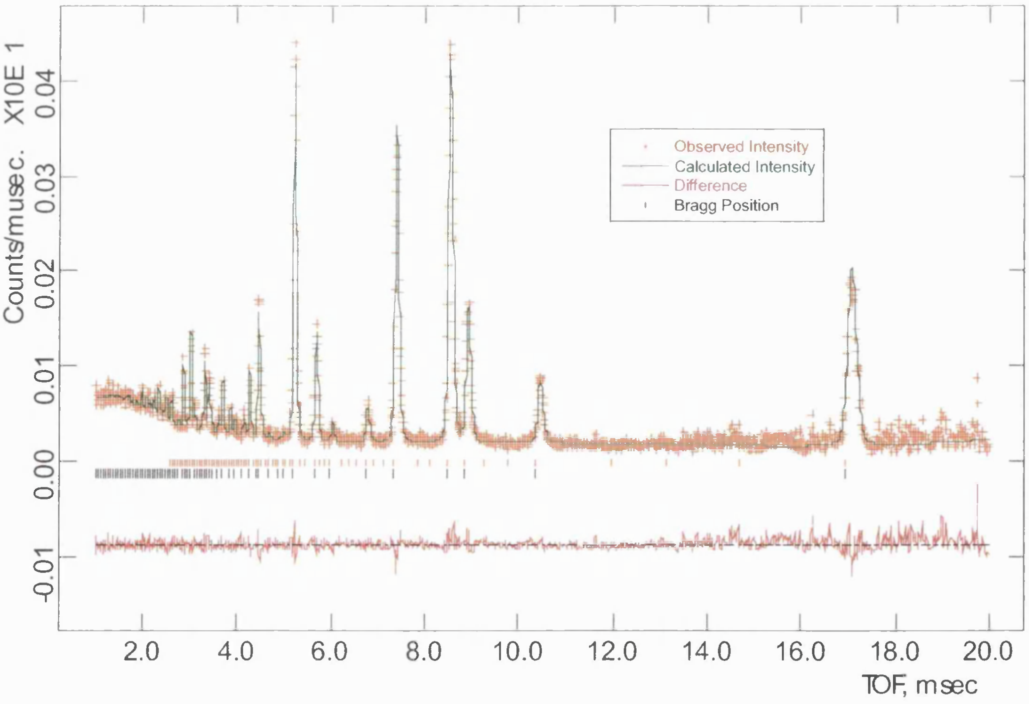

Figure 9.78 *Rietveld refinement of the powder neutron diffraction pattern of* $Cu_{0.09}Zn_{0.91}Cr_2Se_4$ *at 2K in an applied field of 5 Tesla, showing the observed, calculated and difference intensity plots.*

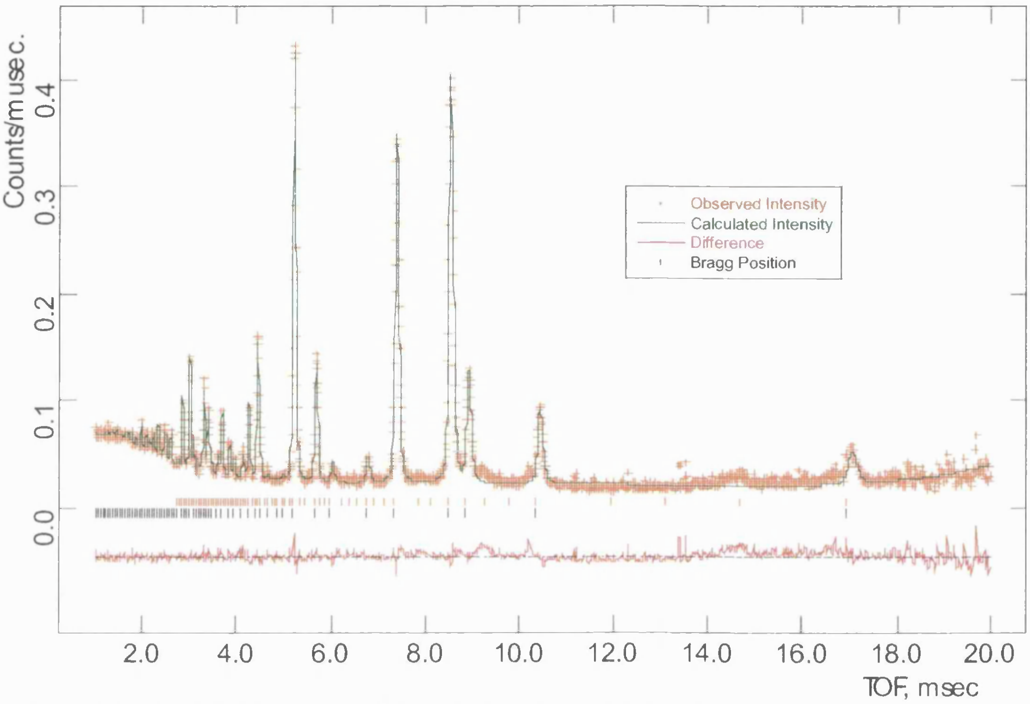

Figure 9.79 *Rietveld refinement of the powder neutron diffraction pattern of* $Cu_{0.09}Zn_{0.91}Cr_2Se_4$ *at 15K, showing the observed, calculated and difference intensity plots.*

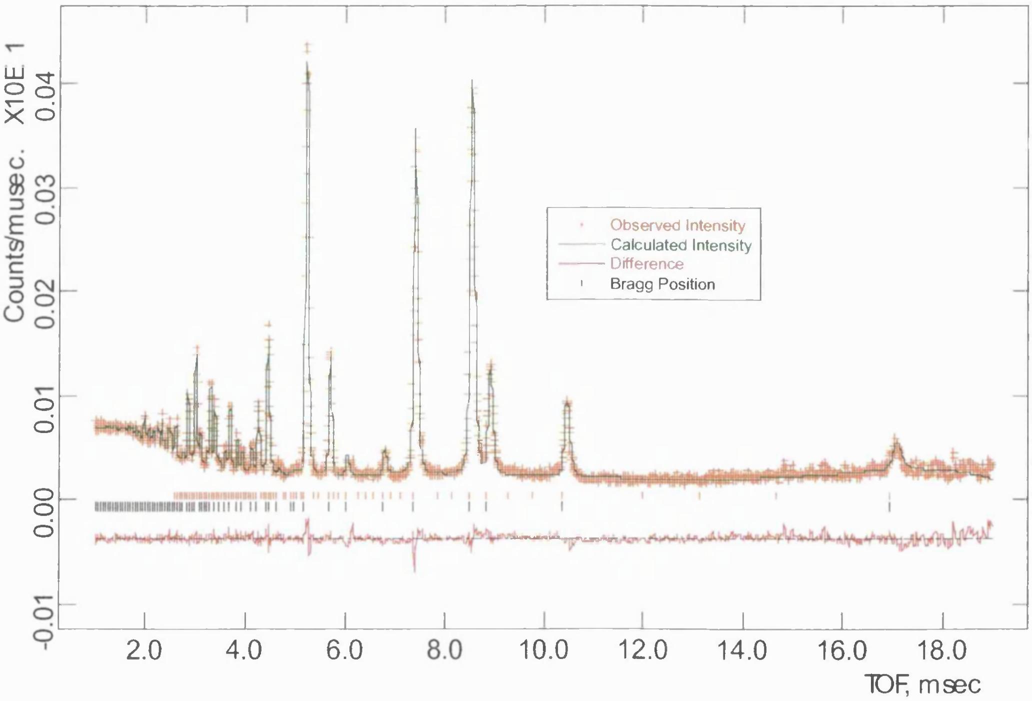

Figure 9.80 *Rietveld refinement of the powder neutron diffraction pattern of* $Cu_{0.09}Zn_{0.91}Cr_2Se_4$ *at 25 K, showing the observed, calculated and difference intensity plots.*

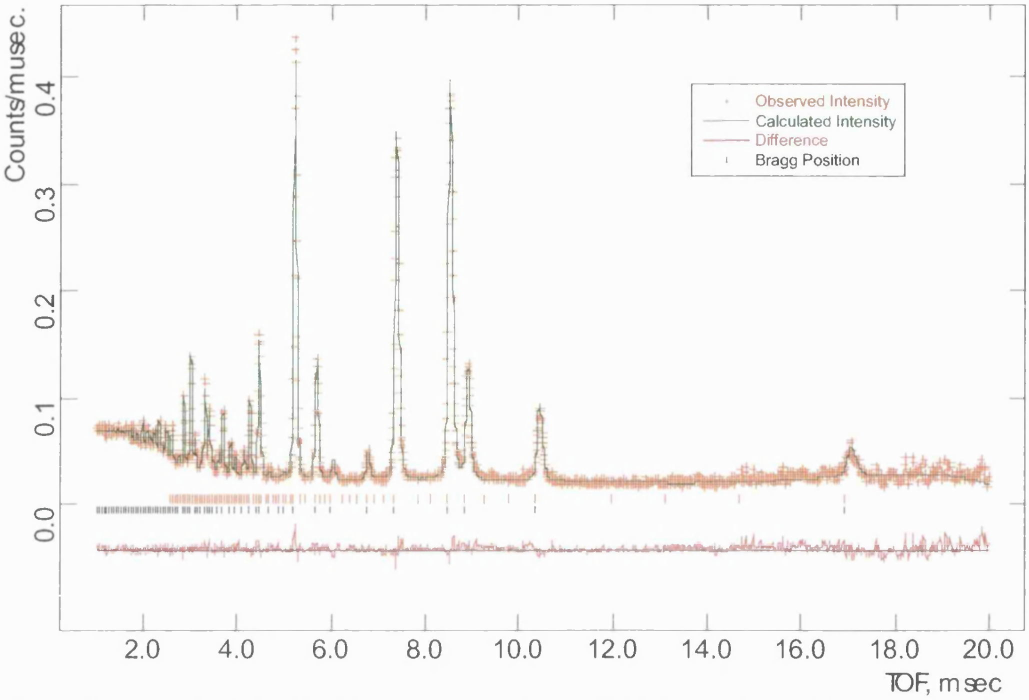

Figure 9.81 *Rietveld refinement of the powder neutron diffraction pattern of* $Cu_{0.09}Zn_{0.91}Cr_2Se_4$ *at 50 K, showing the observed, calculated and difference intensity plots.*

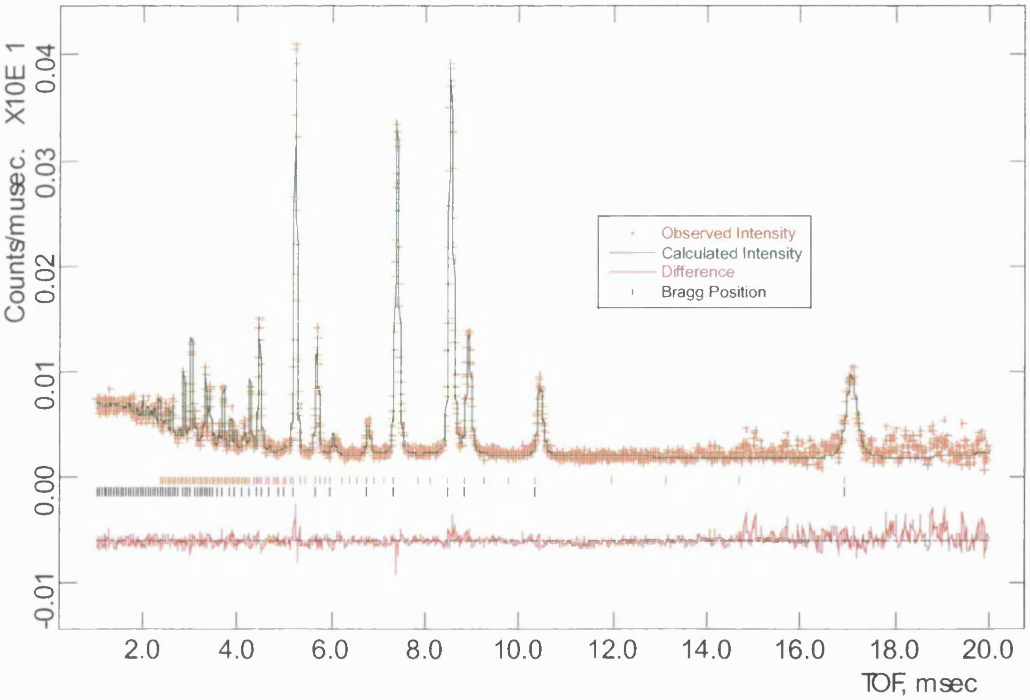

Figure 9.82 *Rietveld refinement of the powder neutron diffraction pattern of* $Cu_{0.09}Zn_{0.91}Cr_2Se_4$ *at 50 K in an applied field of 5 Tesla, showing the observed, calculated and difference intensity plots.*

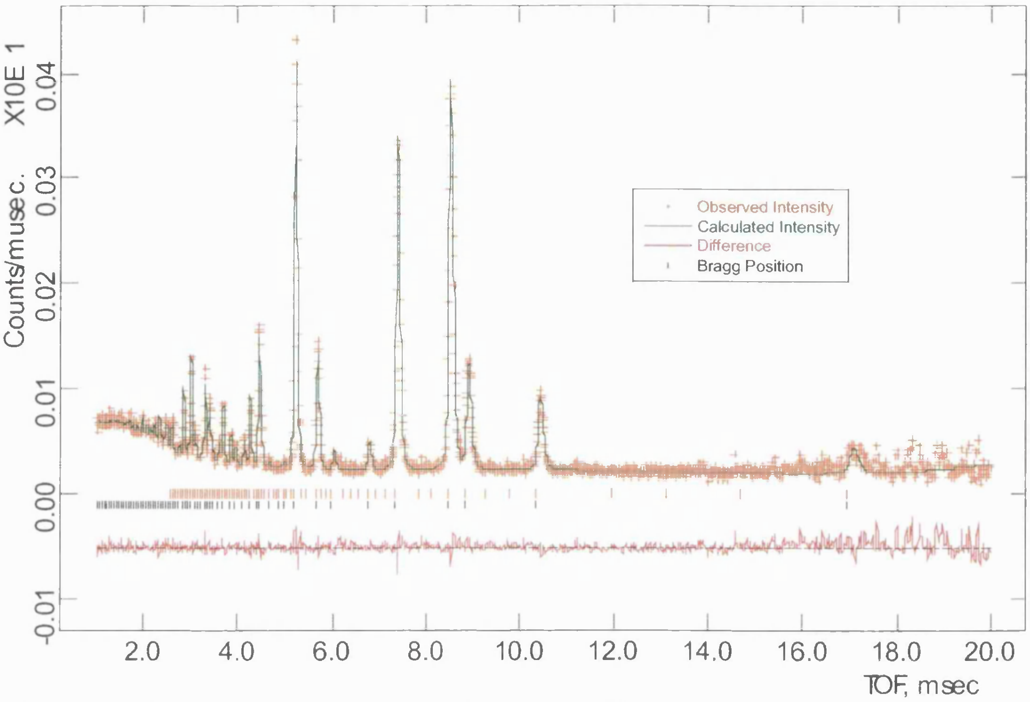

Figure 9.83 *Rietveld refinement of the powder neutron diffraction pattern of* $Cu_{0.09}Zn_{0.91}Cr_2Se_4$ *at 150 K, showing the observed, calculated and difference intensity plots.*

A.4.4 $Cu_{0.25}Zn_{0.75}Cr_2Se_4$

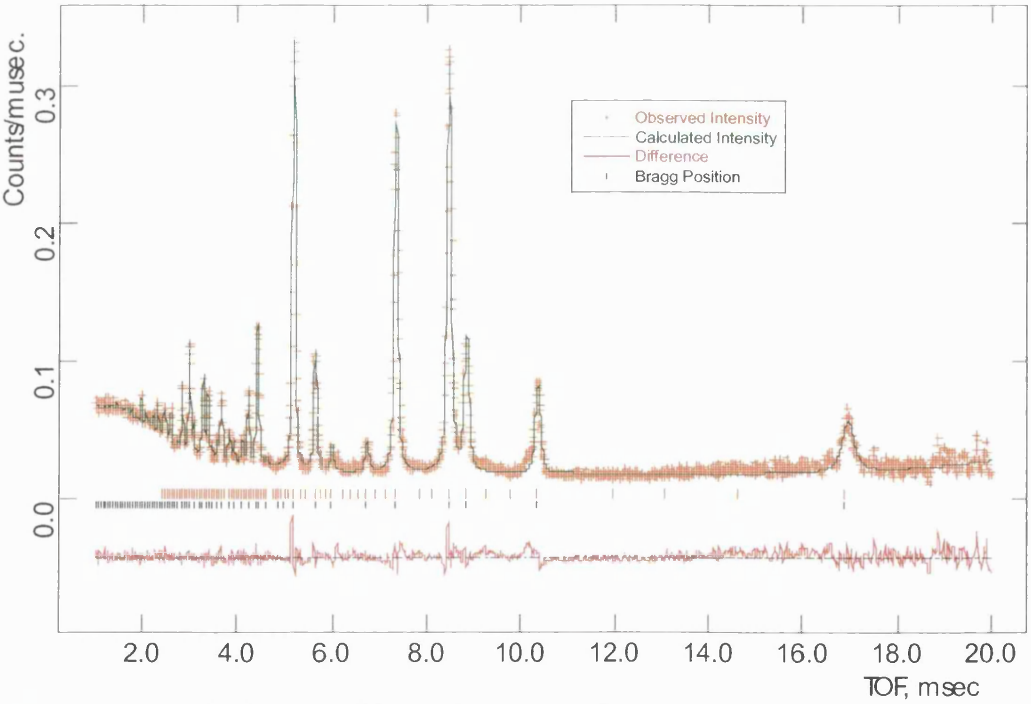

Figure 9.84 *Rietveld refinement of the powder neutron diffraction pattern of* $Cu_{0.25}Zn_{0.75}Cr_2Se_4$ *at 5 K in an applied field of 0.01 Tesla, showing the observed, calculated and difference intensity plots.*

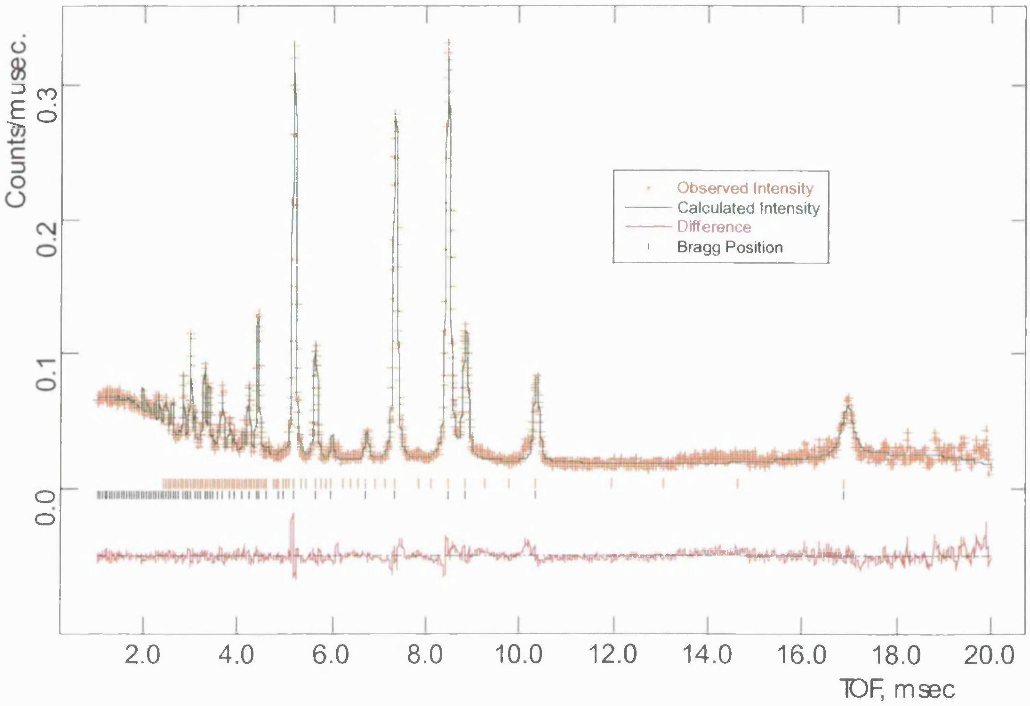

Figure 9.85 *Rietveld refinement of the powder neutron diffraction pattern of* $Cu_{0.25}Zn_{0.75}Cr_2Se_4$ *at 5 K in an applied field of 0.1 Tesla, showing the observed, calculated and difference intensity plots.*

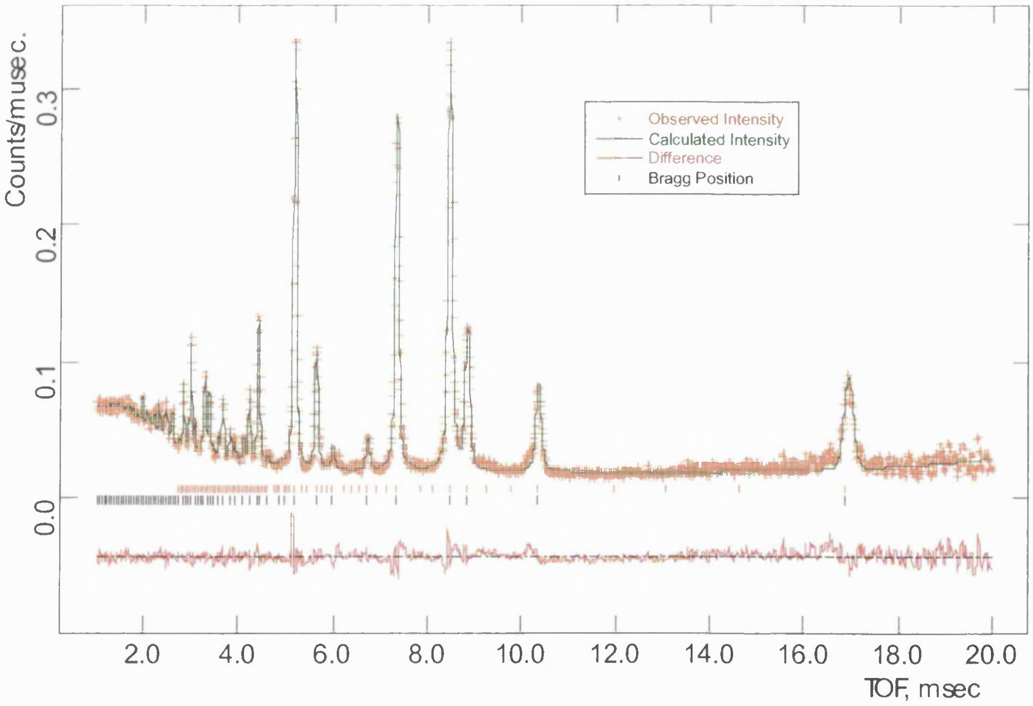

Figure 9.86 *Rietveld refinement of the powder neutron diffraction pattern of* $Cu_{0.25}Zn_{0.75}Cr_2Se_4$ *at 5 K in an applied field of 0.1 Tesla, showing the observed, calculated and difference intensity plots.*

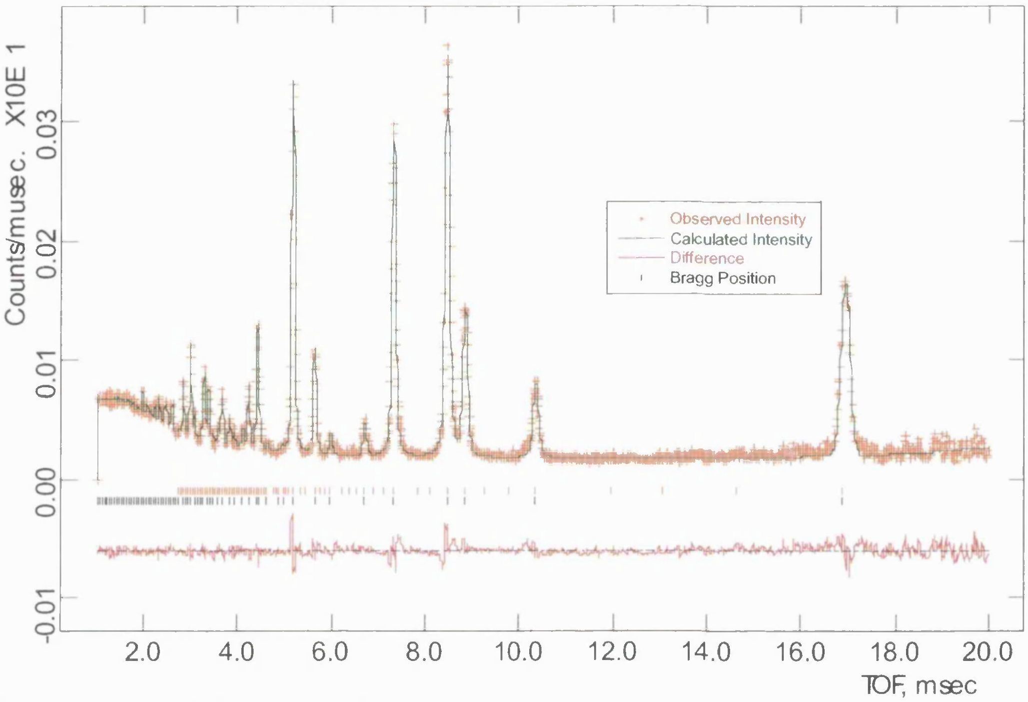

Figure 9.87 *Rietveld refinement of the powder neutron diffraction pattern of* $Cu_{0.25}Zn_{0.75}Cr_2Se_4$ *at 5 K in an applied field of 5 Tesla, showing the observed, calculated and difference intensity plots.*

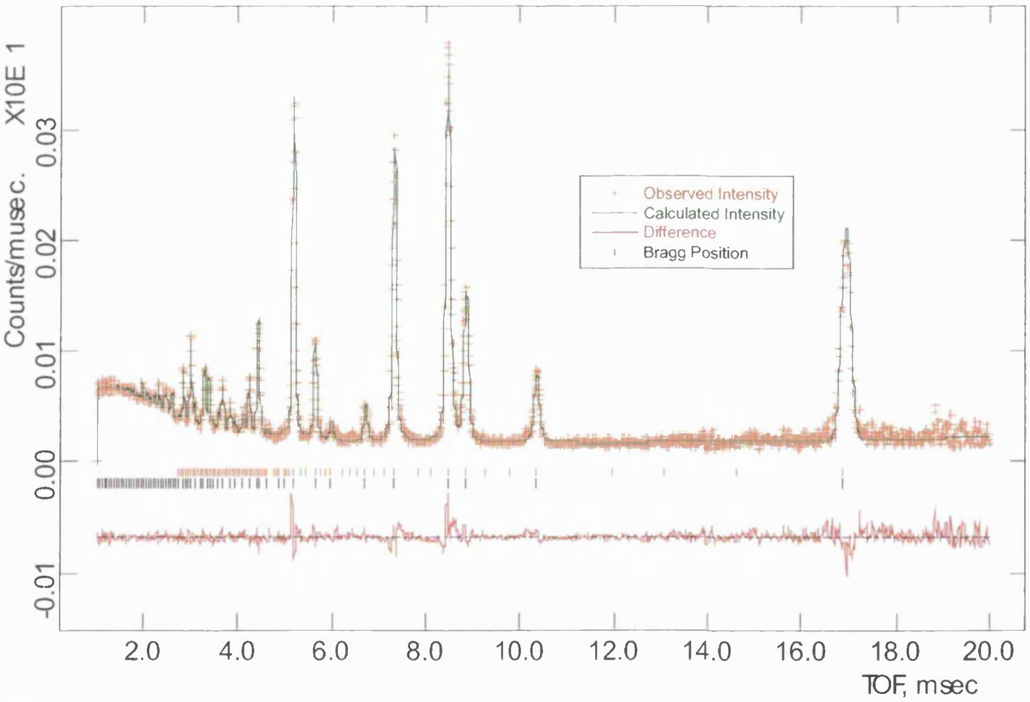

Figure 9.88 *Rietveld refinement of the powder neutron diffraction pattern of* $Cu_{0.25}Zn_{0.75}Cr_2Se_4$ *at 5 K in an applied field of 8 Tesla, showing the observed, calculated and difference intensity plots.*

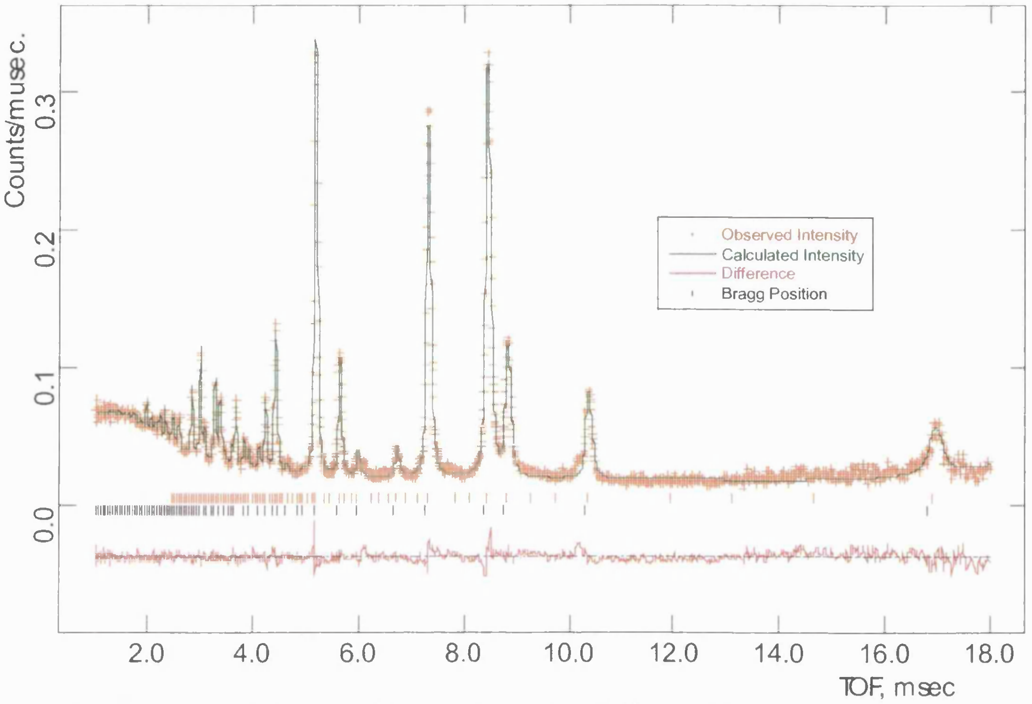

Figure 9.89 *Rietveld refinement of the powder neutron diffraction pattern of* $Cu_{0.25}Zn_{0.75}Cr_2Se_4$ *at 15 K, showing the observed, calculated and difference intensity plots.*

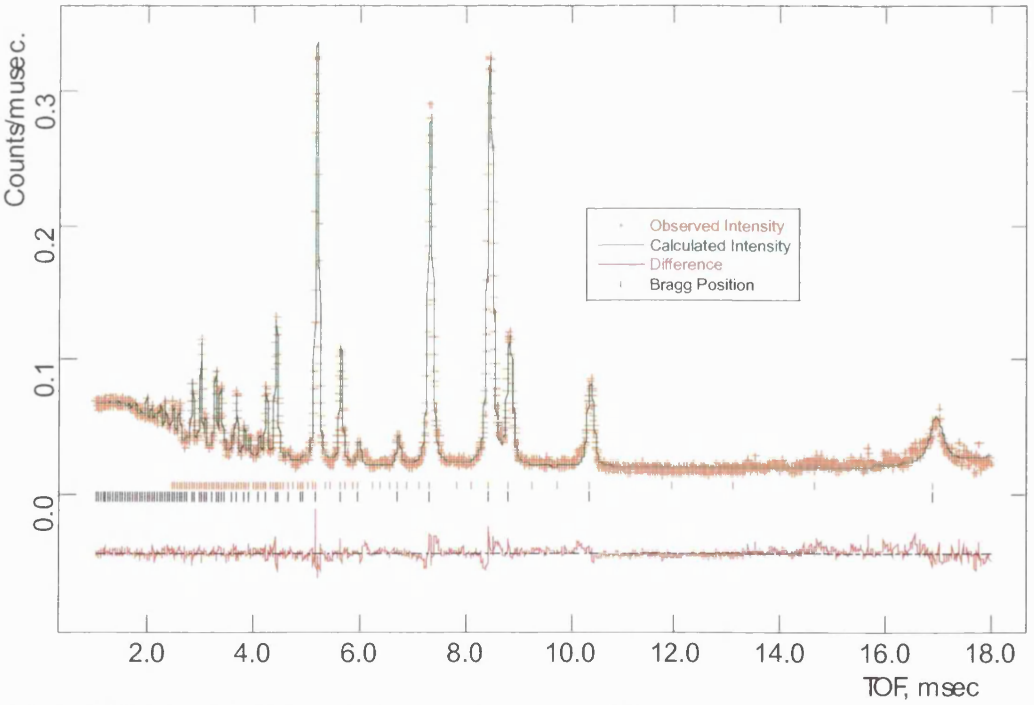

Figure 9.90 *Rietveld refinement of the powder neutron diffraction pattern of* $Cu_{0.25}Zn_{0.75}Cr_2Se_4$ *at 25 K, showing the observed, calculated and difference intensity plots.*

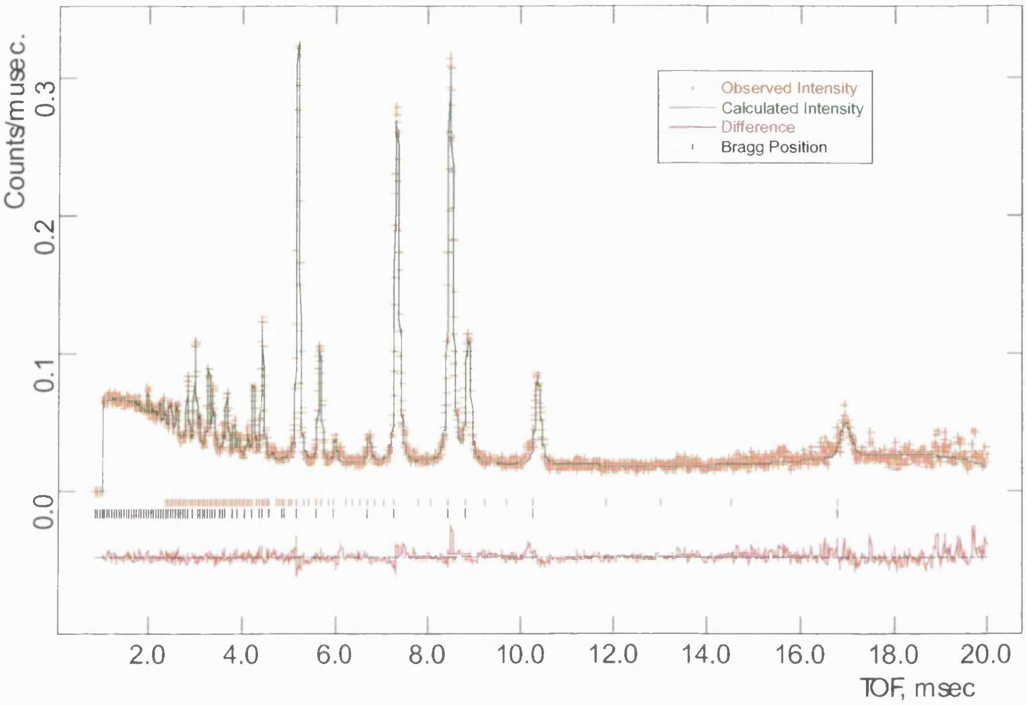

Figure 9.91 *Rietveld refinement of the powder neutron diffraction pattern of* $Cu_{0.25}Zn_{0.75}Cr_2Se_4$ *at 50 K, showing the observed, calculated and difference intensity plots.*

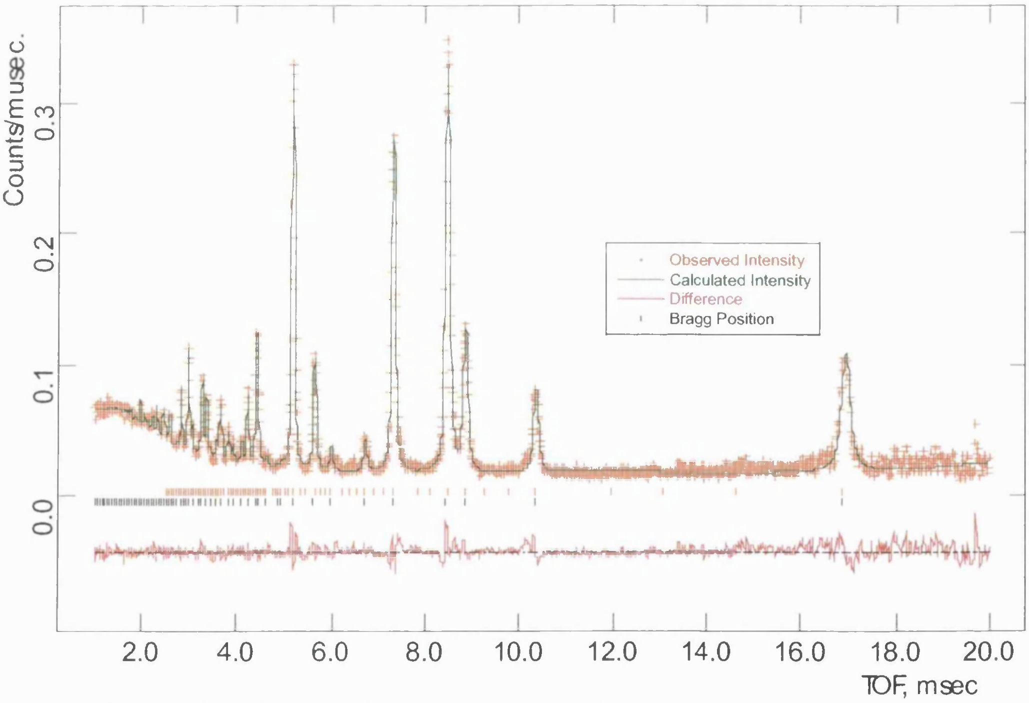

Figure 9.92 *Rietveld refinement of the powder neutron diffraction pattern of* $Cu_{0.25}Zn_{0.75}Cr_2Se_4$ *at 50 K in an applied field of 5 Tesla, showing the observed, calculated and difference intensity plots.*